HYDROMECHANICAL AND FRICTIONAL FAULTING BEHAVIOR OF FLUID-INJECTION-INDUCED EARTHQUAKES

A DISSERTATION
SUBMITTED TO THE DEPARTMENT OF ENERGY RESOURCES ENGINEERING
AND THE COMMITTEE ON GRADUATE STUDIES
OF STANFORD UNIVERSITY
IN PARTIAL FULFILLMENT OF THE REQUIREMENTS
FOR THE DEGREE OF
DOCTOR OF PHILOSOPHY

Jack Hunter Norbeck
November 2016

This dissertation is online at: http://purl.stanford.edu/km278sp0131

I certify that I have read this dissertation and that, in my opinion, it is fully adequate in scope and quality as a dissertation for the degree of Doctor of Philosophy.

Roland Horne, Primary Adviser

I certify that I have read this dissertation and that, in my opinion, it is fully adequate in scope and quality as a dissertation for the degree of Doctor of Philosophy.

Eric Dunham

I certify that I have read this dissertation and that, in my opinion, it is fully adequate in scope and quality as a dissertation for the degree of Doctor of Philosophy.

Mark Zoback

Approved for the Stanford University Committee on Graduate Studies.

Patricia J. Gumport, Vice Provost for Graduate Education

This signature page was generated electronically upon submission of this dissertation in electronic format. An original signed hard copy of the signature page is on file in University Archives.

Abstract

This work serves to advance a fundamental understanding on the role of the coupled interaction between hydromechanical and frictional processes that influence fluid-injection-induced earthquakes. An analysis of the hydraulic stimulation and fluid circulation experiments at the Fenton Hill Enhanced Geothermal System test site supported the hypothesis that permeability enhancement occurred though a mixed-mechanism combination of mechanical opening of fractures and propagation of hydraulic splay fractures from the tips of preexisting natural fractures. A novel field test, called microseismic depletion delineation, was demonstrated to provide useful reservoir engineering information about production trends near horizontal wells in unconventional hydrocarbon reservoirs. An investigation of the 2011 M_{w} 5.6 Prague, Oklahoma earthquake sequence suggested that an initial undrained response resulting from elastic stress transfer from the foreshock followed by transient fluid flow along the fault may have influenced the timing of the main shock. The relationship between wastewater disposal well operational data and statistics of earthquake sequences that inform seismic hazard analyses was investigated using a coupled fluid flow and rate-and-state earthquake model.

Acknowledgments

Many people have contributed intellectually and spiritually to this work, and they deserve my sincere gratitude. Most of all, thank you to my advisor, Dr. Roland Horne, for hosting me in an amazing academic environment over the last five years. Roland's dedication to fostering the success of his students is, in my observation, unmatched.

I have been fortunate to have many opportunities to discuss this work with the faculty at Stanford. Dr. Mark Zoback and Dr. Eric Dunham provided helpful criticism and encouraged close interaction with their research groups. Thank you to Dr. Louis Durlofsky, Dr. David Pollard, Dr. Mohammad Karimi-Fard, Dr. Atilla Aydin, and Dr. Bill Ellsworth for providing useful perspectives on the topics discussed in this dissertation.

I have enjoyed my time as a member of the Stanford Geothermal Program. I will have fond memories of weekly meetings and worldwide travel with Dr. Mohammad Alaskar, Dr. Morgan Ames, Carla Co, Xuhua Gao, Halldora Gudmundsdottir, Renfeng Jiang, Dr. Kewen Li, Dr. Lilja Magnusdottir, Spencer Manley, Dr. Anna Suzuki, Yang Wong, and Yuran Zhang. It is a privilege to have been affiliated with the students and faculty of the Stanford Center for Induced and Triggered Seismicity since the program's inception.

I thank Dr. Mark McClure for the devotion of his time and resources, which have been instrumental throughout the entirety of this work. Dr. David Dempsey provided critical reviews of parts of this work, for which I am grateful. The modeling framework developed in this work was inspired greatly through discussions with Dr. Seong H. Lee. The analysis of the Fenton Hill geothermal system, presented in Chapter 4, was made possible through extensive collaboration with participants of the US Department of Energy Geothermal Technologies Office geothermal code comparison study including Dr. Mark White, Ms. Signe White, Dr. Pengcheng Fu, Dr. Sharad Kelkar, and Dr. Don Brown. The software package called MDSBI, made available by Dr. Eric Dunham, was used to benchmark the numerical model used in this work. The AD-GPRS software package was also used in benchmark comparisons with the assistance of Dr. Timur Garipov. The open-source finite element software package provided by Dr. D.V. Griffiths, Professor of Civil Engineering, Colorado School of Mines, was modified for use in this work. The assistance of Claudia Baroni, Joleen Castro, Rachael Madison, Joanna Sun, and Yolanda Williams has been invaluable.

The financial support of the industrial affiliates of the Stanford Center for Induced and Triggered Seismicity are gratefully acknowledged. Financial support was also provided by the US Department of Energy Geothermal Technologies Office. The numerical simulations in this work were performed at the Stanford Center for Computational Earth and Environmental Science using their high performance computing resources.

Thank you to my sisters, Dagny, Hilevi, and Lakin, as well as each of my family and friends for your enduring encouragement.

Nomenclature

All variables are defined when they are first introduced in the text. The following lists of variables, subscripts, and superscripts are provided for reference.

Roman variables

Variable	Description	SI Unit
a	Direct effect parameter in rate-and-state friction model	-
a_{GR}	Earthquake rate in Gutenberg-Richter model	-
A	Area	m^2
$\mathbf{A}$	Matrix of Green's functions in displacement discontinuity method	$Pa \cdot m^{-1}$
b	State evolution parameter in rate-and-state friction model	-
b_{GR}	Frequency-magnitude scaling parameter in Gutenberg-Richter model	-
B	Skempton coefficient	-
$\mathbf{B}$	Strain-displacement matrix in finite element method	m^{-1}
c_r	Heat capacity of rock	$J \cdot kg^{-1} \cdot K^{-1}$
c_φ	Heat capacity of fluid	$J \cdot kg^{-1} K^{-1}$
C_L	Leakoff coefficient	$m \cdot s^{-1/2}$
$\mathbf{d}$	Unit vector in dip-direction	-
D	Fractal dimension	-
D_H	Hydraulic diffusivity	$m^2 \cdot s^{-1}$
D_T	Thermal diffusivity	$m^2 \cdot s^{-1}$
$\langle D \rangle$	Average normal distance	m
$\mathbf{D}$	Stress-strain matrix in finite element method	Pa
e	Hydraulic aperture of fracture	m
e_{res}	Residual hydraulic aperture of fracture	m
e_*	Reference hydraulic aperture in joint stiffness equation	m
E	Void aperture of fracture	m
E_{res}	Residual void aperture of fracture	m

E_*	Reference void aperture in joint stiffness equation	m
f	Friction coefficient	-
f_D	Dynamic (residual) friction coefficient	-
f_{ss}	Steady-state friction coefficient in rate-and-state friction model	-
f_S	Static friction coefficient	-
f_*	Reference coefficient of friction in rate-and-state friction model	-
$\mathbf{f}$	Vector of nodal body forces in finite element method	$\mathrm{Pa} \cdot \mathrm{m}$
F_i	Body force vector	$\mathrm{N} \cdot \mathrm{m}^{-3}$
G	Shear modulus of rock	Pa
h	Energy transfer rate	W
h_f	Fracture height	m
H	Height, or energy	m, or J
i	Reservoir impedance	$\mathrm{Pa} \cdot \mathrm{m}^{-3} \cdot \mathrm{s}$
I	Connectivity index in embedded fracture model	m
k	Permeability, or fracture stiffness	m^2, or $\mathrm{Pa} \cdot \mathrm{m}^{-1}$
k_c	Characteristic fracture stiffness	$\mathrm{Pa} \cdot \mathrm{m}^{-1}$
k_{ij}	Permeability tensor	m^2
$\mathbf{k}$	Stiffness matrix in finite element method	Pa
K	Bulk modulus of rock	Pa
K_d	Spectral wave number (dip-direction) in spatial random field model	m^{-1}
K_s	Spectral wave number (strike-direction) in spatial random field model	m^{-1}
L	Length	m
L_c	Characteristic length for earthquake nucleation	m
m	Mass transfer rate, or earthquake magnitude	$\mathrm{kg} \cdot \mathrm{s}^{-1}$, or -
m_L	Carter mass leakoff rate	$\mathrm{kg} \cdot \mathrm{s}^{-1}$
M	Earthquake magnitude	-
M_0	Earthquake (seismic) moment	$\mathrm{N} \cdot \mathrm{m}$
n_i	Unit vector in normal-direction	-
$\mathbf{n}$	Unit vector in normal-direction	-
N^f	Number of control volumes in the fracture domain	-
N^m	Number of control volumes in the matrix domain	-
$N_{M \geq m}$	Rate of earthquakes with magnitude M larger than a reference magnitude m	s^{-1}
p	Fluid pressure	Pa
p_D	Dimensionless pressure	-
P	Power spectral decay of stress in spatial random field model	Pa
q	Volumetric flow rate	$\mathrm{m}^3 \cdot \mathrm{s}^{-1}$

q_L	Carter leakoff rate	$m^3 \cdot s^{-1}$
Q	Volumetric flow rate, or cumulative volume of fluid	$m^3 \cdot s^{-1}$, or m^3
R	Residual value	$m^3 \cdot s^{-1}$, or m^3
s	Fracture cohesion, or Laplace transformation parameter	Pa, or -
$\mathbf{s}$	Unit vector in strike-direction	-
S	Fault storativity	$m \cdot s$
t_c	Characteristic time	s
t_D	Dimensionless time	-
t_i	Traction vector	Pa
T	Fault transmissivity, or temperature	m^3, or K
T_c	Characteristic fracture transmissivity	m^3
T_D	Dimensionless temperature	-
u_i	Rock displacement vector	m
$\mathbf{u}$	Vector of nodal displacements in finite element method	m
v_i	Fluid velocity vector	$m \cdot s^{-1}$
v_L	Carter leakoff velocity	$m \cdot s^{-1}$
V	Sliding velocity, or volume	$m \cdot s^{-1}$, or m^3
V_*	Reference sliding velocity in rate-and-state friction model	$m \cdot s^{-1}$
x_c	Characteristic distance	m
x_D	Dimensionless distance	-
x_f	Fracture half-length	m
y_D	Dimensionless distance	-
y_E	Fracture spacing	m

Greek variables

Variable	Description	SI Unit
α	Scaling factor in spatial random field model	-
α^P	Biot coefficient	-
α^T	Linear thermal expansion coefficient	K^{-1}
β_f	Compressibility of fracture	Pa^{-1}
β_r	Compressibility of rock	Pa^{-1}
β_t	Total compressibility (sum of fluid and rock/fracture compressibility)	Pa^{-1}
β_φ	Compressibility of fluid	Pa^{-1}
γ	Stress or pressure gradient	$Pa \cdot m^{-1}$

δ_c	Characteristic slip-weakening distance in rate-and-state friction model	m
δ_d	Sliding-mode (dip direction) displacement discontinuity	m
δ_{ij}	Kronecker delta function	-
δ_n	Opening-mode displacement discontinuity	m
δ_s	Sliding-mode (strike direction) displacement discontinuity	m
ϵ	Error	-
ε_{ij}	Strain tensor	-
η	Radiation damping coefficient	$\mathrm{Pa} \cdot \mathrm{m}^{-1} \cdot \mathrm{s}$
θ	Orientation	rad.
κ_{ij}	Thermal conductivity tensor	$\mathrm{W} \cdot \mathrm{m}^{-1} \cdot \mathrm{K}^{-1}$
κ_r	Thermal conductivity of rock	$\mathrm{W} \cdot \mathrm{m}^{-1} \cdot \mathrm{K}^{-1}$
κ_φ	Thermal conductivity of fluid	$\mathrm{W} \cdot \mathrm{m}^{-1} \cdot \mathrm{K}^{-1}$
λ	Inverse fluid viscosity	$\mathrm{Pa}^{-1} \cdot \mathrm{s}^{-1}$
Λ	Lamé coefficient of rock	Pa
μ	Fluid viscosity	$\mathrm{Pa} \cdot \mathrm{s}$
ν	Poisson ratio of rock	-
ξ	Variable normal stress parameter in rate-and-state friction model	-
Π	Energy transfer rate between fracture and matrix domain	W
ρ_r	Density of rock	$\mathrm{kg} \cdot \mathrm{m}^{-3}$
ρ_φ	Density of fluid	$\mathrm{kg} \cdot \mathrm{m}^{-3}$
σ_C	Coulomb stress	Pa
σ_d	Shear stress in dip-direction	Pa
σ_{e*}	Reference normal stress in joint stiffness equation	Pa
σ_{E*}	Reference normal stress in joint stiffness equation	Pa
σ_n	Normal stress	Pa
$\bar{\sigma}_n$	Effective normal stress	Pa
σ_s	Shear stress in strike-direction	Pa
σ_{ij}	Stress tensor	Pa
ς	Dimensionless parameter in *Gringarten et al.* (1975) heat transfer model	-
τ	Shear stress	Pa
$\bar{\tau}$	Shear strength	Pa
Υ	Transmissibility for mass flux	$\mathrm{kg} \cdot \mathrm{s}^{-1} \cdot \mathrm{Pa}^{-1}$
ϕ	Porosity	-
φ_e	Shear dilation angle in joint stiffness equation	rad.
φ_E	Shear dilation angle in joint stiffness equation	rad.
χ	Standard deviation of stress in spatial random field model	Pa

ψ	Dimensionless parameter in *Valko and Economides* (1995) hydraulic fracture model	-
Ψ	State parameter in rate-and-state friction model	-
ω	Transmissibility for energy flux	$\mathrm{W} \cdot \mathrm{K}^{-1}$
Ω	Mass transfer rate between fracture and matrix domain	$\mathrm{kg} \cdot \mathrm{s}^{-1}$

Subscripts

Variable	Description
a, b	Indices used as counters
i, j, k	Indices used to represent a generic coordinate system
n, d, s	Indices used to represent a coordinate system centered on a fault element
h, H, V	Indices used to represent a coordinate system in the horizontal and vertical directions
0	Reference state

Superscripts

Variable	Description
f	Fault domain
n	Current time level in a temporal numerical discretization
m	Matrix domain
M	Mechanical loading
P	Poroelastic loading loading
R	Remote loading
T	Thermoelastic loading
w	Well domain

Contents

List of Tables

List of Figures

Chapter 1

Introduction

Historically, Earthquakes have been considered natural phenomena. The elastic potential energy stored in the Earth's crust, which can accumulate over geologic timescales due to tectonic forcing and deformation, is released occasionally as rapid bursts of seismic energy. Although the largest and most damaging earthquakes observed on Earth have occurred as a result of natural processes, there is an abundance of scientific evidence that suggests that it is possible for seismic activity to be influenced directly by anthropogenic forcing. Human-induced earthquakes have been associated with a range of civil engineering, mining engineering, and energy-related projects including reservoir impoundment behind dams (*Carder*, 1945; *Ge et al.*, 2009), conventional oil production (*Segall*, 1989), hydraulic fracturing in unconventional hydrocarbon resources (*Holland*, 2013; *Atkinson et al.*, 2016), hydraulic stimulation in deep geothermal resources (*Majer et al.*, 2007; *Häring et al.*, 2008), CO_2 storage and sequestration (*Kaven et al.*, 2015), and wastewater disposal by injection into deep subsurface aquifers (*Ellsworth*, 2013; *Healy et al.*, 1968).

It has been recognized that assessment of the potential for induced seismicity hazard must be a principal consideration of subsurface-energy-related projects that involve injection or extraction of large quantities of fluid (*NRC*, 2013). The purpose of this research was to investigate the nature of the hydromechanical and frictional processes that influence fluid-injection-induced earthquakes. An improved understanding of the mechanics of injection-induced seismicity will inform subsurface data acquisition and site characterization strategies, operational design of fluid injection projects, and seismic hazard assessment.

1.1 Background on injection-induced earthquakes

The first well-documented case of injection-induced seismicity occurred during the period of 1962 though 1967 near Denver, Colorado, USA (*Healy et al.*, 1968; *Hsieh and Bredehoeft*, 1981; *van Poollen and Hoover*, 1970). In 1962, the US Army began operating a wastewater disposal well at

the Rocky Mountain Arsenal. The well was drilled to a depth of 3.7 km and was completed in Precambrian crystalline basement rock. Over the five year period from 1962 through 1966, roughly 165 million gallons of chemical waste fluid was injected at rates that did not exceed 300 gallons per minute. The first earthquakes occurred in 1962, and over 100 earthquakes large enough to be felt at the surface occurred in the following years. In 1966, the US government ordered that the well be shut-in for fear of triggering a damaging earthquake. At this time, the US Geological Survey installed a seismic array at the site. In 1967, following shut-in of the well, the three largest earthquakes were recorded (M 4.8, 5.1, and 5.3). The preferred mechanism relating fluid injection and the earthquake activity was that increased fluid pressures at depth caused by injecting fluid mass into the subsurface counteracted the normal stress that provides frictional strength to preexisting faults. *van Poollen and Hoover* (1970) suggested that thermal effects caused by rock cooling may also have contributed to a reduction in the frictional strength of faults at depth.

In order to test the hypothesis that fluid injection could explain the events at the Denver Rocky Mountain Arsenal, the US Geological Survey, in partnership with the US Department of Defense and Chevron Oil Company, conducted a field experiment at the Rangely Oil Field in Colorado, USA (*Raleigh et al.*, 1976). A geomechanical model at the site was developed based on minifrac measurements and estimates of the overburden gradient. The frictional properties of the reservoir rock were measured in laboratory experiments. Beginning in 1969 and continuing through the early 1970s, earthquake activity was monitored with a local seismic network consisting of 14 seismometers. The field was operated as a waterflood project at this time. Analysis of the distribution of observed seismicity and focal plane solutions of individual earthquake events suggested the presence of a fault zone near the injection wells used for the study. A critical reservoir pressure threshold was estimated based on the state of stress, frictional properties, fault orientation, and the theory that effective stress (i.e., the difference between the normal stress acting on the fault and the fluid pressure) controls the frictional strength of faults. By cycling between periods of fluid injection and extraction, reservoir fluid pressure was oscillated about the critical pressure level. A remarkable agreement was observed between the occurrence of seismicity during periods when fluid pressure was maintained above the critical threshold and a lack of seismicity when fluid pressure was maintained below the critical threshold. This field experiment lent credit to the theory that earthquakes can be influenced by changes in the effective normal stress. In 1970, a similar scientific fluid injection field experiment was performed in Matsushiro, Japan in order to investigate injection-induced seismicity, the results of which ultimately supported the effective stress theory (*Ohtake*, 1974).

1.1.1 Geothermal energy

Thermal energy from deep geothermal resources can be can be converted to electricity by drilling wells into a formation, circulating fluid through the hot rock to recover heat, and passing the hot fluid through a heat exchanger or steam turbine located at the surface. Geothermal energy is considered

a renewable, low-carbon-intensity resource (*Horne and Tester*, 2014; *Tester et al.*, 2006). Geothermal energy can be extracted from conventional hydrothermal systems, where permeability exists naturally, or from Enhanced Geothermal Systems (EGS), which require permeability enhancement though stimulation. Induced seismicity has been associated with the exploitation of both forms of geothermal resources (*Häring et al.*, 2008; *Majer and Peterson*, 2007).

One of the first geothermal projects to report the generation of seismicity associated with fluid injection was at the Fenton Hill Enhanced Geothermal System (EGS) site operated by the US Department of Energy in New Mexico, USA (*Brown et al.*, 2012). In December 1983, a hydraulic stimulation treatment was performed by injecting fluid at high pressure into a well completed at a depth of 3.6 km in a crystalline granitic formation. A total of 21,000 cubic meters of fluid was injected over a period of 2.5 days. A local seismic monitoring network recorded thousands of earthquakes too small to be felt by humans at the surface (i.e., microearthquakes). At Fenton Hill, the pattern of microseismicity offered a unique opportunity to characterize the stimulated reservoir volume at the site in order to inform the reservoir management strategy for extracting heat and generating electricity at the site.

In 2006, a hydraulic stimulation treatment was performed at a geothermal well as part of an EGS project in Basel, Switzerland (*Häring et al.*, 2008). At Basel, fluid was injected into a well completed to a depth of 5 km in granitic basement rock. A total of 11,500 cubic meters of water was injected over a period of six days (*Mukuhira et al.*, 2013). The stimulation treatment was scheduled to last for 21 days, but microseismic activity that occurred in the first six days was severe enough to cause the operator to suspend injection based upon a predefined seismic response procedure (*Häring et al.*, 2008). During injection, the largest event was M 2.6. The well was vented for a short period of time and then shut-in. About five hours after shut-in, the largest event of M 3.4 was recorded. Three events of magnitude greater than M 3.0 were recorded over the next two months (*Häring et al.*, 2008; *Majer et al.*, 2007). The project was ultimately canceled in 2009 as a response to the hazard of induced seismicity.

In 2013, a geothermal project near St. Gallen, Switzerland was halted due to hazard of induced seismicity (*Obermann et al.*, 2015; *SED*, 2013). Several hydraulic stimulation treatments were performed, beginning on July 14, 2013. The stimulation treatments targeted a limestone formation at a depth of 4.0 to 4.5 km. Microseismicity was observed following the initiation of injection, and the intensity and magnitude of the events increased over the first few days. On July 20, 2013, a M 3.6 event occurred during an acid stimulation treatment that was located to a depth of 4 km (*SED*, 2013). Coincident with this event, the well experienced an unexpected kick of methane gas. Well control operations were initiated by injecting heavy mud followed by well shut-in. The Swiss Seismological Service received notification from over 400 nearby residents that were affected within a 15 km radius of the site, but only very minor damage was reported. The St. Gallen project was suspended in response to this incident.

1.1.2 Hydraulic fracturing

Unconventional hydrocarbon reservoirs are low-permeability formations that contain significant amounts of organic material, oil, or gas. Traditionally, these formations have served as the source rocks where hydrocarbons are formed before migrating to more porous and permeable formations, and were, until recently, considered uneconomic due to their intrinsically low permeability. The ability to drill horizontal wells and enhance permeability through hydraulic fracturing has enabled commercial-scale oil and gas production from these types of formations. Shale gas formations exploited currently in the United States include the Barnett, Eagle Ford, and Marcellus formations. An example of a shale oil formation is the Bakken.

Hydraulic fracturing involves completing the lateral section of a horizontal well with many isolatable stages and injecting fluid into each stage sequentially in order to pressurize the rock and create a newly formed fracture. Injection into each stage may last from 20 minutes up to several hours depending on the design of the fracturing treatment. *King* (2012) reported that the average injected fluid volume used during hydraulic fracturing is on the order of 20,000 cubic meters for each well. In some cases, seismic stations are placed on the surface and downhole in nearby wells in order to record seismicity associated with a particular hydraulic stimulation treatment to aid interpretation of fracture propagation (*Warpinski*, 2009; *Warpinski et al.*, 2012).

A study performed by *NRC* (2013) concluded that the risk of induced seismicity related to hydraulic fracturing is low based on the observation that over 35,000 individual shale gas wells have been stimulated with hydraulic fracturing in the United States (each well is completed with many fracturing stages) with no major incident. *Warpinski et al.* (2012) reported that microearthquakes triggered during hydraulic fracturing are typically on the order of -3 $\leq$ M $\leq$ 0. Occasionally, earthquakes with magnitudes larger than M 0 have been reported to have been induced during or as a direct result of hydraulic fracturing. *de Pater and Baisch* (2011) reported on a M 2.3 event that occurred during a hydraulic fracture treatment in Blackpool, England in 2011. *Friberg et al.* (2014) performed a seismological analysis of a cluster of seismicity that occurred in close temporal and spatial proximity to a series of hydraulic fracture treatments in Ohio, USA in 2013 and suggested that a preexisting fault may have been reactivated by fluid migration from the stimulation treatment. *Holland* (2013) presented evidence of a causal relationship between hydraulic fracturing and seismicity that included a M 2.9 earthquake. The largest induced earthquakes associated with hydraulic fracturing operations are believed to be two M 4.4 events that occurred in 2014 in Alberta and British Columbia (*Rubinstein and Mahani*, 2015), and two M 4.5 and 4.6 events that occurred in 2015 in British Columbia (*Atkinson et al.*, 2016).

1.1.3 Wastewater disposal

The central and eastern United States (CEUS) is an intraplate region that historically has remained relatively aseismic. The average rate of earthquakes with M≥3 in the CEUS between 1967 through 2000 was observed to be 21 events per year (*Ellsworth*, 2013). *Ellsworth* (2013) documented an unprecedented increase in the seismicity rate starting in about 2001 and accelerating again in about 2009. In 2014, there were more earthquakes with M $\geq$ 3 in Oklahoma than in California for the first time in recorded history (*McGarr et al.*, 2015). Several case studies of relatively large earthquake events (M $\geq$ 4) in the CEUS suggested that the increased rate of seismicity may have been related to oil and gas activities in the area, in particular, the disposal of large volumes of saltwater into deep subsurface aquifers (*Frohlich et al.*, 2011; *Horton*, 2012; *Hornbach et al.*, 2015; *Keranen et al.*, 2013; *Kim*, 2013).

In the United States, wastewater disposal wells are regulated as class-II underground injection control (UIC) wells. Wells used for the purposes of waterflooding and enhanced oil recovery are also regulated as class-II UIC wells. There are over 140,000 wells permitted for deep injection in the United States, and over 30,000 of those wells are permitted specifically for the purpose of wastewater disposal (*Ellsworth*, 2013). *Walsh and Zoback* (2015) analyzed injection well data reported by the operators to the state regulatory body for all wells operating in Oklahoma. *Walsh and Zoback* (2015) demonstrated that in three study areas within the state where the majority of the recent seismicity was observed, the increased rate of seismicity followed significant increases (5- to 10-fold) in rates of wastewater disposal. In areas where no significant operational changes occurred, the seismicity rate was observed to remain unchanged from the background levels (*Walsh and Zoback*, 2015). Furthermore, the analysis of *Walsh and Zoback* (2015) found that in Oklahoma, the vast majority of the disposal fluid was comprised of saltwater coproduced from conventional oil fields rather than flowback water from hydraulic fracturing operations. An analysis performed by *Weingarten et al.* (2015) suggested that seismicity occurred preferentially near wells that disposed of fluid at high injection rates ($>$ 300,000 barrels per month). Here, we review several recent case studies that provide insight into the nature of injection-induced seismicity related to wastewater disposal.

In the area near Guy, Arkansas, eight wastewater disposal wells became active starting in April, 2009 (*Horton*, 2012). The area had been prone to seismic activity in the past, with recent seismic swarms in nearby Enola, Arkansas in 1981 and 2001. However, after the start of injection in 2009, the rate of earthquakes with M $\geq$ 2.5 rose significantly. *Horton* (2012) reported that there was "one [earthquake] in 2007, two in 2008, 10 in 2009, 54 in 2010, and 157 in 2011," and that 98% of the earthquake epicenters were located less than 6 km from the injection wells. Several large faults near the injection sites had been mapped previously, but the recent seismicity was observed to occur along a linear trend suggesting the activation of a previously unidentified fault (*Horton*, 2012). Many of the earthquakes occurred in Precambrian basement rock beneath the target injection formation (*Horton*, 2012). In February, 2011, a M 4.7 earthquake occurred along the newly identified

Guy-Greenbrier fault (*Ellsworth*, 2013; *Horton*, 2012; *Zoback and Gorelick*, 2012). Subsequently, the two wells closest to the fault were shut in. The earthquakes did not stop, but the rate and size of the earthquakes did reduce. A third well was shut in voluntarily by the operator, and a fourth well was ordered to be shut in by the Arkansas Oil and Gas Commission. Six small earthquakes were recorded following the shutdown of these injection well (*Horton*, 2012).

Although the disposal of flowback fluids from hydraulic fracturing operations has not appeared to influence seismicity significantly in Oklahoma (*Walsh and Zoback*, 2015), that may not be the case elsewhere. Hydraulic fracturing fluids from shale gas projects in the Marcellus have been disposed of across the state border in Ohio (*Kim*, 2013). In December, 2010, a wastewater injection well began operation near Youngstown, Ohio. Over that year, nine events ranging between $1.8 \leq M \leq 2.8$ were recorded (*Kim*, 2013). The first event occurred 13 days following the start of injection, but due to sparse seismic arrays the events could not be located accurately. On December 1, 2011, four portable seismic stations were installed around Youngtown. On December 24, 2011 a M 2.7 event occurred. The event was able to be located accurately, and was observed to have occurred within 1 km of the injection well (*Kim*, 2013). The well was ordered to be shut in by the Ohio Department of Natural Resources on December 30, 2011. Within 24 hours of shut-in, the largest event (M 3.9) occurred (*Ellsworth*, 2013; *Kim*, 2013; *Zoback and Gorelick*, 2012). The located events defined a subsurface fault located in the Precambrian basement (*Kim*, 2013).

1.1.4 Monitoring, mitigation, and hazard analysis

Davis and Frohlich (1993) presented a list of criteria designed to guide analyses of potentially induced earthquakes. The *Davis and Frohlich* (1993) criteria involved developing an integrated assessment of background seismicity, temporal and spatial correlation between seismicity and injection, well operational data (bottomhole pressure of injection wells), and hydrological factors (for example, reservoir fluid pressure distribution and known geologic structures). In practice, these types of data can be difficult to obtain and the observations can be interpreted ambiguously. For example, *Davis and Frohlich* (1993) suggested that a 5 km distance between an earthquake and an injection well is sufficient correlation. In Oklahoma, there are over 10,000 class-II UIC wells operated by many different private interests (*OCC*, 2016). In 2014 and 2015, the Oklahoma Corporation Commission mandated reductions to injection volume for wells located within a specified radial distance of several different earthquakes with $M > 4$ (*OCC*, 2016), but it was generally unclear whether there was a scientific basis that related any individual wells to the observed seismicity.

Ideally, assessment of the hazard related to induced seismicity should reflect a combination of the benefits of a successful project, an expected risk of ground shaking if an earthquake is triggered, and the exposure to damage of life or property. In the geothermal community, a traffic-light system has been applied at several EGS projects in order to characterize the seismic hazard during and after hydraulic stimulation (*Bommer et al.*, 2006; *Häring et al.*, 2008). In the traffic-light approach, several

different thresholds related to seismicity (i.e., earthquake magnitude, peak ground acceleration, seismicity rate) are determined prior to the start of a project. Seismicity is monitored throughout a project, and the scheduled operational plan can be modified to reduce hazard if necessary. Traffic-light systems cannot always incorporate all possible negative consequences of injection. At the Basel EGS project, for example, application of the traffic-light system ultimately caused the injection well to be vented and shut-in, but the largest earthquake occurred after shut-in (*Häring et al.*, 2008). At the St. Gallen geothermal project, the fact that the well experienced a dangerous kick of methane precluded the ability of engineers to stop injection (*SED*, 2013). These examples highlight some of the shortfalls of the traffic-light approach to hazard mitigation.

Walters et al. (2015) introduced a framework for seismic hazard assessment focused on understanding the risk related to wastewater disposal and hydraulic fracturing operations. *Walters et al.* (2015) emphasized the importance of considering the level of tolerance of different stakeholders, including the public, operators, and regulators. The hazard analysis workflow suggested by *Walters et al.* (2015) extended the traffic-light system to incorporate the exposure to hazard and tolerance to risk of various stakeholders. *Yeck et al.* (2016) reported a positive example of how academia, government, and industry are able to work together to make proactive decisions to mitigate risk. After significant levels of seismicity in northeastern Colorado were determined likely to have been caused by wastewater disposal, seismic monitoring stations were deployed by the University of Colorado and the US Geological Survey. The data were used to inform the state regulator, which placed a temporary moratorium on injection in the area. The operator took mitigation actions by cementing the bottom of the well to minimize the hydraulic connection with the underlying crystalline basement rock, where the earthquakes had occurred. Ultimately, the seismicity diminished and injection was permitted to resume at reduced rates (*Yeck et al.*, 2016).

1.2 Scope of work

As with other subsurface engineering disciplines, the primary challenges confronted in the field of induced seismicity involve an inherently imperfect and incomplete understanding of the physical processes that occur deep in the Earth. Direct measurements of the physical properties and condition of the subsurface (e.g., hydraulic properties of the rock, fluid pressure, or temperature) can be made only at the specific locations at which wells are drilled. Indirect measurements (e.g., earthquake source mechanism) are able to probe a larger spatial domain, but require the application of assumptions to interpret the measurements in a useful way. Moreover, although many theoretical, laboratory, field-scale, and numerical experiments have improved our fundamental understanding of the earthquake rupture process, there is a stochastic element to the nature of earthquakes that can be difficult to quantify from an engineering perspective.

This work serves to advance a fundamental understanding on the role of the coupled hydromechanical and frictional processes that influence fluid-injection-induced earthquakes. Numerical modeling was applied to investigate several field cases of induced seismicity in a variety of geological and operational settings. The philosophy adopted in this work was to use numerical models as a tool to test, refute, and validate hypotheses of faulting mechanism and conceptual models of reservoir geologic structure. Although it is rare in subsurface problems that sufficient data exist to validate a hypothesis completely, if a model is able to reproduce behavior unique to a particular system then it may be useful for learning about the physics governing that system. Here, the studies that were performed in this research are introduced, and the most significant conclusions drawn from each study are reviewed.

In Chapter 2, a detailed description of the numerical model used in this research is provided. The model was capable of calculating the coupled interaction between fluid flow, heat transfer, and mechanical deformation in fractured and faulted porous media. A rigorous treatment of the faulting process was considered within a rate-and-state friction framework. The process of hydraulic fracture propagation was incorporated in the model. For each of the model components, except for the hydraulic fracture component, both two- and three-dimensional formulations were developed. Hydraulic fracturing was only considered in two-dimensional models. The fluid flow and heat transfer calculations were performed using an embedded fracture modeling approach. The embedded fracture modeling strategy is an extension of a traditional finite-volume discretization strategy that is more flexible for handling arbitrary fracture geometries. The embedded fracture model's ability to handle nonconforming discretizations was critical for modeling hydraulic fracture propagation problems efficiently. Mechanical deformation of faults and fractures was calculated using a boundary element approach. Poroelastic and thermoelastic deformation of the rock volume surrounding the fractures and faults was calculated using a finite element method. In Chapter 3, the results from a range of benchmark tests that were performed to verify the accuracy of the model developed in this work are presented.

In Chapter 4, a comprehensive analysis of the Fenton Hill Enhanced Geothermal System test site is presented. The hydraulic stimulation treatment and fluid circulation experiments performed at Fenton Hill were investigated in detail. We developed a conceptual model of the Fenton Hill reservoir in an attempt to reconcile two conflicting observations: 1) the overall migration of the stimulated zone, as observed through microseismic monitoring, did not trend in the direction of the maximum principal stress, and 2) injection occurred at pressures significantly above the pressures required to generate hydraulic fractures. Our modeling results support the plausibility that permeability enhancement at Fenton Hill occurred through a mixed-mechanism combination of mechanical opening of fractures and propagation of hydraulic splay fractures from the tips of preexisting natural fractures. This result is in contrast to the original design of the project, which intended to create several extensive vertical hydraulic fractures, and with other interpretations that suggest that no

hydraulic fractures were created during the stimulation treatments because they were not observed directly at the wellbore. Provided that the mixed-mechanism conceptual model is appropriate in lithologies other than granite, this study has important implications for the characterization and design of future enhanced geothermal system projects.

In Chapter 5, the results of a study on microseismic monitoring are presented. Numerical modeling was applied to investigate a novel field test called microseismic depletion delineation that has been proposed previously to learn about behavior in unconventional hydrocarbon reservoirs. The field study was based loosely on field data from the Bakken shale oil formation. Microseismic depletion delineation is a method that has been proposed for characterizing depletion trends near horizontal wells. The technique takes advantage of a change in the state of stress that occurs as a result of pressure depletion during production. In the zone of altered stress state, preexisting fractures are more prone to shear failure. The microseismic depletion delineation test involves reinjecting fluid at carefully determined pressures into a well that has been on production previously. Our results indicated that the locations of microseismic events that occur during reinjection can be used to demarcate heterogeneous pressure distributions near horizontal wells. This type of field test has economic implications for informing reservoir engineering analyses, including the determination of appropriate infill well spacing for horizontal wells or the design of refracturing treatments.

In Chapter 6, we present a study that focused on the largest earthquake observed thus far to have been associated with wastewater disposal, the 2011 M_w 5.6 earthquake near Prague, Oklahoma, USA. In this study, mechanisms that could plausibly explain the one day delay between the M_w 4.8 foreshock and M_w 5.6 main shock were investigated. The results suggest that a hydromechanical response to the static stress change caused by the foreshock that induced flow along the fault zone coupled with transient friction evolution could explain the delayed triggering process that was observed. Based on several plausible assumptions, the modeling results were used to estimate appropriate constraints for in-situ fault transmissivity and compliance. This study has implication for informing other physics-based models of induced seismicity in terms of the range of values of certain fault properties as well as relevant physical processes to consider.

In Chapter 7, a theoretical study on the relationship between wastewater disposal operations and earthquake statistics is presented. Important statistics that can influence earthquake hazard analysis include the maximum expected magnitude, the rate of seismicity, and the frequency-magnitude scaling relationship. In practical seismic hazard analysis, these statistics are assumed to be stationary. In this study we performed several analyses to determine whether these types of statistics are influenced significantly by fluid injection operations or driven by geologic and tectonic factors. A practical and simple faulting criterion was developed to determine whether the maximum magnitude of earthquakes triggered by fluid injection could be expected to be controlled by tangible operational parameters, such as injection rate. In another study, fault stress heterogeneity was modeled along two-dimensional fault surfaces using a spatial random field model. The goal was to assess whether

frequency-magnitude distributions that exhibit the type power-law scaling observed empirically in nature could be modeled realistically using a rate-and-state friction formulation. This study has implications for understanding how physics-based models of injection-induced seismicity can be used to supplement statistically-driven hazard analyses.

Chapter 2

Numerical Model Formulation

In many reservoir engineering and geophysics applications, it is imperative to incorporate a realistic description of the geologic structure of the reservoir into conceptual models and numerical models in order to establish appropriate interpretations of subsurface behavior. Several examples include hydraulic fracture treatment design, interpretation of microseismic monitoring data, and development of response strategies related to induced seismicity at wastewater disposal sites. In each of these cases, the interaction between fluid flow and the geomechanical response of fractured and faulted rock will have a direct influence on the reservoir behavior, and therefore also on the engineering decisions that must be made.

Subsurface engineers and scientists are often disadvantaged because of the inherent inability to collect sufficient data to describe deep earth systems fully. Therefore, it is common to make use of empirical or statistical observations in many types of analyses. As an example, consider the National Seismic Hazard Model developed by the U.S. Geological Survey. That model is used to inform the public, regulators, construction codes, and insurance companies of the risk of experiencing damaging earthquakes throughout different areas in the United States. In their analysis, the prediction for the probability of experiencing a given-magnitude earthquake in a specific location depended on the frequency-magnitude statistics of historic seismicity in the nearby area (*Petersen et al.*, 2014).

This seemed a logical and reasonable approach, until it became clear that oil and gas activity had contributed significantly to the earthquake activity observed recently in much of the Central and Eastern United States. It was recognized that wastewater disposal well operational data (such as well location, injection rate, and injection pressure) should be included in the seismic hazard assessment (*Ellsworth et al.*, 2015; *McNamara et al.*, 2015a). Although the most recent publication of the hazard model did incorporate the seismicity data for events that were likely induced by fluid injection, it did not incorporate any injection well operational data (*Petersen et al.*, 2016). Quantifying how seismicity can be affected by transient processes caused by injection operations remains a difficult task. Physics-based numerical modeling can provide the critical translation that

is necessary to integrate seismologic, geologic, and reservoir engineering data in a coherent manner. A major goal of this work was to develop an engineering tool that could be applied in order to improve our understanding of the physical behavior of deep fractured and faulted systems and to aid in practical decision making.

In this chapter, we present the details of a numerical model that is capable of calculating the coupled interactions between fluid flow, heat transfer, mechanical deformation, and earthquake mechanics in subsurface systems. Chapter 2 is organized as follows. In Sect. 2.1, we review an approach called embedded fracture modeling that is well-suited for modeling fluid flow in porous and fractured media. The numerical formulations for fluid flow and heat transfer in a fractured reservoir are described in detail. In Sect. 2.2, the displacement discontinuity method for solving fracture mechanics problems is presented. We describe the procedure that was used to couple fluid flow and fracture deformation within the embedded fracture modeling framework. In Sect. 2.3, we introduce a novel numerical method for coupling poroelastic and thermoelastic deformation of the rock surrounding fractures with the deformation of the fractures themselves. In Sect. 2.4, we present the formulation used to model earthquake nucleation, rupture, and arrest in three dimensions within the context of rate-and-state friction constitutive law.

2.1 Embedded fracture model

In geologic settings in which fractures and faults are expected to have first-order impacts in terms of flow behavior, it is important to recognize that the reservoir systems are active mechanically. During development and operation of a resource, local-scale and reservoir-scale permeability and storativity can evolve as fractures deform, fail in shear, or as intact rock fails in tension. The local state of stress throughout the reservoir controls the manner in which the permeability and storativity changes manifest. It is often necessary to make use of numerical modeling to investigate these types of reservoir processes for practical applications, but many traditional reservoir simulators neglect geomechanical processes or are based upon a set of limiting assumptions that obviate the influence of significant physical mechanisms.

Here, we introduce a novel numerical modeling framework that is able to simulate the coupled physical processes of fluid flow and mechanical deformation of fractures, faults, and surrounding matrix rock. The framework is able to incorporate an explicit representation of the geologic structure of the reservoir by using an embedded fracture modeling (EFM) strategy (*Li and Lee*, 2008), which provides significant advantages over more traditional discrete fracture modeling (DFM) techniques. A fracture mechanics-based approach to mechanical modeling allows for accurate calculation of the complex stress distributions that arise near fracture tips, so fracture propagation problems are approached in a rigorous manner. Detailed models of friction evolution along fracture and fault surfaces are included in order to model shear failure and seismicity. To accommodate different types

of rock, the model is flexible enough to incorporate a range of constitutive relationships necessary to describe permeability and storativity evolution of fracture networks due to changes in effective stress and shear failure.

The integration of the EFM approach into a geomechanical and fracture propagation simulator is a principal achievement of the present work. The embedded fracture approach is an efficient and flexible numerical scheme that provides the translation necessary to attack problems that would otherwise be intractable from a computational standpoint. The key aspect of the EFM formulation that was taken advantage of in this work is the ability to treat the fracture system and the surrounding matrix rock volume as two separate computational domains (*Lee et al.*, 2000, 2001; *Li and Lee*, 2008). This allows for the two domains to be discretized completely independently, negating the cumbersome requirement of a matrix discretization that must conform to the fracture discretization that is associated with traditional discrete fracture models.

In the embedded fracture approach, mass flux between the two domains is permitted and mass conservation is enforced strictly through the application of physics-derived coupling terms that appear in the governing equations as source terms. In this manner, as tensile fractures nucleate and propagate subject to geomechanical considerations, it is possible to incorporate new fracture control volumes into the numerical model during a simulation with no loss of generality and a negligible amount of computational overhead.

Previous authors have applied EFM to investigate geomechanical effects in fractured reservoirs, but this work has been limited in scope to simplified models that embody the geomechanics into purely empirical relationships (*Moinfar et al.*, 2013; *Karvounis et al.*, 2014). In this work, the fracture-mechanics-based reservoir model introduced by *McClure* (2012) and *McClure and Horne* (2013) was extended to incorporate the EFM strategy in order to combine the effects of matrix-fracture mass exchange and a rigorous treatment of geomechanics under a unified framework. The fluid flow and geomechanical calculations were performed in a fully coupled, fully implicit manner. Fracture propagation was permitted, and was based upon evaluating the mode-I stress intensity factor near fracture tips. Shear failure of preexisting fractures was permitted subject to a modified Mohr-Coulomb criterion (*Jaeger et al.*, 2007). The mechanical interaction between fractures as they deform was considered in the model. Reservoir-scale permeability evolution emerged as a result of deformation of individual fracture and fault planes, shear failure on preexisting fractures and faults, and propagation of tensile fractures. Some limitations of the model include: fluid flow was single-phase, the mechanical properties of the rock were assumed to be homogeneous and constant, elastic deformation was quasistatic, and the fractures were represented mathematically as infinitely thin surfaces (therefore, we cannot resolve some types of mechanical processes that may occur at scales within a fault zone).

The remainder of Sect. 2.1 is organized as follows. In Sect. 2.1.1, the numerical formulation for the EFM framework for single-phase flow in porous media is presented. The traditional DFM,

one-dimensional leakoff approximation model, and zero leakoff approximation model that were used for comparison with the EFM approach are also discussed. In Sect. 2.1.2, our method for integrating heat transfer within the EFM framework is presented.

2.1.1 Fluid flow

The reservoir model introduced by *McClure* (2012) and *McClure and Horne* (2013) was developed originally to simulate reservoir stimulation treatments in low-permeability settings, such as hydraulic fracturing in shale gas reservoirs or shear stimulation in geothermal reservoirs. The model assumed that intrinsic matrix permeability in these settings is low enough to justify neglecting mass transfer between the fracture systems and surrounding matrix rock. In the present work, this model was extended to include the effects of matrix-fracture mass transfer. An EFM strategy was adopted in order to overcome several severe numerical and practical limitations of more traditional DFM approaches for application to reservoir stimulation problems.

Here, the numerical formulation for the embedded fracture model is described in detail. In the sections that follow, we describe studies where we compared the EFM approach with a DFM approach that had been implemented previously in the *McClure* (2012) model. We describe the details of the DFM model for the reader's reference. In addition, the EFM and DFM models were compared with two relatively computationally efficient approximate models, namely the one-dimensional leakoff approximation model and the zero leakoff approximation model. The details of these models are described briefly.

Embedded fracture model description

In traditional reservoir simulation, fractured reservoirs are often modeled using the double porosity model (*Kazemi*, 1969; *Warren and Root*, 1963). This model is applicable if the fracture orientations and lengths are distributed relatively randomly and the fracture system is connected extensively. More importantly, application of the double porosity model typically assumes that the properties and geometry of the fracture network remain constant.

In order to honor more realistic representations of fractured reservoir geology, discrete fracture approaches have been developed. For example, *Karimi-Fard et al.* (2004) presented a DFM in which the geometry of the fractures and faults were captured by discretizing them explicitly in lower-dimensional space, and creating a matrix discretization that conformed to the fractures. In general, DFM approaches are useful in settings where production is dominated by flow through fractures (e.g., formations with low matrix permeability) or if fractures tend to have preferred orientations. However, traditional DFM techniques are subject to several drawbacks. Most notable is that a matrix discretization that conforms to the fractures inevitably results in a large number of "small" matrix control volumes in areas where there are many fractures or where fractures intersect at

low angles. In some cases, the geologic structure of the reservoir must be sacrificed for numerical convenience.

Moreover, DFM techniques are not well suited for fracture propagation problems in which the fracture networks are growing over time. Previous work has been done in the area of developing models that apply adaptive grid refinement as fractures propagate (*Hunsweck et al.*, 2008; *Rangarajan et al.*, 2015). This requires a significant level of computational overhead, and the numerical results have been observed to be grid-dependent. Alternatively, it is possible to define planes where hydraulic fractures potentially may propagate in advance of a simulation, and then prediscretize the system around these potentially forming planes. Naturally, this approach will require an unnecessarily high number of additional degrees of freedom, and, perhaps worse, involves making implicit assumptions about the mechanics of fracture propagation.

In the present work, the use of traditional DFM techniques was avoided, and instead the EFM approach was adopted. In the EFM approach, the fracture and matrix domains are treated as separate computational domains. The two systems are discretized completely independently (i.e., a conforming mesh is not required; see Fig. 2.1), and mass conservation is enforced strictly through physics-derived coupling terms. In fact, EFM is very similar conceptually to dual porosity or dual permeability models, but is able to maintain a more realistic representation of complex geologic features. As demonstrated in the numerical examples presented in Chapter 3, the ability to define realistic representations of the geologic structure of a reservoir and the use of a nonconforming grid are the critical features that make the EFM approach an attractive modeling strategy to perform rigorous geomechanical analyses.

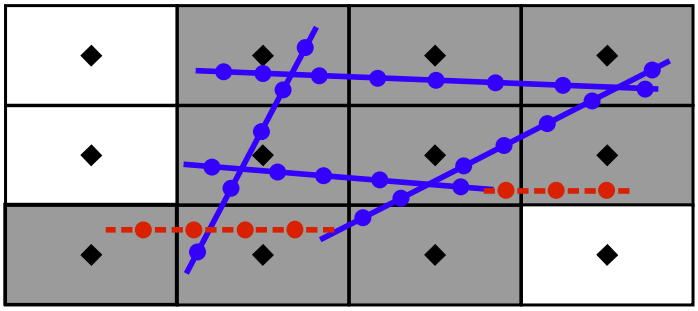

Figure 2.1: Schematic of the embedded fracture discretization strategy. The *solid blue lines* are natural fractures, and the *dashed red lines* are hydraulic fractures. The *circles* represent the centers of fracture control volumes, and the *diamonds* represent the centers of matrix control volumes. The matrix control volumes that require EFM coupling terms are *shaded gray*.

The EFM approach was introduced originally by *Lee et al.* (2000, 2001), and later expanded upon by *Li and Lee* (2008). *Karvounis* (2013) and *Karvounis and Jenny* (2016) developed a heat and mass transfer geothermal simulator based on EFM, and demonstrated that EFM can obtain a suitable degree of accuracy with improved computational performance compared to traditional simulators.

Hajibeygi et al. (2011) and *Tene et al.* (2016) incorporated EFM into an iterative multiscale finite volume scheme. *Moinfar et al.* (2012), *Pluimers* (2015), and *Yan et al.* (2016) compared DFM to EFM for multiphase flow problems and demonstrated that EFM was able to capture a high degree of accuracy at a reduced computational expense. *Ding et al.* (2014) drew upon EFM fundamentals and calculated the matrix-fracture transmissibility numerically to be able to capture pressure transients in the near-fracture region more accurately.

Recently, EFM has also been used in geomechanics applications. *Moinfar et al.* (2013) incorporated a simple treatment for calculating fracture permeability evolution due to changes in effective stress within an EFM framework, but did not include a formal treatment for geomechanics. *Karvounis et al.* (2014) extended their simulator to include a proxy geomechanical model based on changes in pore pressure to investigate injection-induced seismicity. *Norbeck et al.* (2014) introduced an EFM-based model that integrated a rigorous treatment of fluid flow, fractured reservoir mechanics, and fracture propagation. *Norbeck and Horne* (2015a) performed a study of porothermoelastic effects on injection-induced seismicity using a rate-and-state earthquake model. *Norbeck and Horne* (2016a) investigated how poroelastic effects caused by pressure depletion could be leveraged to learn about the extent of the depleted zone in unconventional reservoirs.

It should be noted that in some of the works cited previously, the concept of EFM was applied in a context related to upscaling techniques (*Hajibeygi et al.*, 2011; *Li and Lee*, 2008). In those applications, it was assumed that fractures that existed at a relatively small scale could be homogenized in order to obtain effective "damaged matrix rock" properties, and the geometries of the larger fracture systems expected to contribute to flow at a reservoir scale were maintained explicitly. For the purposes of this work, it is sufficient to recognize this distinction purely at the conceptual level. In the remainder of this dissertation, it is assumed that any reference to matrix permeability may imply an effective upscaled permeability, and any fracture domain is representative of a scale of practical engineering interest.

Numerical formulation for the embedded fracture model

Throughout this chapter we use indicial notation where repeated subscript indices imply summation. The key insight introduced by *Li and Lee* (2008), that the fracture and matrix domains can be discretized independently, is leveraged by expressing the mass conservation equations for the matrix and fracture domains separately. For a porous medium saturated with single-phase fluid, the mass balance equations can be written, for flow in the matrix domain, as:

$$\frac{\partial}{\partial x_i}\left(\rho\lambda k_{ij}^{m}\frac{\partial p^{m}}{\partial x_i}\right)+\widetilde{m}^{wm}+\widetilde{\Omega}^{fm}=\frac{\partial}{\partial t}\left(\rho\phi\right), \tag{2.1}$$

and, for flow in the fracture domain, as:

$$\frac{\partial}{\partial x_i}\left(\rho\lambda T^f\frac{\partial p^f}{\partial x_i}\right)+\widetilde{m}^{wf}+\widetilde{\Omega}^{mf}=\frac{\partial}{\partial t}\left(\rho E\right). \tag{2.2}$$

Here, p^m is fluid pressure in the matrix domain, p^f is fluid pressure in the fracture domain, ρ is fluid density, λ is inverse of fluid viscosity, k_{ij}^m is the diagonal matrix permeability tensor, T^f is the fracture transmissivity, ϕ is matrix porosity, E is fracture void aperture, $\widetilde{m}^{wm}$ is a normalized mass source term related to wells in the matrix domain, and $\widetilde{m}^{wf}$ is a normalized mass source term related to wells in the fracture domain. The fracture transmissivity was assumed to behave according to the cubic law for flow between parallel surfaces (*Snow*, 1965; *Witherspoon et al.*, 1980):

$$T^f=\frac{e^3}{12}, \tag{2.3}$$

where e is hydraulic aperture. In Eq. 2.2, T^f and E can evolve in a highly nonlinear fashion as a result of mechanical deformation of fractures and faults. We applied an empirical model introduced originally by *Bandis et al.* (1983) and *Barton et al.* (1985) in order to describe the nonlinear relationship between mode-I deformation and effective stress as well as the effect of shear-slip induced dilation. We chose to apply the form of the constitutive model proposed by *Willis-Richards et al.* (1996):

$$e\left(\sigma_n,p^f,\delta_s\right)=\frac{e_*}{1+9\left(\dfrac{\sigma_n-p^f}{\sigma_{*e}}\right)}+\delta_s\frac{\varphi_e}{1+9\left(\dfrac{\sigma_n-p^f}{\sigma_{*e}}\right)}+e_{res}. \tag{2.4}$$

In Eq. 2.4, σ_n is the total normal stress acting on the fracture, δ_s is cumulative shear slip, e_* and σ_{*e} are laboratory-derived properties that describe the fracture stiffness, φ_e is the shear dilation angle, and e_{res} is the residual fracture aperture. An equivalent formulation is also used to describe fracture void aperture, E, where the empirical constants are allowed to be different.

In addition to the usual terms related to flux, wells, and storage, the terms $\widetilde{\Omega}^{fm}$ and $\widetilde{\Omega}^{mf}$ are introduced to account for mass transfer between the two domains. To ensure continuity upon integration over the respective control volumes, these mass transfer terms take the following form (*Hajibeygi et al.*, 2011):

$$\widetilde{\Omega}^{fm}=\Upsilon\left(p^f-p^m\right)/V, \tag{2.5}$$

and

$$\widetilde{\Omega}^{mf}=\Upsilon\left(p^m-p^f\right)/A, \tag{2.6}$$

where the parameter Υ is a transmissibility called the fracture index and is analogous to the Peaceman well index (*Peaceman*, 1978). The normalization parameters in Eqs. 2.5 and 2.6 are V, the bulk volume of the matrix control volume, and A, the surface area of the fracture control volume,

respectively.

Similar to the treatment of wells in traditional reservoir simulators, the fracture index serves to capture subgrid behavior of the pressure gradient near fractures. In this work, the derivation provided by *Li and Lee* (2008) was followed to calculate the fracture index. The assumptions in the derivation are: a) flow in the vicinity of the fractures is linear (i.e., one-dimensional), b) the fractures fully penetrate the matrix control volume in the out-of-plane direction, and c) the matrix and fracture pressures represent average pressures over their respective control volumes.

The rate of mass exchange from a fracture control volume into a matrix control volume is defined as:

$$\Omega^{fm} = \Upsilon \left(p^f - p^m \right), \tag{2.7}$$

This term has units of mass per time. Assuming that flow is one-dimensional in the local region near the fracture, the mass exchange rate can be described alternatively by integrating the Darcy flux over the surface area of the fracture:

$$\Omega^{fm} = \rho \lambda k^* A^f \frac{\partial p}{\partial x_i} n_i, \tag{2.8}$$

where A^f is the total fracture surface area (i.e., both faces of the fracture), k^* is an effective matrix-fracture permeability in the direction perpendicular to the fracture (calculated using a harmonic average), n_i is the unit normal vector to the fracture face, and the pressure gradient term is:

$$\frac{\partial p}{\partial x_i} = \frac{\left(p^f - p^m \right)}{\langle D \rangle} n_i. \tag{2.9}$$

Equating the right hand side expressions in Eqs. 2.7 and 2.8 allows for the determination of the transmissibility:

$$\Upsilon = \rho \lambda k^* I, \tag{2.10}$$

where I is a grid dependent property called the connectivity index with units of length. The connectivity index can be calculated as:

$$I = \frac{A^f}{\langle D \rangle}. \tag{2.11}$$

In Eqs. 2.9 and 2.11, $\langle D \rangle$ represents the average normal distance from the fracture surface within a particular matrix control volume (*Hajibeygi et al.*, 2011):

$$\langle D \rangle = \frac{\int_V D\left(\mathbf{x}'\right) \, d\mathbf{x}}{V}. \tag{2.12}$$

Equation 2.12 can be evaluated numerically for complex geometries. The normal distance of interest is:

$$D\left(\mathbf{x}'\right) = \left| \mathbf{x}' \cdot \mathbf{n} \right|. \tag{2.13}$$

In two dimensions, for example, $V = \Delta x \Delta y$ is the area of the matrix control volume and the vectors $\mathbf{x}$, $\mathbf{x}'$, and $\mathbf{n}$ are:

$$\mathbf{x} = \begin{Bmatrix} x \\ y \end{Bmatrix}, \quad \mathbf{x}' = \begin{Bmatrix} x - x^f \\ y - y^f \end{Bmatrix}, \quad \mathbf{n} = \begin{Bmatrix} \sin\theta \\ \cos\theta \end{Bmatrix}. \tag{2.14}$$

The point $\left(x^f, y^f\right)$ is the location of the fracture control volume center, the point (x, y) is a location within the matrix control volume, and θ is the orientation of the fracture measured from the x-axis.

With the matrix-fracture mass flux terms that appear in Eqs. 2.1 and 2.2 now fully defined, the utility of the EFM approach for problems that involve fracture propagation is clear. The coupling between the fracture and matrix domains has been reduced to a collection of simple source terms. Numerical complexities associated with conforming mesh approaches that would tend to make fracture propagation problems become intractable for problems with many fractures are avoided with EFM.

Equations 2.1 and 2.2 were discretized using a standard two-point flux approximation finite volume scheme into a total of N^{m+f} control volumes (*Aziz and Settari*, 1979; *Karimi-Fard et al.*, 2004), resulting in residual equations of the form:

$$R_a = \sum_b \Upsilon_{ab} \left(p_b - p_a\right) + m_a + \Omega_a - \Delta_t M_a \equiv 0, \quad \text{for } a = 1, \ldots, N^{m+f}. \tag{2.15}$$

Here, Υ are the transmissibilities between adjacent control volumes, m is a well source term with units of mass per time, Ω is the mass transfer rate between the matrix and fracture domains, and $\Delta_t M$ is the time derivative of fluid mass stored in the control volume.

Discrete fracture model description

The DFM was implemented using the finite volume method and a conforming mesh of the rock volume around the fractures. The volume around the fractures was discretized with triangular control volumes, aided by the program Triangle (*Shewchuk*, 1996). Triangle is an algorithm designed to create Delaunay triangularizations of two-dimensional regions. The finite volume method was implemented according to the method described by *Karimi-Fard et al.* (2004).

An important problem is that Delaunay triangularization does not guarantee uniform or smoothly varying line-segment length along domain edges, which in this case are the fracture elements. This can create problems in the boundary element mechanical calculations described in Sect. 2.2, which are inaccurate unless fracture element length is uniform or gradually varying. Therefore, Triangle could not be used to generate a true Delaunay triangularization.

To guarantee uniform fracture element size, the fractures were discretized first by imposing a constant element length (with some minor and unavoidable deviation from constant length at fracture tips and intersections). Next, a uniform grid of matrix nodes was superimposed over the fracture network. Third, nodes were identified that were in close proximity to fracture elements, and

they were removed. Finally, the list of fracture elements and matrix nodes was provided to Triangle, which was used to produce a constrained Delaunay triangularization. The triangularization was "constrained" in the sense that the algorithm was required to use only the fracture elements and matrix nodes provided and was not permitted to subdivide the fracture elements. Because of the constraint, the mesh was not guaranteed to be truly Delaunay, which degraded the quality of the mesh and the accuracy of the calculations of flow in the matrix. Despite this problem, the approach was used because it was more important to avoid inaccuracy in the mechanical calculations due to unevenly sized fracture elements than inaccuracy in matrix flow calculations due to high aspect ratio triangles. It should be noted that this entire issue is avoided with the EFM approach, which does not require a conforming mesh between the matrix and fracture elements.

One-dimensional leakoff approximation model description

For a well connected to a highly conductive fracture within an infinite reservoir, flow near the fracture has been shown to be linear at early times (*Gringarten et al.*, 1974; *Horne*, 1995). This suggests that a useful approximation to model the leakoff behavior near fractures is to assume one-dimensional flow away from the fracture. In this work, the semianalytical method of *Vinsome and Westerveld* (1980) was used to develop an approximate model that was relatively efficient computationally compared to the EFM and DFM approaches. The purpose of the simplified model was to avoid numerical discretization of the volume of rock surrounding the fractures, while still accounting for fluid exchange between the two domains.

The model treats fluid leakoff at each fracture control volume using a sink term that is independent from all other fracture control volumes. The key advantage of the *Vinsome and Westerveld* (1980) method is that it gives a highly accurate and efficient solution to the diffusivity equation in one dimension, even for arbitrarily varying pressure in the fracture. In contrast, the Carter leakoff model assumes constant pressure in the fracture, a simplifying assumption that reduces model generality considerably (*Howard and Fast*, 1957).

The *Vinsome and Westerveld* (1980) method was created originally as a model of heat loss due to conduction into cap rock. However, the equation for heat conduction is identical to the equation for single-phase fluid flow in a porous medium with constant pore and fluid compressibilities, matrix permeability, and fluid viscosity. Therefore, the method can be adapted easily by changing the variables in the original equations of *Vinsome and Westerveld* (1980) to their equivalents for flow in porous media, assuming that the aforementioned variables are considered as constants.

The assumptions of one-dimensional leakoff and no interference between fractures are justified if the fracture spacing is sufficiently large relative to the penetration distance of the pressure signal and if the injection duration is short enough to preclude a change in the flow regime (e.g., towards late-time radial flow). If fractures are in pressure communication with other nearby fractures, then the one-dimensional leakoff approximation tends to overestimate the amount of leakoff. Relatively

high leakoff suppresses pressure within the fracture domain, which discourages shear failure and fracture propagation.

Zero leakoff approximation model description

In geologic settings where the intrinsic permeability of the matrix rock is extremely low, a useful approximation is that the matrix rock is impermeable. In this case, fluid flow can occur only within a network of connected fractures and no fluid is able to leakoff into the surrounding rock. Under this assumption there is no flow in the matrix rock, and the volume surrounding the fractures does not require discretization. The improvement in computational efficiency that can be achieved by avoiding discretization of the matrix rock volume can be tremendous.

This approximation represents a lower bound on the amount of leakoff that would occur during a stimulation treatment. Neglecting leakoff tends to promote elevated pressure in the fracture domain, which encourages both shear stimulation and fracture propagation. Even in scenarios in which the implicit assumptions of this approximation are not strictly valid, the model can be used to provide informative constraints on reservoir behavior.

2.1.2 Heat transfer

Fluid was assumed to be in thermal equilibrium with the reservoir rock. Energy conservation can be described, in the matrix domain, as (*Charoenwongsa et al.*, 2010; *Jaeger et al.*, 2007):

$$\frac{\partial}{\partial x_i}\left(\kappa_{ij}^m \frac{\partial T^m}{\partial x_i}\right) - \frac{\partial}{\partial x_i}\left[\rho_\varphi c_{p\varphi} v_i^m \left(T^m - T_0^m\right)\right] + \rho_\varphi c_{p\varphi} \widetilde{q}^{wm}\left(T^w - T_0^m\right) + \widetilde{\Pi}^{fm} = \frac{\partial}{\partial t}\left\{\left[\phi^m \rho_\varphi c_{v\varphi} + \left(1-\phi^m\right)\rho_r c_r\right]\left(T^m - T_0^m\right)\right\} \quad (2.16)$$

and, in the fractured domain, as:

$$\frac{\partial}{\partial x_i}\left(\kappa^f \frac{\partial T^f}{\partial x_i}\right) - \frac{\partial}{\partial x_i}\left[\rho_\varphi c_{p\varphi} v_i^f \left(T^f - T_0^f\right)\right] + \rho_\varphi c_{p\varphi} \widetilde{q}^{wf}\left(T^w - T_0^f\right) + \widetilde{\Pi}^{mf} = \frac{\partial}{\partial t}\left\{\left[\phi^f \rho_\varphi c_{v\varphi} + \left(1-\phi^f\right)\rho_r c_r\right]\left(T^f - T_0^f\right)\right\} \quad (2.17)$$

Here, T is rock temperature, T_0 is a reference temperature, κ_{ij} is the diagonal thermal conductivity tensor of rock, $c_{p\varphi}$ is the constant pressure heat capacity of the fluid, $c_{v\varphi}$ is the constant volume heat capacity of the fluid, c_r is the heat capacity of rock, ρ_r is the density of rock, v_i is the Darcy fluid velocity, and $\widetilde{\Pi}$ is EFM heat transfer term. The heat transfer equations have a similar form to the mass balance equations, except that additional advection terms exist to account for the heat

that is transported with the fluid. The fluid velocity was calculated using Darcy's law:

$$v_i = -\lambda k_{ij} \frac{\partial p}{\partial x_i}. \tag{2.18}$$

A traditional upwinding scheme was used to evaluate the advection terms. The thermal conductivity was calculated as a volumetric average of the solid rock and fluid constituents:

$$\kappa = \phi \kappa_\varphi + (1 - \phi)\, \kappa_r \tag{2.19}$$

When modeling heat transfer, a distinction can be made between fractures that act essentially as open voids (i.e., $\phi^f = 1$) and faults that act as a porous media (i.e., $\phi^f \neq 1$) by noting that the effective porosity is related to the void aperture and the physical width of the feature:

$$\phi^f = \frac{E}{W}. \tag{2.20}$$

We used an iterative sequential implicit stategy to couple fluid flow and heat transfer.

The embedded fracture coupling terms for the heat transfer equations have a similar form to Eq. 2.7, but now contain both a diffusion term related to heat conduction and a term related to advection of heat between the two domains:

$$\Pi^{mf} = \omega \left(T^m - T^f\right) + c_{p\varphi} \Omega^{mf} \left(T - T_0\right). \tag{2.21}$$

Upwinding was used to evaluate the advection term. The geometric part of the heat transfer transmissibility, ω, is similar to Eq. 2.10:

$$\omega = \kappa^* I, \tag{2.22}$$

where κ^* is the effective thermal conductivity in the direction normal to the fracture surface. The energy balance equations (Eqs. 2.16 and 2.17) were discretized using a finite volume method using the same computational grid as the mass balance equations. *Karvounis and Jenny* (2016) implemented a technique to overcome discretization dependence for the advection term in Eq. 2.21. The discretization dependence was shown to be significant when the matrix flow velocity field caused heat to advect across a fracture plane. We neglected this issue in our work.

Equations 2.16 and 2.17 were discretized using a standard two-point flux approximation finite volume scheme into a total of N^{m+f} control volumes (*Aziz and Settari*, 1979; *Karimi-Fard et al.*, 2004), resulting in residual equations of the form:

$$R_a = \sum_b \Upsilon^{cond.}_{ab} \left(T_b - T_a\right) + \sum_b \Upsilon^{adv.}_{ab} \left(T_{ab} - T_{0,ab}\right) + h_a + \Pi_a - \Delta_t H_a \equiv 0, \quad \text{for } a = 1, \ldots, N^{m+f}. \tag{2.23}$$

Here, $\Upsilon^{cond.}$ and $\Upsilon^{adv.}$ are the transmissibilities between adjacent control volumes for conduction

and advection, respectively, h is a well source term with units of energy per time, Π is the energy transfer rate between the matrix and fracture domains, and $\Delta_t H$ is the time derivative of energy content stored in the control volume.

2.2 Fracture mechanics model

Momentum balance for a linear elastic isotropic material yields the following equilibrium equation (*Pollard and Fletcher*, 2005):

$$\frac{\partial \sigma_{ji}}{\partial x_j} + F_i = \rho_r \frac{\partial^2 u_i}{\partial t^2}. \tag{2.24}$$

In Eq. 2.24, σ_{ij} is the stress tensor, F_i are vectors of body force per unit volume, ρ_r is the density of the rock, and u_i is the rock displacement vector. The right hand side of Eq. 2.24 represents inertial effects. The inertial term causes stress transfer to propagate through the elastic medium like a wave. It can be important to consider inertial effects in order to understand behavior over short time scales (on the order of seconds) during earthquake rupture on large faults. However, for many other rock mechanics applications, the quasistatic approximation to Eq. 2.24 can be sufficient to describe deformation behavior (*Jaeger et al.*, 2007; *Pollard and Fletcher*, 2005):

$$\frac{\partial \sigma_{ji}}{\partial x_j} + F_i = 0. \tag{2.25}$$

For a linear elastic isotropic material, Hooke's law relates stresses and strains (*Jaeger et al.*, 2007; *Segall*, 2010):

$$\sigma_{ij} = 2G\varepsilon_{ij} + \Lambda \varepsilon_{kk} \delta_{ij}. \tag{2.26}$$

Here, ε_{ij} is the strain tensor, G is the shear modulus of rock, Λ is the Lamé coefficient of rock, and δ_{ij} is the Kronecker delta function. Assuming infinitesimal strains, the strain-displacement relation is:

$$\varepsilon_{ij} = \frac{1}{2}\left(\frac{\partial u_i}{\partial x_j} + \frac{\partial u_j}{\partial x_i}\right). \tag{2.27}$$

Combining Eqs. 2.25 - 2.27 yields partial differential equations in terms of the material displacements:

$$G\frac{\partial^2 u_i}{\partial x_k \partial x_k} + (G + \Lambda)\frac{\partial^2 u_k}{\partial x_i \partial x_k} = -F_i. \tag{2.28}$$

The momentum balance equations in the form of Eq. 2.28 provide the foundation for most analyses of deformation in solid elastic materials.

2.2.1 Fracture deformation

We applied the boundary element method popularized by *Crouch and Starfield* (1983) called the displacement discontinuity (DD) method in order to solve the fracture deformation problem. The DD method is a numerical method used to solve Eq. 2.28 that is based on a boundary integral solution strategy (*Crouch*, 1976; *Detournay and Cheng*, 1987). In the DD method, displacements and stresses everywhere in the domain are continuous except for across specific discrete features. Fracture surfaces are represented by these discrete features. The DD method assumes quasistatic linear elasticity, small strains, and homogeneous and isotropic material properties of the host rock (*Crouch and Starfield*, 1983; *Shou and Crouch*, 1995).

In the DD method, the fracture (fault) surfaces are discretized into a set of discrete elements. Fractures can deform in the normal (opening) mode and tangential (shear or sliding) modes. A schematic illustrating the fracture deformation modes is shown in Fig. 2.2. The displacement discontinuities represent the jumps in the material displacements when transitioning across a plane of interest. Referencing the coordinate system in Fig. 2.2 that is centered on a fracture element, the displacement discontinuities in the normal-, strike-, and dip-directions, respectively, are defined as:

$$\delta_n = u_n^+ - u_n^- \tag{2.29}$$

$$\delta_s = u_s^+ - u_s^- \tag{2.30}$$

$$\delta_d = u_d^+ - u_d^- \tag{2.31}$$

Assuming that superposition holds for a linear elastic solid, the stresses and displacements at each element reflect the combined effect of all elements in the problem. The changes in stress caused by the mechanical deformation of the fractures are related through a matrix of Green's functions. Early so-called fundamental solutions for the Green's functions used in the DD method were given by *Love* (1927), *Mindlin* (1936) and *Timoshenko and Goodier* (1951). It is a practical advantage to express the stress (traction) boundary conditions along the fractures in terms of their normal and shear components. In three dimensions, the stress-displacement relationship is:

$$\begin{Bmatrix} \boldsymbol{\sigma}_n^M \\ \boldsymbol{\sigma}_s^M \\ \boldsymbol{\sigma}_d^M \end{Bmatrix} = \begin{bmatrix} \mathbf{A}_{nn} & \mathbf{A}_{ns} & \mathbf{A}_{nd} \\ \mathbf{A}_{sn} & \mathbf{A}_{ss} & \mathbf{A}_{sd} \\ \mathbf{A}_{dn} & \mathbf{A}_{ds} & \mathbf{A}_{dd} \end{bmatrix} \begin{Bmatrix} \boldsymbol{\delta}_n \\ \boldsymbol{\delta}_s \\ \boldsymbol{\delta}_d \end{Bmatrix}. \tag{2.32}$$

In Eq. 2.32, $\boldsymbol{\sigma}_n^M$, $\boldsymbol{\sigma}_s^M$, and $\boldsymbol{\sigma}_d^M$ are vectors that represent the mechanically-induced stresses at each discrete fracture element (the superscript M indicates a *mechanical* load), the $\mathbf{A}$ matrices are the interaction coefficients (Green's functions), and $\boldsymbol{\delta}_n$, $\boldsymbol{\delta}_s$, and $\boldsymbol{\delta}_d$ are vectors of the opening-mode and sliding-mode displacement discontinuities. In the two-dimensional version of the model, $\mathbf{A}$ was calculated using the fundamental solutions for a distributed loading in an infinite domain presented

by *Shou and Crouch* (1995), and in the three-dimensional version of the model **A** was calculated using the fundamental solutions for a rectangular source in a half-space given by *Okada* (1992). In Sect. 2.4, we discuss a quasidynamic approximation to Eq. 2.24 that can be applied in conjunction with the DD method to solve earthquake rupture problems (*Ben-Zion and Rice*, 1995, 1997; *Lapusta et al.*, 2000; *Rice*, 1993; *Rice and Ben-Zion*, 1996; *Thomas*, 2013).

Although Eq. 2.25 is an elliptic equation and therefore has no time dependence, the stresses and displacements in reservoir simulation problems typically evolve over time due to the influence of transient fluid flow. In order to perform the stress updates, a large number of matrix-vector products in the form of Eq. 2.32 must be performed. The set of algebraic equations in Eq. 2.32 is, in general, a fully-dense system and can be extremely expensive computationally. We used an approach developed by *Bradley* (2014) that approximates the **A** matrices in order to perform the matrix-vector products in Eq. 2.32 efficiently.

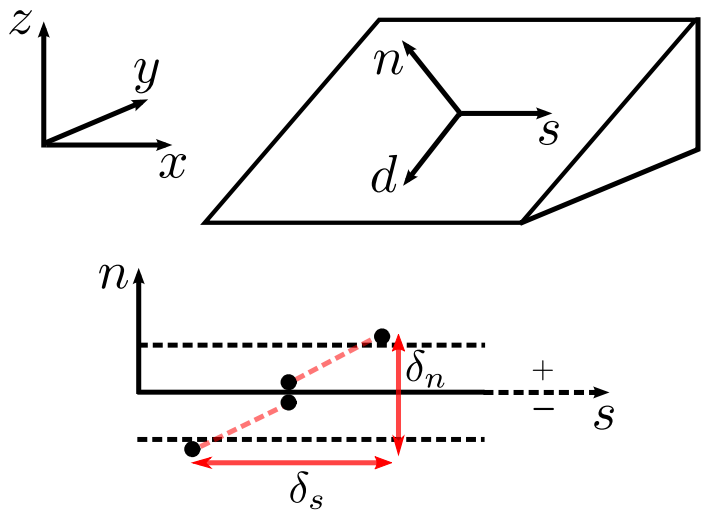

Figure 2.2: (top) Illustration of the (n, s, d)-coordinate system centered on a fault element representing the normal-, strike-, and dip-directions, respectively. (bottom) An example of a combined mode-n and mode-s displacement discontinuity. The *black dots* represent points in the material on opposite sides of the fault element that were initially adjacent to each other but later experienced relative displacement after the fracture opened and slid to a new equilibrium position.

2.2.2 Mechanical equilibrium

In the model, nonplanar fault (fracture) surfaces, geometrically complex fault structures, and interacting faults were considered. We allowed both mode-I (opening) and mode-II/mode-III (sliding) deformations to occur. In order to solve the fault deformation problem, mechanical equilibrium was enforced along the fault surfaces. Throughout a simulation, the state of stress at each discretized

fault element was checked and updated continuously. Fault elements that bore a compressive effective normal stress deformed in the mode-I direction subject to a nonlinear joint stiffness constitutive law (*Willis-Richards et al.*, 1996), and was therefore able to be calculated explicitly. Fracture mechanics theory suggests that if the fluid pressure acting in the fault overcomes the remote tectonic loading, then the opening-mode deformations induce stresses that serve to balance the overpressure. In this case, opening-mode mechanical equilibrium can be expressed as:

$$\sigma_n^R + \Delta\sigma_n = p^f. \tag{2.33}$$

In Eq. 2.33, σ_n^R is the tectonic loading resolved in the fault-normal direction, $\Delta\sigma_n$ is any change in normal stress due to mechanical deformation, poroelastic stress, or thermal stress, and p^f is the fluid pressure acting within the fault zone. In this section we will neglect any porothermoelastic effects so that $\Delta\sigma_n = \sigma_n^M(\boldsymbol{\delta}_n, \boldsymbol{\delta}_s, \boldsymbol{\delta}_d)$. Here, it is useful to define the effective normal stress as:

$$\bar{\sigma}_n = \sigma_n - p^f. \tag{2.34}$$

In order to solve the shear failure problem, we assumed a quasidynamic elasticity formulation where the total shear stress acting on the fault can be described as (*Ben-Zion and Rice*, 1997):

$$\tau = \tau^R + \Delta\tau - \eta V. \tag{2.35}$$

The total shear stress reflects the combined effects of the remote tectonic loading, τ^R, mechanically-induced stresses, $\Delta\tau = \tau^M(\boldsymbol{\delta}_n, \boldsymbol{\delta}_s, \boldsymbol{\delta}_d)$, and a radiation damping term, ηV, which approximates inertial effects (*Rice*, 1993; *Rice and Ben-Zion*, 1996; *Lapusta et al.*, 2000; *Thomas*, 2013). In three dimensions, the total shear stress is the magnitude of the shear traction vector resolved in the direction of sliding:

$$\tau = \sqrt{\sigma_s^2 + \sigma_d^2}. \tag{2.36}$$

To solve the sliding deformation problem, we assumed a Mohr-Coulomb shear failure criterion whereby the frictional strength of a fault, $\bar{\tau}$, can be described as (*Jaeger et al.*, 2007; *Zoback*, 2007):

$$\bar{\tau} = f\bar{\sigma}_n + c. \tag{2.37}$$

Here, f is the friction coefficient and c represents fault cohesion. Mechanical equilibrium is enforced such that the shear stress causing sliding is balanced by the frictional resistance to slip. Therefore, the sliding mechanical equilibrium equation can be expressed as:

$$\tau = \bar{\tau}. \tag{2.38}$$

In the DD method, the fault surfaces are discretized into N^f discrete elements. The equilibrium

equations (Eqs. 2.33 and 2.38) can be expressed in residual form as:

$$R_a = \sigma_{n,a}^R + \Delta\sigma_{n,a} - p_a^f \equiv 0, \quad \text{for } a = 1, \ldots, N^f, \tag{2.39}$$

$$R_a = \tau_a^R + \Delta\tau_a - \eta V_a - f_a\bar{\sigma}_{n,a} - c_a \equiv 0, \quad \text{for } a = 1, \ldots, N^f. \tag{2.40}$$

In order to couple the fluid flow and fault mechanics equations we used a sequential coupling strategy (*Kim et al.*, 2011). Typically, the fluid flow and opening deformation equations (Eqs. 2.15 and 2.39) were used to construct a system of equations and solve simultaneously for $\mathbf{p}^m$, $\mathbf{p}^f$, and $\boldsymbol{\delta}_n$. The solution of the shear deformation equations (Eq. 2.40) required special treatment that depended on the type of problem being solved. In Eq. 2.37, f can be considered as a constant, in a static-dynamic framework, or in a rate-and-state friction framework. When f was constant or static-dynamic, then Eq. 2.40 was solved in an implicit nonlinear framework for the sliding displacement discontinuities $\boldsymbol{\delta}_s$ and $\boldsymbol{\delta}_d$. When f was considered in a rate-and-state framework $\boldsymbol{\delta}_s$, $\boldsymbol{\delta}_d$, $\boldsymbol{\sigma}_n^M$, $\boldsymbol{\sigma}_s^M$, $\boldsymbol{\sigma}_d^M$, and $\boldsymbol{\Psi}$ were each solved for explicitly using a third-order Runge-Kutta method with embedded error estimates (*McClure*, 2012; *Noda et al.*, 2009). In this case, Eq. 2.40 was solved on an element-by-element basis for V in order to update the derivatives in the Runge-Kutta method. A more thorough description of the numerical method for the rate-and-state calculations is given in Sect. 2.4.

2.3 Poroelastic and thermoelastic model

When a rock is subjected to a change in pore fluid pressure or temperature, volumetric deformation can occur (*Coussy*, 2004; *Jaeger et al.*, 2007; *Rana*, 1984; *Segall*, 2010; *Zoback*, 2007). Because rock in the subsurface is typically constrained in some way, if rock attempts to deform it can result in changes in the state of stress. This phenomenon is referred to commonly as porothermoelasticity. These processes can affect reservoir behavior significantly in some settings. *Addis* (1997) reviewed several field cases where reservoir depletion caused a reduction in the minimum horizontal stress which affected wellbore stability and the onset of sand production in oil wells. *Alberty and McLean* (2001) discussed the importance of considering changes in the fracture gradient caused by reservoir depletion when drilling new wells late in the life of an oil reservoir. Although induced earthquakes are typically thought to be associated with increased fluid pressure caused by injection, *Segall* (1989) presented a theoretical framework for extraction-induced seismicity based on poroelasticity. *Segall and Lu* (2015) demonstrated that poroelastic effects can also affect injection-induced seismicity. *Bradford et al.* (2014) presented evidence that thermal stresses played an important role during hydraulic stimulation treatments at a geothermal well. As a final example, *Dohmen et al.* (2014) and *Norbeck and Horne* (2016a) investigated a practical field test called microseismic depletion delineation that leveraged a poroelastic response in order to identify the extent of the reservoir that experienced significant pressure decline in unconventional reservoirs.

Other models have been developed previously that are able to couple fluid flow and mechanical deformation in fractures and the surrounding rock. For example, *Safari and Ghassemi* (2016) introduced a model that used a boundary element method for the matrix flow, poroelastic deformation, and fracture deformation problem. A finite element method was used to solve for flow in the fractures. An advantage of the boundary element approach is that the rock surrounding the fractures does not require discretization and the semianalytical nature of the numerical method is amenable for obtaining highly accurate solutions. A tradeoff is that general heterogeneity cannot be considered. The elastic properties of intact rock do not span wide ranges and don't behave in extremely nonlinear fashion, which is why boundary element methods are popular for fracture deformation problems. However, permeability of rock can vary over many orders of magnitude even within the same formation. For example, *Kurtoglu et al.* (2014) calculated the permeability experimentally for four core samples from the Middle Bakken formation and found that permeability ranged from 0.01 microdarcy to 100 microdarcy, depending on mineralogy and the density of fine-scale fractures. Therefore, the assumption of homogeneous and constant hydraulic properties is a severe limitation for models that solve the flow problem with a boundary element method. In addition, because of the transient nature of the fluid flow problem, a complex convolution is required in the boundary element method (*Kikani*, 1989). The time convolution can be intensive computationally and is difficult to incorporate into a general method that utilizes adaptive timestepping. The method introduced by *Safari and Ghassemi* (2016) required the timestep size to remain constant throughout the duration of the simulation, which is a limiting assumption for application to general purpose reservoir simulation. In an alternative approach, *Garipov et al.* (2016) introduced a model that was based on the finite element method. In that work, deformation of the fractures and surrounding rock were coupled rigorously using a contact formulation. Attractive aspects of this approach are that flow and geomechanics can be solved in a fully-implicit manner so that general nonlinearity and heterogeneity of hydraulic and mechanical properties can be considered. Some disadvantages are that fracture deformation is highly sensitive to the level of discretization, stresses near the crack tips are difficult to resolve, and fracture propagation cannot be handled easily.

In the model presented in this section, different numerical techniques were exploited to solve each part of the problem efficiently. The fluid flow problem was solved using the embedded fracture approach, which is an extension of a traditional finite volume discretization strategy. Because the embedded fracture approach does not require conforming grids for the fractures and matrix rock, fracture propagation is a trivial issue in terms of numerical discretization. The fracture deformation problem was solved using the displacement discontinuity (DD) method, which is a type of boundary element method tailored to crack-like problems. The DD method is useful for solving problems with many mechanically-interacting fractures and is capable of obtaining accurate near-tip stress solutions which are necessary for assessing fracture propagation criteria. Porothermoelastic deformation of the rock surrounding the fractures was solved using a finite element discretization strategy. The

stresses induced throughout the matrix rock due to changes in fluid pressure and temperature were then resolved onto the fracture surfaces using the finite element shape functions and incorporated as additional boundary conditions that were satisfied in the fracture deformation calculations. The various physical processes were coupled using an iterative sequential-implicit strategy.

In the following subsections, we review the set of physical mechanisms that we consider in the model and describe the numerical techniques used to solve the governing differential equations. In our notation, lowercase superscripts refer to different domains (i.e., f for *fracture* volume and m for *matrix* volume) and capital superscripts refer to different loading or deformation mechanisms (i.e., R for *remote* loading, P for *poroelastic* stress, T for *thermal* stress, and M for fracture-*mechanics*-induced stress).

2.3.1 Matrix rock deformation

The numerical formulation for the porothermoelastic framework was presented originally in *Norbeck and Horne* (2016b). For a porous rock volume subjected to a change from a reference state in pressure Δp^m and temperature ΔT^m, Hooke's law for isotropic material properties is (*Jaeger et al.*, 2007):

$$\sigma_{ij}^{P,T} = 2G\varepsilon_{ij}^{P,T} + \Lambda\varepsilon_{kk}^{P,T}\delta_{ij} + \alpha^P \Delta p^m \delta_{ij} + 3\alpha^T K \Delta T^m \delta_{ij}. \tag{2.41}$$

Here, K is bulk modulus, α^P is Biot coefficient (dimensionless), and α^T is linear thermal expansion coefficient (units of $^\circ\mathrm{C}^{-1}$). It is important to recognize that $\sigma_{ij}^{P,T}$ are the changes in total stress that are generated by porothermoelastic effects subject to all boundary conditions. Assuming infinitesimal strains and using Eqs. 2.41 as the constitutive relationships between stress and strain, Eq. 2.25 can be expressed as:

$$G\frac{\partial^2 u_i^{P,T}}{\partial x_k \partial x_k} + (G+\Lambda)\frac{\partial^2 u_k^{P,T}}{\partial x_i \partial x_k} = -F_i - \alpha^P \frac{\partial}{\partial x_i}\Delta p^m - 3\alpha^T K \frac{\partial}{\partial x_i}\Delta T^m, \tag{2.42}$$

where $u_i^{P,T}$ is material displacement vector caused by poroelastic and thermoelastic deformation.

Previous versions of this model incorporated a treatment for poroelasticity that used a finite difference approximation based on elastic potential theory for the mechanics calculations (*Norbeck and Horne*, 2015a, 2016a; *Nowacki*, 1986). In this work, we implemented the finite element formulation described by *Smith et al.* (2014). For the remainder of this section, we use standard finite element notation with bold vectors and matrices representing collections of terms common to finite element analyses. For example, $\mathbf{u}^P$ for a two-dimensional four-node quadrilateral element with an element-centric Cartesian coordinate system now represents the collection of displacements at the

finite element nodes caused by poroelastic deformation:

$$\mathbf{u}^P = \begin{Bmatrix} u_{x1} \\ u_{y1} \\ u_{x2} \\ u_{y2} \\ u_{x3} \\ u_{y3} \\ u_{x4} \\ u_{y4} \end{Bmatrix}^P . \tag{2.43}$$

We envoked the law of superposition for small strain linear elasticity in order to solve for the poroelastic and thermal stresses separately. Because the poroelastic stress and thermal stress problems are analogous, here we will describe the numerical method only for the poroelastic case for the sake of brevity.

Upon discretization with the finite element method, Eq. 2.42 is reduced to a system of equations involving the displacement vectors at the finite element nodes:

$$\mathbf{k}\mathbf{u}^P = \mathbf{f}. \tag{2.44}$$

The finite element stiffness matrix, $\mathbf{k}$, can be calculated as:

$$\mathbf{k} = \iint \mathbf{B}'\mathbf{D}\mathbf{B}\, dxdy \tag{2.45}$$

The strain-displacement matrix involves shape function derivatives. For a four-node quadrilateral element:

$$\mathbf{B} = \begin{bmatrix} \frac{\partial N_1}{\partial x} & 0 & \frac{\partial N_2}{\partial x} & 0 & \frac{\partial N_3}{\partial x} & 0 & \frac{\partial N_4}{\partial x} & 0 \\ 0 & \frac{\partial N_1}{\partial y} & 0 & \frac{\partial N_2}{\partial y} & 0 & \frac{\partial N_3}{\partial y} & 0 & \frac{\partial N_4}{\partial y} \\ \frac{\partial N_1}{\partial y} & \frac{\partial N_1}{\partial x} & \frac{\partial N_2}{\partial y} & \frac{\partial N_2}{\partial x} & \frac{\partial N_3}{\partial y} & \frac{\partial N_3}{\partial x} & \frac{\partial N_4}{\partial y} & \frac{\partial N_4}{\partial x} \end{bmatrix}. \tag{2.46}$$

In Eq. 2.46, N are the nodal shape functions. The stress strain matrix for each element involves only elastic properties. In two-dimensional plane strain:

$$\mathbf{D} = \frac{2G\,(1-\nu)}{(1-2\nu)} \begin{bmatrix} 1 & \frac{\nu}{1-\nu} & 0 \\ \frac{\nu}{1-\nu} & 1 & 0 \\ 0 & 0 & \frac{1-2\nu}{2(1-\nu)} \end{bmatrix}, \tag{2.47}$$

where G is shear modulus and ν is Poisson's ratio. The forms of $\mathbf{B}$ and $\mathbf{D}$ for general three-dimensional elasticity can be found in *Smith et al.* (2014). For an unconstrained material, Eq. 2.41

can be inverted to calculate the strains that would occur due to a change in fluid pressure:

$$\boldsymbol{\varepsilon}^* = \begin{Bmatrix} \varepsilon_{xx} \\ \varepsilon_{yy} \\ 2\varepsilon_{xy} \end{Bmatrix}^* = \begin{Bmatrix} -\frac{\alpha^P}{3K}\Delta p^m \\ -\frac{\alpha^P}{3K}\Delta p^m \\ 0 \end{Bmatrix}. \tag{2.48}$$

The equivalent nodal forces that would cause those strains to occur are:

$$\mathbf{f} = \iint \mathbf{B}'\mathbf{D}\boldsymbol{\varepsilon}^* \, dxdy. \tag{2.49}$$

A significant issue to address here was that a finite volume grid was used for the flow problem where the fluid pressures were calculated as cell-centered values and represent the average pressure over each control volume. If we used, for example, a conventional four node quadrilateral finite element for the poroelastic problem, the fluid pressure was assumed to be continuous at the finite element nodes at the corners of each element. One approach could have been to use staggered grids so that the finite element nodes coincided with the finite volume cell centers. In this work, we chose instead to use the same grids for the finite element and finite volume discretizations. Bilinear interpolation was performed to map the fluid pressure distribution to approximate values at the finite element nodes. Then, Eq. 2.49 was evaluated for each finite element using numerical integration.

Equation 2.44 was assembled into a global system of equations and solved for the nodal displacements $\mathbf{u}^P$. As a post-processing step, the stresses can be calculated anywhere within a finite element by interpolation using the shape functions. At the element level, the total strains can be calculated as:

$$\boldsymbol{\varepsilon}^P = \mathbf{B}\mathbf{u}^P. \tag{2.50}$$

The $\mathbf{B}$ matrix relates displacements at the finite element nodes to strain within the element, and is therefore a function of location within the element. In our application to fractured reservoir problems, we evaluated $\mathbf{B}$ at each discrete fracture element. In this way, we were able to approximate nonuniform distributions of induced stress along fracture surfaces even if there were many fracture elements contained in a single grid block, which was commonly the case in practical applications of the embedded fracture model. Hooke's law was used to calculate the poroelastic stress change:

$$\boldsymbol{\sigma}^P = \mathbf{D}\left(\boldsymbol{\varepsilon}^P - \boldsymbol{\varepsilon}^*\right). \tag{2.51}$$

The concept for coupling between the embedded fracture flow model and the finite element poromechanical model is illustrated in Fig. 2.3.

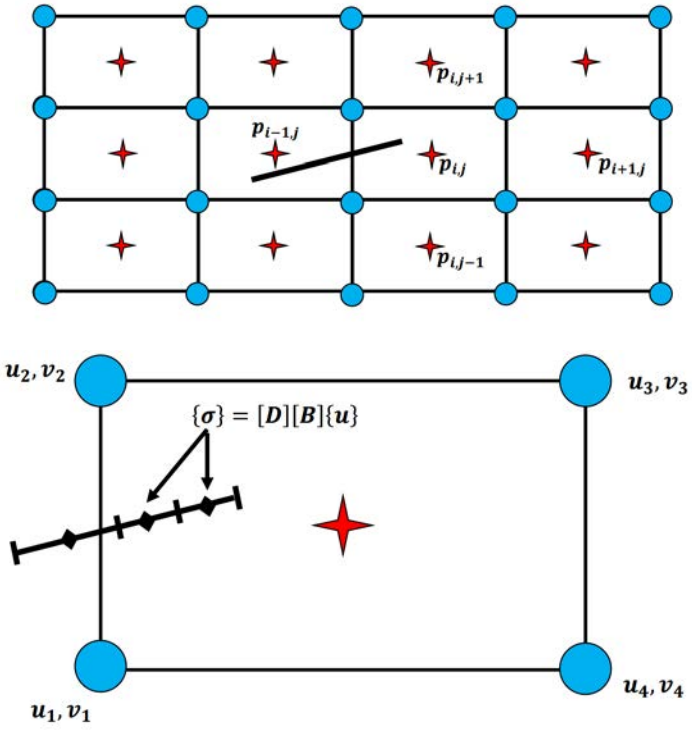

Figure 2.3: Illustration of the embedded fracture discretization concept. (top) A structured Cartesian mesh was used for the matrix fluid flow and poroelastic calculations. The red diamonds represent the cell centers for the finite volume discretization, the blue circles represent the finite element nodes, and the black line represents the fracture. (bottom) Fractures were discretized using the displacement discontinuity method. Poroelastic stresses were resolved onto the fractures using the finite element shape functions, which allowed for the description of nonuniform loading conditions when multiple fracture elements existed at the subgrid scale.

2.3.2 Coupling to fracture deformation

The state of stress at a particular location in the material reflects the superposition of the remote tectonic stress, σ_{ij}^R, mechanically-induced stress caused by fracture deformation, σ_{ij}^M, and porothermoelastic effects:

$$\sigma_{ij} = \sigma_{ij}^R + \sigma_{ij}^M + \sigma_{ij}^P + \sigma_{ij}^T. \tag{2.52}$$

For a fracture surface with outward facing unit normal vector $\mathbf{n}$, the stress tensor can be used to calculate the traction vectors acting on the fracture surface, $\mathbf{t}(\mathbf{n})$, from Cauchy's formula (*Pollard and Fletcher*, 2005):

$$t_i(\mathbf{n}) = \sigma_{ji} n_j. \tag{2.53}$$

The traction vector can then be decomposed into its normal and shear components (*Pollard and Fletcher*, 2005):

$$\mathbf{t} = \mathbf{t}_n + \mathbf{t}_s = (\mathbf{t} \cdot \mathbf{n})\,\mathbf{n} + \mathbf{n} \times (\mathbf{t} \times \mathbf{n}) \tag{2.54}$$

It is common to refer to the magnitudes of $\mathbf{t}_n$ and $\mathbf{t}_s$ as the normal and shear stresses acting on the fracture. In three dimensions:

$$\sigma_n = \mathbf{t}_n \cdot \mathbf{n}, \tag{2.55}$$

$$\sigma_s = \mathbf{t}_s \cdot \mathbf{s}, \tag{2.56}$$

$$\sigma_d = \mathbf{t}_s \cdot \mathbf{d}, \tag{2.57}$$

where $\mathbf{s}$ and $\mathbf{d}$ are the unit vectors in the along-strike and along-dip directions, respectively. The normal and shear components of the stresses induced by poroelastic and thermoelastic deformation were superimposed to the boundary conditions for the fracture deformation problem. Therefore, Eqs. 2.39 and 2.40 were modified such that $\Delta\sigma_n = \sigma_n^M + \sigma_n^P + \sigma_n^T$ and $\Delta\tau = \tau^M + \tau^P + \tau^T$. The DD relationship (Eq. 2.32) was modified to become:

$$\begin{Bmatrix} \boldsymbol{\sigma}_n^M + \boldsymbol{\sigma}_n^P + \boldsymbol{\sigma}_n^T \\ \boldsymbol{\sigma}_s^M + \boldsymbol{\sigma}_s^P + \boldsymbol{\sigma}_s^T \\ \boldsymbol{\sigma}_d^M + \boldsymbol{\sigma}_d^P + \boldsymbol{\sigma}_d^T \end{Bmatrix} = \begin{bmatrix} \mathbf{A}_{nn} & \mathbf{A}_{ns} & \mathbf{A}_{nd} \\ \mathbf{A}_{sn} & \mathbf{A}_{ss} & \mathbf{A}_{sd} \\ \mathbf{A}_{dn} & \mathbf{A}_{ds} & \mathbf{A}_{dd} \end{bmatrix} \begin{Bmatrix} \boldsymbol{\delta}_n \\ \boldsymbol{\delta}_s \\ \boldsymbol{\delta}_d \end{Bmatrix}. \tag{2.58}$$

This ensured that the appropriate boundary conditions along the fracture surfaces were upheld.

2.4 Earthquake rupture model

For injection-induced seismicity applications, it is not sufficient to consider a single earthquake event. While relatively large earthquakes are naturally of interest, the seismicity leading up to and following large events can also be extremely important in terms of characterizing the seismic behavior of a given site. Earthquake sequences associated with fluid injection have often indicated that many earthquakes can be triggered along the same fault plane (*Horton*, 2012; *Kim*, 2013; *McNamara et al.*, 2015a). These observations correspond to the fact that loading distributions that cause earthquake events are changing continually during fluid injection processes. Therefore, when attempting to model injection-induced seismicity, it is necessary to employ a framework that accounts for earthquake nucleation, rupture propagation, rupture arrest, and fault restrengthening in order to allow for the emergence of seismic sequences. Rate-and-state friction is one theory that is able to capture the full earthquake rupture cycle. When combined with a rigorous treatment of elasticity, using rate and-state theory to model friction evolution provides a powerful tool to gain insight into the physical mechanisms of earthquakes. In this section, we present the rate-and-state friction formulation used in our model and discuss the application of the boundary element method as a numerical solution strategy for earthquake rupture problems.

2.4.1 Rate-and-state friction

In the rate-and-state framework, friction depends on sliding velocity, V, and also on a state variable, Ψ, that accounts for the history of sliding. Two common regularizations for the coefficient of friction are (*Dieterich*, 1992; *Rice et al.*, 2001):

$$f\left(V,\Psi\right)=a\sinh^{-1}\left[\frac{V}{2V_{*}}\exp\left(\frac{\Psi}{a}\right)\right], \tag{2.59}$$

and

$$f\left(V,\Psi\right)=a\ln\frac{V}{V_{*}}+\Psi. \tag{2.60}$$

Both Eqs. 2.59 and 2.60 are equivalent at large slip speeds, but the former is more stable numerically as $V\rightarrow 0$. The parameter a controls the magnitude of the direct effect, which causes an immediate strengthening for increasing V. During the coseismic period of an earthquake rupture, Ψ controls the friction weakening behavior along the fault behind the rupture front. As a rupture dies out, Ψ increases to bring the fault back to a steady-state at low V. Two forms of state evolution are commonly applied in earthquake rupture modeling. The slip law allows state to evolve only when the fault is sliding:

$$\frac{\partial\Psi}{\partial t}=-\frac{V}{\delta_{c}}\left[f\left(V,\Psi\right)-f_{ss}\left(V\right)\right]. \tag{2.61}$$

The aging law allows state to evolve even as $V \to 0$:

$$\frac{\partial \Psi}{\partial t} = -\frac{V}{\delta_c}\left\{b - b\exp\left[-\frac{f\left(V,\Psi\right) - f_{ss}\left(V\right)}{b}\right]\right\}. \tag{2.62}$$

Here, δ_c is the characteristic slip distance over which state evolution occurs, b controls the magnitude of state evolution, and f_{ss} is the steady-state friction coefficient that is reached after significant slip has occurred (i.e., $\delta \gg \delta_c$) while sliding at constant V. The two state evolution laws have different physical implications, so we have incorporated both forms of state evolution into the model to allow for further testing.

The particular forms chosen to represent friction and state evolution in Eqs. 2.59 - 2.62 have several interesting advantages both in terms of physics and numerics. State is represented as a dimensionless variable, and has a magnitude on the order of the friction coefficient. Therefore, it is more stable numerically than when represented with units of time, where it can change over many orders of magnitude very rapidly. In addition, the state evolution equations are able to consider any functional form for the steady-state friction coefficient. Recent laboratory experiments have shown that friction can undergo extreme weakening at very high slip speeds approaching $V = 1$ m/s (*Beeler et al.*, 2008). This can have a significant impact, for example, on interpreting earthquake rupture behavior on faults with low normal stress like the San Andreas Fault (*Dunham et al.*, 2011). In this work, we used a more traditional form for steady-state friction:

$$f_{ss}\left(V\right) = f_* - \left(b - a\right)\ln\frac{V}{V_*}. \tag{2.63}$$

Effective normal stress can also be very low in settings of injection-induced seismicity, and so investigating how alternate forms of f_{ss} affect the earthquake rupture process may be a worthwhile pursuit in future research.

Linker and Dieterich (1992) demonstrated through laboratory experiments that $\partial\Psi/\partial t$ can be influenced by changes in normal stress. This effect may be especially important for application to injection-induced seismicity, where earthquake nucleation is triggered by a reduction in fault strength as opposed to increased shear loading. Using the empirical model introduced by *Linker and Dieterich* (1992), Eqs. 2.61 and 2.62 can be modified to include the effects of variable normal stress:

$$\frac{\partial \Psi}{\partial t} = -\frac{V}{\delta_c}\left[f - f_{ss}\right] - \frac{\xi}{\bar{\sigma}_n}\frac{\partial \bar{\sigma}_n}{\partial t}, \tag{2.64}$$

$$\frac{\partial \Psi}{\partial t} = -\frac{V}{\delta_c}\left[b - b\exp\left(-\frac{f - f_{ss}}{b}\right)\right] - \frac{\xi}{\bar{\sigma}_n}\frac{\partial \bar{\sigma}_n}{\partial t}. \tag{2.65}$$

The parameter ξ, which controls the magnitude of the variable normal stress effect, can be measured experimentally, and was found to be 0.2 - 0.5 in the experiments performed by *Linker and Dieterich* (1992).

2.4.2 Numerical discretization, error estimate, and timestep control

During an earthquake rupture, state and sliding velocity can change rapidly causing fault strength to evolve in a highly nonlinear fashion. Therefore, to solve for sliding displacements in the rate-and-state framework we used an explicit third-order Runge-Kutta method to update $\boldsymbol{\delta}_s$, $\boldsymbol{\delta}_d$, $\boldsymbol{\sigma}_n^M$, $\boldsymbol{\sigma}_s^M$, $\boldsymbol{\sigma}_d^M$, and $\boldsymbol{\Psi}$. The third-order method is advantageous because it allows for efficient estimates of the error in the calculation (*Noda et al.*, 2009), which can be used to manage the timestep size optimally as a simulation progresses. Runge-Kutta schemes are a class of numerical methods used to solve nonlinear ordinary differential equations of the form (*Griffiths and Smith*, 2006):

$$\frac{dy}{dt} = g\left(t, y\left(t\right)\right), \quad y\left(t_0\right) = y_0. \tag{2.66}$$

The solution is estimated at discrete time intervals starting from the initial condition and marching though time using steps of Δt (which can vary adaptively). In the third-order method, the solution at timestep $n+1$ is estimated as:

$$y_{\mathcal{O}(3)}^{n+1} = y^n + \frac{\Delta t}{6}\left(k_1 + 4k_2 + k_3\right), \tag{2.67}$$

where the term on the right hand side involves derivatives evaluated at specific points within the time interval:

$$k_1 = g\left(t^n, y^n\right), \tag{2.68}$$

$$k_2 = g\left(t^n + \frac{\Delta t}{2}, y^n + \frac{\Delta t}{2}k_1\right), \tag{2.69}$$

$$k_3 = g\left(t^n + \Delta t, y^n - \Delta t k_1 + 2\Delta t k_2\right). \tag{2.70}$$

A convenient form of a second-order method is chosen because it makes use of derivatives that are already calculated for the third-order method:

$$y_{\mathcal{O}(2)}^{n+1} = y^n + \frac{\Delta t}{2}\left(k_1 + k_2\right). \tag{2.71}$$

The error can then be estimated to second-order accuracy in time and the timestep can be chosen to provide solutions accurate to within a threshold error tolerance:

$$\epsilon_{\mathcal{O}(2)} = \left| y_{\mathcal{O}(3)}^{n+1} - y_{\mathcal{O}(2)}^{n+1} \right| \leq \epsilon_{tol}. \tag{2.72}$$

The magnitude of ϵ can also be used to estimate an appropriate size for the next timestep.

Consider a fault that is discretized with the DD method into a total of N^f fault elements. The following expressions are each written for all fault elements ranging from $a = 1, \ldots, N^f$. In the

rate-and-state framework, each fault element is sliding at some velocity $V = \sqrt{V_s^2 + V_d^2}$. For the sliding displacement discontinuities, the partial differential equations of interest are:

$$\frac{d\delta_{s,a}}{dt} = V_{s,a}, \tag{2.73}$$

$$\frac{d\delta_{d,a}}{dt} = V_{d,a}. \tag{2.74}$$

The DD relationship in Eq. 2.32 indicates that changes in stress are related linearly to the displacement discontinuities. Similarly, the rate of change of the stresses are related linearly to the sliding velocity:

$$\frac{d\sigma_{n,a}^M}{dt} = \sum_{b=1}^{N^f} A_{ns,ab} V_{s,b} + \sum_{b=1}^{N^f} A_{nd,ab} V_{d,q}, \tag{2.75}$$

$$\frac{d\sigma_{s,a}^M}{dt} = \sum_{b=1}^{N^f} A_{ss,ab} V_{s,b} + \sum_{b=1}^{N^f} A_{sd,ab} V_{d,q}, \tag{2.76}$$

$$\frac{d\sigma_{d,a}^M}{dt} = \sum_{b=1}^{N^f} A_{ds,ab} V_{s,b} + \sum_{b=1}^{N^f} A_{dd,ab} V_{d,q}. \tag{2.77}$$

In order to update the state variable, one must choose the desired form of the state evolution formulation. For example, the slip law form of state evolution yields:

$$\frac{d\Psi_a}{dt} = -\frac{V_a}{\delta_{c,a}} \left[f_a \left(V_a, \Psi_a \right) - f_{ss,a} \left(V_a \right) \right]. \tag{2.78}$$

In Eq. 2.78, state evolution is clearly nonlinear because the friction coefficient depends on Ψ. In contrast, Eqs. 2.73 - 2.77 would be trivial forms of Eq. 2.66 if the right hand were constant because the derivatives themselves do not depend on the variables of interest. However, because sliding velocity can be expected to change rapidly over a timestep we must enforce an additional constraint to help guide the solution. The solution strategy involves calculating intermediate values of the primary variables and updating sliding velocity to enforce equilibrium (Eq. 2.40) at specific points within a timestep. A description of the solution strategy for the rate-and-state friction calculations is shown in Algorithm 1.

2.5 Concluding remarks

In this chapter, we presented the mathematical formulation for the numerical model that was applied throughout this work. The model is capable of calculating the coupled interaction of fluid flow, heat transfer, mechanical deformation, tensile failure, and frictional failure in fractured porous media. A principal achievement of this work was the development of a fully-coupled fluid flow and

Algorithm 1 Rate-and-state friction timestep

Store primary variables from previous timestep: $y^n = (\delta_s, \delta_d, \Psi, \sigma_n, \sigma_s, \sigma_d)^n$
Choose timestep size: Δt
Enter Substep 1
    Update intermediate variables: $y_1 = y^n$
    Calculate derivatives: k_1
    Update V to enforce equilibrium (Eq. 2.40)
Enter Substep 2
    Update intermediate variables: $y_2 = y^n + \frac{\Delta t}{2} k_1$
    Calculate derivatives: k_2
    Update V to enforce equilibrium (Eq. 2.40)
Enter Substep 3
    Update intermediate variables: $y_3 = y^n - \Delta t k_1 + 2\Delta t k_2$
    Calculate derivatives: k_3
    Update V to enforce equilibrium (Eq. 2.40)
Calculate third-order estimate of primary variables: $y^{n+1}_{\mathcal{O}(3)} = y^n + \frac{\Delta t}{6}(k_1 + 4k_2 + k_3)$
Calculate second-order estimate of primary variables: $y^{n+1}_{\mathcal{O}(2)} = y^n + \frac{\Delta t}{2}(k_1 + k_2)$
Calculate error: $\epsilon_{\mathcal{O}(2)} = \left| y^{n+1}_{\mathcal{O}(3)} - y^{n+1}_{\mathcal{O}(2)} \right|$
if $\epsilon_{\mathcal{O}(2)} \leq \epsilon_{tol}$ **then**
    Update V to enforce equilibrium (Eq. 2.40)
    Proceed to next timestep
else
    Repeat timestep with smaller Δt
end if

geomechanical model based on an embedded fracture modeling framework. Because the model integrates a realistic description of reservoir geologic structure with the fluid flow and fault deformation calculations, it is possible to address the issue of injection-induced seismicity from a physics-based perspective.

In Chapter 3, we present the results of several numerical experiments that emphasize the embedded fracture model's capability for solving practical engineering problems related to subsurface reservoir geomechanics. Our novel treatment for integrating poroelastic and thermoelastic deformation of rock with the mechanical deformation of fractures was utilized in the investigations presented in Chapters 4 and 5. The rate-and-state friction earthquake rupture model was critical for performing the investigation of the 2011 Prague, Oklahoma earthquake sequence presented in Chapter 6. The study presented in Sect. 7.2 explored the relationship between fluid flow in aquifers targeted for wastewater disposal and fluid flow along fault zone structures, which was enabled by the integration of the embedded fracture and rate-and-state friction models. The extension of the rate-and-state friction component of the numerical model to three dimensions allowed for a rigorous treatment of the stress and frictional heterogeneity expected to be present within natural fault structures. In the study presented in Sect. 7.3, stress heterogeneity was used as a proxy to describe the geometrical complexity of two-dimensional fault surfaces in an attempt to model injection-induced earthquake sequences with realistic frequency-magnitude statistics.

Chapter 3

Verification of Numerical Model Accuracy

The purpose of this chapter is to present the results of several studies that have demonstrated that the numerical model applied in subsequent chapters performs calculations accurately. These test studies were chosen to reflect the range of physical processes that were considered in the analyses that followed. Chapter 3 is organized as follows. In Sects. 3.1 and 3.3, we present investigations of problems related to one-dimensional fluid leakoff while circulating fluid through a fracture. In the example given in Sect. 3.2, we investigated the embedded fracture model's ability to capture the transition between early-time linear and late-time radial flow regimes for the problem of injection into an infinite conductivity fracture. In Sect. 3.3, we present the results for a problem related to heat transfer toward a planar fracture surface. In Sect. 3.4, we demonstrate the model's accuracy for a more complex scenario involving nonisothermal flow through a set of parallel fractures where heat advection dominates within the fractures and conduction dominates in the surrounding rock. In Sect. 3.5, we present the results of a comparison study between EFM and DFM techniques in which shear stimulation in a network of connected fractures gave rise to a highly nonlinear reservoir response. In Sect. 3.6, we present results that verified the accuracy of EFM calculations for a mode-I hydraulic fracture propagation problem. We compared the EFM fracture propagation results against semianalytical models and a DFM approach. Finally, in Sect. 3.7, we demonstrate the model's accuracy for calculating three-dimensional earthquake nucleation, rupture, and arrest within a quasidynamic rate-and-state friction framework.

3.1 Isothermal fluid circulation through a fractured reservoir

This example was presented in *Norbeck et al.* (2014). The purpose of the investigation was to determine whether the EFM matrix-fracture mass transfer term (see Eq. 2.7) is able to capture leakoff behavior of fractured systems accurately. We compared the results of the EFM approach against an analytical solution for a problem involving fluid circulation between two wells connected by a single vertical fracture. We found that the numerical model yielded accurate solutions for the transient evolution of the reservoir pressure distribution. We observed that the numerical method was convergent upon discretization refinement.

3.1.1 Problem description

Our numerical model was compared against the analytical solution presented by *Ghassemi et al.* (2008) for a reservoir that contains one production well and one injection well connected by a single vertical fracture. The problem configuration is illustrated in Fig. 3.1. In the model, fluid was injected at a constant volumetric rate and the production well was maintained at a constant pressure equal to the initial reservoir pressure. Hydromechanical effects were neglected so that the fracture aperture remained constant. The fluid in the fracture was assumed to be incompressible and flow was isothermal.

In order to obtain an analytical expression for pressure distribution in the fracture, the fluid leakoff rate was assumed to be constant along the fracture and also in time. The resulting fracture pressure distribution was then used as a boundary condition to solve the slightly compressible diffusivity equation for the transient pressure distribution in the surrounding matrix rock. Fluid leakoff was assumed to be one-dimensional flow in the direction perpendicular to the fracture. Fluid pressure in the matrix can then given by the following expression (*Ghassemi et al.*, 2008):

$$p^m(x,y,t) = (x-L)\left[C_1(x+L) - C_2\right] \operatorname{erfc}\left(\frac{|y|}{2\sqrt{D_H t}}\right) + p_0, \tag{3.1}$$

where L is the length of the fracture, D_H is hydraulic diffusivity of the matrix rock, and p_0 is the initial reservoir pressure. The two constants are:

$$C_1 = \frac{12 q_L}{\lambda e^3}, \tag{3.2}$$

and

$$C_2 = \frac{12 q_i}{\lambda e^3}, \tag{3.3}$$

where q_L is the constant leakoff rate and q_i is the constant injection rate (both normalized as per unit length in the vertical dimension of the fracture). The hydraulic diffusivity of the matrix rock

is defined as:

$$D_H = \frac{\lambda k^m}{\phi^m \left(\beta_\varphi + \beta_r\right)} \tag{3.4}$$

where β_φ is fluid compressibility and β_r is pore compressibility. All relevant model parameters are listed in Table 3.1. Several levels of matrix discretization refinement were tested.

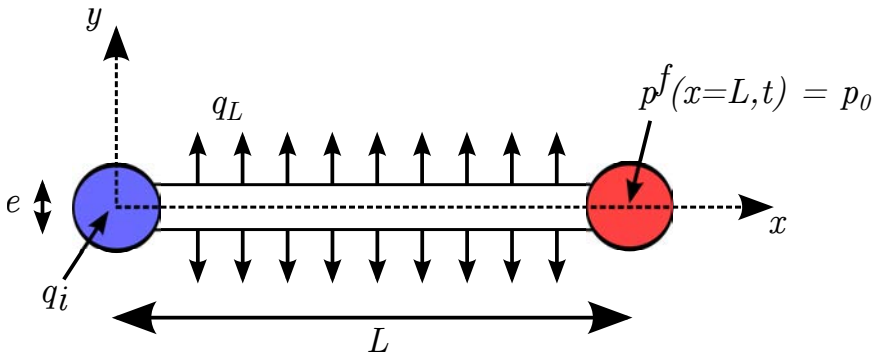

Figure 3.1: The injection well (left) and production well (right) were connected by a vertical fracture with a constant aperture. The leakoff rate was assumed to be uniform along the fracture and constant in time. This figure was modified from *Ghassemi et al.* (2008).

Table 3.1: Model parameters for the investigation of isothermal fluid circulation through a fractured reservoir.

Parameter	Value	Unit
p_0	40	MPa
q_i	3×10^{-4}	$m^3 \cdot s^{-1} \cdot m^{-1}$
q_L	3×10^{-7}	$m^3 \cdot s^{-1} \cdot m^{-2}$
λ^{-1}	0.001	$Pa \cdot s$
D_H	2.2×10^{-5}	$m^2 \cdot s^{-1}$
e	0.001	m
L	1000	m

3.1.2 Results

In Fig. 3.2, the analytical solution is compared to the numerical solution for the times of 100 days and 1000 days after the start of injection and production. The numerical solution with the highest level of grid refinement was able to capture the leakoff behavior accurately at both early times and late times. The late-time solutions were slightly different near the boundaries of the domain. This difference was due primarily to boundary effects because the analytical solution assumed an infinite domain. In addition, the analytical solution assumed one-dimensional flow while the numerical solution calculated the more realistic case of two-dimensional flow.

The reservoir pressures yielded from finite volume schemes represent an average pressure over the control volume, therefore accuracy must be quantified with respect to volume averages. To quantify the error introduced by the numerical scheme, the root mean square error relative to the analytical solution was calculated across the domain and normalized by the pressure drop between the injection and production well. The error is presented in Fig. 3.3 for five different levels of grid refinement at different solution times. The error for the lowest level of grid refinement ranged between 1% and 6% over the duration of the simulation. The error for the highest level of grid refinement ranged between roughly 1% and 2%.

The goal of this numerical experiment was to verify that the EFM matrix-fracture mass transfer approach was capable of calculating leakoff behavior accurately by treating fractures essentially like wells, in contrast to more conventional DFM approaches. These results indicate that the assumptions involved in deriving the EFM fracture index were well founded, at least for this simple model of a single vertical fracture. A limitation of this study was that the fracture pressure was held constant. This was done in order to compare with the analytical solution presented by *Ghassemi et al.* (2008). In later sections, we present studies where we investigated the accuracy of the EFM approach for more complex scenarios in which fluid pressure distributions in both the fractures and the matrix rock exhibit transient behavior. Nonetheless, we have demonstrated that the conceptual approach of using two separate computational domains for the fracture and matrix system can provide reasonably accurate solutions without the need of an unstructured, conforming grid.

3.2 Injection into a highly conductive fracture in an infinite domain

This example was presented in *Norbeck and Horne* (2016a). In Sect. 3.1 we observed that the EFM implementation achieved a suitable degree of accuracy for a problem involving one-dimensional leakoff from a single fracture that connected an injection and production well. This was a relatively benign scenario because the EFM fracture index (see Eq. 2.10) was derived assuming linear flow near the fracture.

3.2.1 Problem description

In this example, injection into a vertical infinite-conductivity fracture in an infinite reservoir was considered. The reservoir response for this problem is a linear flow regime at early times, followed by a transition to radial flow at later times. A closed-form solution exists for the transient pressure

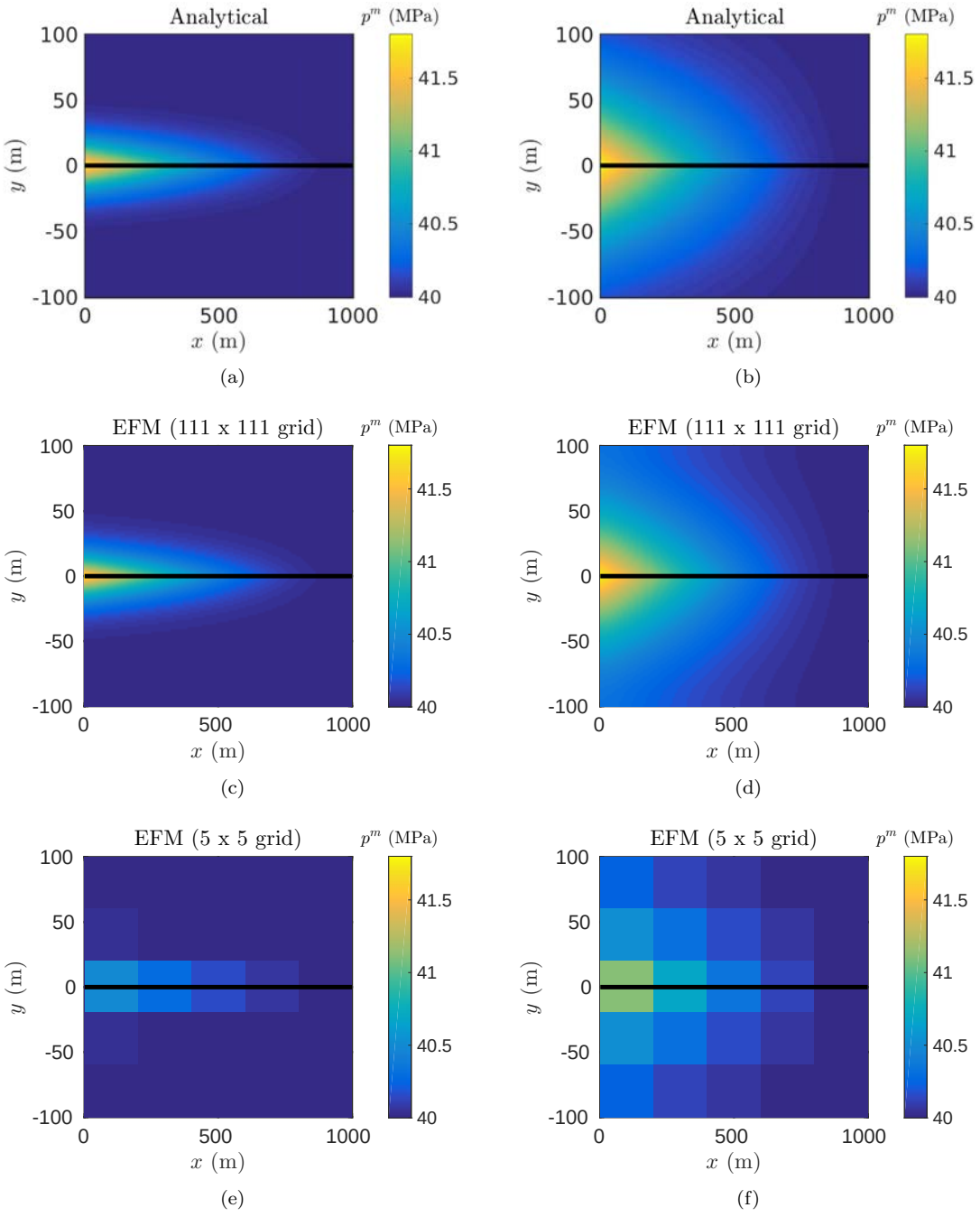

Figure 3.2: Comparison between (top row) the analytical solution, (middle row) EFM solution using 111 x 111 control volumes, and (bottom row) EFM solution using 5 x 5 control volumes. The matrix pressure distribution is shown at (left) 100 days and (right) 1000 days . The *black line* represents the fracture.

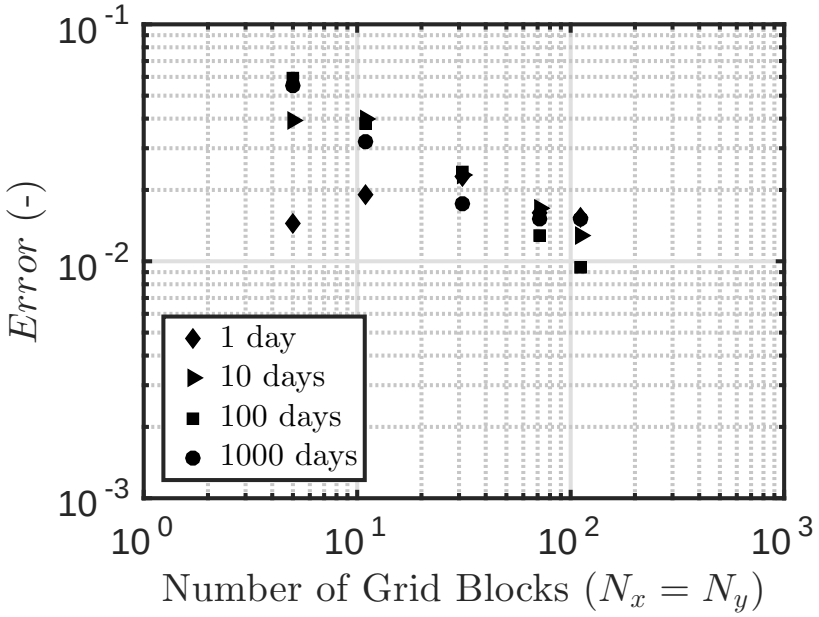

Figure 3.3: Normalized mean square error for different levels of matrix domain grid refinement. The different symbols represent the error at various times in the simulation. Errors were calculated with respect to volumetric averages of the analytical solution and normalized by the maximum pressure drop across the system.

response at the well (*Gringarten et al.*, 1974):

$$p_D^w(t_D) = 0.5\sqrt{\pi t_D}\left[\text{erf}\left(\frac{0.134}{\sqrt{t_D}}\right) + \text{erf}\left(\frac{0.866}{\sqrt{t_D}}\right)\right] + 0.067\text{Ei}\left(\frac{0.018}{t_D}\right) + 0.433\text{Ei}\left(\frac{0.750}{t_D}\right). \quad (3.5)$$

Here, the dimensionless pressure variable, p_D^w, is defined as:

$$p_D^w = \frac{2\pi\lambda k^m h_f}{q^w}\left(p^w - p_0\right), \quad (3.6)$$

and the dimensionless time variable, t_D, is defined as:

$$t_D = \frac{\lambda k^m}{\phi^m\left(\beta_\varphi + \beta_r\right)x_f^2}t, \quad (3.7)$$

where h_f is the fracture height (which is equal to the reservoir thickness), q^w is the volumetric injection rate, p^w is the wellbore pressure, p_0 is the initial reservoir pressure, x_f is the fracture half-length, and t is the time since the start of injection.

The model parameters used in the simulations are given in Table 3.2. In the model, fluid was injected at a constant rate for a period of 48 hours. Wellbore storage effects were neglected. Geomechanical effects were not considered, so the properties of the fracture remained constant throughout the simulations (i.e., the length and permeability of the fracture were fixed).

The EFM, DFM, and one-dimensional leakoff approximation models were compared. In each case, the same fracture discretization was used. For the EFM nonconforming matrix discretization, a structured Cartesian mesh comprised of 90,601 control volumes was used. For the DFM conforming matrix discretization, a triangular mesh comprised of 80,876 control volumes was used.

3.2.2 Results

The wellbore pressure response curves observed in the three simulations are compared against Eq. 3.5 on a log-log plot in Fig. 3.4. The time derivative of the EFM pressure response was evaluated numerically, and is also plotted in the same figure. The 1/2 slope of both the pressure and pressure derivative curves at early times is indicative of the linear flow regime that developed when flow was dominated by the presence of the fracture (*Horne*, 1995). Each of the three numerical models captured this behavior accurately. There are slight discrepancies observed for the EFM and DFM models at very early time ($t_D < 4 \times 10^{-3}$), but the magnitude of the errors were small and appear exaggerated in the figure due to the logarithmic scale. The one-dimensional leakoff approximation performed extremely accurately during the linear flow regime.

At a time of $t_D \approx 4 \times 10^{-2}$, the pressure response calculated using Eq. 3.5 begins to diverge from the linear flow regime and transitions toward a radial flow regime. We observed that both the EFM and DFM models were able to capture the transition from linear to radial flow accurately. As expected, the one-dimensional leakoff approximation was not valid for simulation times that extended well beyond the linear flow regime.

In addition to demonstrating the accuracy of the three numerical models, this example also revealed a very interesting characteristic of the EFM approach. While the fracture index embodies an implicit assumption that flow is purely linear in the vicinity of the fracture, in this example the global pressure response of late-time radial flow was captured accurately. In this light, it is evident that the concept of EFM may be applied in scenarios that involve more complex flow regimes, for example, in naturally fractured reservoirs in which nearby fractures affect each other.

3.3 One-dimensional heat conduction toward a fracture surface

In low-permeability rocks, flow occurs predominantly through the fractures. Heat transfer is encouraged if fluid is injected into the reservoir that has a different temperature than the host rock. When

Table 3.2: Model parameters for investigation of injection into an infinite-conductivity fracture.

Parameter	Value	Unit
x_f	50	m
h_f	10	m
e	0.01	m
k^m	20×10^{-15}	m^2
ϕ^m	0.2	-
$\beta_\varphi + \beta_r$	8.8×10^{-10}	Pa^{-1}
λ^{-1}	0.001	$Pa \cdot s$
q^w	0.01	$m^3 \cdot s^{-1}$
p_0	40	MPa

fluid flow in the matrix rock is negligible, then conduction dominates the heat transfer process in the matrix rock and the fractures act as heat sources or sinks. In this section, we present the results of a verification study that focused on demonstrating the model's accuracy for solving thermal conduction problems for boundary conditions along fracture surfaces that remain constant in time.

3.3.1 Problem description

In this numerical example, we compared the results of the numerical model against an analytical solution for one-dimensional heat conduction towards a planar surface that is held at a constant temperature within an infinite domain. The problem represented an idealized conceptual model for understanding heat conduction near a fracture that has been cooled due to fluid injection. For example, *Tester et al.* (1989) applied this type of model in an investigation of secondary thermal fracturing in geothermal reservoirs.

For a fracture that exists in the x-plane subjected to an instantaneous temperature change, the solution to the one-dimensional thermal diffusion problem is (*Carslaw and Jaeger*, 1959; *Jaeger et al.*, 2007):

$$T^m(y,t) = T_0^m + \left(T_0^f - T_0^m\right) \operatorname{erfc}\left(\frac{|y|}{2\sqrt{D_T t}}\right), \tag{3.8}$$

where T_0^m is the initial reservoir temperature, T_0^f is the temperature of the fracture surface, and the thermal diffusivity, D_T, is:

$$D_T = \frac{\kappa}{\phi^m \rho_\varphi c_\varphi + (1-\phi^m)\rho_r c_r}. \tag{3.9}$$

An assumption in the analytical model was that the fracture surface was infinitely long in the direction normal to heat flow. In the numerical model, the fracture was 1000 m long and was discretized into 1000 elements. The matrix domain extended from $x = \pm 500$ m and $y = \pm 1000$ m. The matrix domain was discretized using a structured Cartesian mesh with 101 grid blocks in the x-direction and 501 grid blocks in the y-direction, for a total of 50,601 control volume elements. The

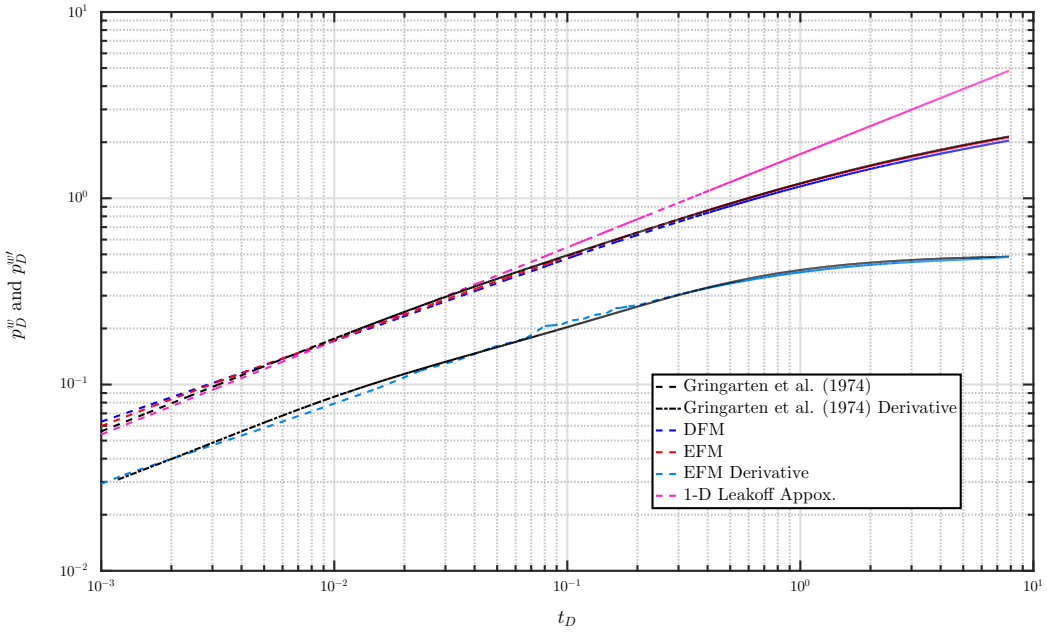

Figure 3.4: Wellbore pressure and pressure derivative versus time for the problem of injection into an infinite conductivity fracture in an infinite domain. The 1/2 slope in both the pressure and pressure derivative at early times reflects a linear flow regime. At late times, the solution transitions toward a radial flow regime (reflected by the derivative tending toward a slope of zero). The embedded fracture model captured the transition in behavior accurately when compared against the DFM and analytical solution (see Eq. 3.5).

duration of the simulation was 10,000 days. Although the analytical solution assumed an infinite half-space, zero heat flux conditions were enforced along each boundary in the model. The matrix temperature was recorded along the centerline ($x = 0$ m) in order to reduce any apparent effects of the boundary conditions. Table 3.3 lists the parameters used in this study.

3.3.2 Results

In Fig. 3.5, the matrix temperature evolution is shown at several over the 10,000 day simulation duration for three different distances away from the fracture surface. The solid lines show the analytical solution (see Eq. 3.8) and the open circles shown the numerical solution. A close agreement was achieved. After 100 days, the thermal transient was able to propagate roughly 15 m away from the fracture surface. After 10,000 days, the thermal transient reached a distance of only 130 m. This suggests that boundary effects did not influence the solution.

In this example, the fracture surface was held at a constant temperature. Through the embedded fracture heat transfer term (see Eq. 2.21), heat was removed from the system which drove the thermal diffusion in the matrix rock. Therefore, this example demonstrated that the EFM approach was

Table 3.3: Model parameters for one-dimensional heat conduction towards a fracture surface.

Parameter	Value	Unit
κ_r	2	$W \cdot m^{-1} \cdot °C^{-1}$
κ_φ	0.6	$W \cdot m^{-1} \cdot °C^{-1}$
ρ_r	2650	$kg \cdot m^{-3}$
ρ_φ	1000	$kg \cdot m^{-3}$
c_r	816	$J \cdot kg^{-1} \cdot °C^{-1}$
c_φ	4150	$J \cdot kg^{-1} \cdot °C^{-1}$
ϕ^m	0.1	-
T_0^m	275	°C
T_0^f	100	°C

able to calculate the heat transfer between the fracture and matrix domains accurately for problems where conduction in the matrix dominates and the fracture remains at constant temperature. In the following section, the results of a more challenging numerical example are presented.

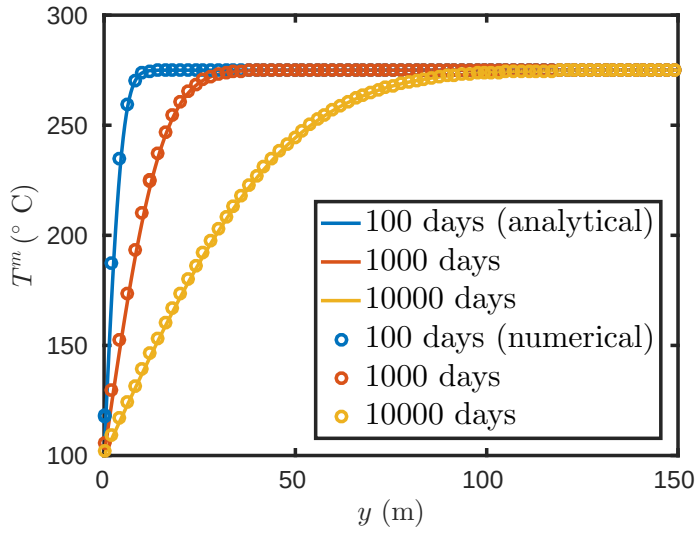

Figure 3.5: Matrix temperature distribution with increasing distance away from the fracture surface after 100 days, 1000 days, and 10,000 days of cooling. The *colored circles* represent the EFM numerical solution and the *colored lines* represent the analytical solution (see Eq. 3.8). The thermal front propagated away from the fracture at a rate controlled by the thermal diffusivity of rock.

3.4 Nonisothermal fluid circulation through a fractured reservoir

In the previous section, the accuracy of the EFM approach was verified for a problem involving heat conduction in the matrix rock towards a fracture surface held at constant temperature. In fractured reservoir problems of practical interest, the fractures do not act as constant temperature boundaries. Large flow velocities within fractures suggest that advection dominates heat transfer along the fractures. For low-permeability rocks like granite, conduction dominates heat transfer in the matrix. There is a tight coupling between these two processes that can influence how reservoir temperature evolves. In this numerical example, the problem of nonisothermal fluid circulation through a fractured reservoir was addressed.

3.4.1 Problem description

The conceptual model and assumptions for this problem are described in detail by *Gringarten et al.* (1975). The problem geometry is illustrated in Fig. 3.6. The analysis assumed that one injection well and one production well were connected by a set of several parallel fractures. The fractures were spaced equidistantly by a distance of $2y_E$. The distance between the wells was L, the fractures each had the same aperture e that remained constant, and an out-of-plane width W. The rock between the fractures was impermeable and existed initially at temperature T_0^m. Water was injected at a constant temperature T_i^w such that the mass flow rate entering each individual fracture was $\dot{m}$. The thermal properties of the matrix rock were constant. The properties used in the simulations are listed in Table 3.4.

Gringarten et al. (1975) chose to introduce several dimensionless parameters in order to solve the problem analytically. The dimensionless temperature of the fluid in the fracture is defined as:

$$T_D^f = \frac{T_0^m - T^f(x,t)}{T_0^m - T_i^w}. \tag{3.10}$$

The temperature of the produced fluid is $T_p^w(t) = T^f(x = L, t)$. The dimensionless fracture spacing is defined as:

$$y_{ED} = \left(\frac{\rho_\varphi c_\varphi}{\kappa_r}\right)\left(\frac{Q}{x}\right) y_E, \tag{3.11}$$

and dimensionless time is defined as:

$$t'_D = \left[\frac{(\rho_\varphi c_\varphi)^2}{\kappa_r \rho_r c_r}\right]\left(\frac{Q}{x}\right)^2 t'. \tag{3.12}$$

In Eq. 3.12, time was shifted to account for the speed of the fluid in the fracture:

$$t' = t - \frac{x}{v}, \tag{3.13}$$

where v is the fluid velocity which is related to the injection rate, fluid properties, and fracture geometry though the following expression:

$$v = \frac{\dot{m}}{\rho_\varphi e W}. \tag{3.14}$$

In Eqs. 3.11 and 3.12, Q is the volumetric flow rate entering each individual fracture normalized by the out-of-plane dimension:

$$Q = \frac{\dot{m}}{\rho_\varphi W}. \tag{3.15}$$

Because the boundary conditions along the fracture surfaces do not remain constant in time, *Gringarten et al.* (1975) applied the Laplace transformation technique in order to arrive at a solution. In transformed space, the solution for the dimensionless fracture temperature is:

$$\bar{T}_D^f(x_D, s) = \frac{1}{s} \exp\left[-x_D s^{1/2} \tanh\left(\frac{y_{ED}^* - 1}{\varsigma} s^{1/2}\right)\right], \tag{3.16}$$

where s is the Laplace variable. In Eq. 3.16, several new dimensionless quantities were defined:

$$x_D = \frac{x}{L}, \quad y_{ED}^* = \frac{2y_E}{e}, \quad t_D^* = \left[\frac{(\rho_\varphi c_\varphi)^2}{4\kappa_r \rho_r c_r}\right]\left(\frac{Q}{L}\right)^2 t', \quad \varsigma = \frac{4\kappa_r L}{\rho_\varphi c_\varphi Q e}. \tag{3.17}$$

In order to compare the analytical solution with the EFM numerical model, Eq. 3.16 was inverted numerically using an open-source algorithm (*Abate and Whitt*, 2006).

Table 3.4: Model parameters for investigation of nonisothermal fluid circulation through a fractured reservoir.

Parameter	Value	Unit
e	0.002	m
L	1000	m
W	700	m
κ	2	$W \cdot m^{-1}$
ρ_r	2650	$kg \cdot m^{-3}$
ρ_φ	1000	$kg \cdot m^{-3}$
c_r	4150	$J \cdot kg^{-1} \cdot °C^{-1}$
c_φ	816	$J \cdot kg^{-1} \cdot °C^{-1}$
$\dot{m}$	20	$kg \cdot s^{-1}$
T_0^m	275	°C
T_i^w	100	°C

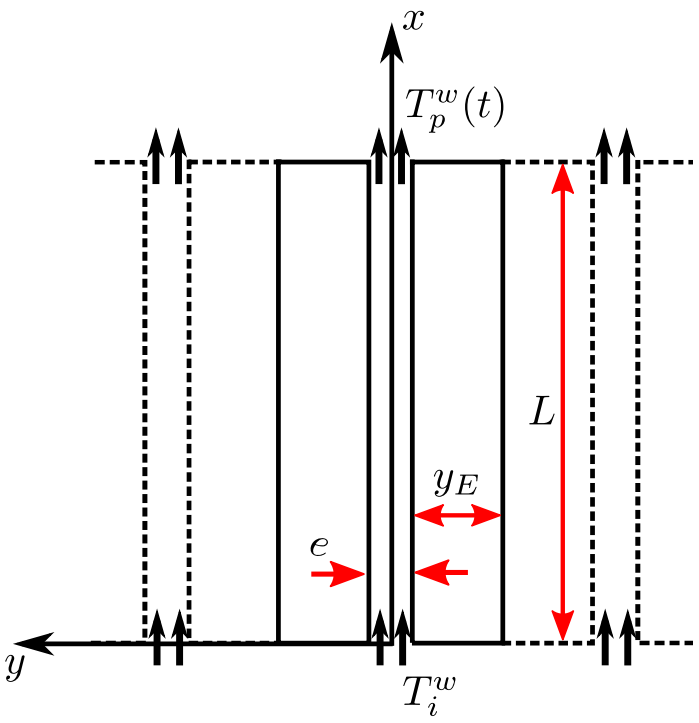

Figure 3.6: Illustration of the conceptual model for nonisothermal fluid circulation through a set of multiple parallel fractures. Injection occurred on the bottom edge at a constant mass flow rate and constant temperature. Heat transfer in the rock matrix was predominantly conduction, and heat transfer in the fractures was predominantly advection. This schematic was based on *Gringarten et al.* (1975) and reproduced using the notation presented in this section.

3.4.2 Results

We performed two different sets of simulations. In Case A, we modeled fracture spacing ranging from $y_{ED} = [1, \infty]$ in an artificial sense by simulating flow through a single fracture and changing the extent of the model domain boundary in the y-direction to mimic the no-heat-flux boundaries that exist theoretically between fractures. In Case B, we modeled a case where $y_{ED} = 4$ by simulating flow through three discrete fractures. The results of the simulations were compared against Eq. 3.16, and are shown in Figs. 3.7 and 3.8 for Cases A and B, respectively. In both scenarios, the numerical solutions achieved close agreement with the analytical solution. The results from this numerical example demonstrate that the model is able to calculate the complex coupled interaction between heat advection within a fracture (which is controlled by the solution to the fluid flow equations) and transient heat conduction in matrix rock subject to boundary conditions that changed over time as the thermal front propagated along the fractures.

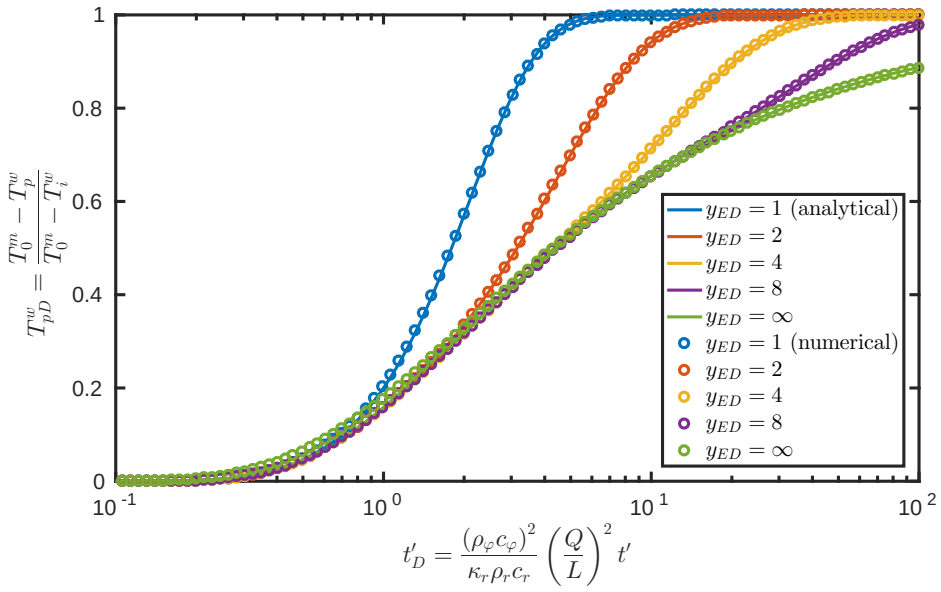

Figure 3.7: Dimensionless production well temperature versus dimensionless time for different fracture spacing tested in Case A. The *colored circles* represent the numerical solution and the *colored lines* represent the analytical solution (see Eq. 3.16). In this scenario, the problem was modeled by simulating flow though a single fracture and modifying the extent of the domain boundaries in the $y-$direction.

3.5 Shear stimulation in a fractured reservoir

This example was presented in *Norbeck et al.* (2016a). In geothermal settings, it is commonly assumed that hydraulic stimulation occurs due to shear stimulation, a process in which fluid injection triggers slip and permeability enhancement on natural fractures. Shear stimulation involves injecting fluid at a pressure less than the magnitude of the minimum principal stress into a network of preexisting natural fractures in order to reduce the effective normal stress acting on the individual fracture planes and thereby reducing their resistance to shear failure. The premise is that some types of rock may be conducive to a self-propping behavior upon shear failure that can lead to a permanent enhancement of permeability (*Lee and Cho*, 2002). In addition, shear failure of natural fractures is responsible for causing microseismic events that are observed commonly during hydraulic fracture treatments, so principles related to shear stimulation can be applied to interpret the microseismic activity generated during hydraulic fracturing (*Vermylen and Zoback*, 2011).

During shear stimulation treatments, the emergent behavior of an altered reservoir permeability is a nonlinear process involving a tight coupling between fluid flow, mechanical deformation of fractures, shear failure of fractures, and a constitutive relationship describing fracture transmissivity evolution. As fractures deform, stresses are transferred elastically throughout the domain, and it

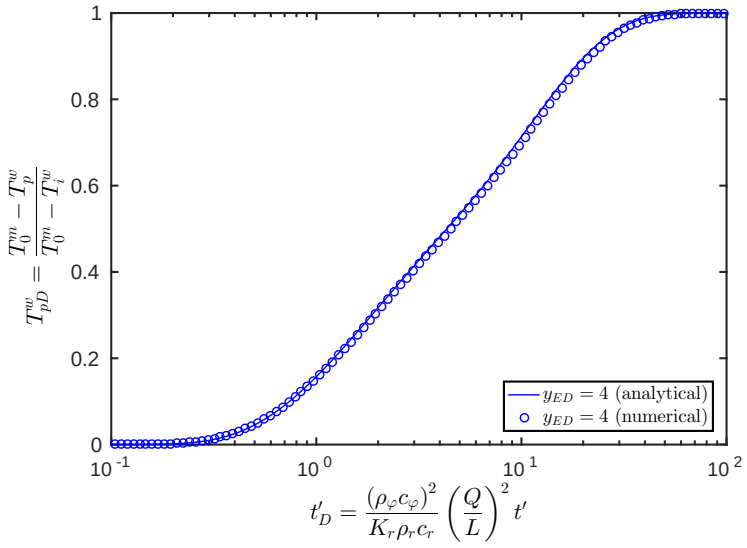

Figure 3.8: Dimensionless production well temperature versus dimensionless time for fracture spacing $y_{ED} = 4$ tested in Case B. The *colored circles* represent the numerical solution and the *colored line* represents the analytical solution (see Eq. 3.16). In this scenario, the problem was modeled by simulating flow though a set of three discrete fractures.

can be extremely important to solve the full geomechanics problem in order to resolve these effects. *McClure and Horne* (2011) demonstrated that stress transfer effects can significantly influence the rate at which shear stimulation propagates along individual fractures, giving rise to a mechanism they called crack-like shear stimulation. Localized shear stress concentrations that develop ahead of the zone that has experienced slip previously and can cause slip to occur before the pressure front reaches that location, further enhancing permeability and promoting flow. In this manner, shear stimulation is able to propagate at a rate related to the enhanced fracture transmissivity, rather than the initial fracture transmissivity. Considering this mechanism, models that employ simplified geomechanical models based purely on pressure diffusion, such as those presented by *Moinfar et al.* (2013) or *Karvounis et al.* (2014), may not be sufficient to predict reservoir response realistically in many injection and production scenarios of practical interest. In this section, we show several numerical simulations in order to demonstrate that the EFM approach can be applied to solve coupled fluid flow and geomechanics problems with nonlinear fracture permeability evolution.

3.5.1 Problem description

In this numerical example, shear stimulation of a relatively complex network of preexisting fractures was considered. The domain was two-dimensional (i.e., all fractures were vertical and had fixed

heights equal to the reservoir thickness). The stress regime was strike-slip. A 150 m open-hole section of a horizontal well penetrated several natural fractures. Fluid was injected at a constant pressure such that the reservoir fluid pressure never exceeded the minimum principal stress, ensuring that tensile fractures would not propagate. Therefore, changes in injectivity were due purely to permeability changes caused by the shear stimulation effect. The fracture network and well geometry are illustrated in Fig. 3.9, and the model parameters are listed in Table 3.5.

Fluid was injected for a period of seven days at a constant pressure of 12.4 MPa. The magnitude of the minimum principal stress was 14.5 MPa. The metrics for comparison were injection rate as a function of time, cumulative mass transfer between the matrix and fracture domains as a function of time, and the spatial distribution of shear displacement throughout the fracture network at the end of the stimulation treatment. The DFM results should be considered the "most true" solutions because they employed the standard conforming discretization strategy that is commonly used in reservoir simulation practice.

Four test cases were modeled. In Cases 1 through 3, the results of the EFM, DFM, one-dimensional leakoff approximation model, and zero leakoff approximation model were compared for a range of matrix permeability. In Case 4, a discretization refinement study for the EFM was performed. The same fracture network discretization (with a total of 16,547 fracture control volumes) was used in each of the simulations. In Cases 1 through 3, the EFM employed a nonconforming structured Cartesian mesh with 251,001 control volumes for the matrix discretization. The DFM employed a conforming triangular mesh with 351,569 control volumes for the matrix discretization. The one-dimensional and zero leakoff approximation models did not require discretization of the matrix rock volume. In Case 4, the number of EFM matrix control volumes was varied from 121 to 251,001 to test for the property of convergence upon refinement and to evaluate the EFM's ability to obtain suitable degrees of accuracy with coarser grids.

3.5.2 Results

The flow behavior in the reservoir was affected strongly by the geometry, connectivity, and hydraulic properties of the natural fracture network. The EFM pressure distribution in the matrix rock at the end of the simulation, shown in Fig. 3.10, indicates that fluid leakoff was limited to regions close to the fractures. Flow did not propagate away from the well symmetrically due to the nonlinearities, but rather occurred preferentially along a natural fracture in the upper-right corner of the domain.

The main comparison metric for these numerical experiments was injection rate as a function of time. The injection profiles for each case are shown in Fig. 3.11. Case 1 represents the base case simulation. The matrix permeability was $k^m = 1 \times 10^{-18}\,\mathrm{m}^2$. The injection rate during the stimulation for Case 1 is shown in Fig. 3.11(a). Because the boundary condition on the injection well was constrained at a constant pressure, sudden increases in the slope of the injection rate corresponded to shear stimulation events. As the critical pressure required to cause shear failure

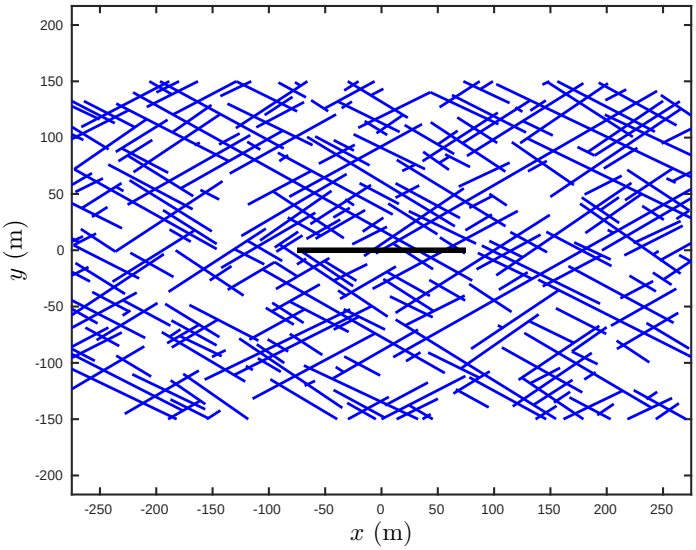

Figure 3.9: Plan view of the fracture network geometry for the shear stimulation example problem. The *black line* is the horizontal wellbore and the *blue lines* are the natural fractures.

was reached at one particular location, the resulting elastic stress transfer tended to cause cascading failure in nearby fractures, which is the reason why several distinct stimulation events are observed in Fig. 3.11(a).

For Case 1, the EFM and DFM results are indistinguishable, suggesting that EFM was able to achieve a high degree of accuracy in the global flow behavior. To further verify the accuracy of the EFM results, the total amount of fluid that leaked off from the fractures into the matrix domain was compared to the DFM simulation and is shown in Fig. 3.12. The cumulative mass exchange for both models was normalized by the total mass of fluid injected in the DFM simulation. It is clear that by treating the mass exchange as source terms via the EFM framework, the matrix-fracture mass exchange behavior was captured accurately for a complex fracture geometry. These results demonstrate that the EFM approach can indeed perform well for problems involving coupled flow, geomechanics, and nonlinear permeability evolution in highly fractured reservoirs.

For Case 1, the one-dimensional leakoff model performed well in terms of capturing the timing and magnitude of the major shear stimulation events and the late time injection rate. The zero leakoff model predicted that shear stimulation events occurred relatively early, which is physically intuitive because pressure everywhere in the fracture network was higher without the leakoff effect. It is interesting to note that each of the four models showed the same general trends in reservoir response, and the effect of fluid leakoff impacted only the onset of each individual stimulation event.

Figures 3.11(b) and 3.11(c) show the injection rate histories for Cases 2 and 3, which correspond to matrix permeability of $k^m = 0.1 \times 10^{-18}\,\mathrm{m}^2$ and $k^m = 10 \times 10^{-18}\,\mathrm{m}^2$, respectively. For each of these cases, the EFM and DFM injection profiles were nearly identical. For Case 2, which

Table 3.5: Model parameters for study on shear stimulation in a naturally fractured reservoir

Parameter	Value	Unit
h_f	100	m
e_0	5×10^{-5}	m
E_0	5×10^{-3}	m
σ_e^*	90	MPa
σ_E^*	90	MPa
φ_e	5	deg.
φ_E	0	deg.
f	0.6	-
η	3	MPa $\cdot$ m^{-1} $\cdot$ s
k^m	10^{-19} to 10^{-17}	m^2
ϕ_0	0.03	-
β_r	1.9×10^{-9}	Pa^{-1}
ρ_0	1000	kg $\cdot$ m^{-3}
β_φ	4.6×10^{-10}	Pa^{-1}
μ	0.001	Pa $\cdot$ s
p_0	8.7	MPa
σ_{xx}^R	23.8	MPa
σ_{yy}^R	14.5	MPa
σ_{xy}^R	0	MPa

had a relatively low matrix permeability, the range of predictions for the four models narrowed significantly. The full matrix discretization approaches provided only modest improvements over the one-dimensional leakoff approximation. For Case 3, which had a relatively high matrix permeability, the results were again consistent with intuition. The range in model predictions was largest for this case because fluid leakoff effects were more pronounced than in any of the previous cases. At later times, the one-dimensional leakoff approximation predicted a significantly higher injection rate than the EFM and DFM simulations. This can be attributed to the fact that for nearby fractures, the distance of investigation of the pressure transient was large enough that they began to affect each other. The one-dimensional leakoff model was fundamentally unable to resolve this behavior.

For the EFM discretization refinement study, seven levels of matrix refinement were tested. Both the zero leakoff and one-dimensional leakoff approximation results are also shown for reference. In all cases, the same fracture discretization was used. The matrix permeability was the same as Case 1 ($k^m = 1 \times 10^{-18}\,\mathrm{m}^2$). The injection rate history is shown in Fig. 3.11(d), and the error in the fracture shear displacement at the end of the simulations is shown in Fig. 3.13. The results indicate that the EFM approach was convergent upon grid refinement. More interestingly, a high degree of accuracy was still obtained even after a significant reduction in the total number of degrees of freedom. In this example, reducing the number of control volumes from roughly 250,000 down to 90,000 resulted in a negligible loss of accuracy. Further reducing the number of control volumes to about 40,000 still gave acceptable results in terms of predicting a similar injection rate curve and

maintaining shear displacement errors less than 5%. Note that for a given fracture discretization, it is difficult to arbitrarily reduce the number of degrees of freedom for conforming discretization techniques such as DFM.

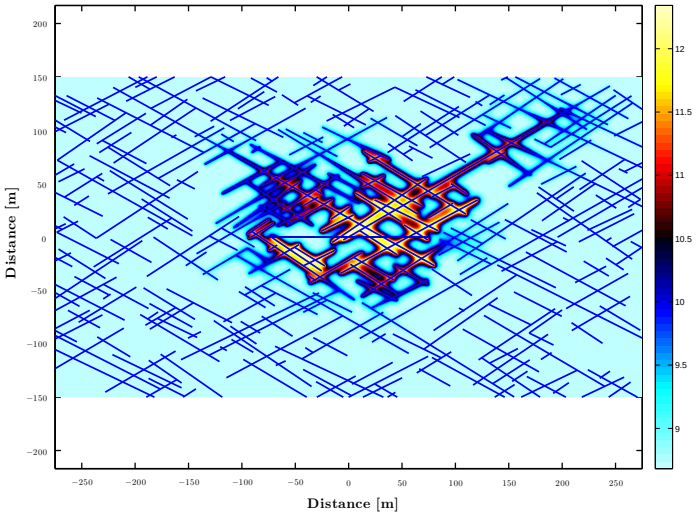

Figure 3.10: Matrix pressure distribution at the end of the stimulation treatment (EFM Case 1). The color bar scale ranges from 8.7 to 12.4 MPa. The nonlinear evolution of fracture transmissivity caused nonuniform flow to occur through the reservoir.

3.6 Hydraulic fracture propagation

This numerical exercise was presented in *Norbeck et al.* (2016a). Hydraulic fracturing and horizontal drilling are two of the key technological advancements that have allowed for the economic development of unconventional shale gas and shale oil resources. Hydraulic fracturing may also prove to be key for the future development of engineered geothermal systems (*Shiozawa and McClure*, 2014). The goal of a hydraulic fracture treatment is to expose the wellbore to a larger reservoir surface area in order to enhance recovery rates and ultimate recovery from low-permeability reservoirs. The process involves injecting fluid at a pressure greater than the magnitude of the minimum principal stress so that new tensile fractures nucleate and propagate through the reservoir. In many applications, the desired effect of a hydraulic fracture treatment is to create a set of large, planar vertical fractures that extend laterally away from the horizontal wellbore.

The embedded fracture modeling framework is particularly well-suited to solve the fracture propagation problem. Because the fracture and matrix domains are coupled by simple source terms, new fracture control volumes that are created through fracture propagation can be integrated into the

model easily. The goal of this numerical exercise was to demonstrate that the approximations introduced by the EFM discretization strategy are capable of describing the time-dependent behavior of fracture growth during hydraulic fracturing for a pure mode-I fracture.

3.6.1 Problem description

One technique that is commonly applied for the design of hydraulic fracture treatments was due to *Geertsma and de Klerk* (1969), who introduced what is referred to as the KGD fracture model. For vertical KGD fractures, plane strain conditions are assumed in the vertical direction such that each horizontal cross-section of the fracture has the same geometry. *Gidley et al.* (1990) provided a closed-form solution that describes fracture half-length as a function of time for constant injection rate and assuming no leakoff of fluid into the formation:

$$x_f = 0.679 \left[\frac{\lambda G q_i^3}{(1-\nu)\, h_f^3} \right]^{1/6} t^{2/3}, \tag{3.18}$$

where q_i is half of the total volumetric injection rate (i.e., the flow rate entering one of the fracture wings), and h_f is the height (vertical extent) of the fracture. For the case where leakoff is considered, *Valko and Economides* (1995) performed a material balance that yielded a nonlinear function for fracture length (given here, neglecting spurt-loss):

$$x_f = \frac{\bar{e} q_i}{4\pi C_L^2 h_f} \left[\exp\left(\psi^2\right) \operatorname{erfc}\left(\psi\right) + \frac{2\psi}{\sqrt{\pi}} - 1 \right], \tag{3.19}$$

where $\bar{e}$ is the average aperture of the hydraulic fracture and C_L is the leakoff coefficient. The time variable is included in the parameter, ψ:

$$\psi = \frac{2 C_L \sqrt{\pi t}}{\bar{e}}. \tag{3.20}$$

The nonlinearity arises because the average fracture aperture at any time depends on the length of the fracture. *Gidley et al.* (1990) suggested that the fracture aperture at the wellbore, e_w, is:

$$e_w = 2.27 \left[\frac{x_f\,(1-\nu)\, q_i}{\lambda G h_f} \right]^{1/4}. \tag{3.21}$$

For the KGD fracture geometry, the average value of the fracture aperture is:

$$\bar{e} = \frac{\pi}{4} e_w. \tag{3.22}$$

If the leakoff coefficient is known, Eqs. 3.20 - 3.22 can be substituted into Eq. 3.19, so that Eq. 3.19 becomes only a function of time and fracture length. In this study, leakoff from the fracture was

considered to be slightly compressible flow driven purely by diffusion into the matrix rock. Under this assumption, the leakoff coefficient, C_L, is (*Economides and Nolte*, 2000):

$$C_L = \left[\frac{k^m \lambda \phi^m \left(\beta_\varphi + \beta_r\right)}{\pi}\right]^{1/2} \Delta p, \tag{3.23}$$

where $\Delta p = p^f - p_0$, is the pressure drop driving leakoff.

In this numerical example, the models' ability to simulate pure mode-I fracture propagation was examined. Propagation of a single two-wing vertical fracture was considered. The domain was assumed to be homogeneous in terms of fluid flow and mechanical properties, and no preexisting natural fractures were present. Plane strain conditions in the vertical direction were assumed. The numerical solutions were compared with KGD semianalytical solutions (*Gidley et al.*, 1990; *Valko and Economides*, 1995). Three sets of simulations were performed. In the first case, the matrix rock was assumed to be completely impermeable, such that no leakoff occurred. The zero leakoff model was compared to Eq. 3.18. In the second case, the matrix rock was assigned a permeability value of $k^m = 0.1 \times 10^{-15}\,\mathrm{m}^2$ in order to investigate the effects of leakoff. The one-dimensional leakoff model, EFM, and DFM were compared to Eq. 3.19. In the third case, a discretization refinement study for the EFM was performed under the permeable rock scenario. The metric used for comparison was the hydraulic fracture length as a function of time.

The model parameters for this problem are given in Table 3.6. In the model, fluid was injected at a constant rate of 0.05 m^3/s for 30 minutes. The hydraulic fracture had a fixed height of 100 m. The magnitude of the least principal stress was 5 MPa above the initial reservoir pressure, so the relatively high pressure in the fracture necessary to drive propagation encouraged leakoff to occur for the case of permeable matrix rock. To determine the leakoff coefficient used to calculate the semianalytical solution to the problem (see Eq. 3.23), the pressure drop was assumed to be $\Delta p = 5.2$ MPa. This value was based on the average pressure in the fracture observed during the numerical simulations. The same fracture discretization was used for the DFM and EFM simulations. The DFM and EFM matrix discretizations had 102,012 and 160,801 control volumes, respectively.

In general, the numerical models were not expected to achieve an exact match with the semianalytical solutions because there are some significant differences in the respective underlying assumptions. For example, the semianalytical solutions are based purely on volume balances, whereas the numerical solutions allow fracture propagation to occur subject to a criterion based on the mode-I stress intensity factor.

3.6.2 Results

The comparison between the numerical and semianalytical models of the temporal evolution of fracture length is illustrated in Fig. 3.14. The numerical models captured the fracture growth behavior

Table 3.6: Model parameters for mode-I hydraulic fracture propagation problem

Parameter	Value	Unit
q_i	0.05	$m^3 \cdot s^{-1}$
h_f	100	m
k^m	0.1×10^{-15}	m^2
ϕ^m	0.2	-
$\beta_\varphi + \beta_r$	8.8×10^{-10}	Pa^{-1}
λ^{-1}	0.001	$Pa \cdot s$
G	15	GPa
ν	0.25	-
K_{IC}	1	$MPa \cdot m^{1/2}$
p_0	40	MPa
σ_3	45	MPa
Δp	5.2	MPa
C_L	7.8×10^{-6}	$m \cdot s^{-1/2}$

accurately over the duration of injection. The numerical solutions matched the semianalytical solutions extremely accurately at early times during the period of rapid growth of the fracture. The numerical models tended to underestimate the fracture length slightly at later times. A summary of the fracture half-length at the time fluid injection stopped is given in Table 3.7. For the case of no leakoff, the zero leakoff approximation model underestimated the KGD solution by 2.7%. For the cases where leakoff occurred, the difference between the numerical and semianalytical models ranged from -1.0% to -4.4%.

The effect of fluid leakoff during the hydraulic fracturing is that some of the fluid can be lost into the formation and therefore is no longer useful for creating new fracture volume. A summary of the reduction in fracture length due to leakoff observed in the model results is provided in Table 3.8. In these calculations, the KGD solutions were compared to each other, and the DFM, EFM, and one-dimensional leakoff model were each compared to the zero leakoff model. The numerical models predicted a reduction in fracture length ranging from 18.8% to 21.5%, which compares favorably with the semianalytical solution of 20.1%.

The results of the EFM matrix grid refinement study are illustrated in Fig. 3.15 and summarized in Tables 3.9 and 3.10. For coarse levels of grid refinement, the amount of fluid leakoff tended to be underestimated resulting in longer hydraulic fractures. The solutions were convergent upon grid refinement, which is an attractive numerical property of EFM. Interestingly, the solutions converged toward the one-dimensional leakoff approximation solution. Because the duration of injection was very short and the matrix permeability was relatively low, the assumption of one-dimensional flow away from the newly forming fracture was reasonable. In this light, the one-dimensional leakoff approximation model could be considered the “most true” numerical solution, and it is encouraging that the EFM solution approached the one-dimensional leakoff model.

Quantitatively, the EFM approach was able to model the growth of a single mode-I hydraulic fracture accurately. When compared to the semianalytical KGD solutions, the magnitude of the mismatch of the numerical solutions were within reason for practical purposes. It is worth noting that the literature provides several alternatives to Eqs. 3.18 and 3.19 that predict differences in fracture half-length on the order of 10% (*Valko and Economides*, 1995). The present numerical solutions fell within that range. These results indicate that the EFM framework can be applied successfully to scenarios in which fractures are propagating and fracture systems are growing over time.

Table 3.7: Fracture half-length at end of injection for the model comparison study.

	Eq. 3.18	Zero Leakoff Model	Eq. 3.19	1-D Leakoff Model	DFM	EFM
x_f [m]	370.0	360.0	295.5	282.5	292.5	285.0
Difference [%]	N/A	-2.7	N/A	-4.4	-1.0	-3.6

Table 3.8: Reduction in fracture half-length due to the leakoff effect for the model comparison study.

Model	Reduction in x_f [%]
Semianalytical KGD	20.1
1-D Leakoff Model	21.5
DFM	18.8
EFM	20.8

Table 3.9: Fracture half-length at end of injection for the EFM discretization refinement study.

	Eq. 3.19	1-D Leakoff Model	251001	90601	40401	2601
x_f [m]	295.5	282.5	285.0	288.7	291.3	303.8
Difference [%]	N/A	-4.4	-3.6	-2.3	-1.4	2.8

Table 3.10: Reduction in fracture half-length due to the leakoff effect for the EFM discretization refinement study.

Model	Reduction in x_f [%]
Semianalytical KGD	20.1
1-D Leakoff Model	21.5
251001	20.8
90601	19.8
40401	19.1
2601	15.6

3.7 Earthquake rupture and arrest in three dimensions with rate-and-state friction

McClure and Horne (2011), *Norbeck and Horne* (2015a), and *Norbeck and Horne* (2015b) performed investigations of injection-induced seismicity on two-dimensional faults. As described in Sect. 2.4, we extended that model to solve the full three-dimensional quasidynamic elasticity problem. In the three-dimensional model, faults were represented as two-dimensional planar surfaces. We allowed for heterogeneous distributions of stress and frictional properties across the fault surfaces. In this section, we present the results of an accuracy verification study in order to demonstrate the model's ability to solve problems related to earthquake nucleation, rupture, and arrest in three dimensions.

We compared the present model (called CFRAC), which is based on the displacement discontinuity method, against a similar elastodynamic numerical model called MDSBI (Multi-Dimensional Spectral Boundary Integral Code) (*Dunham*, 2008). The MDSBI model is based on a boundary integral equation method. The model performs the spatial convolution required to calculate the quasistatic stress transfer in the Fourier domain using fast Fourier transforms (FFT) as described by *Dunham and Rice* (2008), *Noda et al.* (2009), and *Rice et al.* (2010). The MDSBI model makes use of an open-source FFT library called FFTW3 (*Frigo and Johnson*, 2005).

3.7.1 Problem description

In this numerical example, we considered an 8 km long by 4 km high vertical strike-slip fault. The center of the fault was buried at a depth of 10 km. A 3 km long by 2 km wide patch near the center of the fault was prescribed velocity-weakening frictional properties (i.e., $(b-a) > 0$). This fault patch was surrounded by velocity-strengthening material (i.e., $(b-a) < 0$). The effective normal stress resolved on the fault was 100 MPa. The shear stress resolved on the fault was 60 MPa in the velocity-weakening zone and 30 MPa in the velocity strengthening zone. A small patch located at $(x, z) = (0\text{km}, -10.5\text{km})$ was prescribed a slightly lower normal stress of 95 MPa to encourage nucleation to trigger at that specific location. A uniform shear stress loading rate was applied to the fault in order to trigger nucleation. In this problem, a single earthquake rupture nucleated and propagated through the velocity-weakening zone. Eventually, the rupture front reached the edge of the velocity-strengthening zone which caused the rupture to arrest. Fluid flow did not play a role in this problem. The problem configuration is illustrated in Fig. 3.16 and the model parameters are listed in Tables 3.11 through 3.13.

In CFRAC, the fault was discretized into 256 elements in the horizontal direction and 129 elements in the vertical direction. In MDSBI, the fault was discretized into 256 elements in the horizontal direction and 128 elements in the vertical direction. In CFRAC, the initial sliding velocity was set equal to the reference sliding velocity (i.e., $V_0 = V_*$), and initial state was set equal to

the steady-state value at the initial sliding velocity (i.e., $\Psi_0 = \Psi_{ss}(V_0)$). The metrics used for comparison were contours of the timing of the rupture front arrival and the final distribution of shear slip. The rupture front was defined as the location where V first exceeded 0.001 m/s.

Table 3.11: General model parameters for the three-dimensional rate-and-state friction earthquake rupture example problem.

Parameter	Value	Unit
$\bar{\sigma}_n^R$	100	MPa
G	30	GPa
ν	0.25	-
η	5	$\text{MPa} \cdot \text{m}^{-1} \cdot \text{s}$
f_*	0.6	-
V_*	1×10^{-6}	$\text{m} \cdot \text{s}^{-1}$
δ_c	0.005	m
s	0	MPa

Table 3.12: Model parameters for the velocity-weakening region of the fault.

Parameter	Value	Unit
τ^R	60	MPa
a	0.008	-
b	0.014	-

Table 3.13: Model parameters for the velocity-strengthening region of the fault.

Parameter	Value	Unit
τ	30	MPa
a	0.016	-
b	0.014	-

3.7.2 Results

The progression of the earthquake nucleation, rupture, and arrest process for the CFRAC simulation is shown in Fig. 3.17. Each subpanel shows the spatial distribution of different fault properties along the two-dimensional fault surface, and Figs. 3.17(a) through 3.17(f) show snapshots at different points in time. The slipping patch of the fault is the region where V is on the order of 1 m/s (seismic slip speeds).

Figure 3.17(b) shows the point in time at which earthquake nucleation occurred. At this point, stress drop behind the rupture front and stress concentration ahead of the rupture front began to encourage sustained rupture propagation. Figure 3.17(c) shows a point at which the rupture was

propagating without being affected by the material boundary. Slightly later in time, Fig. 3.17(d) illustrates the effect of the material boundary, which caused the rupture to arrest at the edge where the material transitioned between velocity-weakening and velocity-strengthening. Figure 3.17(e) shows the moment before rupture arrest when the rupture had reached the material boundary entirely. Because sliding velocity was large across the entire fault patch, this was the moment when the largest amount of slip accumulation occurred. Finally, Fig. 3.17(f) shows the rupture arrest process as sliding velocity diminished and the permanent amount of sliding displacement was established.

In Fig. 3.17 we show contours of the timing of the rupture front arrival calculated using CFRAC and MDSBI. The contour intervals are 0.1 seconds over the range of [0,1.3] seconds following nucleation. Both models were observed to produce behavior that was qualitatively and quantitatively similar. This comparison of the rupture front arrival timing is an appropriate benchmark to verify the accuracy of the quasidynamic formulation for earthquake rupture propagation.

In Fig. 3.18(b), contours of the final slip distribution are shown for both models. The contour intervals are 0.05 m over the range of [0,0.35] m. Both models were able to capture the sharp transition toward zero slip near the material transition boundaries. The peak slip at the center of the slipped patch was observed to be 0.36 m and 0.37 m for the CFRAC and MDSBI models, respectively, corresponding to a mismatch of 2.7%. The mismatch may have been caused by minor differences in the the distribution of the "low-stress" patch at the rupture nucleation site. This comparison of the final slip distribution is an appropriate benchmark to verify the accuracy of the spatial convolution required to calculate the quasistatic stress transfer.

3.8 Concluding remarks

The numerical modeling results presented in this chapter have verified the present model's ability to perform calculations accurately for a wide range of problems related to reservoir engineering and reservoir geomechanics. The test problems considered in this chapter were selected to reflect the numerical challenges that were expected to arise in the field studies and theoretical studies that followed. When possible, the model was compared against analytical or semianalytical problems. Problems involving tight coupling between several physical processes (e.g., fluid flow and geomechanics) or highly nonlinear constitutive laws (e.g., deformation-induced fault transmissivity changes or rate-and-state-dependent fault friction) are not amenable to analytical treatment. Therefore, in some cases we compared the present model against other software packages that have been verified elsewhere in the literature. Although the numerical methods and physics-coupling strategies applied in this work introduced approximations to the governing equations described in Chapter 2, it was observed that the model performed calculations with sufficient accuracy to provide useful insight into the behavior of fractured and faulted porous media at scales of practical engineering interest.

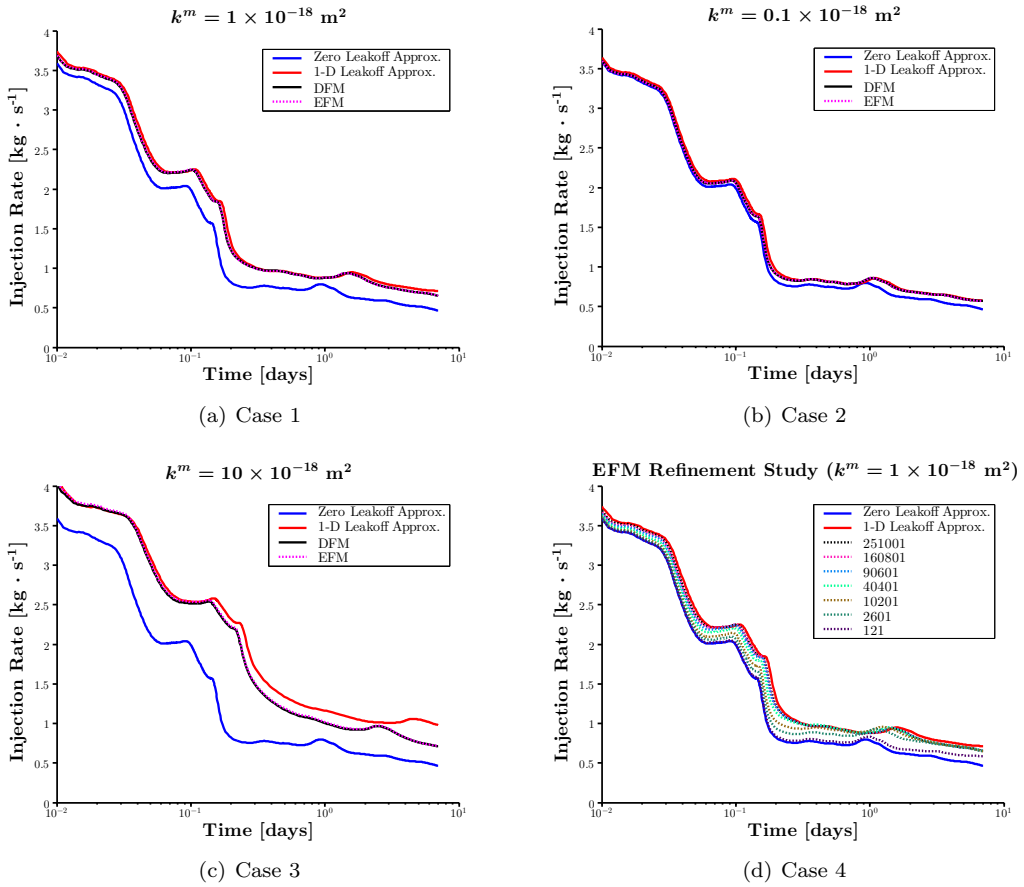

(a) Case 1

(b) Case 2

(c) Case 3

(d) Case 4

Figure 3.11: Injection rate over the duration of the stimulation treatment for Cases 1 through 4. Permeability evolution caused by episodic shear failure events was responsible for the nonlinear response in injection rate while injecting at constant pressure. The numbers in the legend of subfigure (d) represent the total number of matrix control volumes used for the various simulations performed in the grid refinment study.

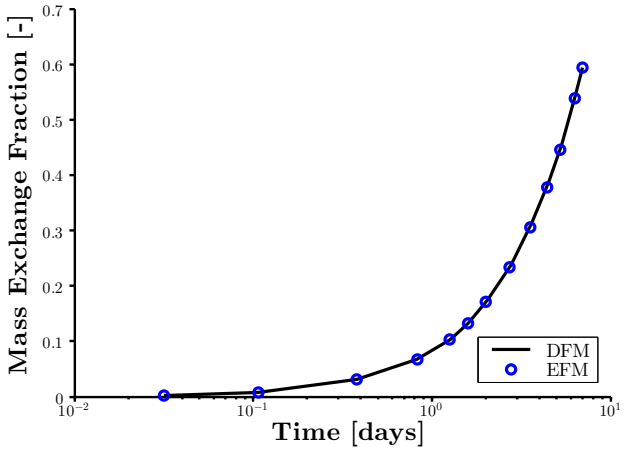

Figure 3.12: Cumulative mass transfer between the matrix and fracture domains normalized by the total mass of water injected of the the entire stimulation treatment for Case 1.

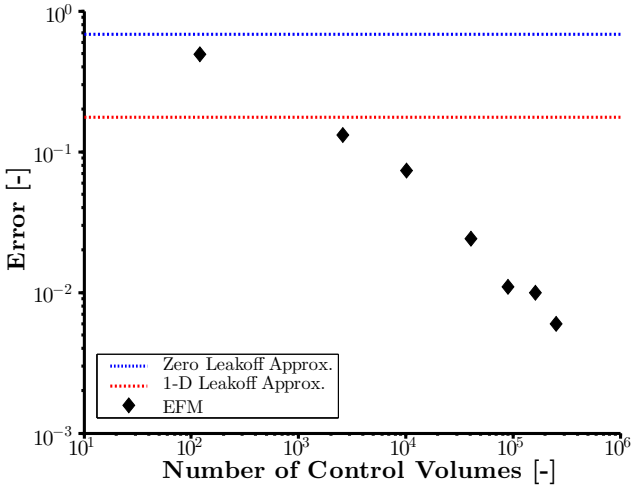

Figure 3.13: The error in cumulative shear displacement at the end of the stimulation treatment for various levels of EFM grid refinement. The error was calculated relative to the DFM simulation. The *blue* and *red lines* represent the error for the zero leakoff and one-dimensional leakoff approximations, respectively.

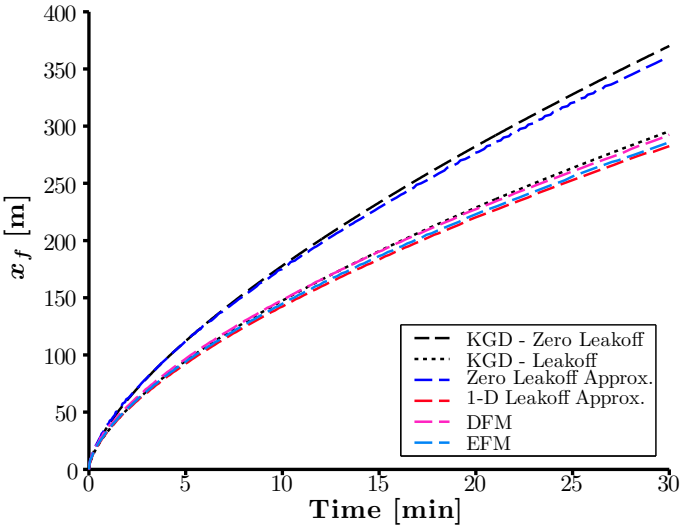

Figure 3.14: Hydraulic fracture half-length as a function of injection time for the fracture propagation example problem. The numerical models were compared against the semianalytical models (see Eqs. 3.19 and 3.19).

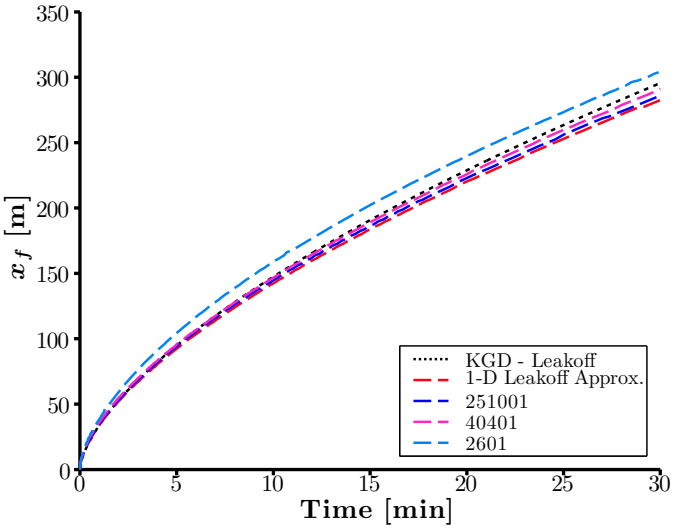

Figure 3.15: EFM grid refinement study for the fracture propagation example problem. The solutions were convergent upon grid refinement. The solutions were observed to converge toward the solution of the one-dimensional leakoff approximate model. The numbers in the legend indicate the total number of matrix control volumes used in the various simulations performed in the grid refinement study. The results from the simulation with 90,601 control volumes are not shown here for the sake of clarity.

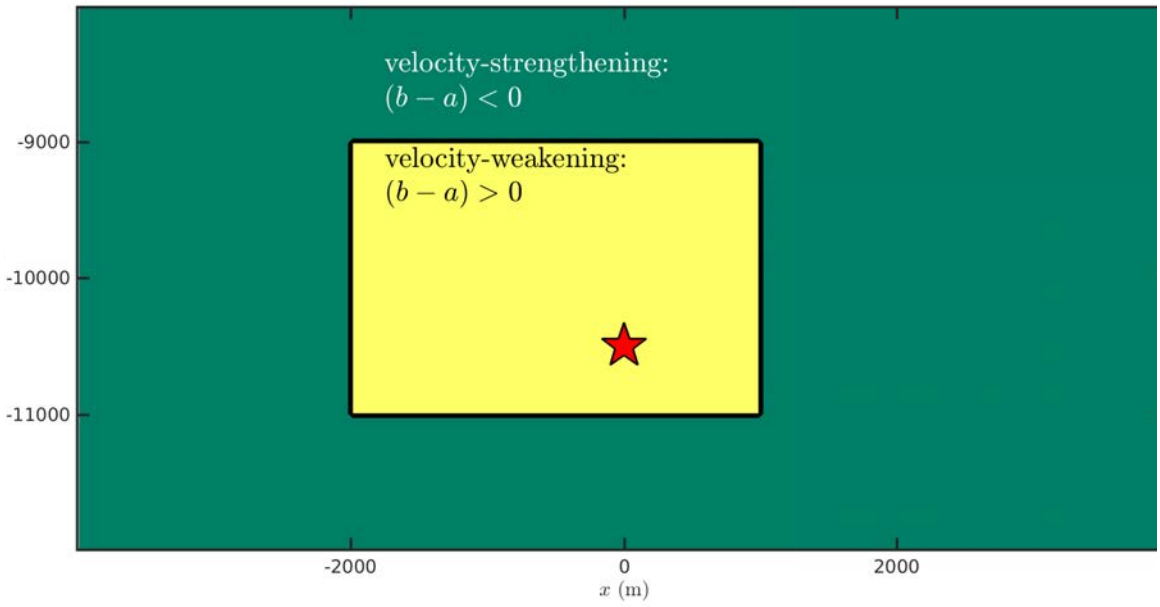

Figure 3.16: Illustration of the problem configuration for the three-dimensional rate-and-state friction example problem. A patch of velocity-weakening fault material (*yellow*) was surrounded by velocity-strengthening material (*green*). The earthquake rupture was nucleated at the site marked by the *red star*.

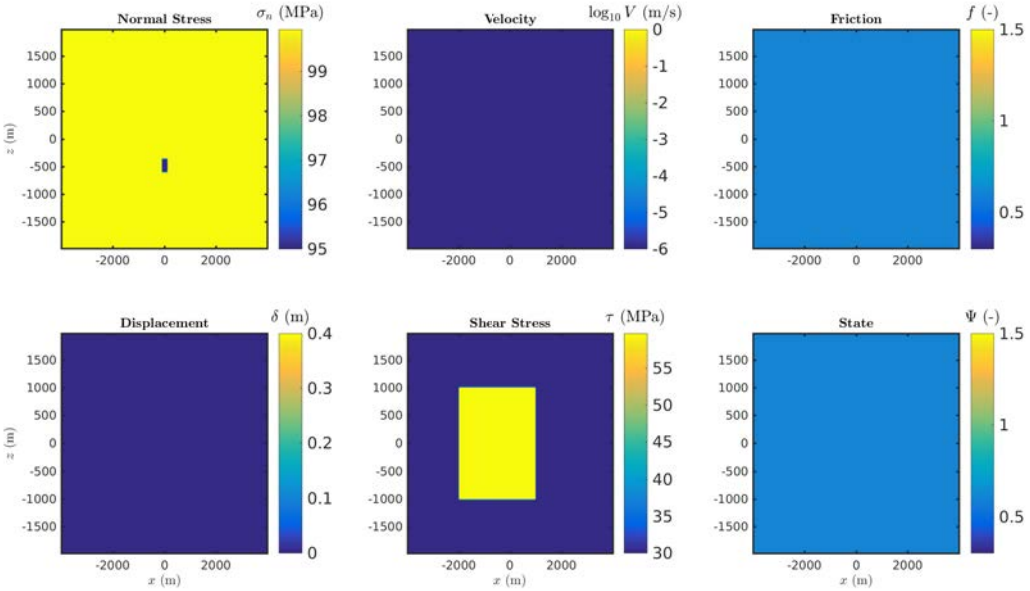

(a) initial condition

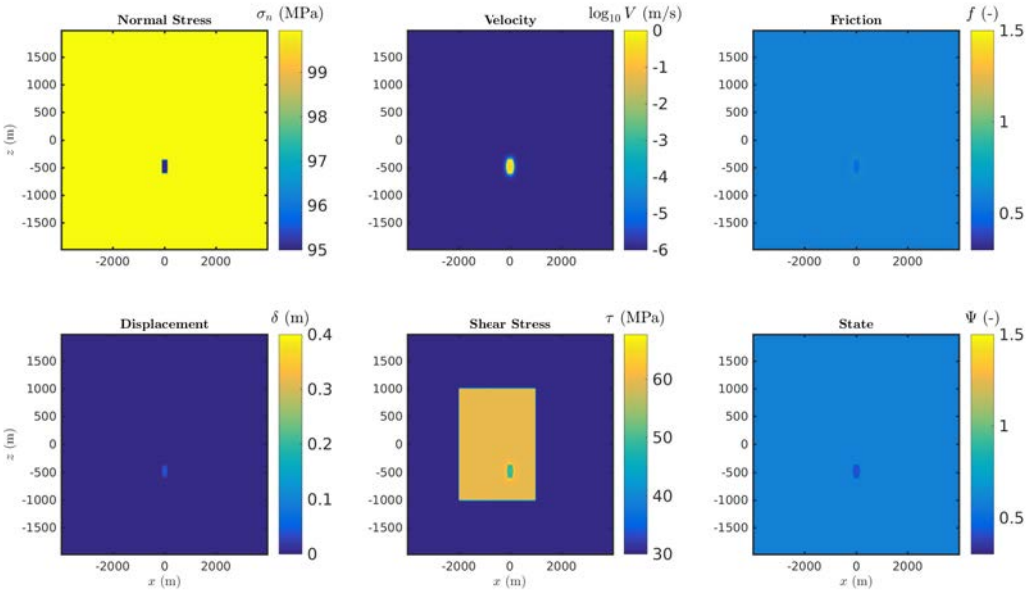

(b) rupture nucleation

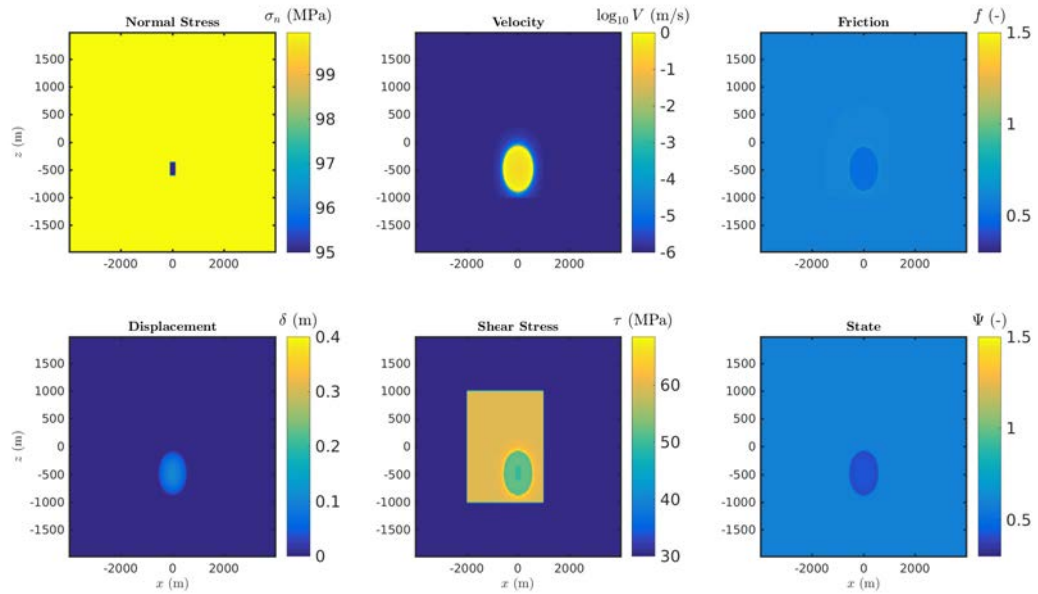

(c) unconstrained rupture propagation

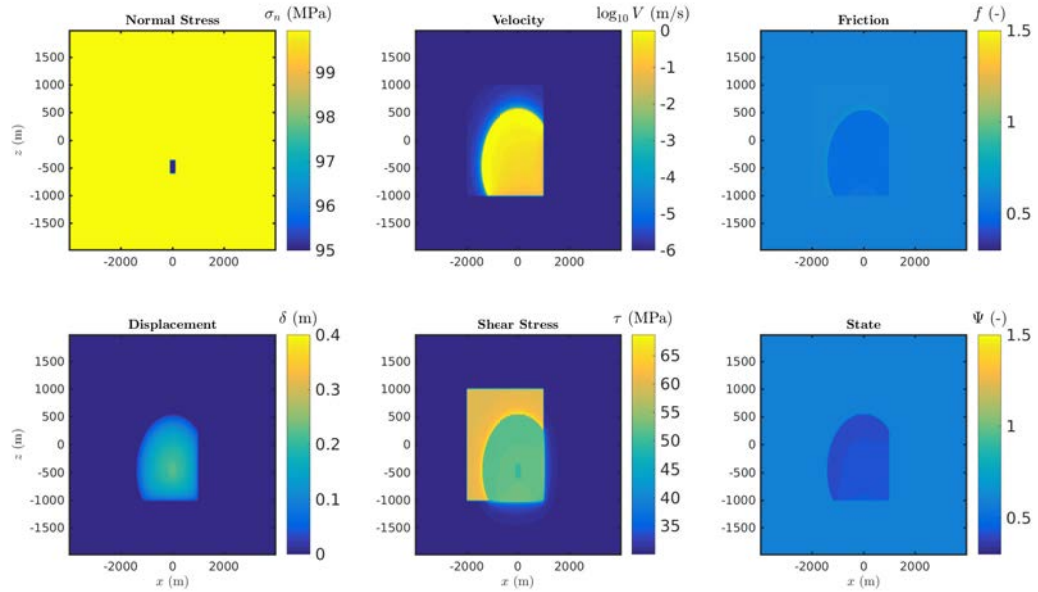

(d) rupture propagation constrained by material contrast

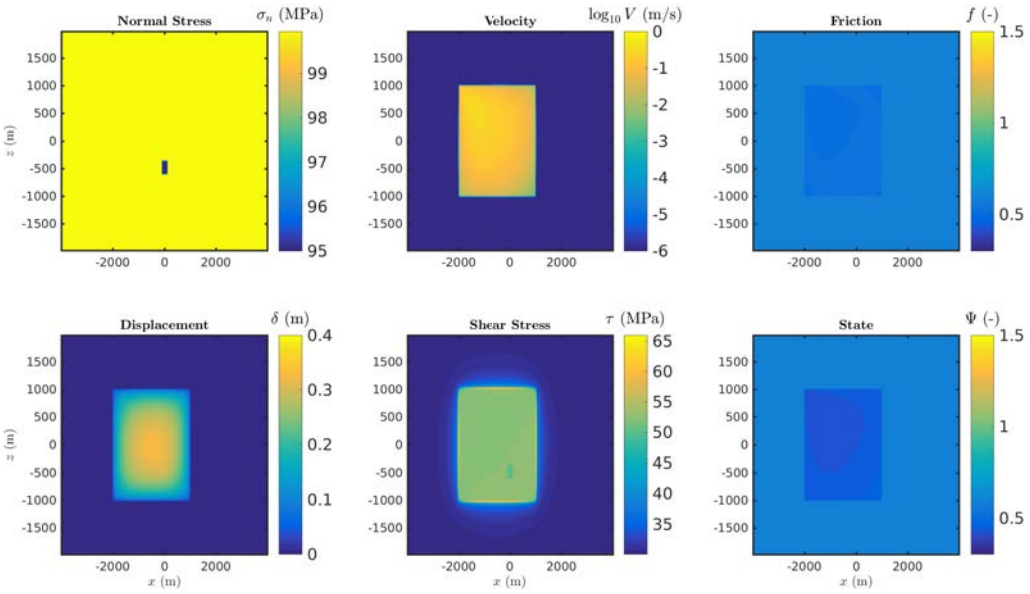

(e) peak slip accumulation

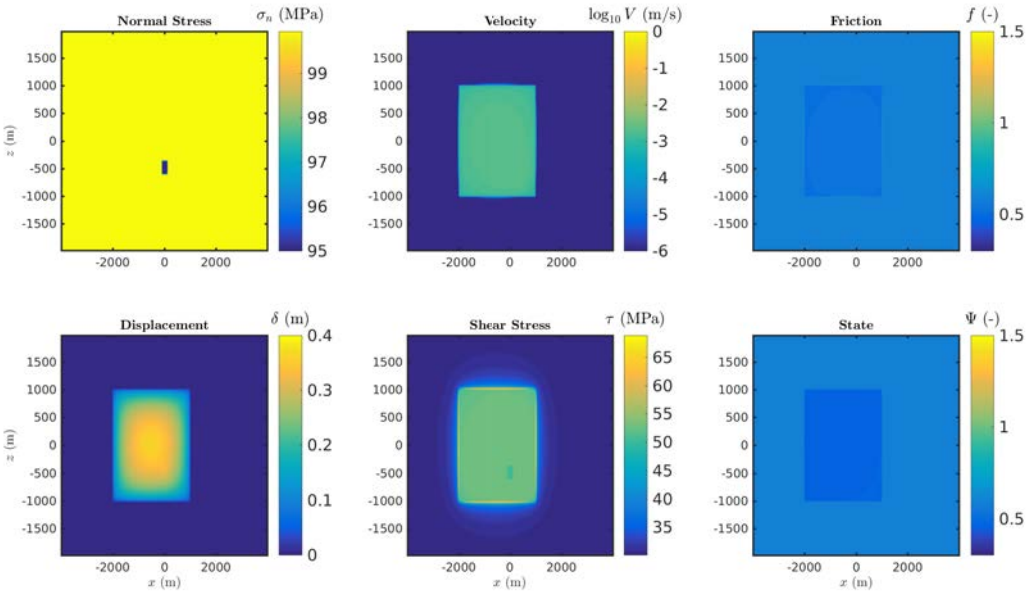

(f) rupture arrest

Figure 3.17: Distribution of fault properties relevant to the earthquake rupture process for the simulation using the CFRAC model. The subfigures in (a) through (f) each represent a snapshot in time during the rupture.

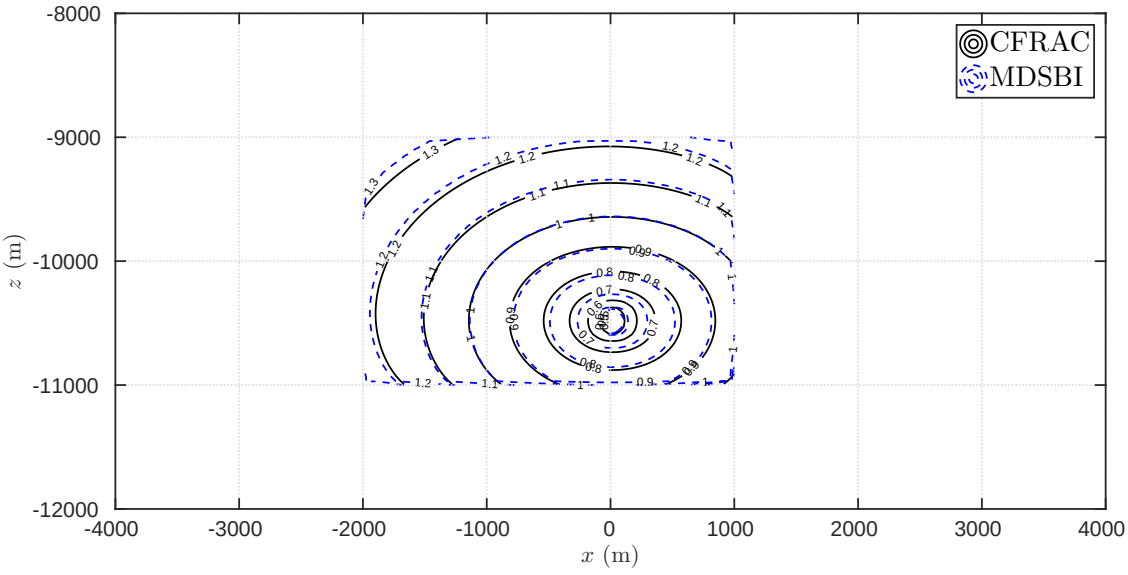

(a)

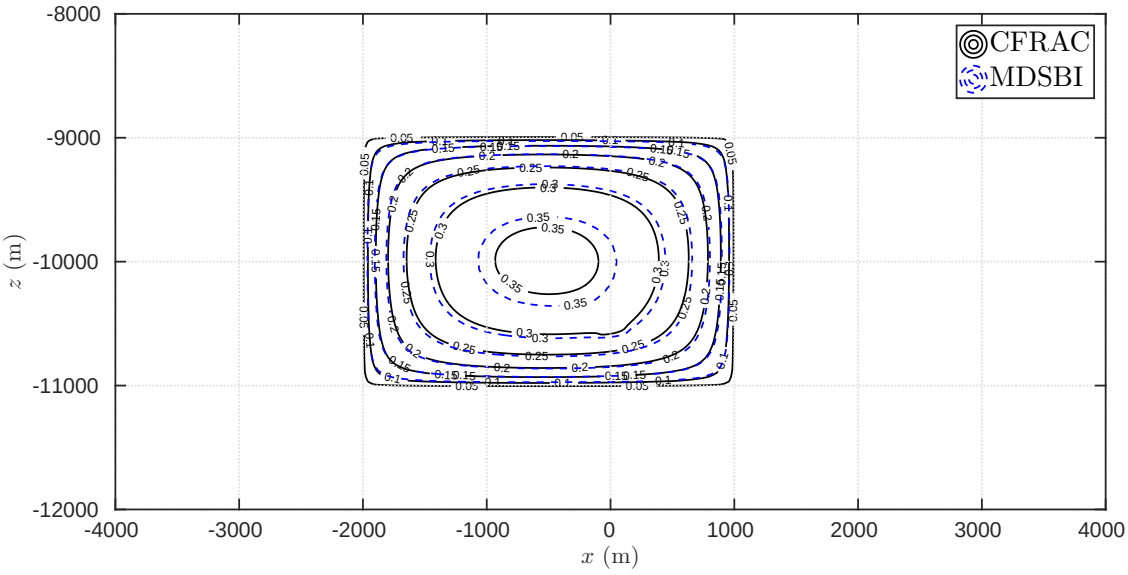

(b)

Figure 3.18: (a) Contours of the rupture front arrival time at intervals of 0.1 seconds over the range of [0,1.3] seconds following nucleation. (b) Contours of the final slip distribution at intervals of 0.05 m over the range of [0,0.35] m. The *solid black contours* are the CFRAC results, and the *dashed blue contours* are the MDSBI results.

Chapter 4

Investigation of Hydromechanical Response at the Fenton Hill Enhanced Geothermal System Test Site

This work was presented originally in *Norbeck et al.* (2016b) and *Norbeck et al.* (2016c) and was performed as part of a collaborative effort led by the US Department of Energy (DOE) Geothermal Technologies Office. The overarching goal of the DOE-led geothermal code comparison project was to learn about how the characteristics of the fractured reservoir system influenced the reservoir stimulation and fluid circulation processes at the Fenton Hill Enhanced Geothermal System (EGS) test site located in New Mexico, USA. An advantage of working as part of the DOE code comparison team was that we were able to leverage diverse backgrounds to help analyze and interpret complex, interdisciplinary datasets that were generated during the Fenton Hill EGS project to develop improved conceptual models. In the code comparison study each team was tasked with developing their own conceptual model of the geological structure of Fenton Hill reservoir and then to use a reservoir simulator to model various field experiments performed at the site. We applied the coupled fluid flow, heat transfer, and geomechanics numerical model developed in this work to investigate reservoir stimulation and fluid circulation efforts at Fenton Hill.

In our numerical experiments, we hypothesized that reservoir stimulation (i.e., permeability enhancement) at Fenton Hill occurred though a mixed-mechanism process caused by mechanical opening of natural fractures and propagation of hydraulic splay fractures. During the stimulation phase, our simulation results were consistent with observations recorded during the actual field

experiments in three distinct ways:

1. Extremely low injectivity at Well EE-2 was observed until reaching a threshold injection wellhead pressure of 5500 psi, whereupon injectivity increased significantly.

2. Low injectivity (at low pressure) at Well EE-2 was observed consistently throughout multiple stimulation treatments. That is, near wellbore permeability enhancement following each stimulation treatment was not permanent.

3. An overall North-South migration of microseismicity was observed. This was despite of the fact that injection occurred at pressures significantly above the fracturing pressure, which would tend to cause hydraulic fractures to propagate in the direction of the maximum principal stress (N30°E at Fenton Hill).

Our simulation results demonstrate that several different independent hydromechanical observations could be explained reasonably by the mixed-mechanism stimulation conceptual model. In contrast, the observations could not be explained by a pure mode-I hydraulic fracture conceptual model (because the microseismic cloud would have been oriented predominantly N30°E instead of N-S) or a pure shear stimulation conceptual model (because the injectivity of the natural fractures intersecting Well EE-2 was not enhanced by prior stimulation treatments).

Following the stimulation treatments, fluid circulation through the reservoir was modeled. During the fluid circulation phase, our simulation results were consistent with the reported data in four distinct ways:

1. The overall reservoir impedance was improved by operating the production well at higher back-pressure.

2. The accessible reservoir volume grew larger over time.

3. The difference between injected and produced fluid volumes reduced over time.

4. Thermal breakthrough was not observed over the duration of circulation considered.

The goal of the DOE Geothermal Technologies Office code comparison study was to obtain a sense of the range of conceptual models that are able to reconcile the observed data. Given that our modeling results for both the stimulation phase and the fluid circulation phase were generally consistent with the field observations, we submit these modeling results in defense of one conceptual model of the Fenton Hill EGS reservoir geologic structure and stimulation mechanism. Our model was based on several plausible assumptions (most importantly, interpretations of the state of stress at depth), which affected the simulation results significantly. We recognize that sufficient uncertainty in the state of stress is present that other models cannot be precluded.

This project provided an opportunity to demonstrate the practical utility of the numerical model developed in this work for learning about coupled processes in fractured reservoirs. We considered

several different fluid injection and extraction experiments performed in what was referred to as the "deep phase-II" reservoir at Fenton Hill between July 1982 through July 1995. The simulations incorporated several real-world complexities that were important to consider, including:

- Four individual stimulation treatments in Well EE-2 that each included multiple step-rate changes in injection rate.
- One stimulation treatment in Well EE-3A.
- Fluid circulation between Wells EE-3A and EE-2 during the Initial Closed-Loop Flow Test (ICFT).
- Sidetracking of Well EE-2 to form Well-2A in order to intersect the stimulated region with a significantly longer open-hole section of well.
- Fluid circulation between Wells EE-3A and EE-2A during the Long-Term Flow Test (LTFT).
- Variable injection and production well operational controls during each of the extended fluid circulation experiments.

Throughout this study, we relied heavily upon the book titled *Mining the Earth's Heat: Hot Dry Rock Geothermal Energy*, written by *Brown et al.* (2012). That resource provided detailed insight into the nature of how the experiments at Fenton Hill were carried out. The datasets presented in that book constitute the basis for many of the analyses in our study. More detailed information about the nature of the DOE Geothermal Technologies Office code comparison study can be found in the following references: *Ghassemi et al.* (2015); *Kelkar et al.* (2016); *McClure et al.* (2016a); *White and Phillips* (2015); *White et al.* (2015, 2016a,b).

4.1 Motivation

The deep Phase II reservoir at Fenton Hill existed at a depth of roughly 3 to 4 km in fractured granitic rock. The geothermal system was comprised of two wells, Well EE-2 and Well EE-3. Both of these wells were eventually sidetracked to form Well EE-2A and Well EE-3A. The goal of the hydraulic stimulation treatments was to create a hydraulic connection between the two wells to allow for fluid circulation and heat extraction from the geothermal reservoir that would enable electricity generation using a small power plant located at the surface. The original design of the geothermal heat exchange system was very similar fundamentally to the conceptual model studied by *Gringarten et al.* (1975) and discussed in Sect. 3.4. In this idealized stimulation strategy, a set of vertical hydraulic fractures would connect two highly deviated wells. However, after the initial stimulation experiments carried out in the late 1970's, it became clear that two competing hypotheses of the hydraulic stimulation mechanism were held by the scientists and engineers involved

in the project (*Brown et al.*, 2012). One camp believed that planar hydraulic fractures were forming in the reservoir, while the other camp believed that stimulation was attributed to deformation of preexisting fractures and no hydraulic fractures were forming.

In the present study, we were interested in understanding how fracture pressurization, poroelastic stress, and thermal stress affected the stimulation process and the evolution of microseismicity that was observed during various injection experiments carried out during the 1980s. We focused on four stimulation treatments in well EE-2 leading up to and including the massive hydraulic fracture (MHF) experiment (Expts. 2018, 2020, MHF prepump, and Expt. 2032). The DOE provided microseismic event locations and timing recorded during Expt. 2032 (MHF). In Fig. 4.1, the event locations are shown in plan and cross-section views and are colored by event timing. During injection, events migrated away from the well. In plan view, the microseismic cloud tended to migrate in an overall NNW-SSE direction. This is an extremely important observation, and helped to form the basis for our conceptual reservoir model. Figure 4.2 shows the radial distance away from the well of each event over time. During injection, events tended to occur across the entire stimulated region. Upon shut-in after 2.5 days of injection, the events occurred predominantly at the edges of the stimulated region, and the events migrated back towards the well. In Fig. 4.3, the microearthquake event rate overlies the injection pressure recorded during the MHF experiment. At early times, no events were recorded which was likely due to the Kaiser effect as a result of previous injection experiments. During injection at constant flow rate, the pressure was observed to be relatively constant, however, the seismicity rate could be characterized by several distinct rate spikes. Following shut-in, the event rate decayed steadily over the period of about 1 day.

Following the massive hydraulic fracture stimulation treatment in Well EE-2, the other well (Well EE-3A) was pressure-stimulated. Ultimately, during the stimulation of Well EE-3A a hydraulic connection with Well EE-2 was observed. In the summer of 1986, the initial fluid circulation experiments were performed. Well EE-3A served as the injection well, and Well EE-2 was the production well. The most significant circulation experiment during this period was called the Initial Closed-Loop Flow Test (ICFT). The ICFT involved two periods of relatively steady-state operation over the period of one month. For the first 15 days, the injection well was operated at a nominal wellhead pressure of 3890 psi (26.8 MPa), the production well was operated at a wellhead pressure of 350 psi (2.4 MPa), and a production rate of 3.2 BPM (8.5 L/s) was achieved (*Brown et al.*, 2012). After 15 days, engineers decided to increase the injection rate, injection pressure, and production backpressure. A key observation was that the overall reservoir impedance was reduced (improved) at higher mean reservoir pressure.

Although fluid circulation during the ICFT was successful from a technical perspective, it was concluded that commercial circulation rates had not been achieved. Well EE-2 was sidetracked and redrilled though the microseismic cloud observed during the MHF treatment. This resulted in a production well with a significantly longer section of open-hole interacting with the stimulated

reservoir zone. In the summer of 1995, the second significant fluid circulation experiment was performed. This experiment was called the Long-Term Flow Test (LTFT) and consisted of roughly two months of constant circulation. Electricity was generated successfully throughout this phase of circulation. The LTFT marked the final experiment performed at the Fenton Hill EGS site.

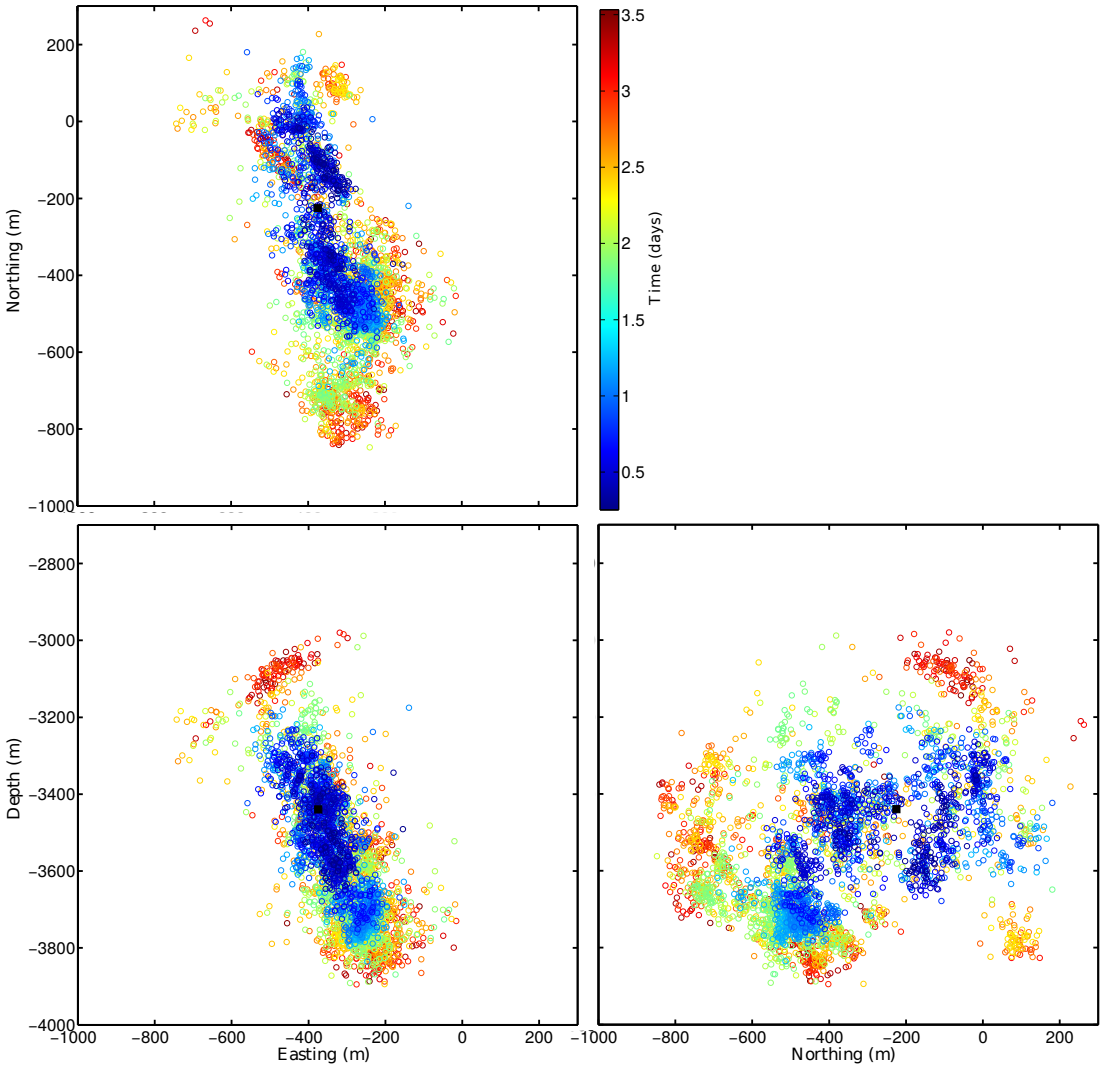

Figure 4.1: Microearthquake locations recorded during the Expt. 2032 (MHF) stimulation treatment. The events are colored by event timing. The well was shut-in after roughly 2.5 days of injection. The earthquake catalog data was provided by Los Alamos National Laboratory and Pacific Northwest National Laboratory as part of the US DOE Geothermal Technologies Program geothermal code comparison study.

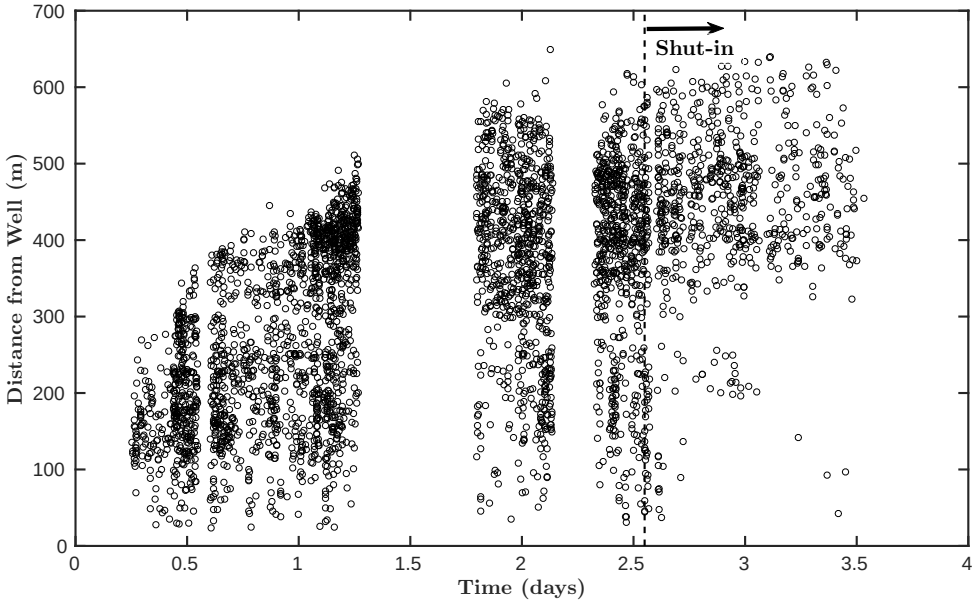

Figure 4.2: Location of each individual earthquake event calculated as distance relative to the injection well.

4.2 Conceptual reservoir model

The injection experiments took place in well EE-2, which had an openhole interval at a depth of roughly 3.6 km in the Phase II reservoir at Fenton Hill. Our interpretation for the state of stress in the Phase II reservoir is based on wellbore stress measurements (*Barton et al.*, 1988), earthquake focal mechanisms (*House et al.*, 1985), minifrac tests (*Brown*, 1989; *Kelkar et al.*, 1986), and observations during step-rate tests (*Brown et al.*, 2012). Varying estimates of the fracture gradient are available in the literature. *Kelkar et al.* (1986) summarized a large number of minifrac tests to estimate that the minimum principal stress gradient was 19 MPa/km, implying a value of 68.4 MPa at 3.6 km depth. However, *Kelkar et al.* (1986) noted that tests shallower than 3.3 km depth indicated a much lower fracture gradient. Based on these and other observations, *Brown* (1989) proposed that the minimum principal stress gradient was 13 MPa/km, implying a minimum horizontal stress of 46.8 MPa at depth. *Brown* (1989) hypothesized that due to the high tensile strength of granite, hydraulic fractures were unable to form at the wellbore, and so the fracturing pressure observed during injection tests corresponded to the pressure required to exceed the normal stress on preexisting fractures intersecting the well. If these fractures are oblique to the principal stresses, then their opening pressure will be greater than the minimum principal stress. Therefore, *Brown* (1989) proposed that the apparent increase in fracturing pressure at 3.3 km was caused by

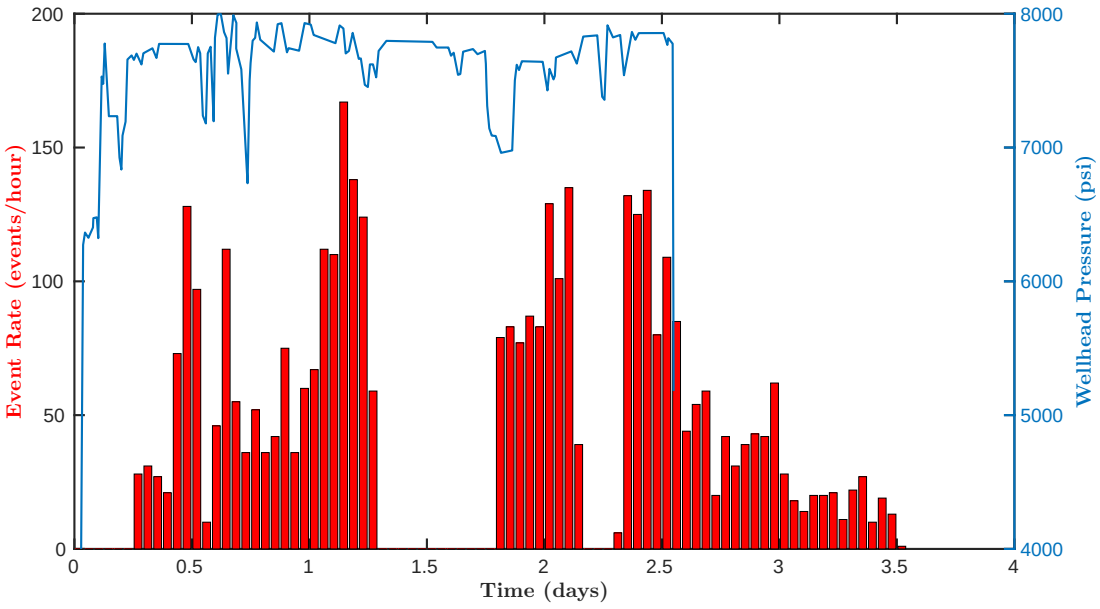

Figure 4.3: Event rate (*red bars*) and wellhead pressure (*blue line*) recorded during Expt. 2032 (MHF). The gap in the data around 1.5 days was due to an operational failure of the seismic data acquisition system.

a discontinuity in natural fracture orientation, rather than stress, and that the tests shallower than 3.3 km reflected the true value of the minimum principal stress.

In our model, we chose to use the *Brown* (1989) estimate for the magnitude of the minimum principal stress. In the injection tests in EE-2, the well injectivity was observed to increase very sharply and nonlinearly at a bottomhole pressure of around 74 MPa (at 3.6 km depth), and so for either stress profile, the bottomhole pressure exceeded the minimum principal stress during the injections (Figures 6-5, 6-9, 6-18, and 6-21 from *Brown et al.* (2012)). We assumed a strike-slip stress regime where the state of stress at depth was $\sigma_H^R \approx \sigma_V^R = 90$ MPa, $\sigma_h^R = 46$ MPa, and $p_0 = 31$ MPa. The orientation of σ_H^R was N30°E based on interpretations of wellbore breakouts (*Barton et al.*, 1988). The fractures were assumed to have a constant coefficient of friction of $f = 0.7$ (rate-and-state friction was not used in the Fenton Hill study). The host rock was assumed to have a very low permeability of $k^m = 1 \times 10^{-19}$ m^2 (0.1 nd) and a porosity of $\phi^m = 0.05$. The initial reservoir temperature at the injection interval was $T_0 = 230$ °C. Elastic properties of the matrix rock were assumed to be typical of granite (*Jaeger et al.*, 2007).

Microseismic events observed during hydraulic fracturing treatments are often interpreted as shear slip events on natural fractures that surround the main hydraulic fracture. At Fenton Hill, if this was the appropriate mechanism, then the microseismic cloud would be expected to migrate in

the direction of maximum horizontal stress (N30°E), but this was not the case. Nonetheless, injection pressures during the hydraulic stimulation treatments typically exceeded the magnitude of the least horizontal stress significantly (see Fig. 4.3), which would suggest that hydraulic fractures were indeed forming in the reservoir. In addition, a consistent observation during multiple step-rate tests was that near wellbore injectivity increased substantially after exceeding a pressure corresponding to a bottomhole pressure of about 74 MPa (*Brown et al.*, 2012). A conventional minifrac analysis would interpret this value as the fracture opening or fracture propagation pressure. Finally, a key observation was that wellbore temperature logs indicated three or four distinct feedzones during Expt. 2018, suggesting that natural fractures (not hydraulic fractures) were taking flow in the near wellbore region and that flow was localized into a small number of highly permeable pathways with vertical separation on the order of 30 m (Figure 6-6 from *Brown et al.* (2012)).

We developed a conceptual model for the Fenton Hill Phase II reservoir that was consistent with each of these observations. The reservoir was considered to be naturally fractured with a primary set of near-vertical fractures oriented with an average strike of NNW-SSE. Hydraulic fractures propagated as splays off the tips of the natural fractures during injection at high pressure. The hydraulic fractures did not form into large, continuous features because they sometimes terminated against natural fractures due to mechanical interference. This conceptual model is the "mixed-mechanism" stimulation concept that has been applied in oil and gas settings (*Weng et al.*, 2011). *McClure* (2012) and *McClure and Horne* (2014a) argued that this is the dominant mechanism of stimulation in many (but not all) EGS projects.

The orientation of the primary fracture set was determined based on three independent datasets that each support one another. First, the "fracture opening pressure" of 74 MPa was interpreted as the fluid pressure required to overcome the normal stress acting on natural fractures intersecting the well. Given the stress state measured at Fenton Hill, the fracture orientation corresponding to a normal stress of 74 MPa is roughly N23°W. Second, analysis of the focal mechanisms for several of the largest observed microearthquakes yielded solutions with a nodal plane suggesting the presence of fracture or fault structures oriented N30°W (*House et al.*, 1985). Finally, the overall migration of the seismicity was in the NNW-SSE direction (see Fig. 4.1). We generated a stochastic realization of a fractured reservoir based on this conceptual model for the simulations performed in this study. The reservoir model and Mohr circle representation of the stress state are shown in Figs. 4.4 and 4.5, respectively.

It was necessary to consider hydraulic fracture propagation in the model for several reasons. First, the fluid pressure exceeded the minimum principal stress, and so it is plausible that hydraulic fractures would form. Even if the high tensile strength of the rock prevents hydraulic fractures from forming at the well, concentrations of stress created by natural fracture opening and sliding would facilitate the formation of hydraulic fractures away from the well. Because the fluid pressure increased well-above the minimum principal stress, the hydraulic fractures can open mechanically

to large apertures and provide the bulk of the fluid storage during injection. However, it was critical for the hydraulic fractures to terminate against the natural fractures, because otherwise, they would propagate continuously across the formation, and the microseismic cloud would orient primarily perpendicular to the minimum principal stress. In the simulations, fracture termination was assumed to occur 50% of the time when a hydraulic fracture reached a natural fracture.

4.3 Description of numerical experiments

The numerical simulations we performed for this study involved modeling the most significant phases of stimulation and circulation history of the deep geothermal reservoir at Fenton Hill over a period ranging from 1982 through 1995. In an attempt to remain true to the field experiments, the range of different injection and circulation experiments were modeled coherently as a single simulation covering the entire timespan. Specifically, we modeled the following field experiments:

- Expt. 2018 (July 1982)
- Expt. 2020 (October 1982)
- Expt. 2032 prepump (December 1983)
- Expt. 2032 massive hydraulic fracture treatment in Well EE-2 (December 1983)
- Expt. 2062 stimulation treatment in Well EE-3A (July 1985)
- Initial Closed-Loop Flow Test (May - June 1986)
- Long-Term Flow Test (May - July 1995)

We based the injection well and production well operational parameters on the data described by *Brown et al.* (2012).

It was important to consider several practical factors that influenced the behavior at Fenton Hill significantly. The initial design of the Fenton Hill EGS reservoir involved circulating fluid through two main wells. Well EE-2 was to be the injection well, and Well EE-3 was to be the production well. Well EE-2 was the first to be pressure-stimulated. Following the stimulation treatment, it was decided to switch the roles of the two wells. After redrilling well EE-3 to form EE-3A, the stimulation treatment of Well EE-3A was successful at creating a hydraulic connection with EE-2. The ICFT was performed using EE-3A as the injection well and EE-2 as the production well. At this time, the circulation rates were determined to be insufficient for commercial electricity production. Well EE-2 was sidetracked to form Well EE-2A resulting in a well with a significantly longer open-hole section intersecting the stimulation zone. The LTFT was performed using EE-3A as the injection well and EE-2A as the production well. Each of these wells were drilled directionally. In our model, we assumed a two-dimensional domain with vertical fractures. We modeled each of the wells

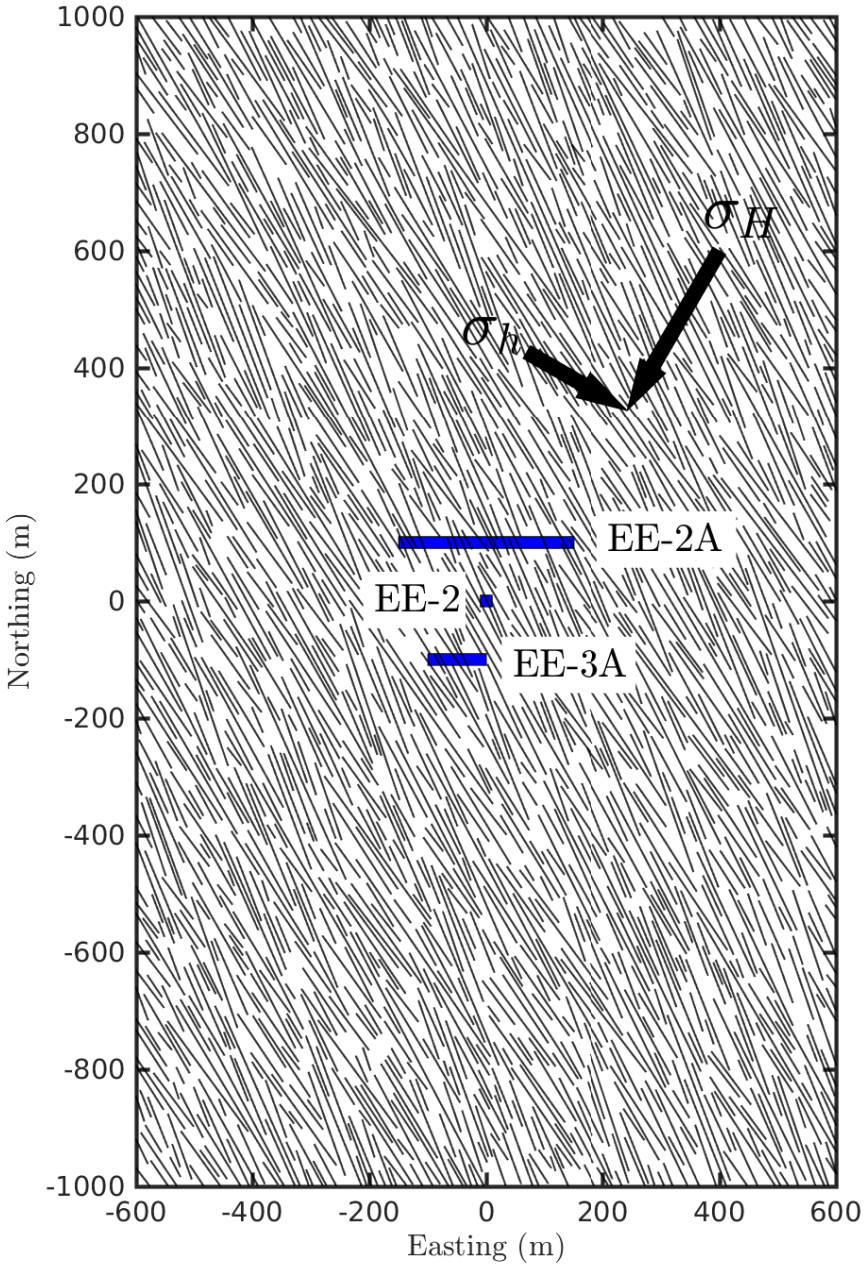

Figure 4.4: Illustration of the fractured reservoir model used in the simulations. A primary set of natural fractures oriented with an average strike of N23°W was surrounded by low-permeability granite. The *black lines* represent the natural fractures, the *blue lines* represent the locations of the deviated wellbores, and the *black arrows* represent the orientations of the horizontal stresses.

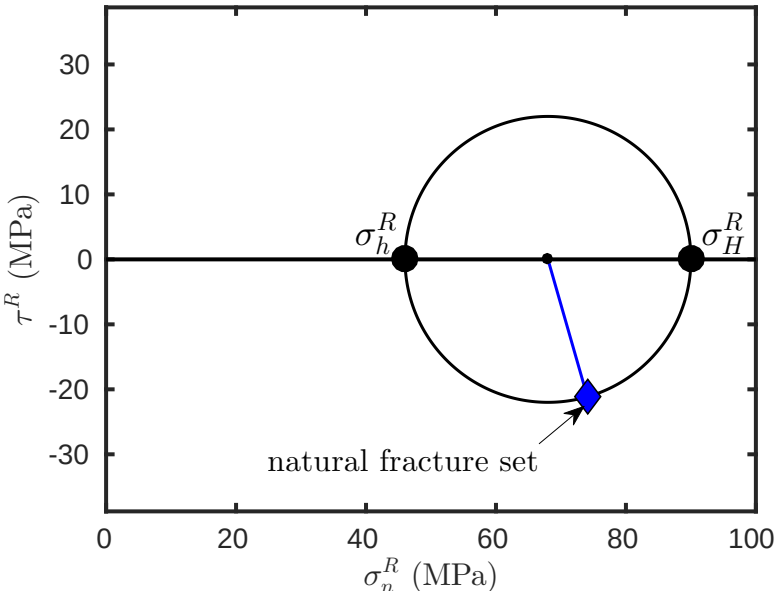

Figure 4.5: A Mohr-Coulomb representation of the regional state of stress specified in the simulations. The joint opening pressure of approximately 74 MPa observed during the actual injection experiments at Fenton Hill was one of the constraints used to determine the orientation of the predominant fracture set.

as horizontal wells, and attempted to reconcile the true open-hole lengths using descriptions of the wellbore completion schematics provided by *Brown et al.* (2012). The wellbore geometries are shown as blue lines in Fig. 4.4.

We performed four simulations in order to isolate the effects of different physical processes that potentially could have contributed to the hydromechanical behavior observed at the site. We investigated the relative impact of fluid pressurization in the fractures, poroelastic stress, and thermal stress (Cases B, C, and D, respectively) and also performed one simulation that incorporated all of the mechanisms (Case A). Fluid pressurization is the most common mechanism associated with injection-induced seismicity. Poroelastic stresses can be generated as fluid pressure in the rock surrounding the fractures changes due to leakoff or production (*Segall*, 1989). Thermal stresses can be generated as the rock is cooled during injection (*Mossop*, 2001; *Rana*, 1984). The full schedule of injection, production, and shut-in history over the course of roughly 13 years was simulated. During all periods of fluid injection, the injected fluid temperature was assumed constant at 130 °C bottomhole temperature. Important model parameters are provided in Table 4.1.

Table 4.1: Model properties for the Fenton Hill numerical simulations.

Parameter	Value	Unit
Depth	3.6	km
h	200	m
σ_{H0}	90	MPa
σ_{h0}	46	MPa
θ_{σ_H}	N30°E	-
p_0	31	MPa
T_0	230	°C
T_i^w	130	°C
κ_φ	0.6	$\mathrm{W \cdot m^{-1} \cdot °C^{-1}}$
κ_r	2.4	$\mathrm{W \cdot m^{-1} \cdot °C^{-1}}$
α^P	0.4	-
α^T	8×10^{-6}	$\mathrm{°C^{-1}}$
k^m	1×10^{-19}	$\mathrm{m^2}$
ϕ^m	0.05	-
K_{IC}	1.5	$\mathrm{MPa \cdot m^{-1/2}}$
c_φ	4200	$\mathrm{J \cdot kg^{-1} \cdot C^{-1}}$
c_r	800	$\mathrm{J \cdot kg^{-1} \cdot C^{-1}}$
G	15	GPa
ν	0.25	-
e_*	0.0004	m
E_*	0.0004	m
σ_{*e}	8	MPa
σ_{*E}	8	MPa
e_{res}	0	m
E_{res}	0	m
φ_e	0	deg.
φ_E	0	deg.
f	0.7	-
s	0.5	MPa
λ^{-1}	0.15×10^{-3}	Pa · s
$\rho_{\varphi,0}$	930	$\mathrm{kg \cdot m^{-3}}$
β_φ	4.4×10^{-4}	$\mathrm{MPa^{-1}}$
ρ_r	2650	$\mathrm{kg \cdot m^{-3}}$
β_r	4.4×10^{-4}	$\mathrm{MPa^{-1}}$

4.4 Hydraulic stimulation phase

Hydraulic stimulation efforts at Well EE-2 consisted of Expts. 2018, 2020, 2032 (prepump), and 2032 (MHF). The massive hydraulic fracture treatment (Expt. 2032) was the most significant stimulation treatment at Fenton Hill. Many microseismic events were recorded during this injection experiment (see Fig. 4.1). Repeated stimulation treatments in Well EE-2 provided a unique opportunity to interpret reservoir response to fluid injection. Hydraulic stimulation efforts at Well EE-3A consisted primarily of Expt. 2062. No significant seismicity was observed during this experiment.

4.4.1 Stimulation of Well EE-2

In Fig. 4.6 the stimulated fracture network at the end of the massive hydraulic fracture treatment is shown. Injection occurred through Well EE-2 (the blue line). The red lines indicate the hydraulic fractures that propagated as splays off of the natural fractures. The hydraulic fractures propagated in the direction of the maximum principal stress (N30°E), but tended to terminate against neighboring natural fractures. This resulted in an overall N-S migration of the stimulated zone. Hydraulic fracture termination, which was a model assumption, was requisite to control the spatial migration of the stimulated zone.

The microseismicity associated with the stimulation is shown in Fig. 4.7. The location of the microseismic events were calculated by assuming that the rate of sliding deformation of the fractures (which was calculated as part of the numerical solution) was related directly to the generation of seismicity. The dimensions of the cloud of seismicity (roughly 1 km in the N-S direction and 400 m in the E-W direction) was in agreement with the field observations. Seismicity was observed to propagate relatively uniformly away from the injection well.

Comparing the trends in seismicity rate shown in Figs. 4.3 and 4.8, we observe several qualitative similarities. The lack of seismicity in the first several hours of injection, most likely attributable to the Kaiser effect, was captured well by the model. In the model results, bursts of seismicity were observed to occur as hydraulic fractures terminated against natural fractures which allowed for rapid sliding along newly connected natural fractures. This is a plausible mechanism for the bursts in seismicity observed in the field experiments.

The rate at which seismicity propagated away from the well was replicated accurately, which can be seen by comparing Figs. 4.2 and 4.9. In the model, the rate of extension of the stimulated zone was influenced by the density of natural fractures and their initial transmissivity. In the model, the maximum event distance was 550 m, which compares favorably with the observed maximum distance of 600 m. This is an important result that suggests a plausible basis for the hydraulic properties of natural fractures in granitic rock. In the model, it was necessary to use the following values controlling natural fracture aperture to match the data: $e_* = 0.004$ m, $\sigma_{*e} = 8$ MPa, $e_{res} = 0$, $\varphi_e = 0$. Following shut-in of the injection well, the modeled seismicity occurred only at the edges of the stimulated region, which was similar to the behavior observed in the field. This behavior supports the observation discussed by *McClure and Horne* (2011) and *McClure* (2015) that pressure is able to rise near the edges of the stimulated region even while pressure is falling in the near-wellbore region after shut-in. This type of behavior is encouraged by nonuniform fracture transmissivity throughout the reservoir.

The injection rate and pressure model results are compared against the field observations for each of the four stimulation treatments in Well EE-2 in Figs. 4.10 through 4.13. One of the most important observations made in each of these injection experiments that we attempted to model accurately was the sharp transition in the injectivity of Well EE-2 at a wellhead pressure of 5500

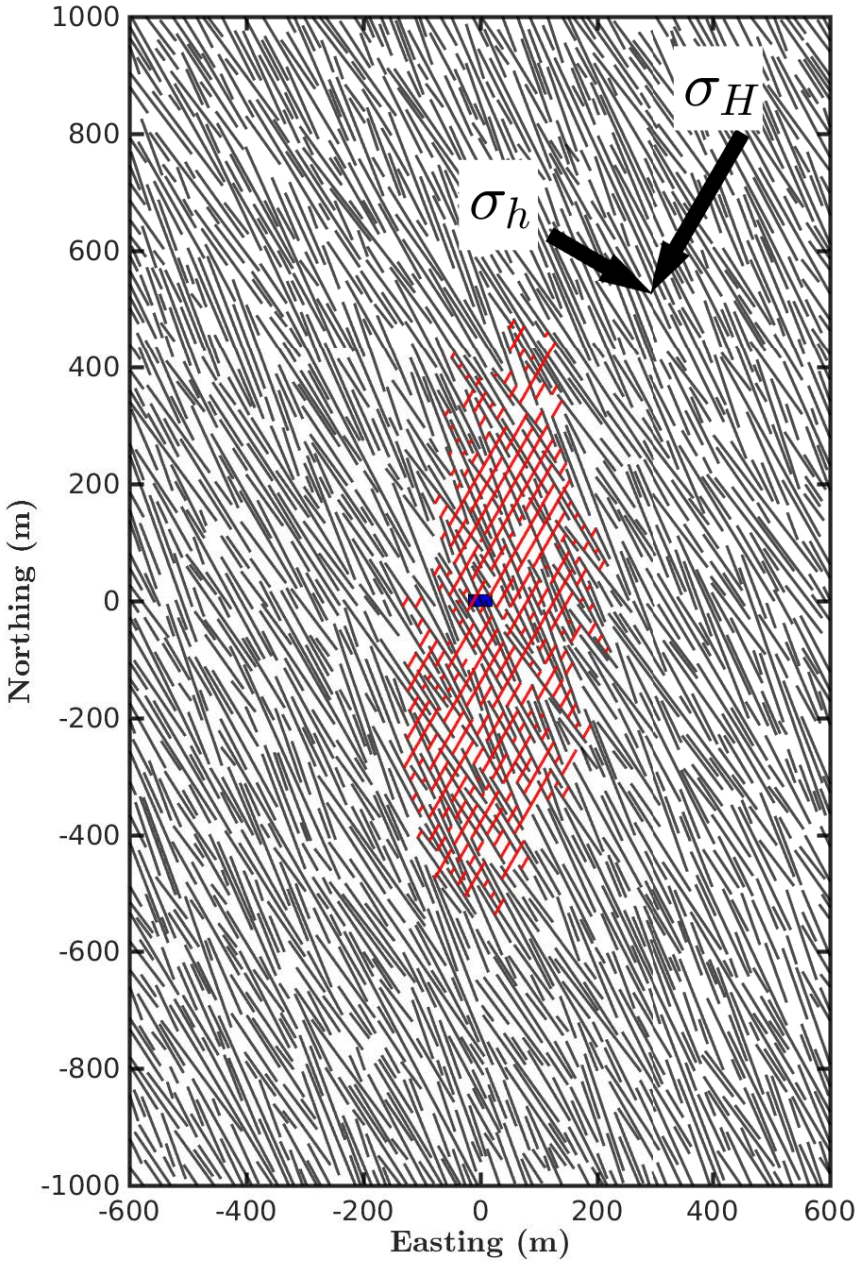

Figure 4.6: Stimulated fracture network at the end of Expt. 2032 (MHF) for Case A. The *red lines* represent the hydraulic splay fractures that were generated during high-pressure injection. Stimulation occurred through a mixed-mechanism combination of mechanical opening and propagation of hydraulic fractures.

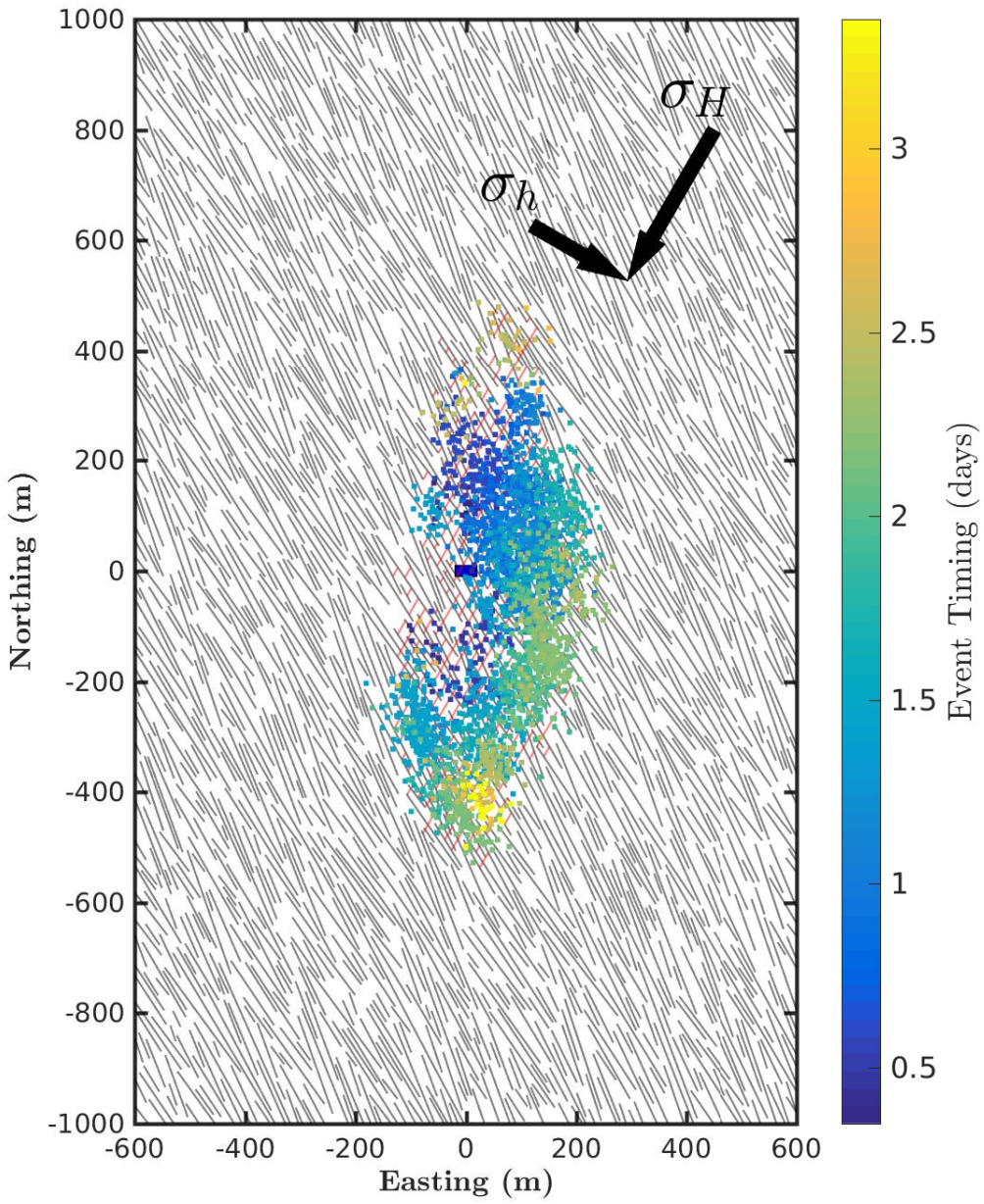

Figure 4.7: Microseismic event locations overlying the stimulated fracture network at the end of Expt. 2032 (MHF) for Case A. Termination of the hydraulic fractures against neighboring natural fractures controlled the overall N-S migration of the stimulated region.

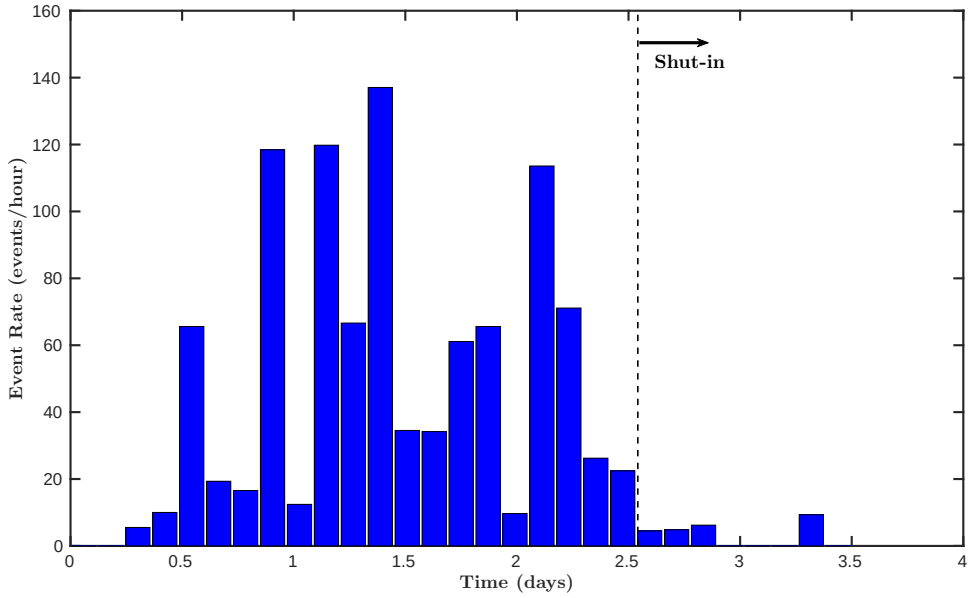

Figure 4.8: Modeled microseismic event rate during Expt. 2032. The Kaiser effect, which precluded seismicity from occurring at early times in the near-wellbore region that had been stimulated previously, was captured accurately by the model. Bursts of seismicity occurred as hydraulic fractures created new connections with natural fractures.

psi. The change in injectivity is characterized by an initial rapid pressurization at low injection rates up until a critical pressure level, followed by only modest increases in pressure even for relatively large changes in injection rate when pressure is above the critical threshold. This was observed in the field data in each of the four repeated stimulation treatments, suggesting that any near-wellbore permeability enhancement achieved during the stimulation treatments was not permanent.

Our modeling results matched the injectivity transition accurately for Expts. 2018, 2020, and 2032. In the model, this behavior was caused by the nonlinear opening-mode fracture stiffness constitutive model that was used to calculate fracture aperture for fractures bearing compressive normal stress (see Eq. 2.4). As the injection pressure approached the magnitude of the normal stress acting on the fractures that intersected the well, fracture transmissivity was able to increase dramatically. While the fractures had high transmissivity, they were able to accommodate large changes in flow rate with negligible resistance.

During the MHF prepump, the pressure rollover behavior occurred at a significantly lower pressure than observed in the field experiment (see Fig. 4.12). To reconcile this mismatch, we first note that a significant number of hydraulic fractures were created out in the reservoir during the first two stimulation treatments. The hydraulic fractures bore a significantly lower normal stress relative to the natural fractures, and therefore they were able to open easily to provide fluid storage volume. In

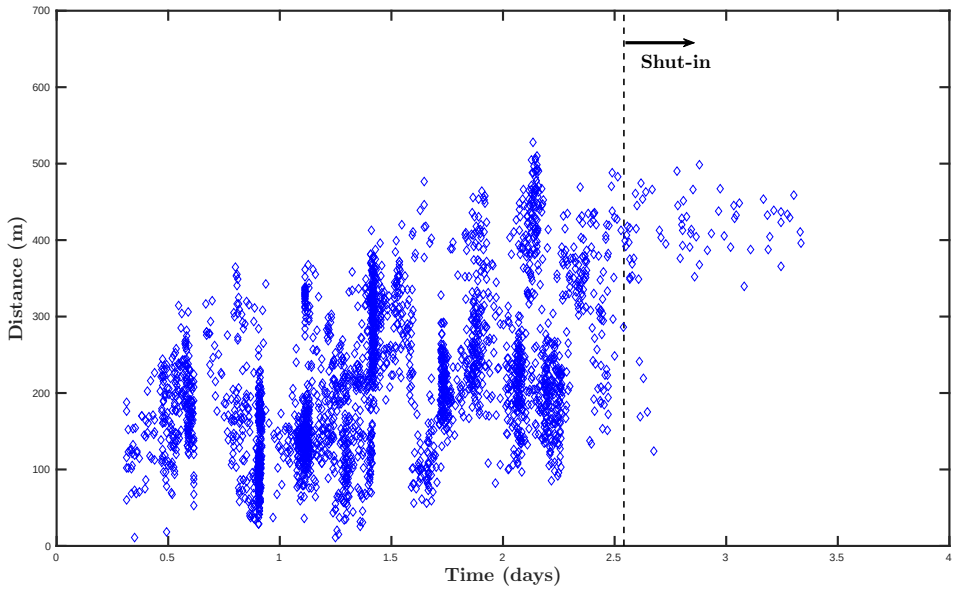

Figure 4.9: Modeled microseismic event locations measured relative to the injection well in the horizontal plane during Expt. 2032. Consistent with the field observations, seismicity occurred across the entire stimulated region during injection, but occurred predominantly at the edges of the stimulated region following shut-in. The overall extent of the seismicity and the rate at which seismicity propagated away from the well were quantitatively similar to the observed data.

the model, the rate of pressurization during the prepump was controlled by the connectivity between the well and the hydraulic fractures (i.e., the length of the natural fracture pathway before reaching the hydraulic fractures) and the fracture aperture stiffness parameters that dictate the transmissivity evolution of the natural fractures. Once the pressure transient was able to reach the hydraulic fractures, they were able to act effectively as constant pressure sinks that absorbed the flow. Due to the stochastic nature of the model, it was not possible to control the exact distance between the well and the hydraulic fractures, which resulted in this slight discrepancy observed in the prepump behavior. Based on this rationale, we argue that this discrepancy does not refute our hypothesized conceptual model.

We reiterate that the injectivity at low flow rates did not change even after several repeated stimulation treatments in well EE-2. In order to model this behavior, we used a shear dilation angle of zero. Therefore, our simulation results suggest that shear stimulation was not effective at enhancing the permeability of natural fractures at Fenton Hill. In addition, the MHF treatment was performed at extremely high net-pressures for 2.5 days. The assumed stress state indicated a fracturing pressure of roughly 1440 psi (wellhead pressure), and injection pressures were nearly 7000 psi for most of the treatment. Traditional mode-I fracture propagation analyses based on the

theory of linear elastic fracture mechanics would predict unrealistically large hydraulic fractures for these operational conditions. These observations support the fracture termination and branching assumption that formed the basis of our conceptual and numerical models. Our analysis supports the hypothesis that stimulation occurred as a mixed-mechanism combination of mechanical fracture opening (as the fluid pressure in natural fractures approached their normal stress) and creation of hydraulic splay fractures.

4.4.2 Stimulation of Well EE-3A

Nearly two years following the stimulation treatments in Well EE-2, the other well (Well EE-3A) was pressure-stimulated. The stimulation treatment lasted 3.5 days. *Brown et al.* (2012) indicated that no significant microseismicity was observed during this experiment, and argued that most of the work generated by injecting fluid went into dilating the stimulated fracture network created previously. Our modeling results were consistent with this observation in that no new hydraulic fractures were formed during injection and no seismicity was generated. In Fig. 4.14, the injection rate and pressure profiles are compared against the observed data. In the model results, no signature of the injectivity transition was observed which was in contrast to the field data. This occurred because, in the model, Well EE-3A was connected directly to several hydraulic fractures and natural fractures. In reality, the well may not have intersected hydraulic fractures directly and therefore exhibited similar behavior as Well EE-2. The discrepancy is simply an unavoidable artifact of our model setup, and does not influence our conclusions significantly.

4.5 Fluid circulation phase

The first significant fluid circulation experiment performed at Fenton Hill was called the Initial Closed-Loop Flow Test (ICFT). The ICFT lasted roughly 30 days over the summer of 1986. The injection well was Well EE-3A, and the production well was Well EE-2. Circulation rates were determined to be insufficient for commercial electricity generation. Following the sidetracking of Well EE-2 to form Well EE-2A, the second major fluid circulation experiment was performed. The Long-Term Flow Test (LTFT) lasted two months over the summer of 1995. The injection well was again Well EE-3A, and the production well was Well EE-2A. The LTFT marked the final experiment performed at the Fenton Hill EGS site.

4.5.1 ICFT: Flow between Wells EE-3A and EE-2

During the first half of the ICFT, circulation was performed at relatively low injection rates and pressures. In the second half of the ICFT, the injection rate and injection pressures were raised significantly. In addition, the production well backpressure was increased during the second half of

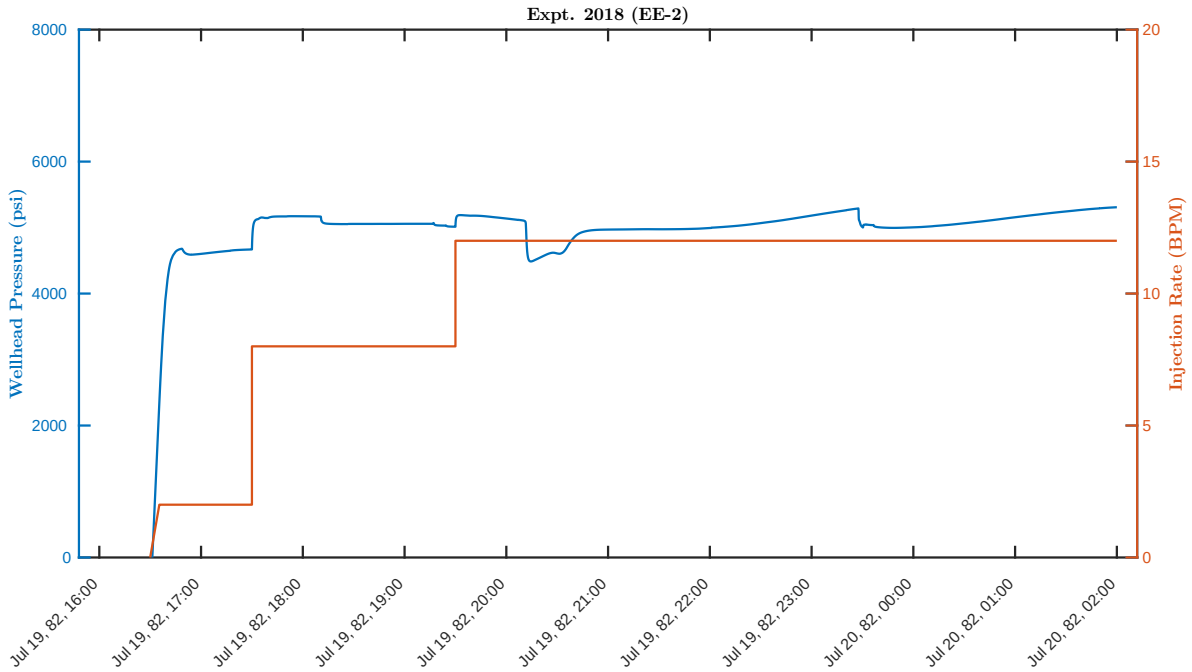

(a)

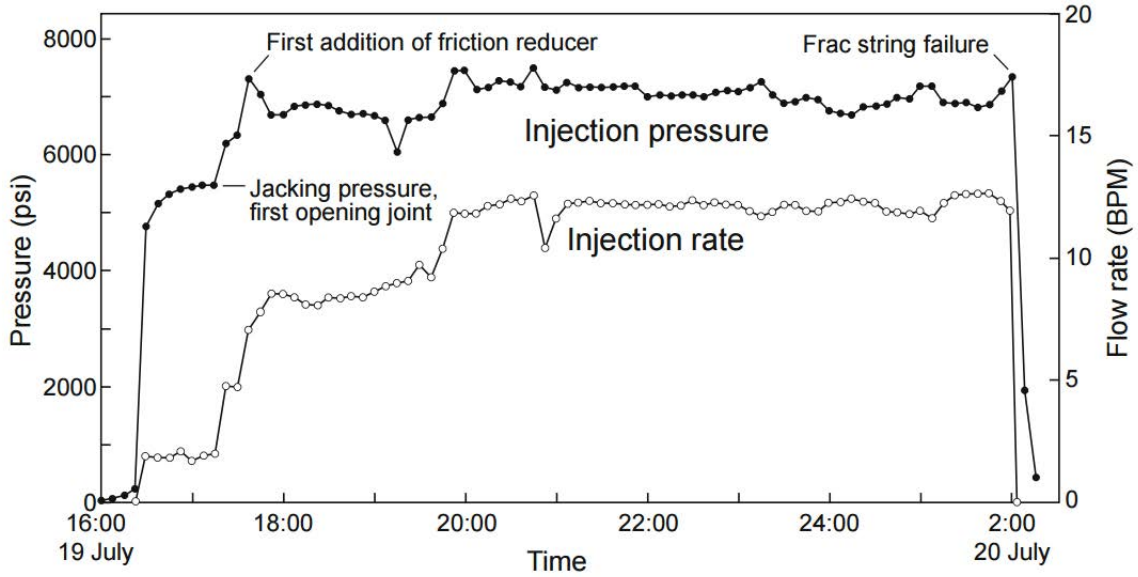

(b) Figure from *Brown et al.* (2012).

Figure 4.10: Comparison of (a) model results and (b) recorded injection rate and pressure data for Expt. 2018.

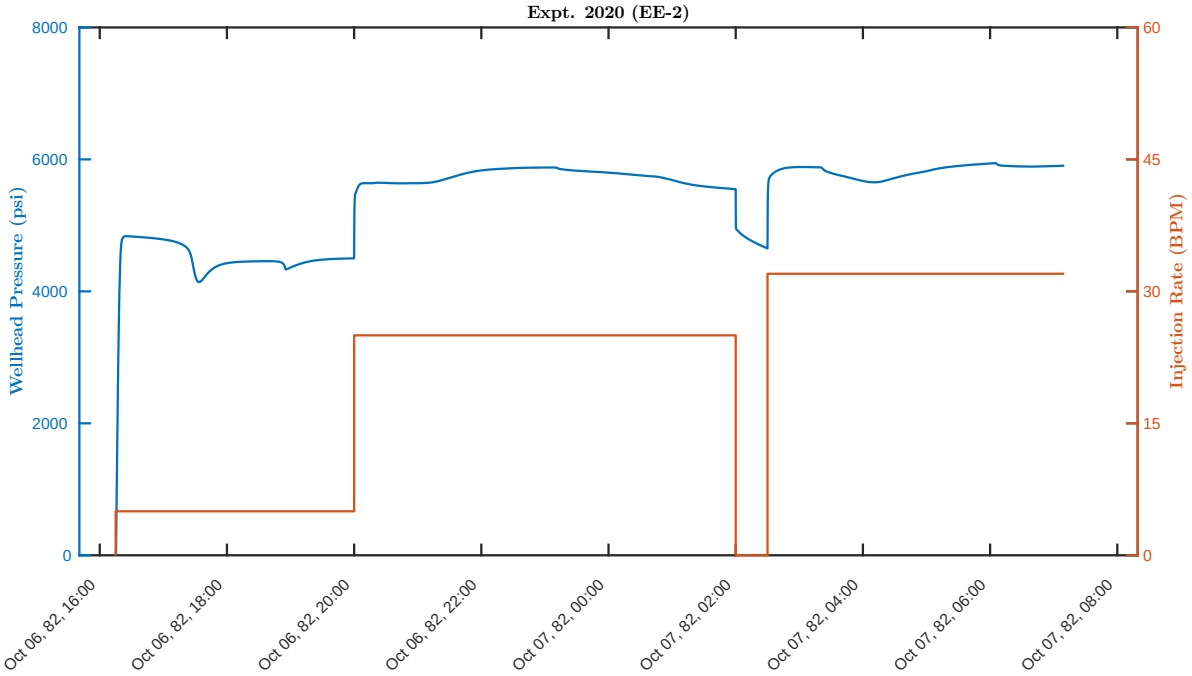

(a)

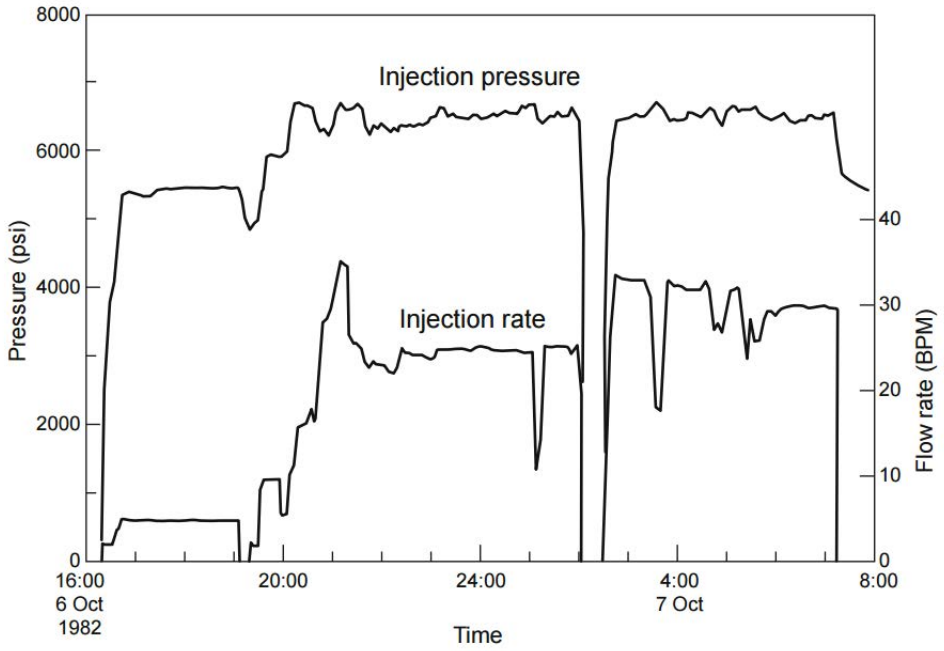

(b) Figure from *Brown et al.* (2012).

Figure 4.11: Comparison of (a) model results and (b) recorded injection rate and pressure data for Expt. 2020.

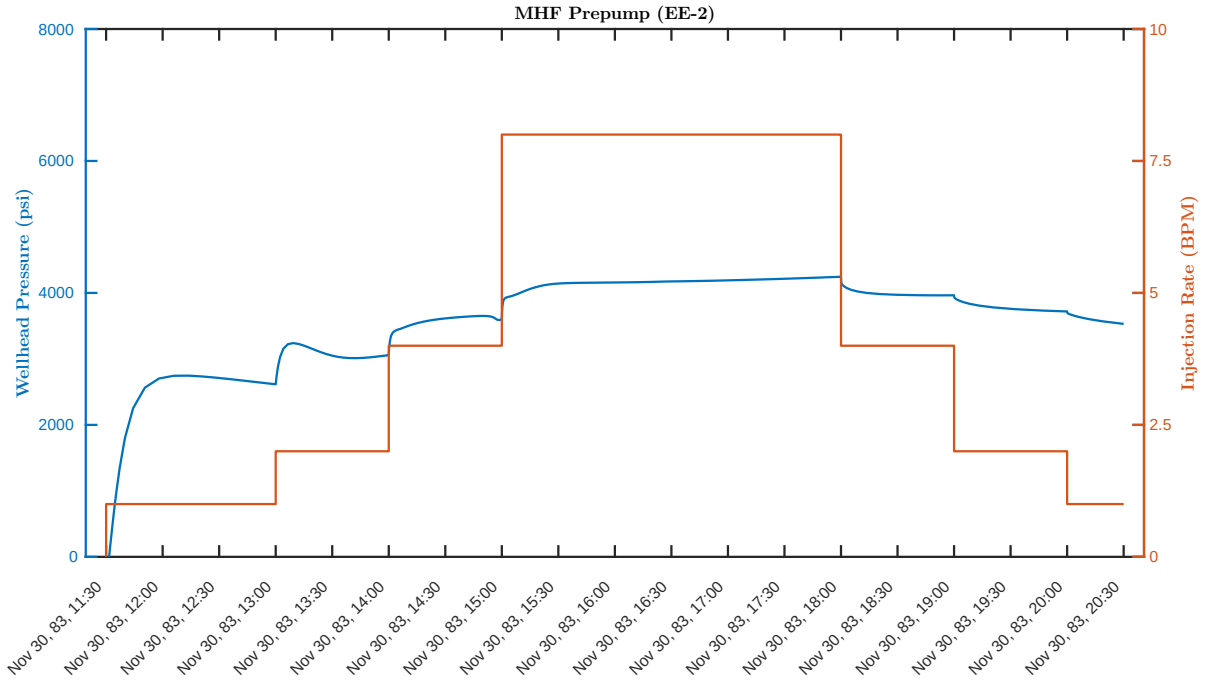

(a)

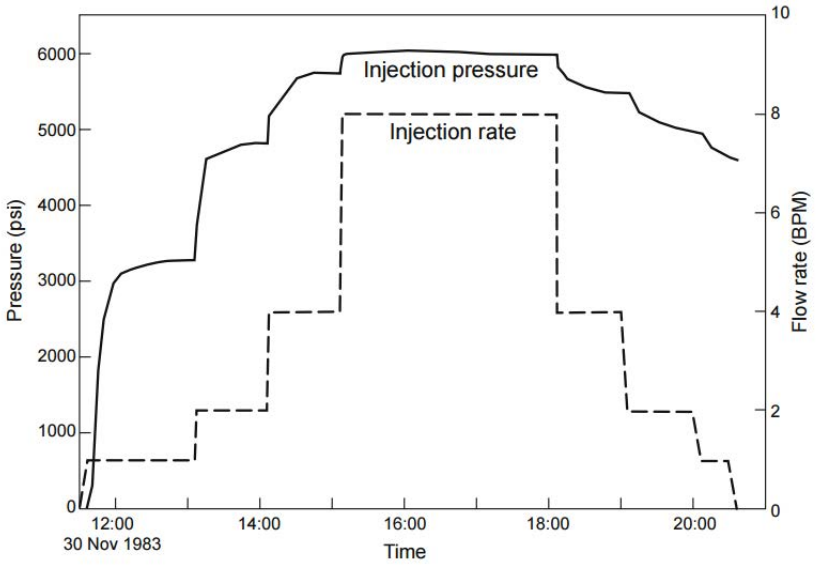

(b) Figure from *Brown et al.* (2012).

Figure 4.12: Comparison of (a) model results and (b) recorded injection rate and pressure data for the MHF prepump.

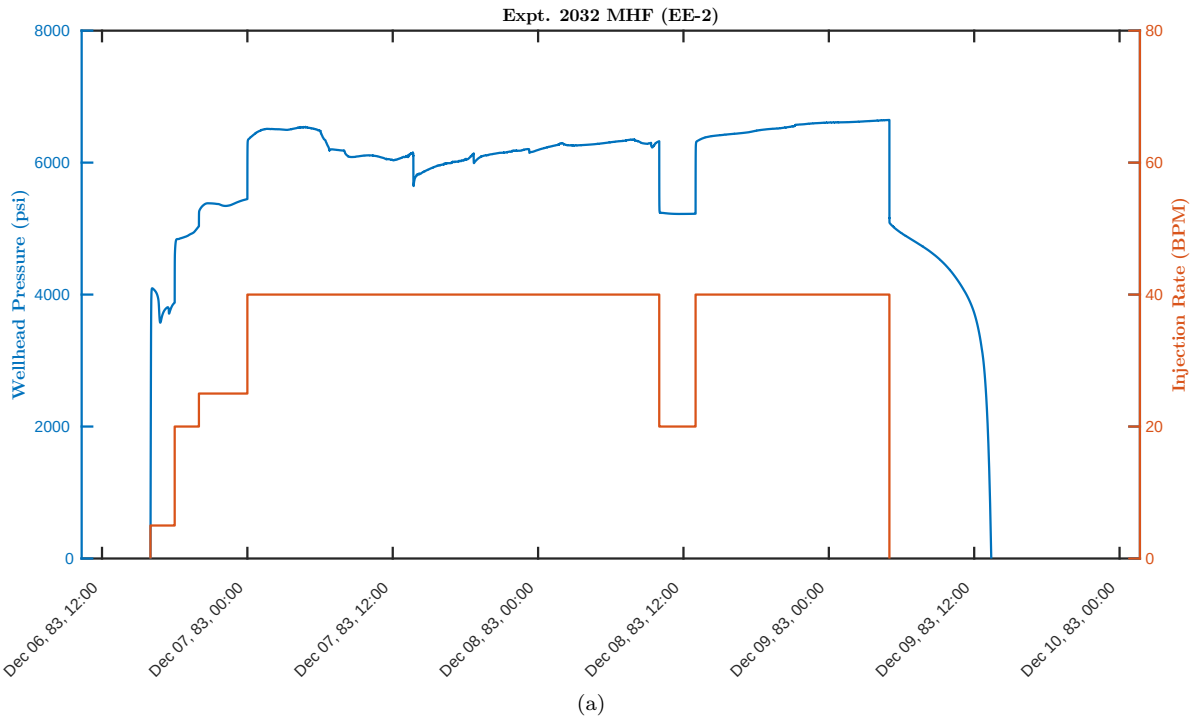

(a)

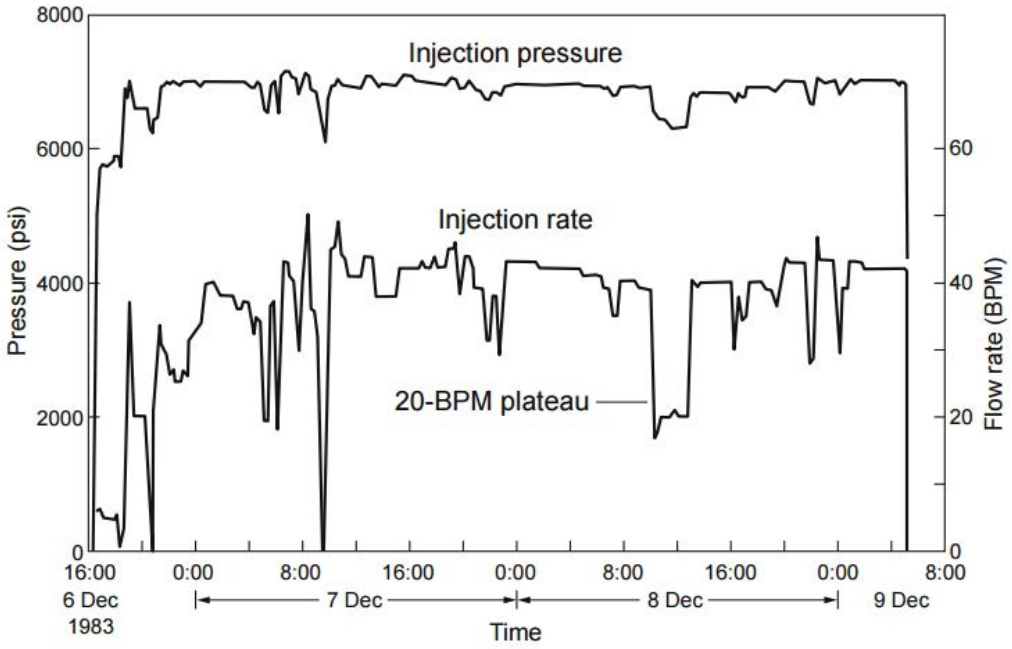

(b) Figure from *Brown et al.* (2012).

Figure 4.13: Comparison of (a) model results and (b) recorded injection rate and pressure data for Expt. 2032 (MHF).

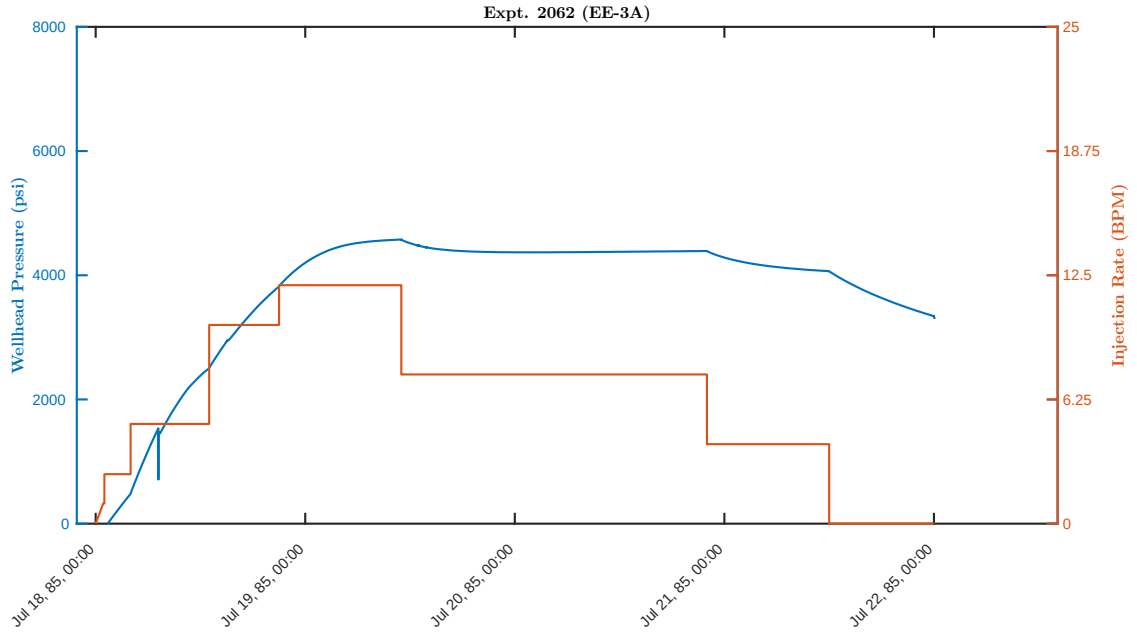

(a)

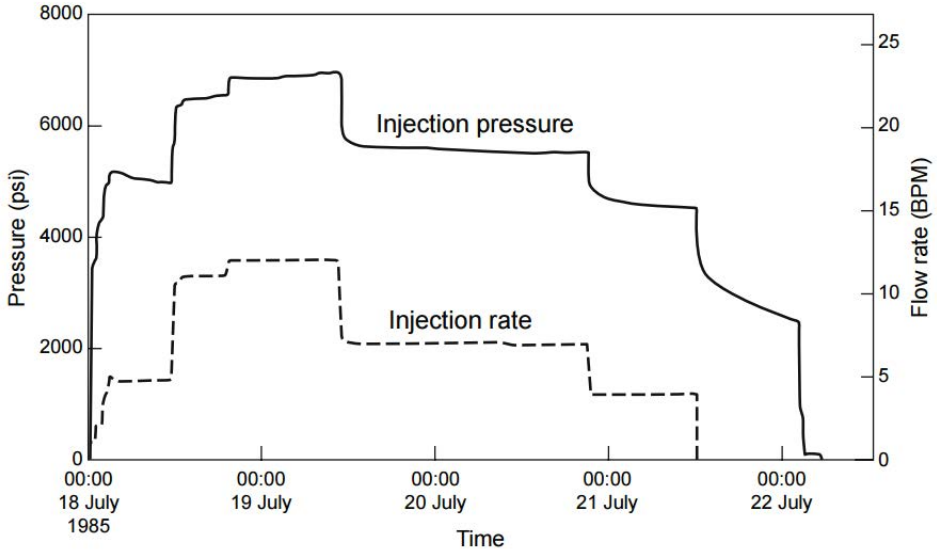

(b) Figure from *Brown et al.* (2012).

Figure 4.14: Comparison of (a) model results and (b) recorded injection rate and pressure data for Expt. 2062.

the ICFT. Important observations included that seismicity only occurred during injection at high pressure and the overall reservoir impedance was reduced (improved) while operating the reservoir at relatively high mean pressure.

The modeling results for the operational controls are compared against the field data in Fig. 4.15. Two periods of relatively steady-state operations were achieved. During the circulation phase, the exact values of injection rate and pressure were more difficult to match than in the stimulation phase. Nonetheless, the trends in the modeled behavior were consistent with the field observations which further justified our conceptual model.

In Fig. 4.16, the locations of microseismicity are compared. Our model matched the behavior accurately in that seismicity did not occur until the injection pressures were increased. Furthermore, seismicity occurred predominantly at the southern edge of the stimulated zone. This behavior is intuitive, because the fluid pressures during the stimulation treatments exceeded those observed during the circulation experiments. Fractures that slipped previously were only able to slip again once they were exposed to relatively high pressure.

For the purposes of our analysis, we defined the reservoir impedance as:

$$i = \frac{p_i - p_p}{q_p}, \tag{4.1}$$

where p_i is the injection pressure, p_p is the production well pressure, and q_p is the volumetric production rate. An important trait of the Fenton Hill reservoir that was recognized during the ICFT was that the reservoir impedance was affected by the mean pressure at which the reservoir was operated. *Brown et al.* (2012) reported a 27% reduction in impedance, and hypothesized that this behavior was caused by the ability for the fracture network to dilate at increased fluid pressure. In our model, this nonlinear behavior was able to be captured through application of Eq. 2.4. In Fig. 4.17, we show the reservoir impedance observed in the model over the duration of the ICFT. A marked reduction in reservoir impedance of 37% occurred immediately following the increase in injection pressure and production backpressure. This improved ability to circulate fluids through the reservoir was sustained throughout the remainder of the ICFT.

4.5.2 LTFT: Flow between Wells EE-3A and EE-2A

There were in actuality three different circulation experiments performed as part of the LTFT experiment at Fenton Hill. The first two occurred during 1992 and 1993. We did not model these two phases of circulation. Our analysis focused on the final phase of the LTFT, which occurred during May through July of 1995. Operations during the LTFT were aimed at assessing the long-term viability of the geothermal system. Well controls were maintained to minimize induced seismicity.

The comparison between modeled and observed operational parameters is shown in Fig. 4.18. The injection well was maintained at relatively constant injection rate and pressure. The production

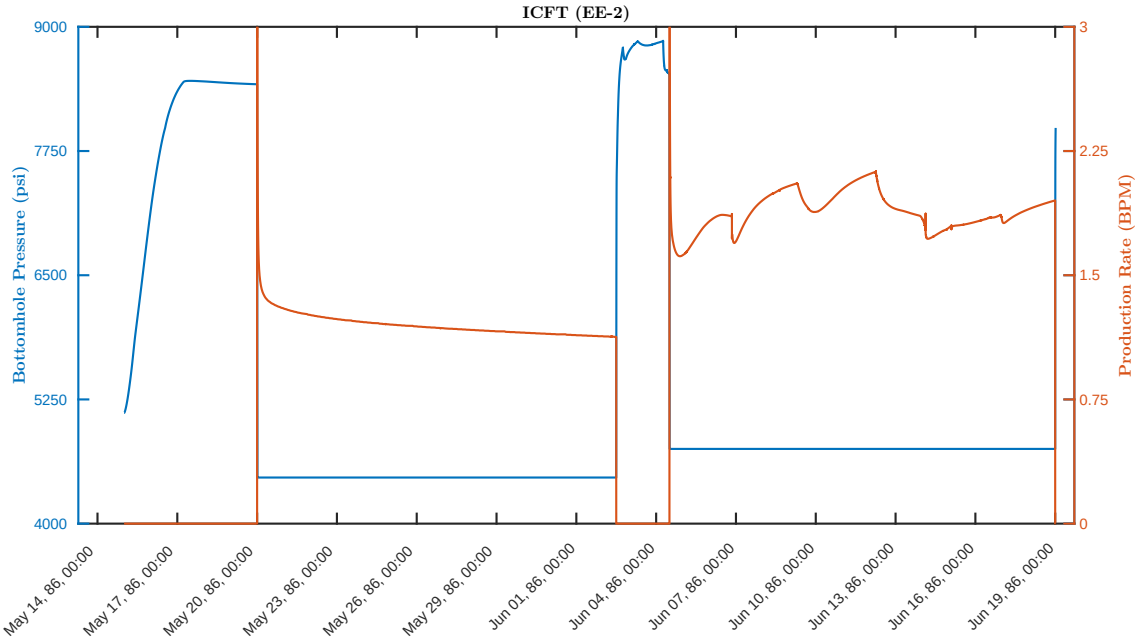
ICFT (EE-2)
Bottomhole Pressure (psi)
Production Rate (BPM)
9000
7750
6500
5250
4000
3
2.25
1.5
0.75
0
May 14, 86, 00:00
May 17, 86, 00:00
May 20, 86, 00:00
May 23, 86, 00:00
May 26, 86, 00:00
May 29, 86, 00:00
Jun 01, 86, 00:00
Jun 04, 86, 00:00
Jun 07, 86, 00:00
Jun 10, 86, 00:00
Jun 13, 86, 00:00
Jun 16, 86, 00:00
Jun 19, 86, 00:00

(a)

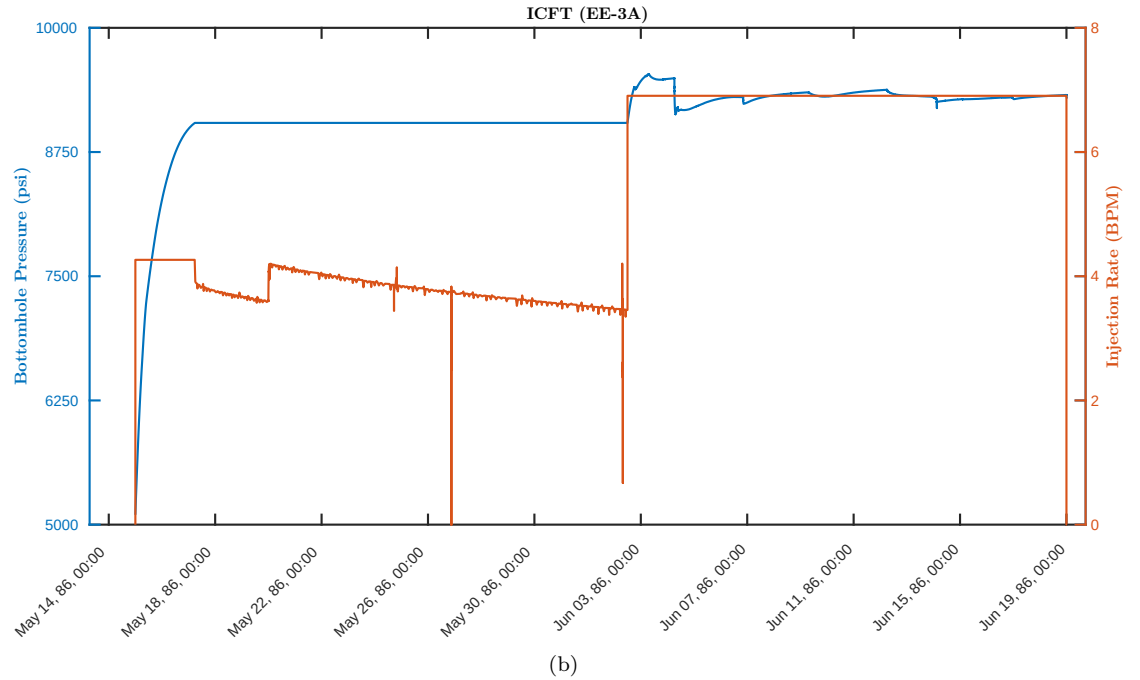
ICFT (EE-3A)
Bottomhole Pressure (psi)
Injection Rate (BPM)
10000
8750
7500
6250
5000
8
6
4
2
0
May 14, 86, 00:00
May 18, 86, 00:00
May 22, 86, 00:00
May 26, 86, 00:00
May 30, 86, 00:00
Jun 03, 86, 00:00
Jun 07, 86, 00:00
Jun 11, 86, 00:00
Jun 15, 86, 00:00
Jun 19, 86, 00:00

(b)

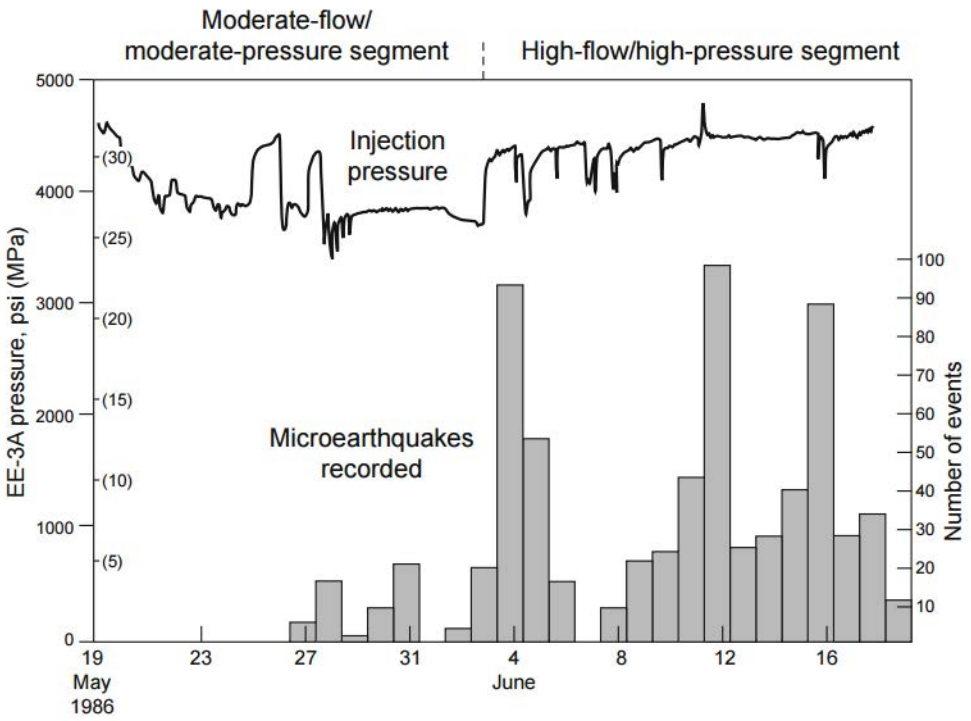

(c) Figure from *Brown et al.* (2012).

Figure 4.15: Comparison of (a) model results for rate and pressure at Well EE-2, (b) model results for rate and pressure at Well EE-3A, and (c) recorded rate and pressure field data for during the ICFT fluid circulation experiment. The ICFT phase involved a low-rate circulation period followed by a period of high-pressure, high-rate circulation between Wells EE-3A and EE-2. At that time during the Fenton Hill project, engineers were attempting to determine whether operating the reservoir at a higher mean pressure improved wellbore deliverability.

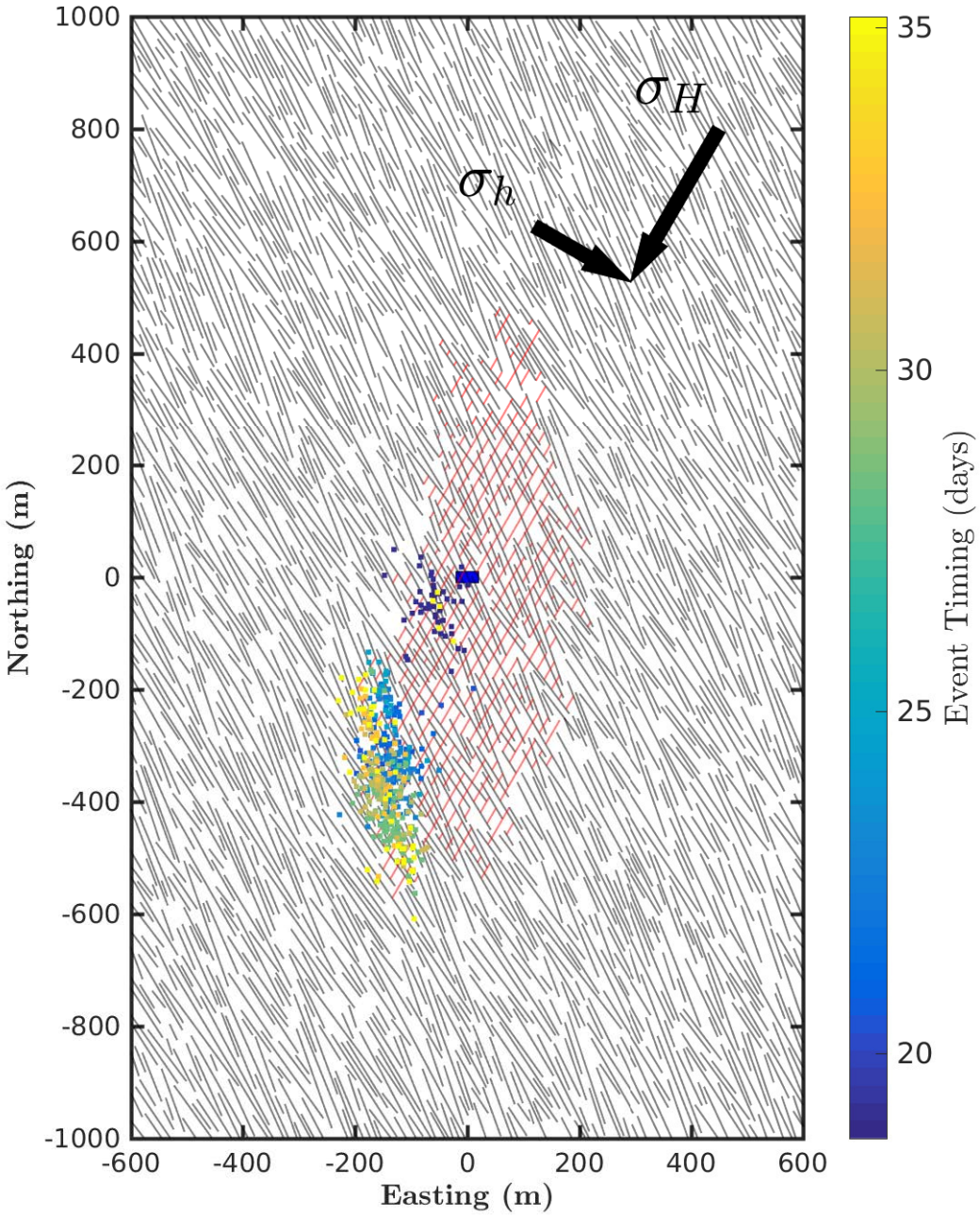
σ_H
σ_h
Northing (m)
Easting (m)
Event Timing (days)
1000
800
600
400
200
0
-200
-400
-600
-800
-1000
-600
-400
-200
0
200
400
600
35
30
25
20

(a)

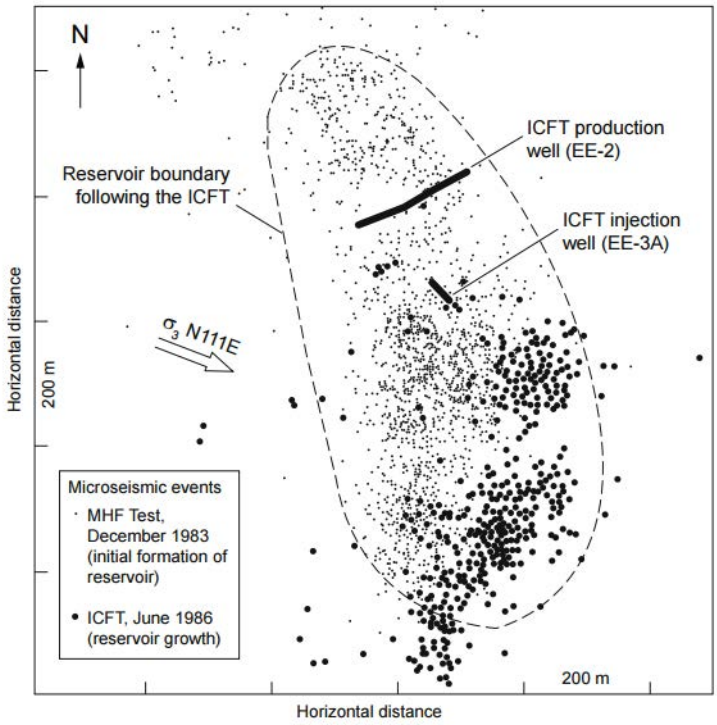

(b) Figure from *Brown et al.* (2012).

Figure 4.16: Comparison between (a) model results of microseismicity and (b) recorded microseismic event locations during the ICFT fluid circulation experiment. Consistent with the field observations, the microseismicity modeled during the ICFT experiment occurred predominantly at the edges of the previously stimulated region following the transition to high-pressure injection.

well backpressure was increased in the middle of the LTFT to test for injectivity changes. We neglected several "load-following" experiments that were designed to test the reservoir's ability to accommodate variable electricity demand by quickly changing the production backpressure.

An interesting observation in the field data is that significant production rates were achieved while operating the production well at a pressure of up to 2200 psi wellhead pressure. This suggests that the bottomhole pressure was significantly higher than the initial reservoir pressure, which has important implications for understanding the hydraulic connection between the two wells. Our model results were unable to match this observation. Specifically, a realistic flow rate was only able to be achieved by operating the production well at pressures much closer to the initial reservoir pressure.

We tested other simulation scenarios (results not shown here) in which the production well was operated at pressures that were similar to the reported field data. In those simulations, fluid was not able to be produced at realistic rates. In fact, by operating the production well at pressures

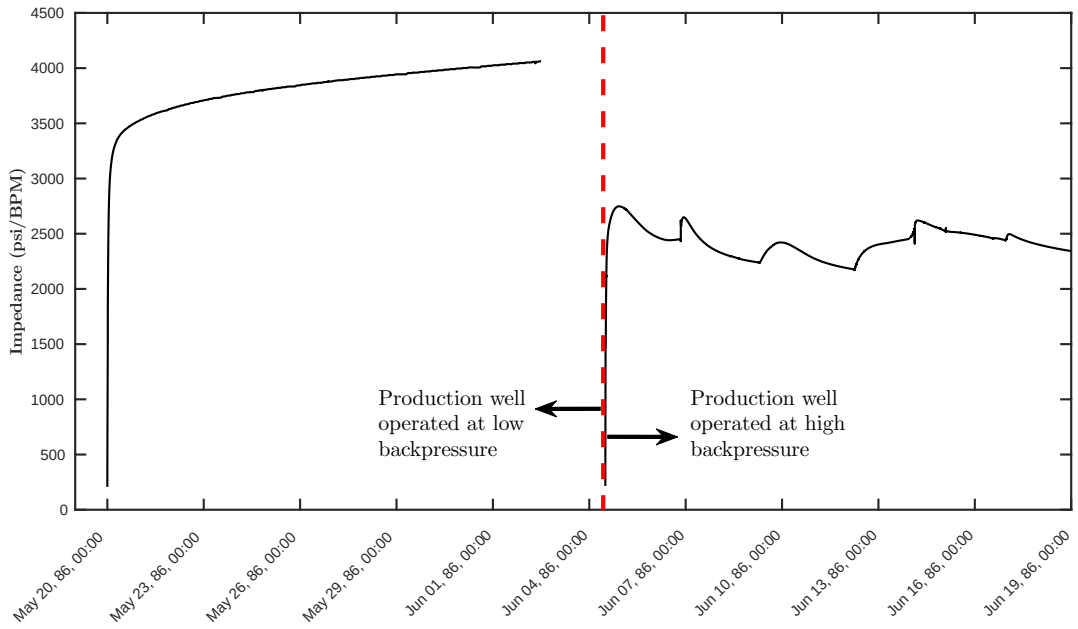

Figure 4.17: Reservoir impedance (calculated as the pressure drop between the injection and production well normalized by the production flow rate) during the ICFT. The impedance was reduced effectively by operating the production well at a higher back-pressure. This behavior was caused by the nonlinear dependence on effective stress of fracture transmissivity.

significantly above the initial reservoir pressure the well was forced to inject fluid. This type of behavior is obviously not consistent with the manner in which the reservoir was operated.

The implication is that the actual hydraulic connection between Well EE-3A and EE-2A must have been much stronger than in our model. The fact the fluid was able to be produced while operating at a wellhead pressure of 2200 psi suggests either a) the reservoir was naturally overpressured at depth, b) the matrix pressure had been pressurized by previous stimulation treatments, or c) the hydraulic connection between the two wells was extremely strong. There is no good evidence supporting a significant natural overpressure. *Brown et al.* (2012) indicated that low flow rates were maintained to pressurize the reservoir for some time around 1990, however, this was five years prior to the LTFT. Therefore, it seems likely that the two wells experienced a direct hydraulic connection involving one or more hydraulic fractures. In this way, the injection well would be able to effectively pressurize the production well enough to permit significant flow rates at elevated pressures. In Sect. 4.8, we will present arguments for why we believe our model was unable to match this behavior, and for why we believe this important observation is entirely supportive of our proposed conceptual model.

A trend that was observed in each of the circulation experiments at Fenton Hill was that the

rate of water loss to the formation (measured as the difference between injected and produced fluid volumes) tended to decline while operating the reservoir at steady-state. The mechanism proposed by *Brown et al.* (2012) was that the leakoff rate into the matrix rock surrounding the fractures would decrease over time as fluid pressure in the matrix rock increased. In Fig. 4.19, we show the fractional water loss rate observed in our simulation during the LTFT. During each phase where the operational controls were maintained relatively constant, the water loss rate was observed to decline up to 10% each month. Comparing the distribution of matrix fluid pressure at the end of the ICFT (Fig. 4.20) and at the end of the LTFT (Fig. 4.21), it is clear that the matrix rock in the region near the stimulated fractures accumulated a significant amount of fluid leakoff during periods of fluid circulation. Our simulation results were consistent with the waterloss mechanism described by *Brown et al.* (2012).

4.6 Investigation of porothermoelastic effects

We performed four sets of simulations to isolate the influence of different physical processes that may have influenced the hydromechanical behavior during stimulation and fluid circulation. The different processes considered were pressurization of the fractures, poroelastic stress, and thermoelastic stress. Case A was the base case simulation in which all physical mechanisms were present. In Case B, both poroelastic and thermoelastic stresses were neglected so that only fracture pressurization was considered. In Case C, fracture pressurization and poroelastic stress were considered. In Case D, fracture pressurization and thermoelastic stress were considered.

In Fig. 4.24, the rate of propagation of microseismicity during the MHF treatment is compared for Cases A though D. It was observed that each of the physical processes considered in the model did influence the seismicity. In Fig. 4.24, the *blue diamonds* represent Case A, the *magenta crosses* represent Case B, the *black circles* represent Case C, and the *red squares* represent Case D. Thermal stresses tended to encourage seismicity to propagate further away from the wellbore. Injection of cold fluid induced less-compressive stresses near the wellbore that improved the mobility of the fluid.

The poroelastic and thermal stresses affected the post shut-in behavior significantly. Cases A was the most consistent with the field observations in that the post shut-in seismicity occurred only at the edges of the stimulated region. In contrast, the post shut-in events were spread across the entire stimulated region for Cases B, C, and D. The combination of poroelastic and thermal stresses discouraged seismicity in the near wellbore region, and encouraged seismicity in the far-field.

The magnitudes of the porothermoelastic stresses were largest at the end of the LTFT due to prolonged circulation. Figures 4.25 through 4.30 show distributions of the induced stresses at the end of the LTFT. The induced stresses were on the order of 1 to 5 MPa. The magnitudes of the stress perturbations were likely underestimated due to discretization effects. *Norbeck et al.* (2014) observed that the EFM discretization strategy tends to underestimate the amount of fluid leakoff

when using a coarse level of grid refinement. Therefore, relatively low matrix fluid pressure produces a weaker source term in the poroelastic calculations. A similar argument holds for the thermoelastic stresses as well. In addition, we used four node quadrilateral finite elements to calculate the induced stresses. *Norbeck and Horne* (2016b) observed that using higher-order finite elements tended to increase the magnitude of the induced stresses. The numerical models in this study were not fully converged to grid refinement, which should be taken into consideration when interpreting the results.

4.7 Alternative conceptual model: interaction with a preexisting fault structure

The purpose of this work was to investigate an alternative conceptual model of the Fenton Hill stimulation treatments. The state of stress at depth was based on the interpretation that pressure-rollover behavior observed in the minifrac tests represented a direct measurement of the least principal stress. In addition, the seismicity was assumed to occur along a preexisting fault structure. In this conceptual model, hydraulic fracture propagation was arrested upon intersecting the preexisting fault structure. Leakoff from the hydraulic fracture into the fault zone triggered the seismicity.

This study can be summarized as follows:

- The fracturing data from nine injection experiments were reinterpreted and were found to be consistent with those reported originally in the literature.
- The mathematical theory of the Carter leakoff model was reviewed, and the model parameters were presented in terms of leakoff from a hydraulic fracture into a permeable fault.
- A numerical model was used to investigate the range of fault hydraulic properties that would accommodate a leakoff rate large enough to prevent hydraulic fracture propagation for the entire pumping duration at Fenton Hill (roughly 60 hours). The hydraulic diffusivity of the fault was well-constrained based on the rate of migration of the microseismic events, which helped to constrain the transmissivity and storativity of the fault. Based on the results of the numerical simulations, the hypothesized mechanism of interaction with a preexisting fault cannot be precluded.

4.7.1 Reinterpretation of fracturing tests

We reinterpreted the hydraulic fracturing rate and pressure data from nine hydraulic fracturing experiments in order to ensure that the depths associated with each stress measurement were accurate. Wellbore completion schematics reported by *Matsunaga et al.* (1983) and wellbore trajectory profiles reported by Brown et al. (2012) were used to identify the injection intervals for each test.

The results of the analysis are presented in Table 4.2 and are illustrated graphically in Fig. 4.31. We found that the depths and bottomhole pressures reported by *Kelkar et al.* (1986) were accurate.

A group of measurements performed at roughly 3.1 km imply a "low" least principal stress gradient of about 13 MPa/km. Other measurements at deeper depths imply a "high" stress gradient of about 19 MPa/km. In Fig. 4.32, the Mohr-circle representations of the state of stress for these two models is shown (stresses were calculated at a depth of 3.6 km). It is clear that the low stress model is consistent with the bounds on stress within the theory of the critically-stressed crust (assuming a friction coefficient $f = 0.7$ and a slight underpressure of $p_0 = 31$ MPa).

In the present study, we assumed that a preexisting fault existed near Well EE–2 that was oriented at N23°W. This fault orientation is illustrated as the blue diamond in Fig. 4.32. This fault is not oriented optimally for shear failure, especially in the high stress model. In fact, injection pressures nearly equal to the least principal stress are required to initiate shear failure on this fault.

Table 4.2: Stress measurement data.

Experiment Label	Well	Openhole Inverval (km)	Rollover Bottomhole Pressure (MPa)	Rate (BPM)
2006	EE–3	3.09 - 3.15	39.5	0.4
2007	EE–3	3.09 - 3.15	41.3	0.75
2011	EE–2	4.25 - 4.36	76.7	0.5
2012	EE–2	4.25 - 4.36	83.3	5.7
2016	EE–2	4.25 - 4.36	81.2	4.8
2018	EE–2	3.46 - 3.60	73.5	1.8
2020	EE–2	3.46 - 3.60	72.8	5.0
2023	EE–3	3.09 - 3.15	44.2	2.4
2025	EE–3	3.35 - 3.44	62.5	2.0

4.7.2 Model constraints

If a fault structure existed in the Fenton Hill site, it must have been relatively isolated and not connected to the far field based on the following lines of evidence:

- The geothermal gradient is conductive, not advective, indicating that no large-scale hydrothermal activity occurs at the site (*Brown et al.*, 2012). Therefore, faults in the Fenton Hill system must not be well-connected.

- During long-term circulation tests, the difference between injected and produced fluid volumes was minimal (*Brown et al.*, 2012). This suggests that fluid losses into the matrix rock or to the far-field was not significant, and therefore the fault structure must have finite extent.

The seismicity can be characterized as a broad cloud of roughly 1 km (north-south) by 1 km (vertical) by 300 m (east-west) dipping slightly to the east (*Phillips et al.*, 1997). The event locations were extremely accurate, with location errors estimated to be 10 to 30 m (*Fehler et al.*, 1987; *Fehler*,

1989; *Phillips et al.*, 1997). The earthquake magnitudes were observed to range between $-3 \leq M \leq 0$ (*Murphy and Fehler*, 1986). This suggests that the entire fault zone was unable to slip coherently (*Fehler*, 1989; *Phillips et al.*, 1997).

In this conceptual model, seismicity was generated by leakoff from the hydraulic fracture into the permeable fault structure. Assuming that this is an appropriate mechanism, the seismicity can provide constraints on the hydraulic properties of the fault. It has been argued that the hydraulic diffusivity of a porous medium, D_H, can be estimated by fitting a curve that is proportional to $\sqrt{D_H t}$ to the leading edge of seismicity propagation in a space-time plot (*Langenbruch and Shapiro*, 2010; *Rothert and Shapiro*, 2007; *Shapiro et al.*, 2005). Based on this approach, *Shapiro et al.* (2005) analyzed the Fenton Hill seismicity and estimated the hydraulic diffusivity to be $D_H = 0.15$ m^2/s. We specified the hydraulic properties of the fault in the numerical model to correspond to this value of diffusivity.

Carter leakoff into fault zones

In the Carter leakoff model (*Economides and Nolte*, 2000), the leakoff rate is largest initially and decays over time as pressure in the porous medium near the hydraulic fracture increases. The fluid leakoff velocity is:

$$v_L = \frac{C_L}{\sqrt{t}} = \left[\frac{\mathrm{m}}{\mathrm{s}}\right], \tag{4.2}$$

where C_L is the Carter leakoff coefficient and t is the time elapsed since the hydraulic fracture intersected the fault. The fault has a vertical height h and a hydraulic aperture e. The total volumetric leakoff rate (accounting for leakoff into the fault from both sides of the hydraulic fracture) is:

$$q_L = \frac{2C_L A}{\sqrt{t}} = \left[\frac{\mathrm{m}^3}{\mathrm{s}}\right], \tag{4.3}$$

where the cross-sectional area of the fault is $A = he$. The mass leakoff rate is:

$$m_L = \rho q_L = \left[\frac{\mathrm{kg}}{\mathrm{s}}\right], \tag{4.4}$$

where ρ is the fluid density.

The Carter leakoff coefficient for diffusion-driven leakoff is:

$$C_L = \sqrt{\frac{k\lambda\phi\beta_t}{\pi}}\Delta p = \left[\frac{\mathrm{m}}{\mathrm{s}^{1/2}}\right], \tag{4.5}$$

where ϕ is fault porosity, k is fault permeability, $\beta_t = \beta_f + \beta_\varphi$ is total compressibility of the fault pore volume and fluid within the fault zone, λ is inverse fluid viscosity, and $\Delta p = p_f - p_0$ is the

pressure drop driving leakoff. The hydraulic diffusivity for flow in porous media is typically written as:

$$D_H = \frac{k\lambda}{\phi\beta_t} = \left[\frac{\mathrm{m}^2}{\mathrm{s}}\right]. \tag{4.6}$$

Substituting the definition of hydraulic diffusivity into Eq. 4.5, the leakoff coefficient is:

$$C_L = k\lambda\sqrt{\frac{1}{\pi D_H}}\Delta p. \tag{4.7}$$

Using the notation for one-dimensional fluid flow along a fault zone introduced in Sects. 2.1 and 6.4, the hydraulic diffusivity for flow along faults can be described alternatively as (see Eq. 6.13):

$$D_H = \frac{T}{S} = \frac{ek\lambda}{E\beta_t}, \tag{4.8}$$

where $T = ek$ is the fault transmissivity, $S = E\beta_t\lambda^{-1}$ is the fault storativity, and E is the fault void aperture. Introducing Eqs. 4.7 and 4.8 into Eq. 4.3 yields an expression for the leakoff rate in terms of the fault transmissivity, storativity, and diffusivity:

$$q_L = \frac{2hT\lambda}{\sqrt{t}}\sqrt{\frac{1}{\pi D_H}}\Delta p \tag{4.9}$$

4.7.3 Results

The hydraulic fracture must have arrested upon intersecting the fault, because otherwise the seismicity would have tended to align in the direction of σ_H. The premise of this study is that the preexisting fault must be able to accommodate a leakoff rate equal to the pumping rate. We investigated whether realistic values of the hydraulic properties of the fault would be consistent with the apparent arrest duration.

Throughout the majority of the hydraulic fracturing treatment the injection rate was roughly 100 kg/s. Assuming a two-winged fracture was forming off the well, the critical leakoff rate necessary to arrest the hydraulic fracture is 100 / 2 = 50 kg/s. It is important to note that the Fenton Hill stimulation treatment was much different from hydraulic fracturing treatments performed today. High-rate, high-pressure injection occurred into a single stage for over 60 hours.

Hydraulic properties of the fault

The Carter leakoff rate (Eq. 4.9) can be used to estimate the time-dependent leakoff rate for a given set of fault properties. The fault storativity, S, is a function of fault porosity, fault rock compressibility, water compressibility, and water viscosity. These properties do not vary largely across

different sites. In this study, we used the fault and water properties assumed by *Townend and Zoback* (2000) to calculate S. Because the hydraulic diffusivity was estimated using the microseismicity as $D_H = 0.15\ \mathrm{m}^2 \cdot \mathrm{s}^{-1}$ based on the method introduced by *Shapiro et al.* (2005), we were able to obtain an estimate for the fault transmissivity. We estimated the fault transmissivity to be $T = 1.5 \times 10^{-15}$ m^3. Important model parameters were as follows:

- Water compressibility: $\beta_\varphi = 5 \times 10^{-10}\ \mathrm{Pa}^{-1}$
- Fault rock compressibility: $\beta_f = 2 \times 10^{-11}\ \mathrm{Pa}^{-1}$
- Water viscosity: $\lambda^{-1} = 1.9 \times 10^{-4}\ \mathrm{Pa} \cdot \mathrm{s}$
- Storage aperture = porosity $\times$ fault zone thickness: $E = \phi W = (0.02)(5\ \mathrm{m}) = 0.1\ \mathrm{m}$
- Fault storativity: $S = E\left(\beta_f + \beta_\varphi\right)\lambda^{-1} = 9.8 \times 10^{-15}\ \mathrm{m} \cdot \mathrm{s}$
- Fault height: $h = 1000\ \mathrm{m}$
- Fault hydraulic diffusivity: $D_H = 0.15\ \mathrm{m}^2 \cdot \mathrm{s}^{-1}$
- Fault transmissivity: $T = D_H S = 1.5 \times 10^{-15}\ \mathrm{m}^3$

Hydraulic fracture arrest duration

In Fig. 4.33, the Carter leakoff rate calculated using Eq. 4.9 is shown for two different sets of fault properties (*blue and red solid lines*). The *black dashed line* is the critical leakoff rate required to arrest the hydraulic fracture. The point at which the Carter leakoff rate drops below the critical leakoff rate was used as a first-order estimate of the arrest duration. The *blue and red stars* indicate the arrest duration modeled in the numerical simulations. The analytical solution slightly underestimated the arrest duration because they permit an unrealistically high leakoff rate at early times.

For the fault properties listed above, the arrest duration was estimated to be roughly 5 to 10 minutes, which is two to three orders of magnitude less than the actual pumping time of 60 hours. In Fig. 4.34, the results of the numerical simulation are illustrated. In the simulation, pumping occurred at a constant rate of 100 kg/s. A two-winged hydraulic fracture propagated away from the wellbore. Upon intersecting the permeable fault, hydraulic fracture propagation was arrested temporarily. However, the arrest only lasted for 13 minutes before the hydraulic fracture continued to propagate for the duration of the simulation. No significant slip along the fault structure occurred. For the fault properties and fault geometry used in this study, the numerical simulations suggest that this conceptual model is unlikely.

The fault transmissivity is perhaps the most influential parameter governing the leakoff rate into the fault. If T is increased by an order of magnitude while holding all other parameters constant, the arrest duration increases by two orders of magnitude due to the $\sqrt{t}$-dependence of the leakoff

rate. The fault diffusivity ($D = T/S = 0.15$ m^2/s) is well-constrained based on the seismicity data. Increasing both T and S by an order of magnitude (maintaining $D_H = 0.15$ m^2/s) suggests an arrest duration of roughly 10 to 15 hours, which is a similar order of magnitude as the total pumping time of 60 hours. Assuming that S is an order of magnitude larger does not seem unreasonable, and could be attributed to a higher rock compressibility or higher storage aperture than listed above. Given this set of hydraulic properties, it was found that the conceptual model is plausible.

4.8 Discussion

In Sects. 4.4 and 4.5, it was demonstrated that the numerical modeling results exhibited several distinct traits that were consistent with the behavior observed during hydraulic stimulation and fluid circulation field experiments at Fenton Hill. Therefore, the modeling results provide plausible insights into the nature of how fractured subsurface systems respond to reservoir engineering operations. Understanding the fundamental physical processes that control fractured reservoir behavior has profound implications across a broad spectrum of subsurface energy fields including induced seismicity hazard, geothermal energy, unconventional oil and gas recovery, and CO_2 sequestration.

The modeling results suggest that the Fenton Hill reservoir experienced nonlinear permeability changes that depended on the evolution of the state of stress throughout the reservoir. Fractures were able to dilate as the effective normal stress acting on the fractures decreased during injection. This type of deformation depended on the orientation of the fractures and was reversible. In addition, hydraulic fractures were able to propagate through the reservoir while injecting at pressures above the least principal stress. The hydraulic fractures created new hydraulic pathways which caused an irreversible change in reservoir permeability. The overall stimulated reservoir system was comprised of both natural and hydraulic fractures, which each contributed to the reservoir response uniquely throughout different phases of reservoir operation.

In Fig. 4.35, we show the evolution of the stimulated fracture surface area and the stimulated fracture volume during Expt. 2032 (MHF), Expt. 2062, the ICFT, and the LTFT. Natural fractures were assumed to be stimulated when they experienced a threshold change in fluid pressure of 1.0 MPa. Hydraulic fractures contributed to the stimulated area and volume totals at the instant they nucleated. The major conclusion drawn from Fig. 4.35 is that the connected fracture surface area was dominated by the natural fractures, and the storage volume was dominated by the hydraulic fractures.

Referencing Fig. 4.6, the preexisting natural fractures existed pervasively throughout the reservoir at a predominant orientation of NNW-SSE and were closely spaced. Hydraulic fractures only propagated a short distance (several tens of meters) before terminating against nearby natural fractures, and therefore provided a relatively small fraction of the connected fracture surface area as

the stimulated region grew. However, the hydraulic fractures were essential to success of the stimulation treatment because they provided the new flow connections with natural fractures that did ultimately improve the connected fracture surface area. Heat recovery from geothermal reservoirs is known to be influenced significantly by the surface area available for heat transfer to occur between the working fluid flowing though the fractures and the surrounding rock (*Juliusson*, 2012; *Magnusdottir*, 2013). The ability to recognize the functionality of different fracture sets will assist a characterization of the heat transfer surface area in EGS reservoirs.

The natural fractures were oriented oblique to the principal stresses, while the hydraulic fractures were necessarily oriented perpendicular to the least principal stress. This affected the magnitude of the normal stress acting on each of the fracture sets. The hydraulic fractures bore a lower normal stress, and were therefore able to dilate significantly at relatively low pressure. The ability for the hydraulic fractures to deform easily in the opening-mode direction allowed them to store the majority of the fluid volume in the reservoir at any given time. *Brown et al.* (2012) hypothesized a similar mechanism, but speculated that the two different fracture sets were both preexisting natural fractures. Our modeling results support the *Brown et al.* (2012) storage mechanism except for that newly formed hydraulic fracture are more consistent with other field observations.

Characterizing the fluid storage volume is important for understanding the residence time of the fluids as they circulate through the reservoir. At Fenton Hill, successive tracer tests performed during the ICFT indicated that the storage volume was increasing over time (see Fig. 7-12 in *Brown et al.* (2012)). In Figs. 4.15, it was observed during the ICFT that roughly doubling the injection rate only provided a modest increase in the production rate. In Fig. 4.35, we observe an immediate increase in the storage volume accommodated by the natural fractures in concert with the operational change. The hydraulic fractures were compliant enough to absorb most of the additional flow. Recognizing that this type of nonlinear reservoir response is possible will help to inform reservoir engineering decisions.

It is important to consider alternative hypotheses which may be consistent with the field observations. Our conceptual model relied on the interpretations of the stress state provided by *Barton et al.* (1988), *Brown* (1989), and *Kelkar et al.* (1986). There was disagreement between *Brown* (1989) and *Kelkar et al.* (1986) on the magnitude of the least principal stress derived from minifrac tests performed at the site. Ultimately, we chose to use the relatively low stress gradient of 13 MPa/km suggested by *Brown* (1989) rather than the value of 19 MPa/km suggested by *Kelkar et al.* (1986). In our model, the fracture opening pressure observed in the stimulation treatments corresponded to the magnitude of normal stress resolved on the fractures, which was used to constrain the orientation of the natural fracture set (N23°E). If we had adopted the larger stress gradient in our model, then the least principal stress at depth would have been estimated to be roughly 69 MPa. This stress value could have been consistent with the fracture opening pressure, but it would require fractures that were oriented roughly perpendicular to the least principal stress (i.e., fractures in the

direction of the maximum principal stress which was N30°E). In this case, it is conceivable that the microseismic could would have propagated predominantly in the direction of N30°E, which was not observed. Of course, we must also consider that uncertainty exists in the wellbore breakout interpretation performed by *Barton et al.* (1988) in which the orientations of the principal stresses were estimated.

An important observation at Fenton Hill was that injection pressure was significantly larger than the least principal stress, but hydraulic fractures did not initiate at the wellbore. *Baumgartner and Zoback* (1989) observed this behavior in a shallow vertical wellbore completed in gneiss, and attributed the inability to form a hydraulic fracture to the high tensile strength of the rock. At the same site, *Baumgartner and Zoback* (1989) reported that a subhorizontal plane of weakness was able to be opened without the formation of a hydraulic fracture (the least principal stress was vertical at that site). The Fenton Hill reservoir was a fractured granitic reservoir. Similar behavior has been interpreted at other EGS projects in granite reservoirs including Hijiori, Ogachi, Le Mayet de Montange, and Rosemanowes, and Cooper Basin (*Baisch et al.*, 2015; *Cornet and Morin*, 1997; *Holl and Barton*, 2015; *McClure and Horne*, 2014a; *Pine and Batchelor*, 1984; *Sasaki*, 1998). At Cooper Basin, Australia, the stimulation of well Jolokia 1 behaved in a manner contradictory to most other stimulation treatments at the site (*Baisch et al.*, 2015; *Holl and Barton*, 2015). At Jolokia 1, fluid pressures exceeded the least principal stress by at least 10 to 20 MPa, but the well only achieved injection rates on the order of 1 L/s (only 380 m^3 of fluid were injected over the 8 day injection period), suggesting perhaps that significant hydraulic fracturing did not occur (*Baisch et al.*, 2015). It is not apparent whether this behavior occurs in other types of formations.

If the conceptual model proposed and validated in this study is representative of the true behavior in fractured EGS reservoirs, then the modeling results have important implications for the design of EGS stimulation treatments in the future. First and foremost, the high sensitivity of the reservoir behavior to the in-situ state of stress necessitates the application of techniques that are able to obtain high quality stress measurements. In addition, reservoir engineering well tests must be designed and implemented in order to diagnose a particular reservoir's susceptibility to different types of stimulation mechanism. For example, *McClure and Horne* (2014b) advocated for performing controlled injection experiments in which the injection pressure is maintained below the magnitude of the least principal stress in order to preclude hydraulic fracturing, thereby unambiguously testing for shear-stimulation-enhanced permeability. Devoting the time and resources to characterize the state of stress and stimulation mechanism properly early on is likely to improve the technical and economic viability of future EGS projects.

4.9 Concluding remarks

In this work, we performed an investigation of the Fenton Hill, New Mexico, USA Enhanced Geothermal System (EGS) test site. Our goal was to develop an improved understanding of the geologic structure and hydromechanical behavior of fractured geothermal reservoirs. Using interpretations of the data sets recorded during several field experiments at Fenton Hill, we designed a conceptual model of the geologic structure and stimulation mechanism at the site. We hypothesized that stimulation (i.e., permeability enhancement) occurred though a mixed-mechanism process caused by mechanical opening of natural fractures and propagation of hydraulic splay fractures. We applied a numerical model that coupled fluid flow, heat transfer, elasticity, and fracture propagation in order to validate the hypothesis.

During the stimulation phase, our simulation results were consistent with observations recorded during the actual field experiments in three distinct ways:

1. Extremely low injectivity at Well EE-2 was observed until reaching a threshold injection wellhead pressure of 5500 psi, whereupon injectivity increased significantly.

2. Low injectivity (at low pressure) at Well EE-2 was observed consistently throughout multiple stimulation treatments. That is, near wellbore permeability enhancement following each stimulation treatment was not permanent.

3. An overall North-South migration of microseismicity was observed. This was despite of the fact that injection occurred at pressures significantly above the fracturing pressure, which would tend to cause hydraulic fractures to propagate in the direction of the maximum principal stress (N30°E at Fenton Hill).

Our simulation results demonstrate that several different independent hydromechanical observations could be explained reasonably by the mixed-mechanism stimulation conceptual model. To model the spatial pattern of microseismicity, it was important that hydraulic fractures sometimes terminated against the natural fractures. The observations could not be explained by a pure mode-I hydraulic fracture conceptual model (because the microseismic cloud would have been oriented predominantly N30°E instead of N-S) or a pure shear stimulation conceptual model (because the injectivity of the natural fractures intersecting Well EE-2 was not enhanced by prior stimulation treatments).

Following the stimulation treatments, fluid circulation through the reservoir was modeled. During the fluid circulation phase, our simulation results were consistent with the reported data in four distinct ways:

1. The overall reservoir impedance was improved by operating the production well at higher back-pressure.

2. The accessible reservoir volume grew larger over time.

3. The difference between injected and produced fluid volumes reduced over time.

4. Thermal breakthrough was not observed over the duration of circulation considered.

The goal of the US Department of Energy Geothermal Technologies Office code comparison study was to obtain a sense of the range of conceptual models that are able to reproduce the observed data. Given that our modeling results for both the stimulation phase and the fluid circulation phase were generally consistent with the field observations, we submit these modeling results in defense of one conceptual model of the Fenton Hill EGS reservoir geologic structure and stimulation mechanism. Our model was based on several plausible assumptions (most importantly, interpretations of the state of stress at depth), which affected the simulation results significantly. We recognize that sufficient uncertainty in the state of stress is present that other models cannot be precluded.

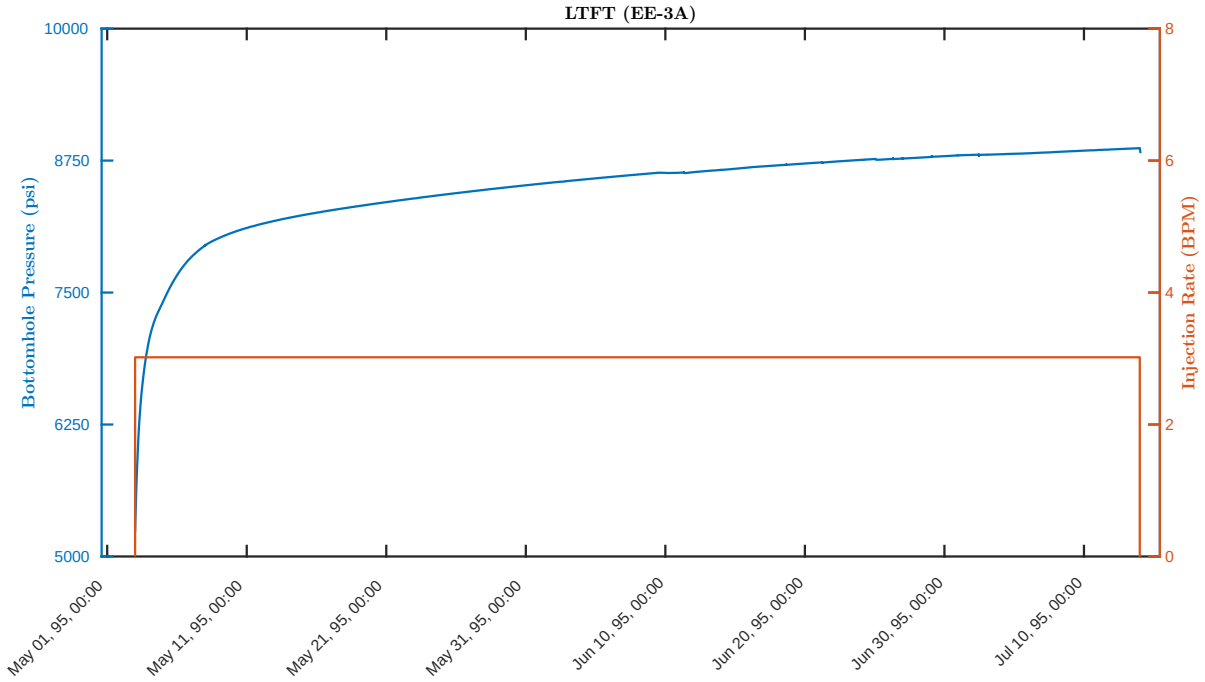
LTFT (EE-3A)
Bottomhole Pressure (psi)
Injection Rate (BPM)
10000
8750
7500
6250
5000
8
6
4
2
0
May 01, 95, 00:00
May 11, 95, 00:00
May 21, 95, 00:00
May 31, 95, 00:00
Jun 10, 95, 00:00
Jun 20, 95, 00:00
Jun 30, 95, 00:00
Jul 10, 95, 00:00

(a)

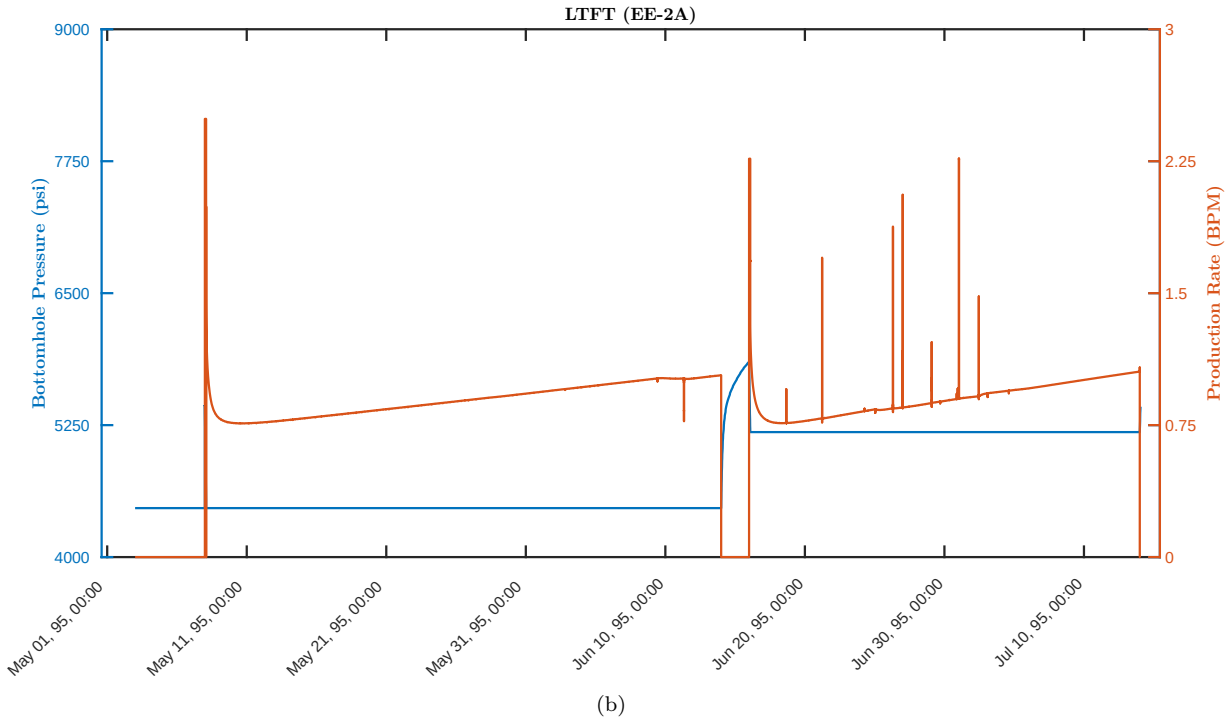
LTFT (EE-2A)
Bottomhole Pressure (psi)
Production Rate (BPM)
9000
7750
6500
5250
4000
3
2.25
1.5
0.75
0
May 01, 95, 00:00
May 11, 95, 00:00
May 21, 95, 00:00
May 31, 95, 00:00
Jun 10, 95, 00:00
Jun 20, 95, 00:00
Jun 30, 95, 00:00
Jul 10, 95, 00:00

(b)

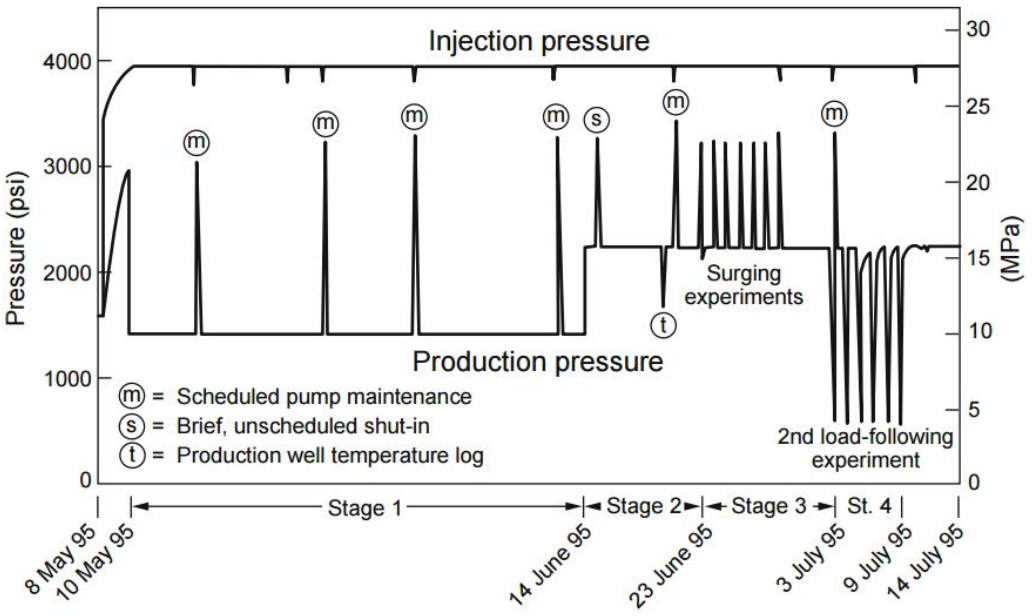

(c) Figure from *Brown et al.* (2012).

Figure 4.18: Comparison of (a) model results of rate and pressure at Well EE-3A, (b) model results of rate and pressure at Well EE-2A, and (c) recorded rate and pressure field data during the LTFT fluid circulation experiment. During the LTFT experiment, flow occurred between Wells EE-3A and EE-2A.

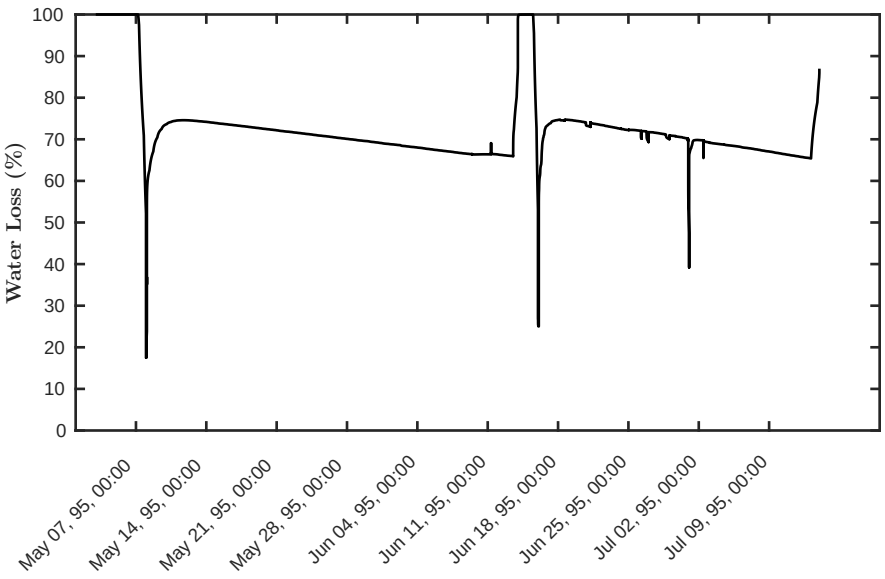

(a)

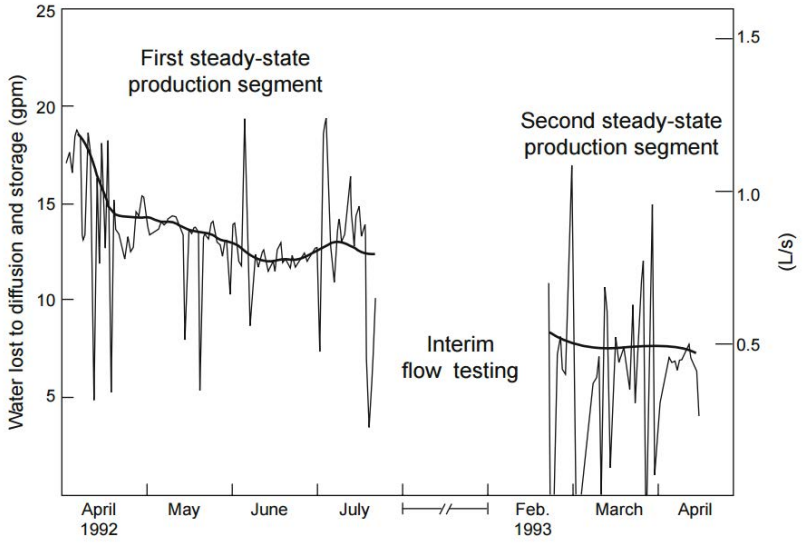

(b) Figure from *Brown et al.* (2012).

Figure 4.19: Fractional water loss observed during the LTFT (calculated as the difference between injected and produced fluid volumes). (a) Model results during the LTFT. (b) Field data recorded during a circulation experiment performed during 1992-1993. The trend of decline in waterloss rate over time was replicated by the model.

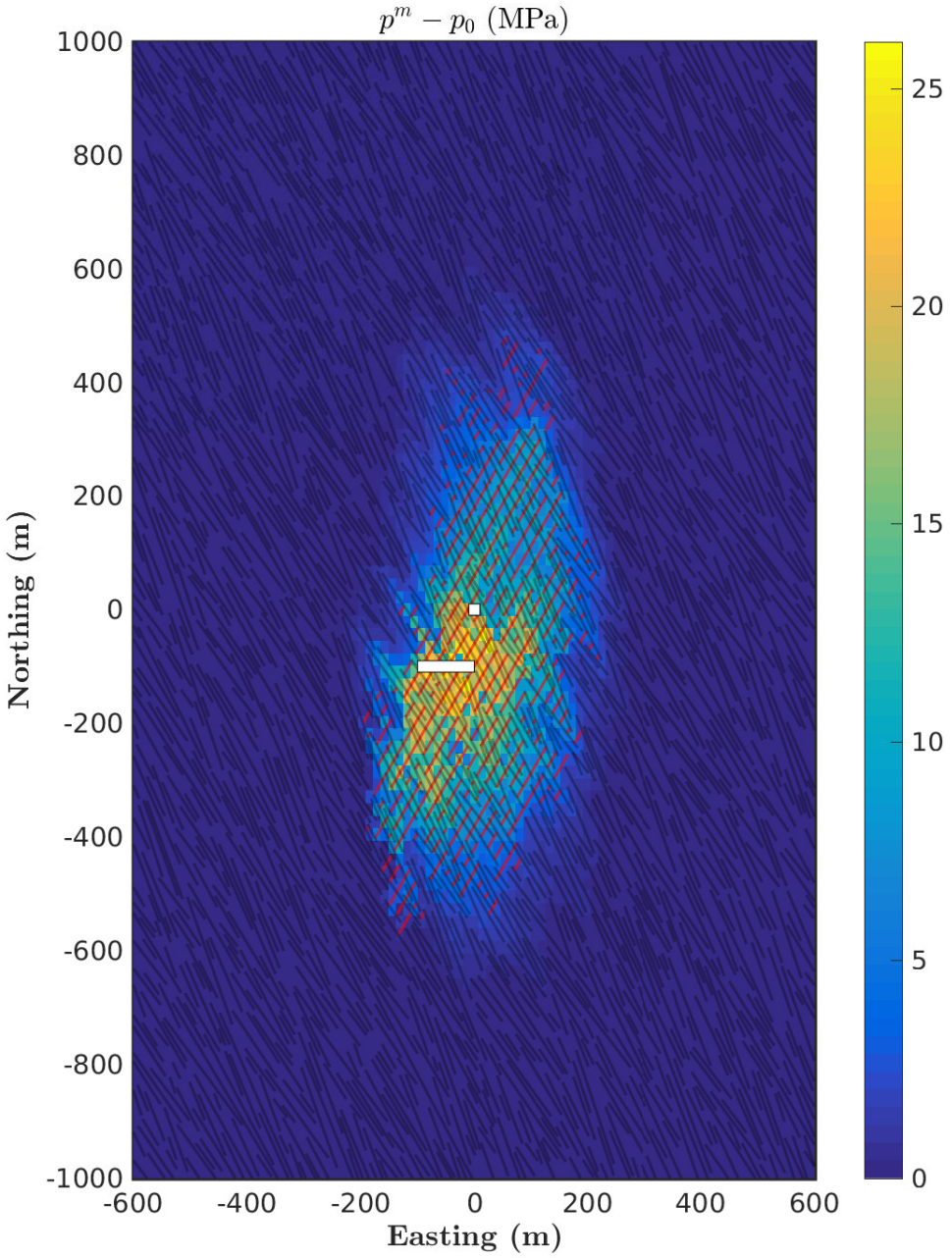

Figure 4.20: Distribution of matrix fluid pressure at the end of the ICFT.

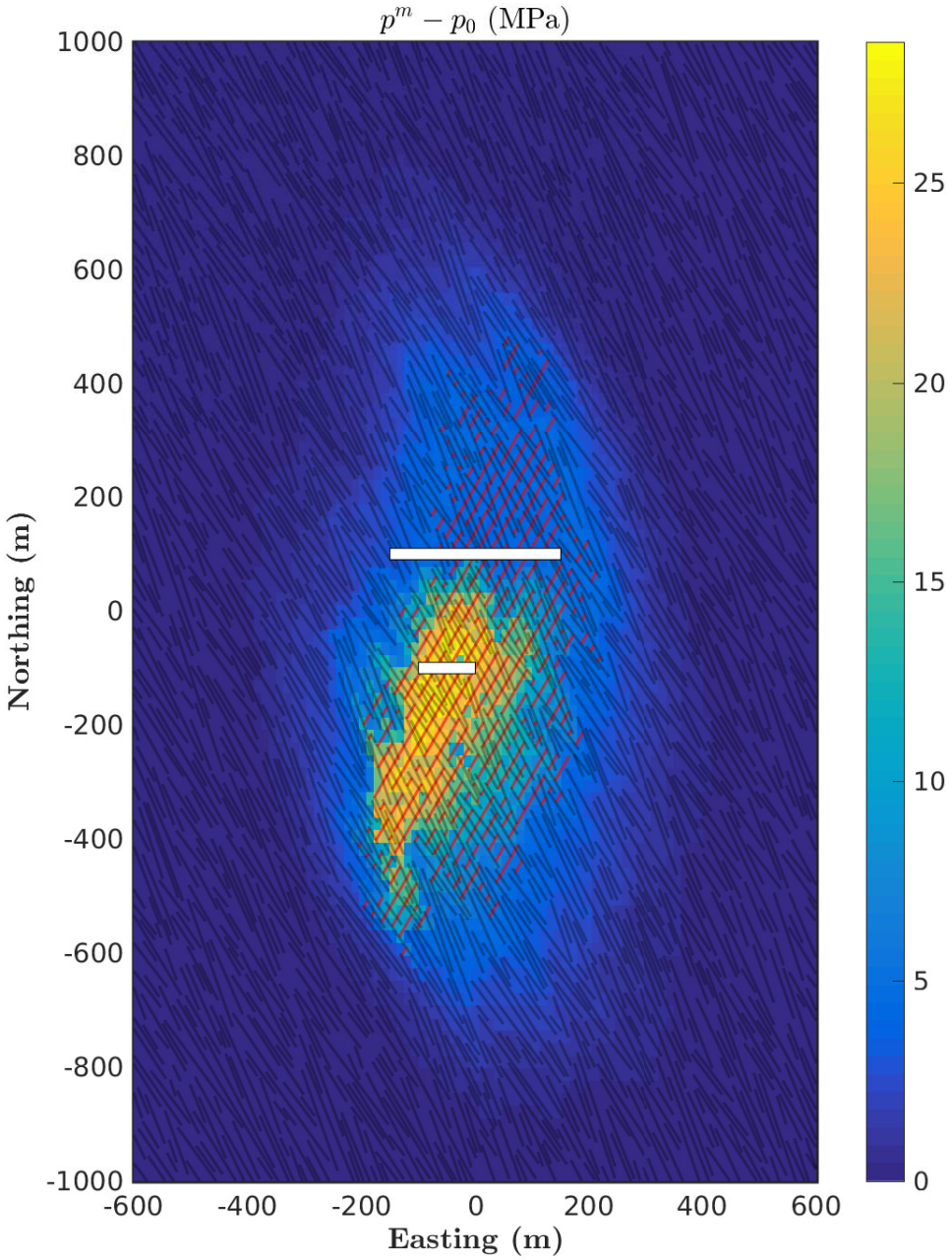

Figure 4.21: Distribution of matrix fluid pressure at the end of the LTFT.

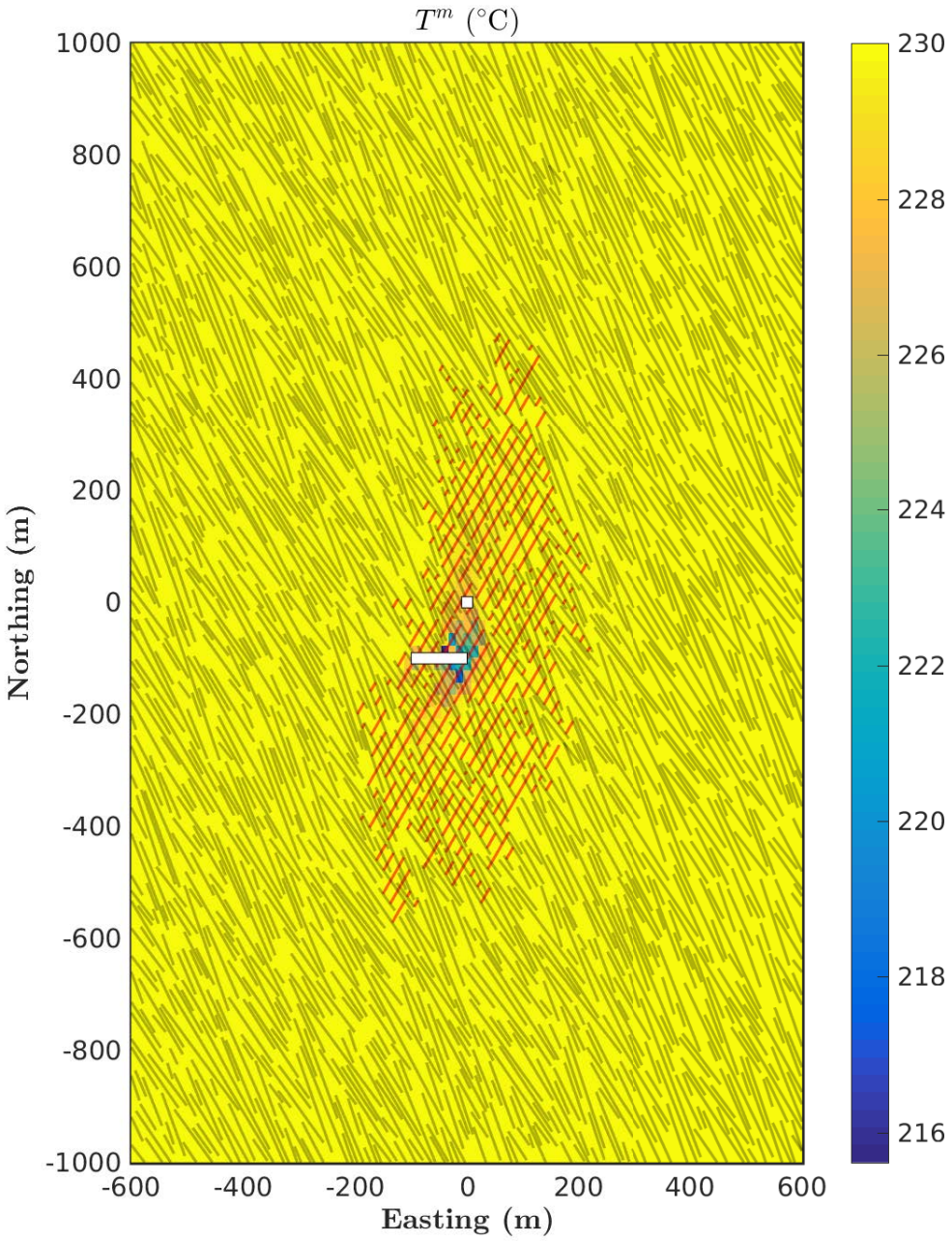

Figure 4.22: Distribution of matrix temperature at the end of the ICFT.

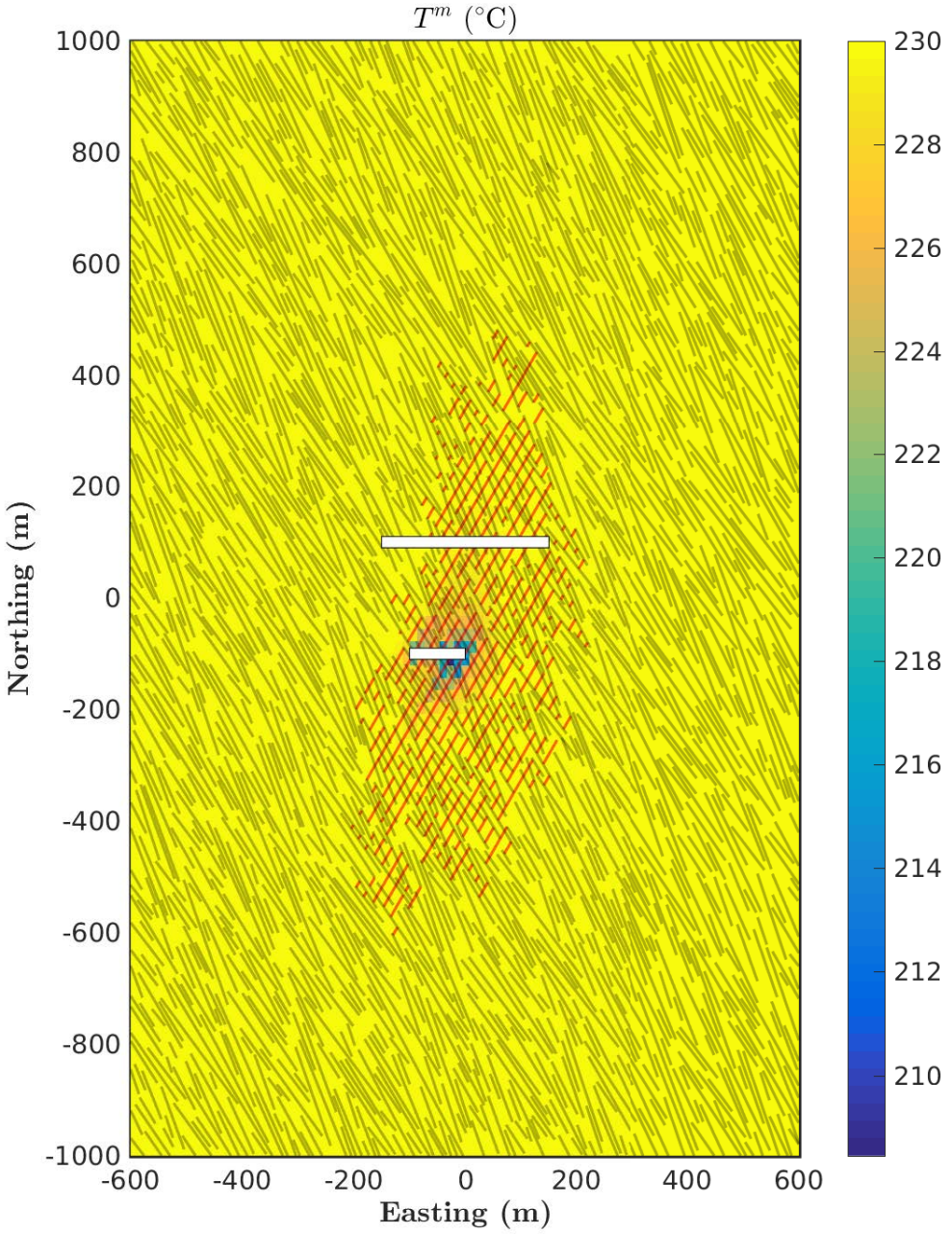

Figure 4.23: Distribution of matrix temperature at the end of the LTFT.

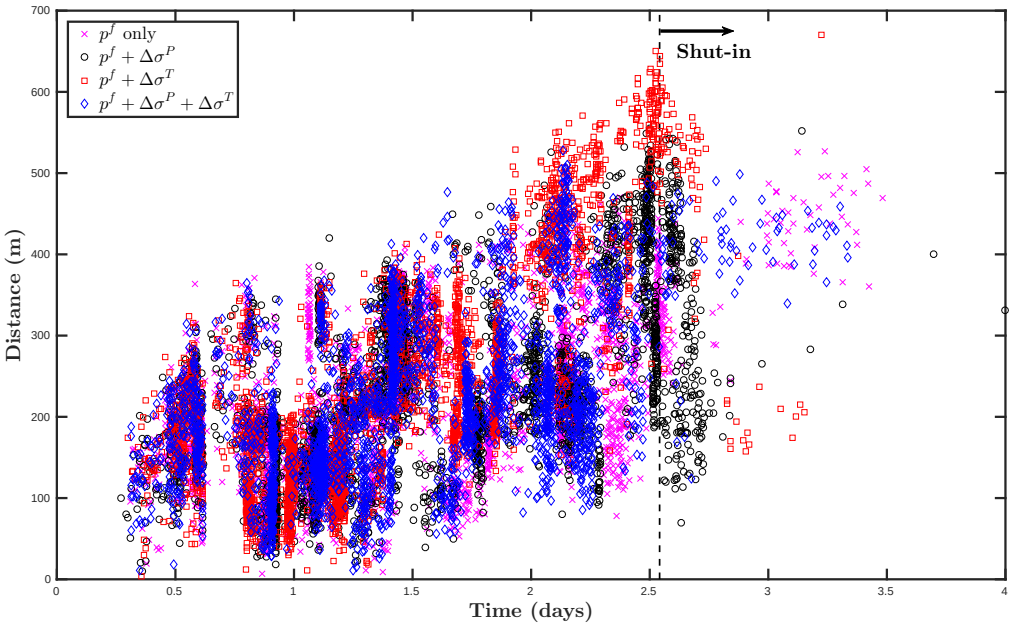

Figure 4.24: Comparison of rate of propagation of microseismicity during the MHF treatment for Cases A through D.

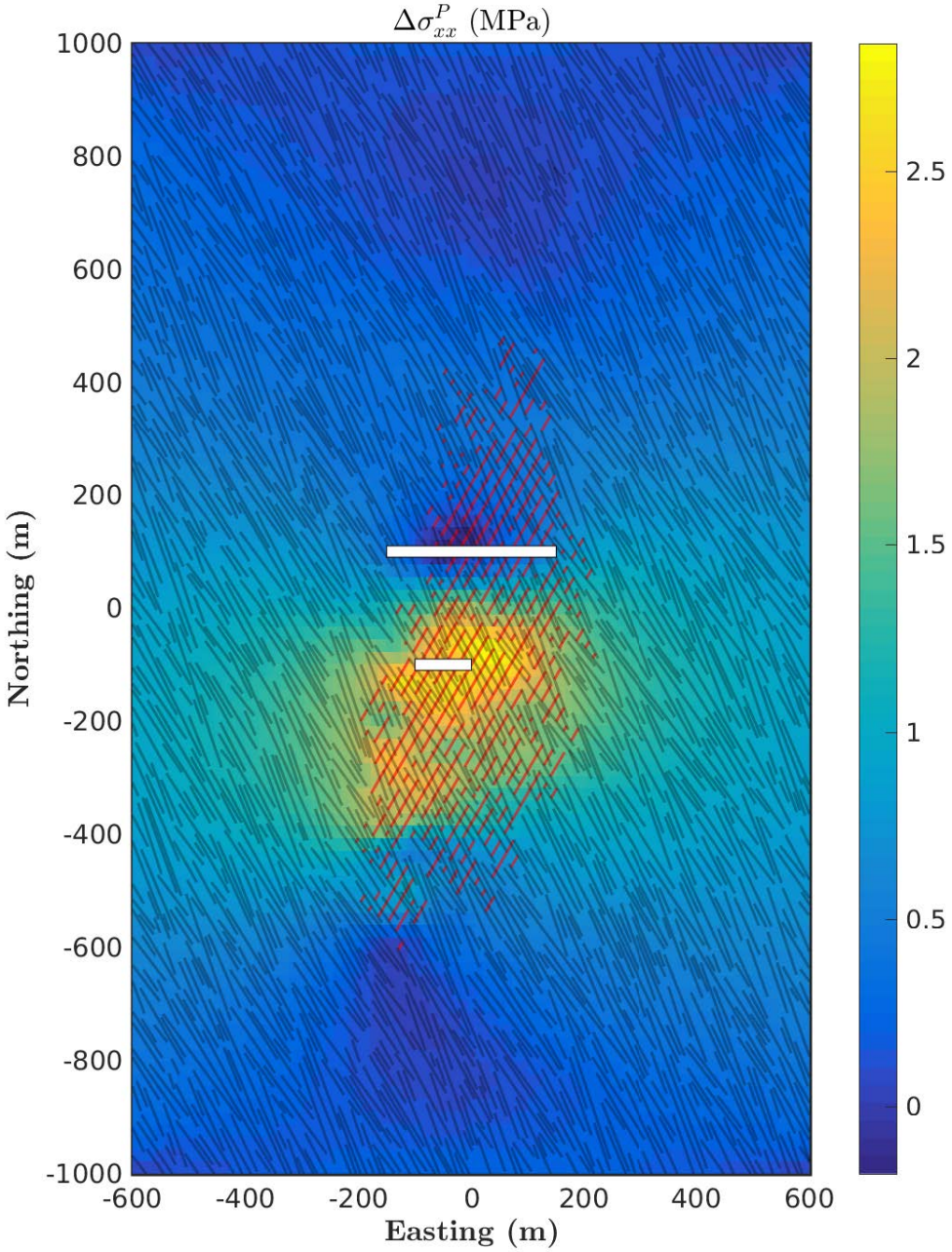

Figure 4.25: Distribution of the poroelastic stress component $\Delta\sigma_{xx}^{P}$ at the end of the LTFT.

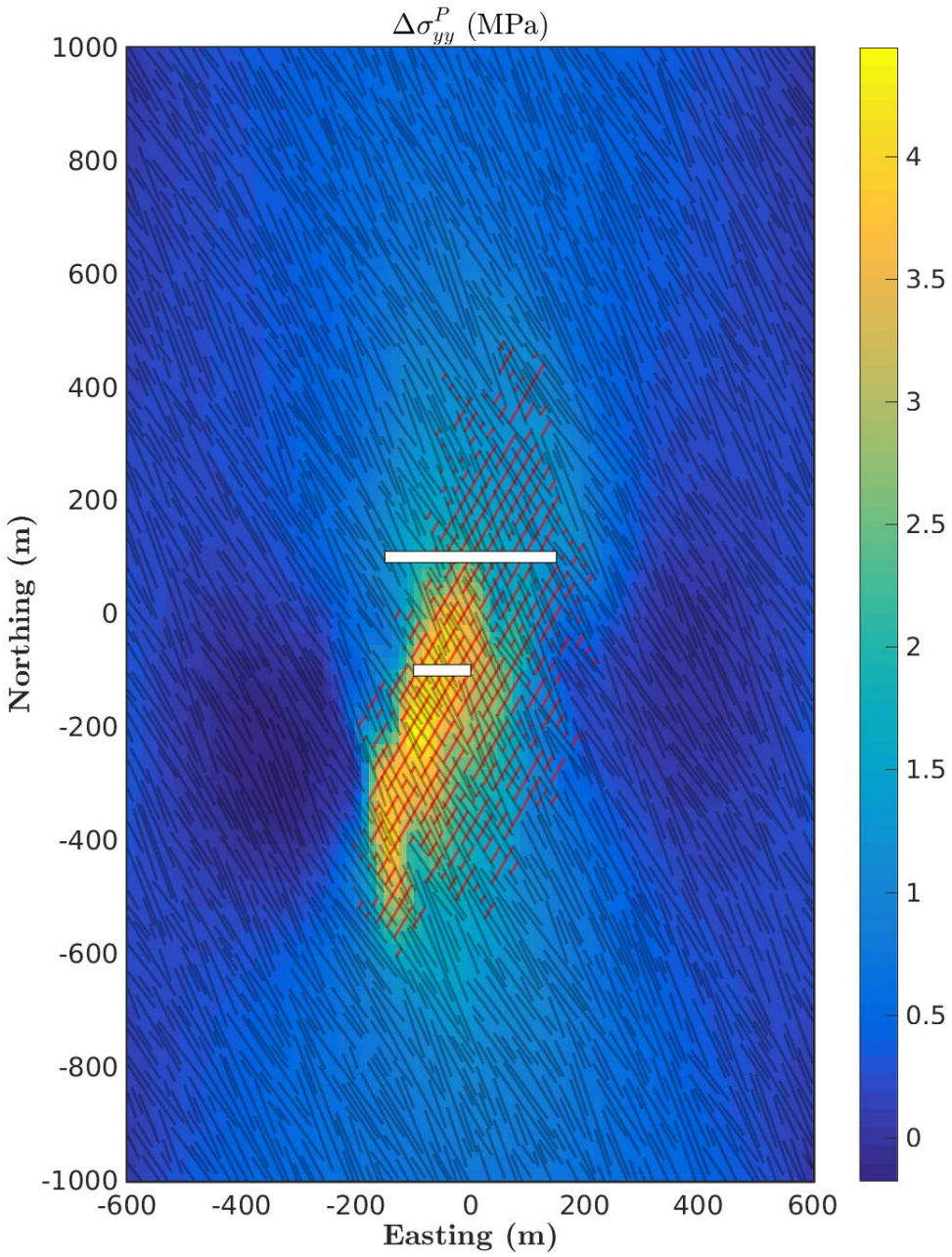

Figure 4.26: Distribution of the poroelastic stress component $\Delta\sigma_{yy}^{P}$ at the end of the LTFT.

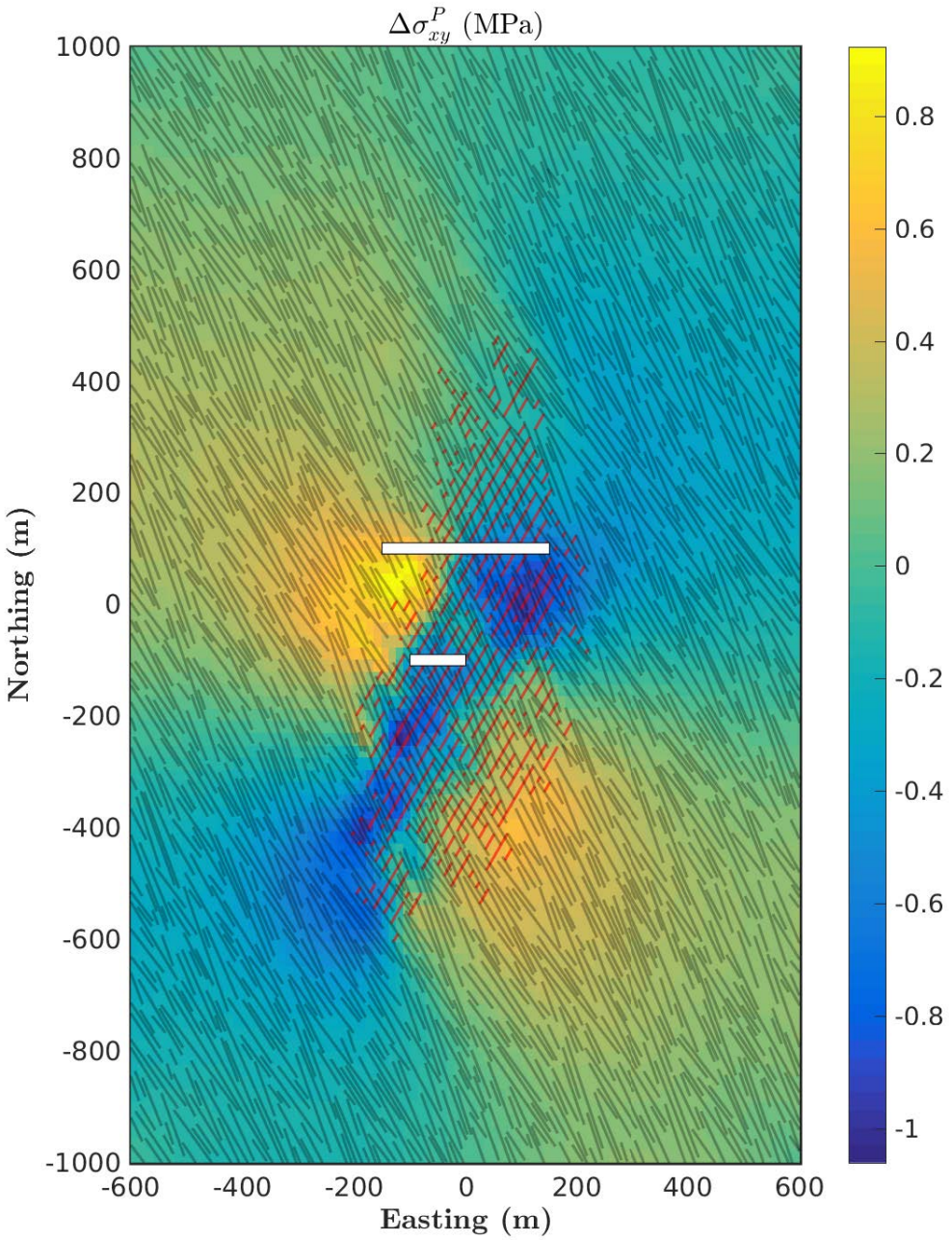

Figure 4.27: Distribution of the poroelastic stress component $\Delta\sigma_{xy}^{P}$ at the end of the LTFT.

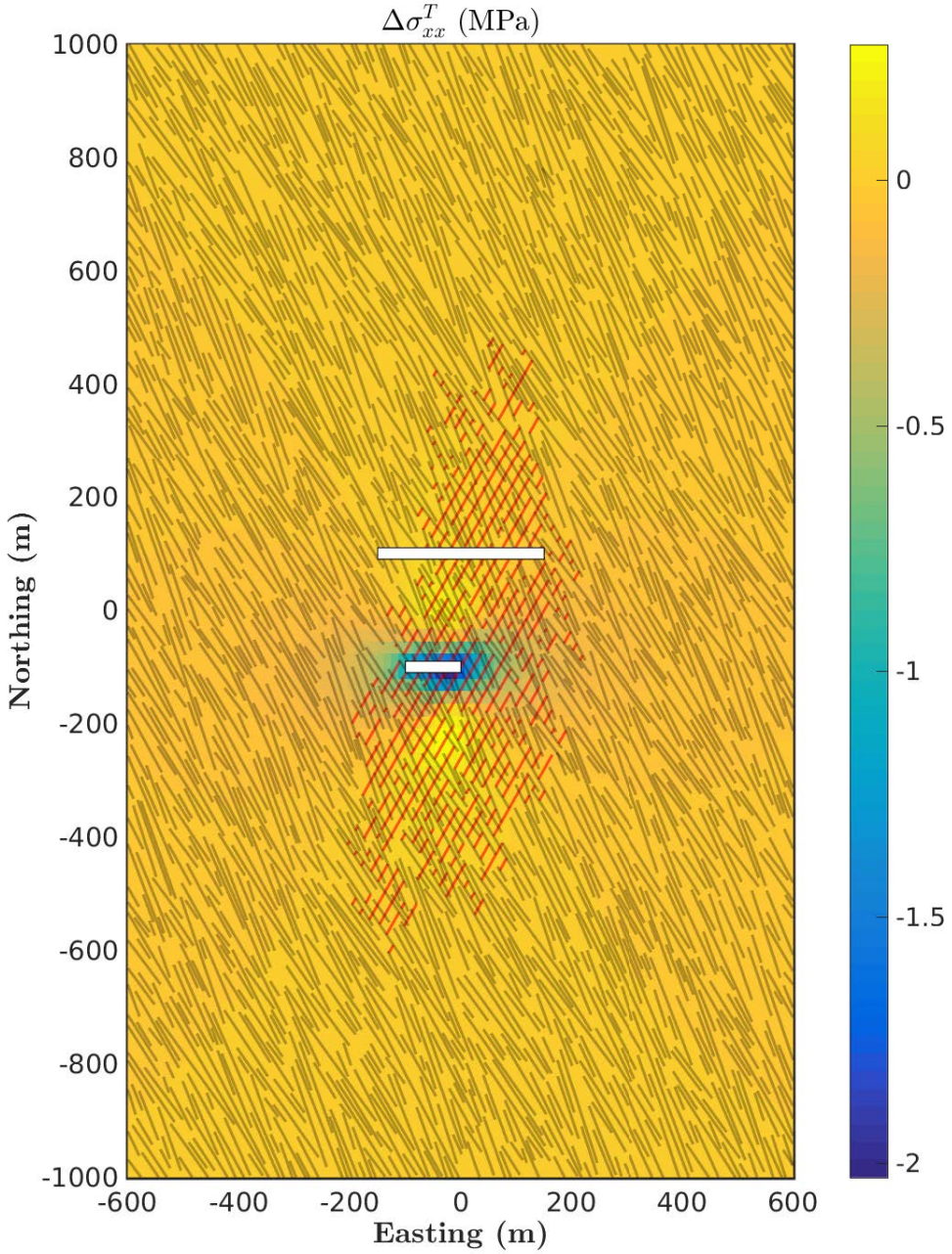

Figure 4.28: Distribution of the thermoelastic stress component $\Delta\sigma_{xx}^{T}$ at the end of the LTFT.

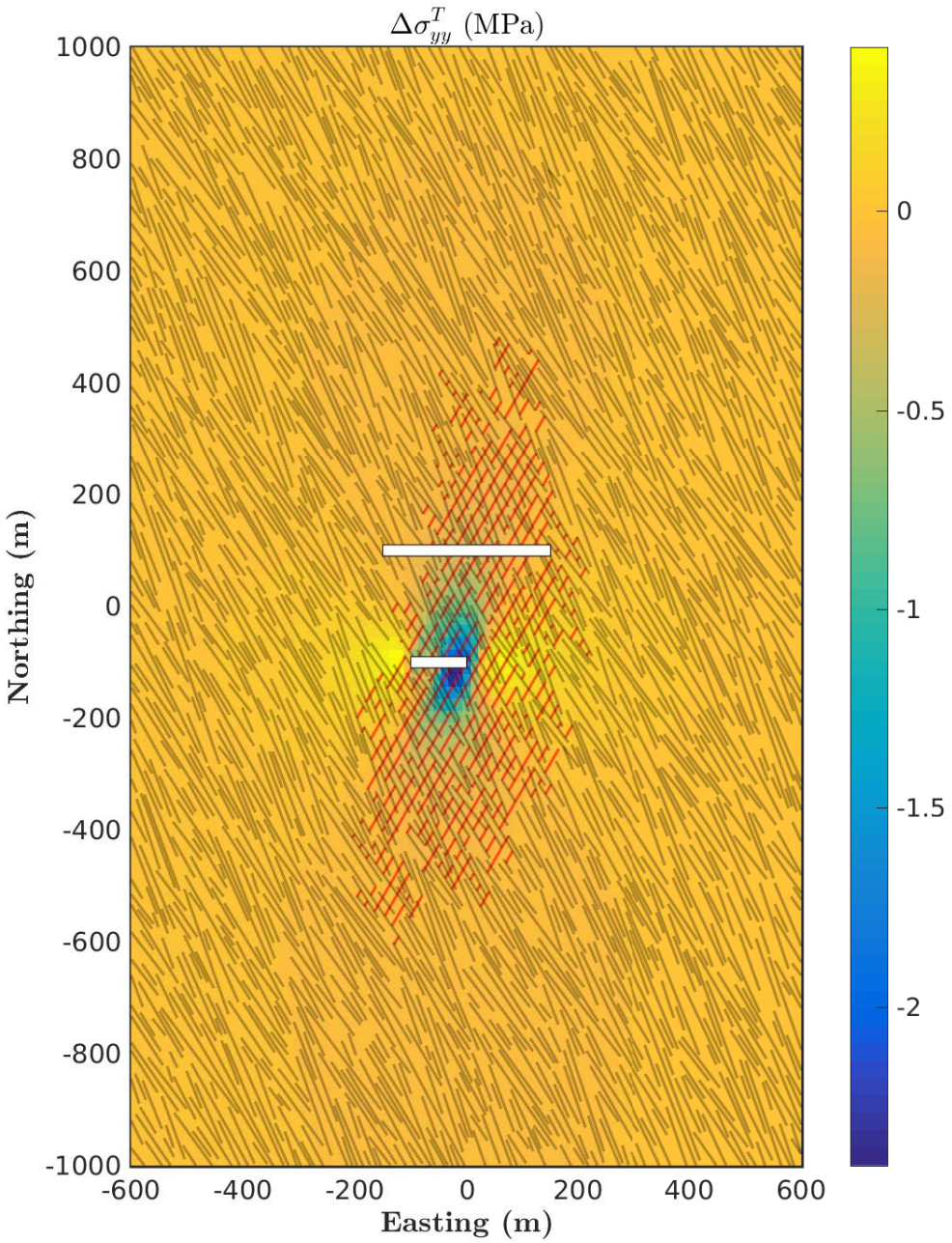

Figure 4.29: Distribution of the thermoelastic stress component $\Delta\sigma_{yy}^{T}$ at the end of the LTFT.

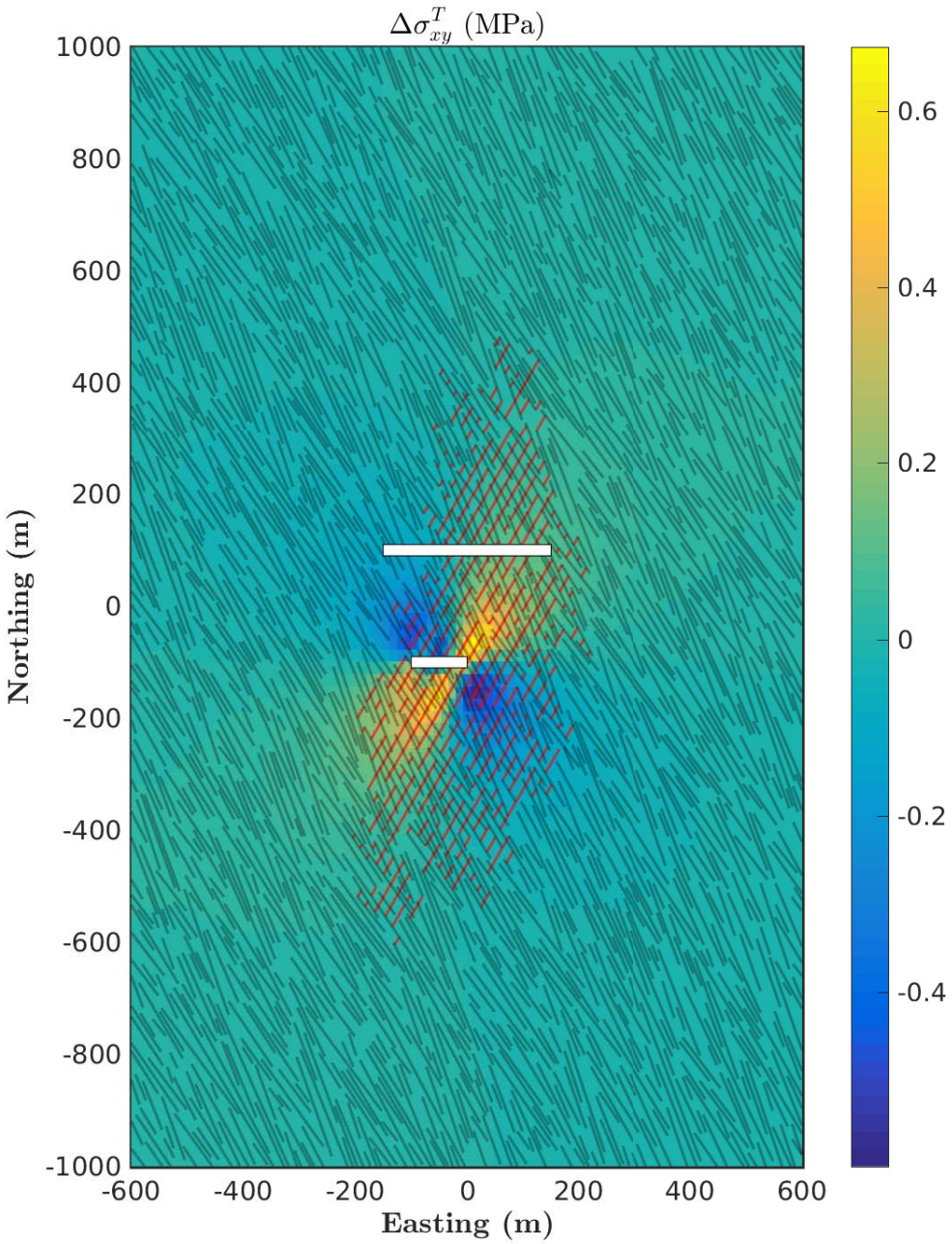

Figure 4.30: Distribution of the thermoelastic stress component $\Delta\sigma_{xy}^{T}$ at the end of the LTFT.

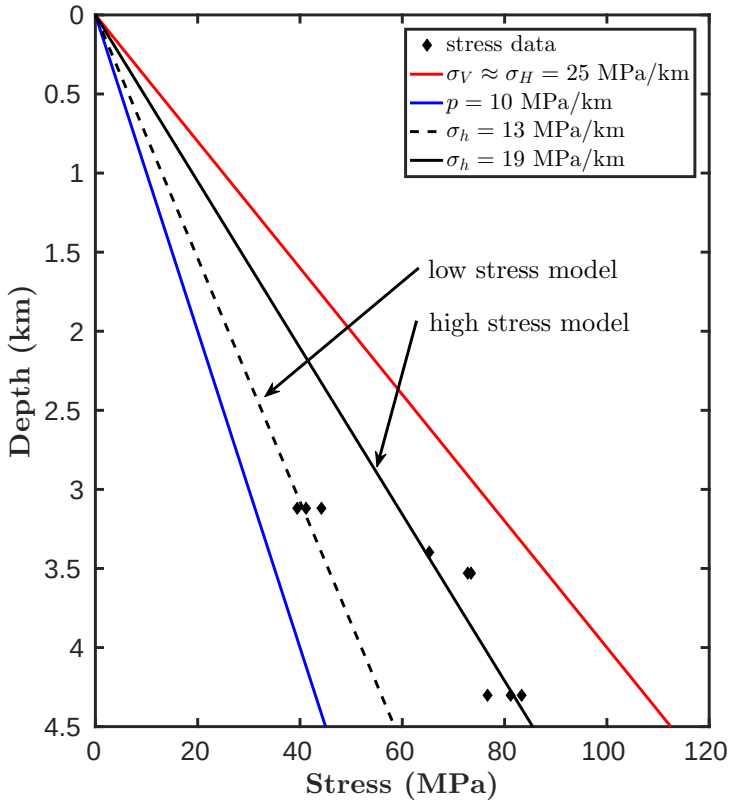

Figure 4.31: Stress profiles at Fenton Hill. The black diamonds represent the measurements of the least principal stress based on the fracturing tests (after *Kelkar et al.* (1986)).

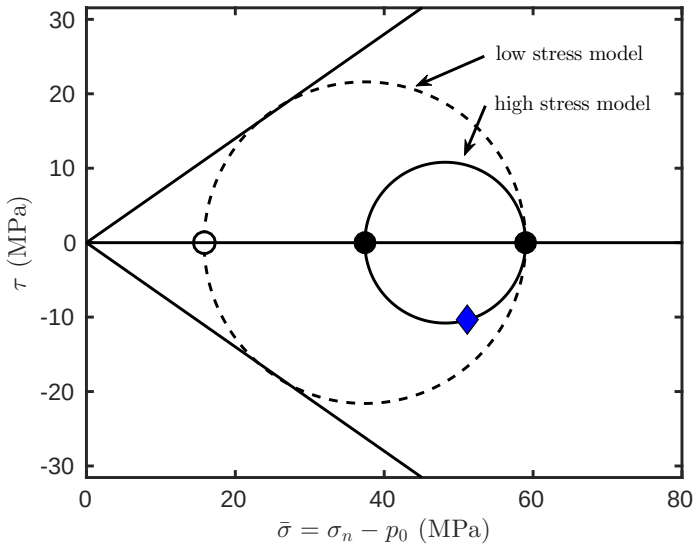

Figure 4.32: Mohr-circle representation of the state of stress at the model depth of 3.6 km. The solid circle represents the high stress model, and the dashed circle represents the low stress model.

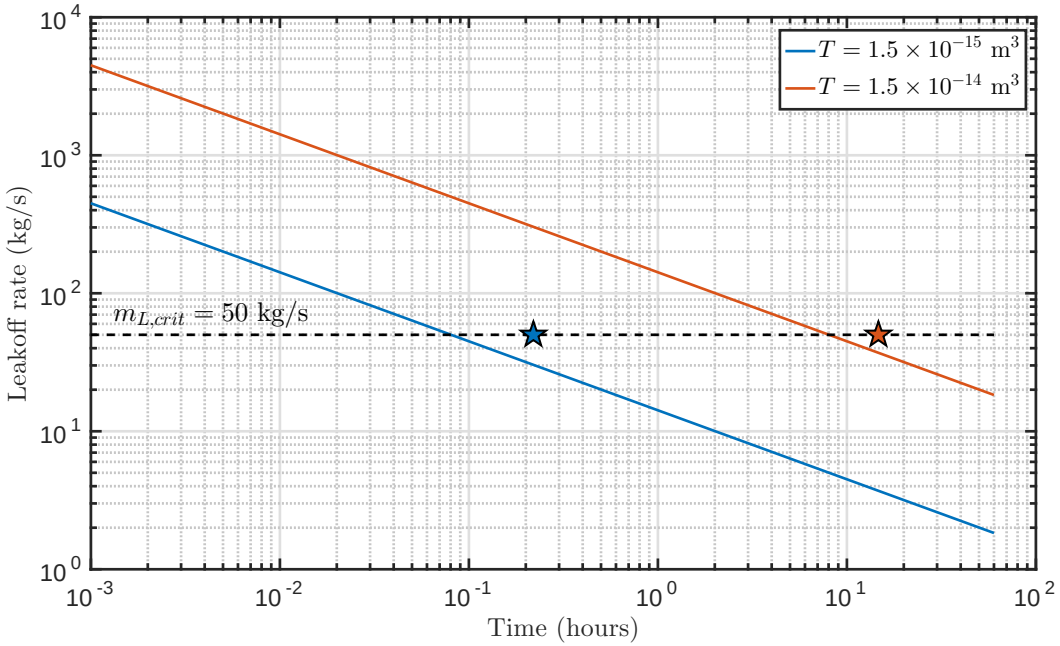

Figure 4.33: Carter leakoff rate for faults with different values of transmissivity (the faults each have the same diffusivity, $D_H = 0.15$ m$^2 \cdot$ s^{-1}). The leakoff rate is largest initially, but then decays as $m_L \sim t^{-1/2}$. The dashed line represent the critical leakoff rate required to arrest the hydraulic fracture. The stars represent the arrest duration calculated using the numerical model.

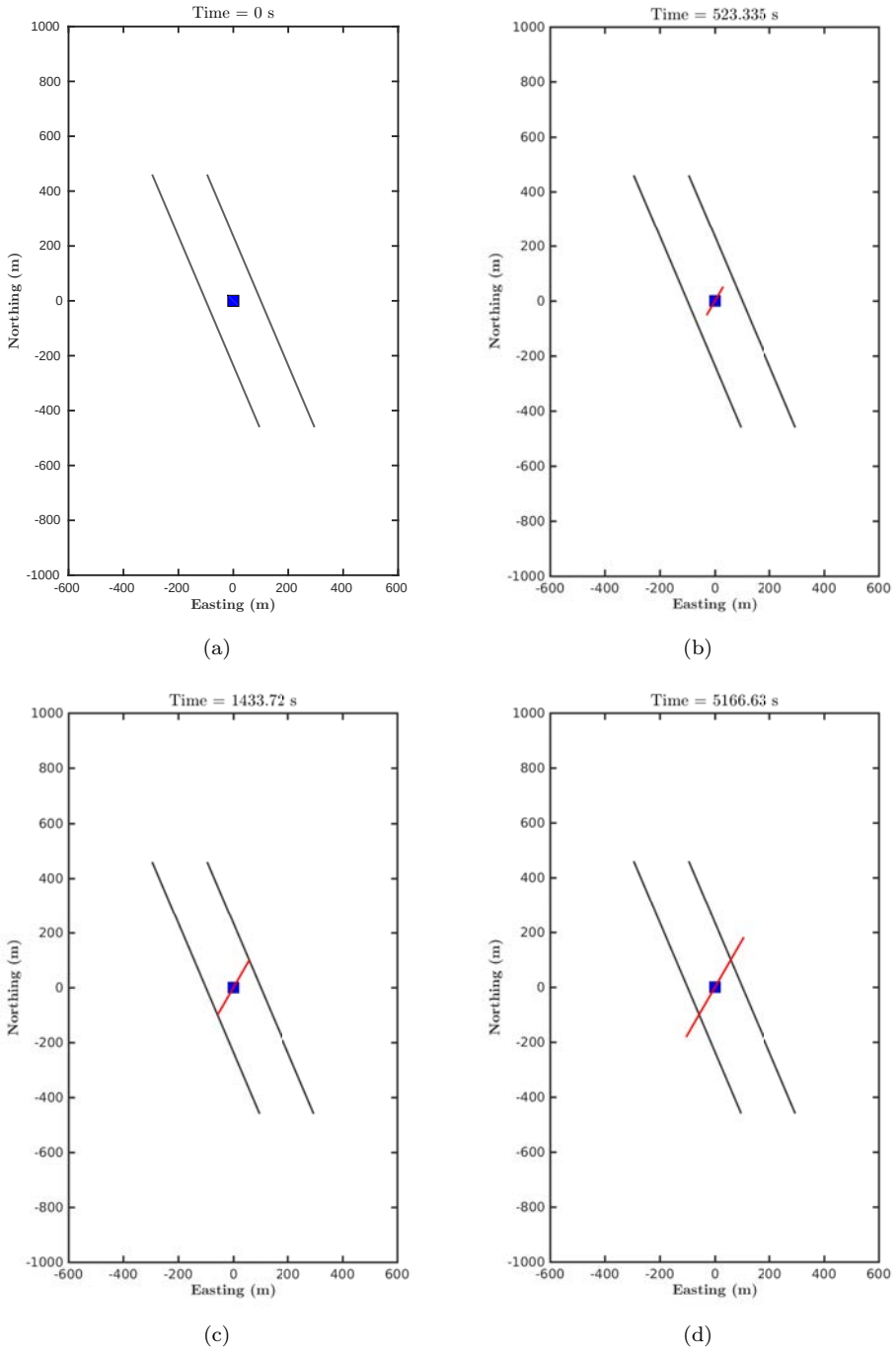

(a) (b)

(c) (d)

Figure 4.34: Numerical simulation result of hydraulic fracture propagation and interaction with a preexisting fault. The fault transmissivity was insufficient to arrest the hydraulic fracture for any significant period of time.

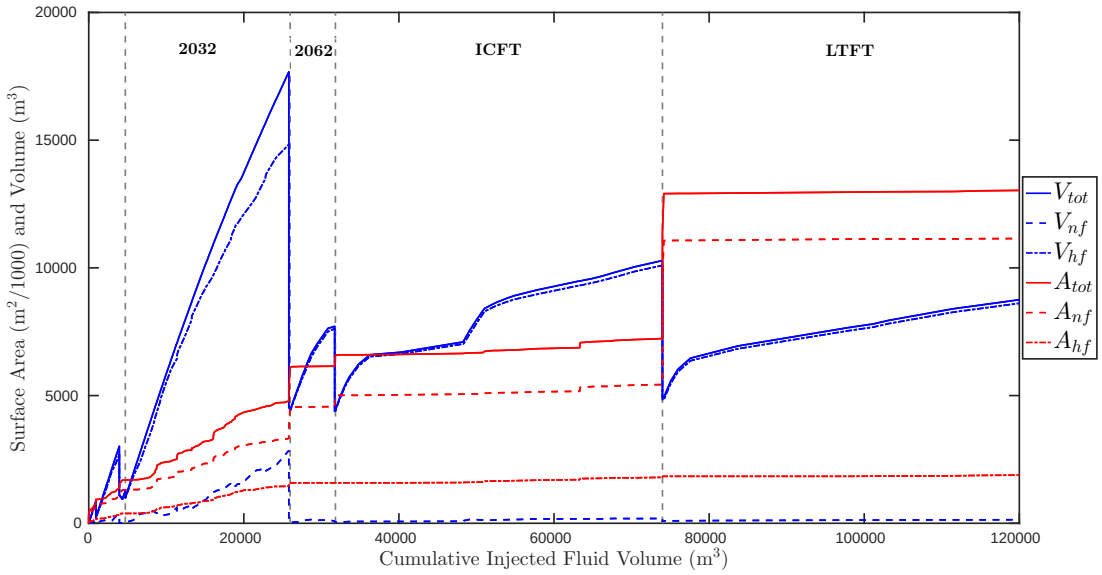

Figure 4.35: Evolution of the stimulated fracture surface area and stimulated fracture volume throughout each phase of the simulation shown as a function of cumulative volume of fluid injected. The *red* and *blue solid lines* represent the total fracture surface area and fracture volume, respectively. The *dashed* and *dot-dashed lines* indicate the values associated with natural fractures and hydraulic fractures, respectively. The stimulated fracture surface area was controlled predominantly by the natural fractures, but the stimulated fracture volume was controlled by the hydraulic fractures.

Chapter 5

Microseismic Depletion Delineation Field Tests: Informing Field Development Strategies for Unconventional Hydrocarbon Resources

This work was presented originally in *Norbeck and Horne* (2016a). In unconventional hydrocarbon resources, determining appropriate infill spacing for horizontal wells is a difficult reservoir engineering task that can have major economic implications. Infill well spacing should be dense enough to maximize contact with the reservoir, but the wells should not overlap into regions that were depleted previously. Similarly, refracturing operations depend heavily on the reservoir response during production and understanding the productivity profile along the well. Techniques must be developed that can be applied in the field to identify the extent of the depleted zones near production wells. Microseismic depletion delineation has been proposed as one such reservoir surveillance technique.

Microseismic depletion delineation takes advantage of a poroelastic stress change that occurs due to reservoir depletion. Fractures within the altered state of stress become more prone to shear failure. Following a significant period of production, water is reinjected into the well at low rates for a short duration in order to cause pressure to rise in the network of fractures connected to the well. Appropriate injection pressures can be determined to ensure that fractures that fail in shear during reinjection must exist within the depleted region. The shape and the extent of the depleted zone could be inferred by monitoring for microseismic activity during the injection test.

In this study, we used numerical modeling to investigate the physical mechanisms that underpin the microseismic depletion delineation technique. We first modeled a multistage hydraulic fracture treatment of a horizontal well in a naturally fractured reservoir. Following the stimulation treatment, we modeled one year of production to cause pressure drawdown and an associated poroelastic response. The field test was then modeled by reinjecting water into the well at low rates and pressures for a short time. Shear slip events on fractures that occurred during reinjection were considered proxies for microseismic events. The heterogeneous distribution of pressure drawdown was demarcated clearly using the locations of the microseismic events. The results indicate that microseismic depletion delineation could be applied in the field as an effective means of reservoir surveillance. The modeling framework we developed could be used to design field tests and interpret field data.

5.1 Motivation

The successful exploitation of unconventional hydrocarbon resources depends on the ability to develop engineering strategies that incorporate economic constraints as primary considerations. In many shale gas or oil fields, horizontal well trajectories and hydraulic fracture treatments are designed in efficient patterns to reduce capital investment. Operational complications during drilling and hydraulic fracturing as well as reservoir heterogeneity can result in suboptimal performance of individual wells (*Moos et al.*, 2011; *Dohmen et al.*, 2013, 2014; *Yang and Zoback*, 2014). It is useful to develop tests that can be applied in the field in order to assess the recovery efficiency of wells and individual completion stages *Norbeck et al.* (2012). This information can be helpful from a reservoir management perspective, for example, in order to estimate ultimate recovery or to determine appropriate spacing for infill drilling.

This study was an investigation of a field test methodology proposed originally by *Dohmen et al.* (2013) called microseismic depletion delineation (MDD). The MDD technique is an approach that can be used to identify the extent of the depleted region near a horizontal well that has been produced for an extended period of time. The MDD test relies on the fact that as depletion occurs and pressure in the reservoir drops, poroelastic effects cause the in-situ stresses throughout the reservoir to change. Naturally existing fractures will be exposed to an altered state of stress not only due to changes in fluid pressure, but also due to the poroelastic stresses that develop. By reinjecting fluid at carefully determined pressures into a well that has been produced previously and monitoring for microseismic activity, the new state of stress can be leveraged to identify zones in the reservoir that have experienced depletion.

Dohmen et al. (2013, 2014) presented a case study of two multistage hydraulic fracture treatments that were performed adjacent to a well that had been stimulated previously and produced for two years. Six vertical observations wells in the vicinity were used to infer the distribution of reservoir fluid pressure at the end of the production period. During several of the fracturing stages in the two

adjacent wells, microseismic activity indicated that shear slip events occurred preferentially near the original well in zones of relatively low fluid pressure, where significant production had occurred. In that study, it was estimated that the microseismic events of interest occurred even though the injection pressure was below the fracture pressure, so they were not attributable to generation of new fractures. *Dohmen et al.* (2014) presented the hypothesis that changes in stress caused by depletion could promote shear failure of fractures at relatively low pressure, and presented empirical field data which demonstrated that horizontal stresses became less compressive with reservoir depletion in their study area in the Middle Bakken formation.

The field observations led *Dohmen et al.* (2014) to suggest the MDD field test as a method to measure the extent of depletion. The underlying physical mechanisms associated with the MDD field test deserve further investigation to explore its range of applications and limitations. In this work, we performed a numerical simulation of a MDD test using a fully-coupled fluid flow and geomechanics reservoir model to investigate the physical processes that underpin the MDD technique. The modeling framework that we developed can be used to design MDD field tests or interpret MDD field data.

The remainder of this chapter is organized as follows. In Sect. 5.2, we review the physical processes that occur during reservoir depletion and reinjection during the MDD test. In Sect. 5.3, we describe a numerical simulation of a MDD test and interpret the results. The practical applications and limitations of the MDD test are discussed in Sect. 5.4. Here, we also discuss the influence of several important assumptions in our numerical model. In Sect. 5.5, we present several concluding remarks.

5.2 Theoretical background

The MDD technique takes advantage of a poroelastic response that occurs throughout the reservoir during depletion (*Jaeger et al.*, 2007; *Zoback*, 2007; *Yang and Zoback*, 2014). A reduction in reservoir pressure can induce a relaxed compressive stress state. In unconventional reservoirs with low permeability, production likely occurs through networks of natural fractures that are connected to the well by new fractures created during hydraulic fracturing. Depletion will occur in the volume of rock surrounding the fractures that have a hydraulic connection to the well, and so poroelastic stresses will influence the mechanical behavior of these fractures.

The premise of the MDD technique is that, following production, the poroelastic stresses will reduce the in-situ (total) compressive normal stress acting on the fractures that exist within the depleted region. Then, fluid could be injected into the well for a relatively short period of time to increase the fluid pressure in the fractures. Assuming that the permeability of the connected fracture system is several orders of magnitude greater than the permeability of the intact rock, pressure will not diffuse into the surrounding rock, and so the poroelastic effects will not be reversed.

At the new stress state, the fractures will be prone to shear failure at a fluid pressure significantly lower than the initial state. By maintaining the injection pressure at appropriately low levels, it can be guaranteed that any fractures that fail in shear must exist within the depleted region. Monitoring for microseismic activity during this period could reveal the shape of the depleted region.

5.2.1 Poroelastic deformation in porous and fractured media

For saturated porous materials, Hooke's law indicates that changes in internal fluid pressure give rise to purely volumetric deformations and that those deformations are related to the effective stress acting on the material (*Jaeger et al.*, 2007):

$$\sigma_{ij} - \alpha p \delta_{ij} = 2G\varepsilon_{ij} + \Lambda \varepsilon_{ij} \delta_{ij}. \tag{5.1}$$

Here, σ_{ij} are the components of the stress tensor, ε_{ij} are the components of the strain tensor, p is fluid pressure, α is Biot's coefficient, G is shear modulus, Λ is Lamé's coefficient, and δ_{ij} is the Kronecker delta function. Compressive stresses have been taken as positive in this sign convention. In Eq. 5.1, the left hand side represents the effective stress. Using Eq. 5.1 as a constitutive relation and assuming infinitesimal strains, momentum balance in the material gives (*Jaeger et al.*, 2007):

$$G\frac{\partial^2 u_i}{\partial x_k \partial x_k} + (G + \Lambda)\frac{\partial^2 u_k}{\partial x_i \partial x_k} = -\alpha \frac{\partial p}{\partial x_i} - F_i, \tag{5.2}$$

where u_i are the components of the displacement vector and F_i are the components of the body force vector. In Eq. 5.2, it is clear that gradients in fluid pressure act as body forces on the material. Of course, pressure gradients must exist in the reservoir for flow to occur.

In unconventional resources where the permeability of the intact matrix rock is very low, the overall flow behavior depends strongly upon an interplay between fractures and matrix rock. Consider the fractures and the matrix rock to be two separate, but connected, domains. Then, mass balance for fractured porous media saturated with a single-phase fluid can be described for flow in the matrix domain as (*Aziz and Settari*, 1979):

$$\frac{\partial}{\partial x_i}\left(\rho \lambda k^m \frac{\partial p^m}{\partial x_i}\right) + \widetilde{m}^{wm} + \widetilde{\Psi}^{fm} = \frac{\partial}{\partial t}\left(\rho \phi\right), \tag{5.3}$$

and for flow in the fracture domain, as:

$$\frac{\partial}{\partial x_i}\left(\rho \lambda T^f \frac{\partial p^f}{\partial x_i}\right) + \widetilde{m}^{wf} + \widetilde{\Psi}^{mf} = \frac{\partial}{\partial t}\left(\rho E\right). \tag{5.4}$$

Here, p^m is fluid pressure in the matrix domain, p^f is fluid pressure in the fracture domain, ρ is fluid density, λ is inverse fluid viscosity, k^m is matrix permeability, T^f is fracture transmissivity, ϕ is

matrix porosity, E is fracture void aperture, $\widetilde{m}^{wm}$ is a normalized mass source term related to wells in the matrix domain, and $\widetilde{m}^{wf}$ is a normalized mass source term related to wells in the fracture domain. The terms $\widetilde{\Psi}^{fm}$ and $\widetilde{\Psi}^{mf}$ account for mass transfer between the two domains (*Lee et al.*, 2000; *Li and Lee*, 2008; *Norbeck and Horne*, 2015a, 2016a).

Eqs. 5.2 - 5.4 constitute a coupled system of equations that can be solved, subject to suitable initial and boundary conditions, for the displacement and pressure fields throughout the domain. In this work, we solved this system of equations numerically using an iterative sequential-implicit strategy (*Kim et al.*, 2011). The numerical model is described briefly in Sect. 5.3.1.

For simple mechanical and flow conditions, Eq. 5.1 actually can be sufficient to provide useful insights into reservoir behavior. For example, if the lateral extent of the reservoir is much greater than its thickness and if the pressure perturbation due to production occurs relatively uniformly throughout the reservoir, then a reasonable assumption is that deformation can only occur in the vertical direction. We can rewrite Eq. 5.1 in the principal coordinate system under the uniaxial strain conditions (here, we assume that the vertical and horizontal directions correspond to the principal directions):

$$\sigma_V - \alpha p = (2G + \Lambda)\,\varepsilon_V, \tag{5.5}$$

$$\sigma_H - \alpha p = \Lambda \varepsilon_V, \tag{5.6}$$

$$\sigma_h - \alpha p = \Lambda \varepsilon_V, \tag{5.7}$$

where the subscripts V, H, and h stand for vertical, maximum horizontal, and minimum horizontal, respectively. The horizontal effective stresses are therefore functions of the vertical effective stress:

$$\sigma_H - \alpha p = \sigma_h - \alpha p = \frac{\Lambda}{2G + \Lambda}\left(\sigma_V - \alpha p\right). \tag{5.8}$$

We emphasize that Eqs. 5.5 - 5.8 are never valid as a means to estimate the magnitudes of the initial regional horizontal stresses from knowledge of the vertical stress (*Zoback*, 2007). However, the relationships can be used effectively to gauge changes in the state of stress. In that light, we first rearrange Eq. 5.8 for the total horizontal stresses:

$$\sigma_H = \sigma_h = \frac{\nu}{1-\nu}\sigma_V + \alpha\left(1 - \frac{\nu}{1-\nu}\right)p, \tag{5.9}$$

Here, we have substituted the elastic moduli used previously for ν, which is Poisson's ratio. In the context of uniaxial strain, the total vertical stress must remain constant. The change in the total horizontal stress with respect to changes in fluid pressure is (*Zoback*, 2007):

$$\frac{\partial \sigma_H}{\partial p} = \frac{\partial \sigma_h}{\partial p} = \alpha\left(\frac{1-2\nu}{1-\nu}\right). \tag{5.10}$$

Poroelastic stresses are caused by the deformation of the material, in this study due to a reduction in the fluid pressure within the pores of the rock, combined with the ability for the surrounding rock to constrain the motion of the material. As the depressurized rock attempts to contract, tensile stresses are generated because the surrounding rock acts to prevent motion. This reduces the magnitude of the compressive stresses acting within the depleted zone (see Eq. 10). Outside of the depleted zone, nonlocal stress transfer can cause either increased or decreased compression in different areas, depending on the pressure distribution within the depleted zone and geometric effects (nonlocal stress transfer is not captured in Eq. 10, but is included in our numerical model).

In this work, we were interested in evaluating heterogeneous flow behavior near horizontal wells that have been stimulated with hydraulic fracturing. If some treatment stages are not as effective as others then the reservoir drawdown will not occur uniformly, and so the assumption of uniaxial strain is not strictly valid. Nonetheless, we can use Eq. 5.10 as a first approximation to help design MDD field tests and guide modeling efforts.

5.2.2 Shear failure on fractures

As fractures fail in shear, they can release seismic energy. The locations of shear failure events can be detected using microseismic monitoring techniques (*Warpinski*, 2009). The mechanical stability of fractures in the reservoir depends on the local state of stress, the fluid pressure in the fractures, and the frictional properties of the fractures. In this work, we assumed a Mohr-Coulomb failure criterion (*Jaeger et al.*, 2007).

For fractures that bear total normal stress, σ_n, and shear stress, σ_s, we define a critical pressure, p^*, that will cause shear failure:

$$p^* = \sigma_n - \frac{\sigma_s - c}{f}, \tag{5.11}$$

where c is the fracture cohesion, and f is the static coefficient of friction. Eq. 5.11 assumes that the Biot coefficient within fractures is equal to one.

The normal stress acting on a fracture reflects the sum of the remote in-situ stress, mechanically-induced stresses caused by interaction with other fractures as they deform, and poroelastically-induced stress caused by changes in fluid pressure in the surrounding rock. For any given fracture, the value of p^* will change throughout the production life of a reservoir. In the MDD field test, we can take advantage of this behavior to determine appropriate injection pressures during reinjection to ensure that observable microseismic events will only occur within the depleted region. The true nature of the geologic structure and fracture network topology is difficult to determine. Assuming a fracture orientation of 30 degrees from the direction of maximum principal stress, p^* likely sets a useful lower bound on injection pressure during a MDD test. In practice, it would be useful to inject slightly higher than p^* to ensure that many different fracture orientations are interrogated. A

useful upper bound on injection pressure is the magnitude of the minimum principal stress at the depleted stress state to preclude refracturing.

5.3 Modeling framework

We used numerical modeling to further enhance our understanding of the physical processes that occur during a MDD field test. We applied the numerical model developed in this work, as described in Chapter 2. In particular, this analysis relied on the embedded fracture model for the fluid flow calculations (see Sect. 2.1), the fracture mechanics model (see Sect. 2.2), and the poroelasticity model (see Sect. 2.3) . We found that modeling was useful to identify some of the practical limitations of MDD. Here, we describe a numerical simulation of a multistage hydraulic fracture treatment, a subsequent production phase, and finally the MDD reinjection test.

5.3.1 Numerical reservoir model

The simulation was performed with a fluid flow, geomechanics, and fracture propagation reservoir model called CFRAC (*McClure*, 2012; *McClure and Horne*, 2013). Fluid flow was assumed to be single-phase water and isothermal. Mass transfer between the fractures and matrix rock was calculated using an embedded fracture discretization strategy (*Lee et al.*, 2000; *Li and Lee*, 2008; *Norbeck and Horne*, 2016a). The model domain was two-dimensional, so all of the hydraulic fractures and natural fractures had the same height, H. Poroelastic effects were considered, but changes in the in-situ stress only affected deformation of the fractures and did not affect the porosity of the matrix rock. Mechanical interaction between fractures as they deformed was accounted for, and was assumed to occur quasistatically. Permeability of the fractures was able to change during the simulation, and depended on the local state of stress and cumulative shear displacement. Proppant transport was not modeled during the hydraulic fracture simulation. For details of the flow, geomechanics, and poroelasticity calculations performed by CFRAC, see *McClure and Horne* (2013), *Norbeck and Horne* (2015a), *Norbeck and Horne* (2016a), and *Norbeck et al.* (2016a).

5.3.2 Geologic setting, well configuration, and reservoir operations

We developed a synthetic model of an unconventional reservoir based loosely on the field data from a well in the Middle Bakken reported by *Dohmen et al.* (2014). We considered a horizontal well in a naturally fractured reservoir. We first modeled a multistage hydraulic fracture stimulation of the well. Following the stimulation treatment, we modeled one year of production from the well in order to cause pressure drawdown throughout the reservoir. Finally, after the production phase, we modeled a short period of reinjection into the well. This last phase was the MDD field test.

In the model, the stress regime was strike-slip. The dominant natural fracture system was

comprised of two conjugate sets of fractures that had average strike orientations of 30 degrees from the direction of maximum principal compression. The permeability of the matrix rock was 1×10^{-18} m^2 (1 microdarcy). The horizontal well, completion configuration, and natural fracture system are illustrated in Fig. 5.1. Five separate completion stages were modeled, numbered starting from the toe of the well (right side) and increasing towards the heel of the well (left side). A list of important model parameters is given in Table 5.1.

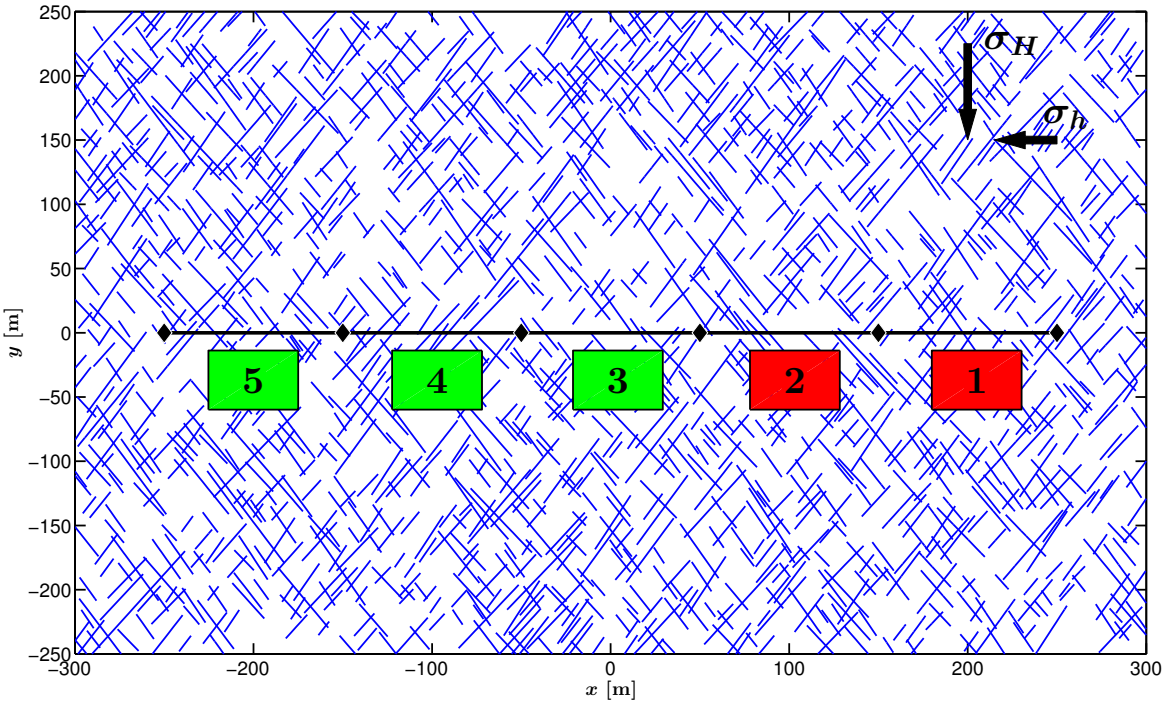

Figure 5.1: Natural fracture network. The *blue lines* represent natural fractures and the *black line* represents the horizontal well. The well was separated using packers (*black diamonds*) into five completion stages (*colored boxes*) with equal spacing. The first two stages (*red boxes*) were skipped to mimic ineffective completions. The full extent of the natural fracture network is shown here, but the matrix rock domain extended to $x = \pm 1000$ m and $y = \pm 1000$ m to reduce boundary effects during the flow and poroelastic stress calculations.

5.3.3 Stimulation phase: Multistage hydraulic fracture treatment

The lateral section of the well was 500 m long. The well was completed by performing hydraulic fracturing in five separate stages (each 100 m long), starting at the toe of the well and proceeding towards the heel. During each fracturing stage, fluid was injected at a constant mass rate of 50 kg/s for a period of 30 minutes.

The maximum horizontal stress was in the y-direction, and the hydraulic fractures were assumed

Table 5.1: Model parameters for the microseismic depletion delineation study.

Parameter	Value	Unit
σ_{H0}	65	MPa
σ_{h0}	55	MPa
p_0	47	MPa
α	0.65	-
ν	0.2	-
G	15	GPa
f	0.6	-
c	0.5	MPa
k^m	1×10^{-18}	m^2
ϕ	0.07	-
λ^{-1}	0.5	mPa $\cdot$ s
H	100	m

to propagate in the direction of the maximum horizontal stress. A large number of potentially forming hydraulic fractures that intersected the well and natural fractures were specified stochastically prior to the simulation, and a subset of them eventually formed during the simulation. The initial reservoir pressure was $p_0 = 47$ MPa, the maximum principal stress was $\sigma_{H0} = 65$ MPa, and the minimum principal stress was $\sigma_{h0} = 55$ MPa.

In order to mimic a scenario where several of the stages were ineffective, the first two stages near the toe of the well were skipped. In practice, this might occur if a fault caused large volumes of the fracturing fluid to be lost to the formation, preventing the energy going into pumping the fluid from creating fracture growth (*Dohmen et al.*, 2014). This is an important component of the scenario we modeled, because the MDD strategy should be able to diagnose zones in the reservoir that were not connected hydraulically to the well during hydraulic fracturing.

Profiles of the bottomhole pressure and injection rate during hydraulic fracturing of Stages 3 - 5 are shown in Fig. 5.2. In contrast to the behavior predicted by theory for a single two-wing hydraulic fracture (e.g., see *Economides and Nolte* (2000)), the injection pressure did not decrease steadily over time upon fracture initiation. Hydraulic fractures tended to connect zones of natural fractures which caused increased resistance to flow in the system that had to be overcome before the next hydraulic fractures could form.

The stimulated fracture network at the end of the hydraulic fracture treatment phase is illustrated in Fig. 5.3. Note that the stimulated region was confined to the final three completion stages. This was expected to influence the evolution of the depleted region during the production phase.

5.3.4 Production phase

Following the stimulation phase, all of the control valves were opened to allow production to occur from the entire lateral section of the well. The well was first bled off at a pressure of 47 MPa for a

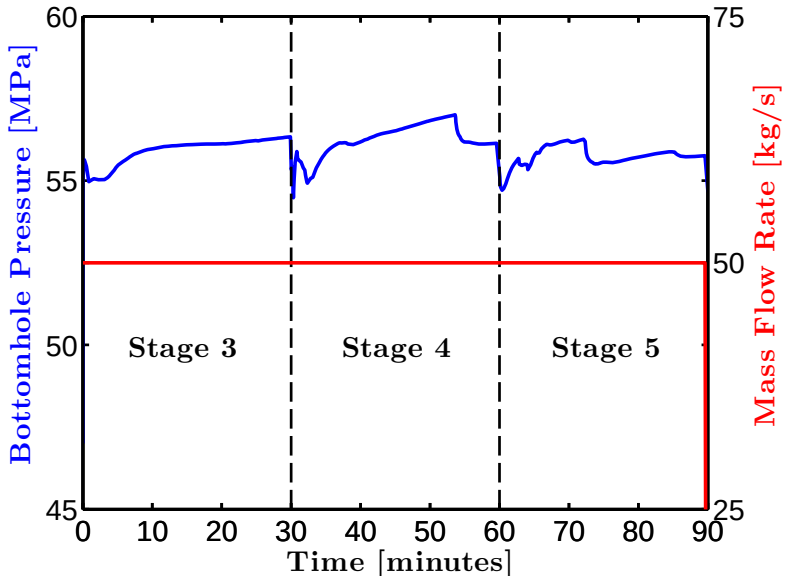

Figure 5.2: Injection pressure and injection rate during the hydraulic stimulation. The *dashed black lines* indicate the transition between completion stages. Stages 1 and 2 at the toe of the well were intentionally skipped to mimic ineffective stages.

period of one week. The well was then set on production for one year. The initial reservoir pressure was 47 MPa, and the full drawdown of 30 MPa was realized by producing the well at constant bottomhole pressures of 37 MPa, 27 MPa, and 17 MPa for four-month intervals.

Reservoir fluid was assumed to be single-phase water and isothermal. During the production phase, we did not simulate multiphase or multicomponent flow. This simplification certainly had an impact on the overall production behavior, and for more practical applications a rigorous treatment of reservoir fluid properties should be considered. However, for the purposes of this work we were interested in understanding the role of poroelastic effects that occur during depletion, and so single-phase flow was sufficient for the investigation.

The bottomhole pressure and production rate profiles over the one-year duration are shown in Fig. 5.4. During each four-month period, the production rate initially declined very rapidly. The production rate never dropped to zero, but instead tended towards a steady "tail" of sustained flow. This behavior is qualitatively similar to that observed in many unconventional oil and gas wells (*Vassilellis et al.*, 2010). In our model, fracture permeability was a function of the overall effective stress. It is generally understood that pressure drawdown increases the effective stress acting on the fractures and therefore can reduce fracture aperture and permeability (*Vassilellis et al.*, 2010), but the poroelastic stresses actually have the opposite effect. The competition between decreased pressure in the fractures and the poroelastic stress relief may play an important role in the long-term

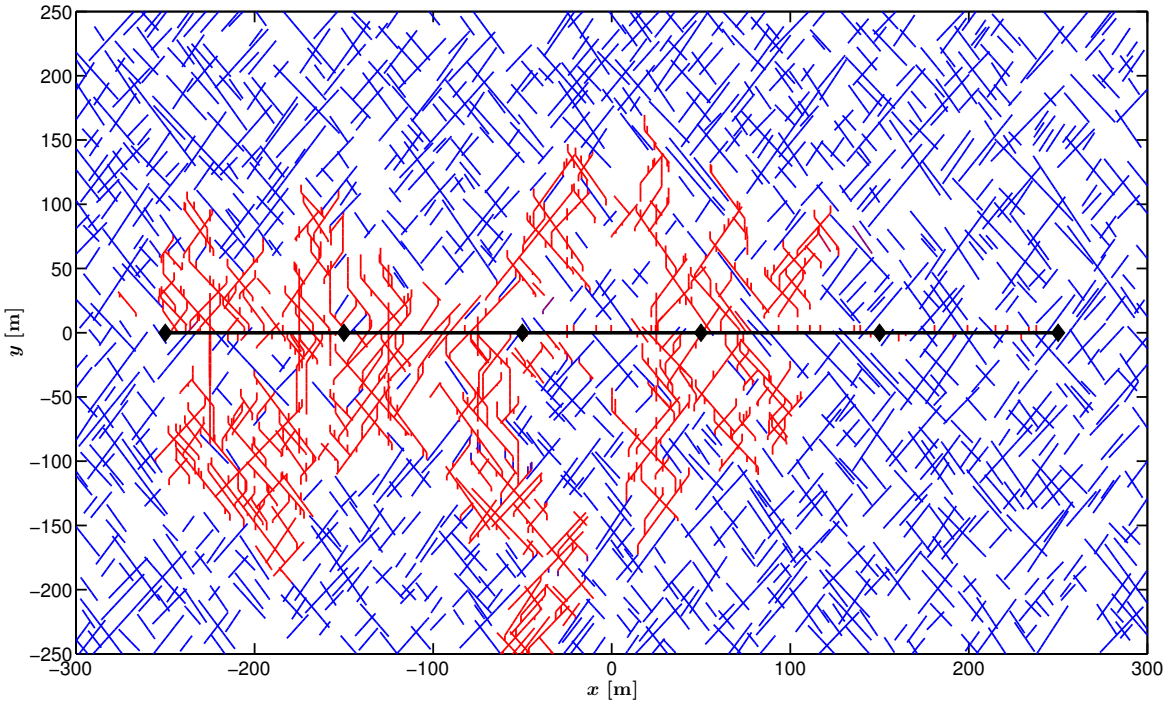

Figure 5.3: Stimulated fracture network. The *red lines* represent newly created tensile fractures or natural fractures that experienced a pressure perturbation of at least 1 MPa during the stimulation treatment. The first two treatment stages from the right side (toe) of the well were not stimulated.

production behavior in fracture-dominated systems.

The production phase caused a significant amount of pressure depletion to occur within the matrix rock. In Fig. 5.5, contours of reservoir pressure at the end of one year of production overlay the stimulated fracture network. It is clear that the rock volume near the three completion stages that were stimulated successfully experienced significantly more drawdown than the region near the first two stages. It is interesting to note that some depletion occurred near networks of natural fractures that were not stimulated directly during the fracturing treatment, but evidently did have a hydraulic connection with the well (e.g., see the set of blue colored fractures around the location $x = -150$ m, $y = -175$ m). The goal was to attempt to identify this type of heterogeneous depletion with the MDD surveillance technique.

We used Eq. 5.10 as a first approximation to predict the magnitude of the poroelastic stress change expected to occur during depletion. For a drawdown of $\Delta p = -30$ MPa and the elastic properties listed in Table 5.1, we calculated that the change in the horizontal stresses would be $\Delta\sigma_H = \Delta\sigma_h = -14.6$ MPa.

The spatial distribution of changes in the horizontal stresses at the end of one year of production calculated by the numerical model are shown in Figs. 5.6 and 5.7. The shape of the depleted region

had a marked effect on the evolution of the poroelastic stresses. Negative changes in the horizontal stress indicate relaxed compression. In terms of the magnitude of the poroelastic effect, it was observed that Eq. 5.10 gave a reasonable estimate for the change in stress within the depleted region. This result is extremely encouraging from a practical perspective, because it provides justification to apply an analytical approximation (Eq. 5.10) to estimate one of the most critical aspects of a MDD test, reducing the dependence on more costly numerical calculations. Outside of the depleted region, some areas of the reservoir experienced increased compressive stress due to nonlocal elastic stress transfer. From the perspective of the MDD test, this nonlocal effect would enhance the contrast in the state of stress between the depleted and undepleted regions, potentially improving the method's capability of detecting the shape of the depleted zone. Note that in the model, the domain extended to $x = \pm 1$ km and $y = \pm 1$ km to reduce boundary effects.

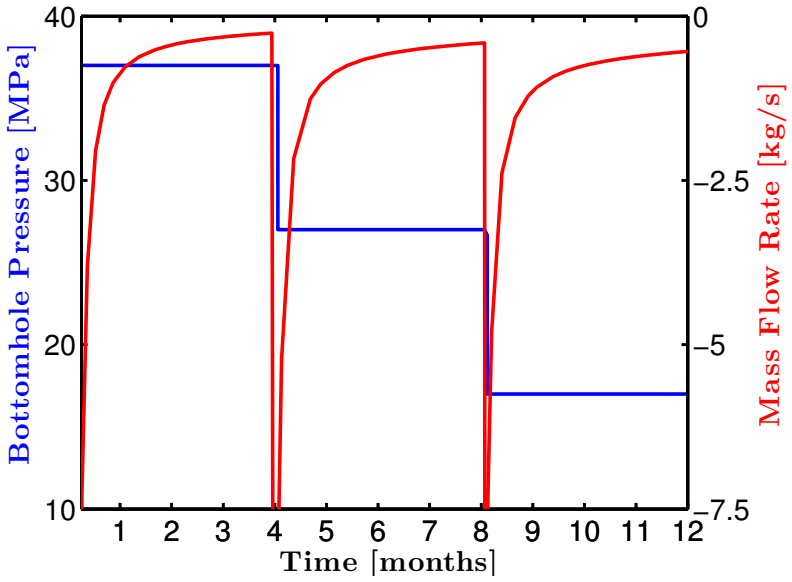

Figure 5.4: Bottomhole pressure and production rate over the one-year duration of the production phase.

5.3.5 Reinjection phase: The MDD test

After stimulation and the subsequent year of production, the state of stress in the reservoir was altered significantly from the initial conditions. Mechanically-induced stress caused by fracture deformation and poroelastically-induced stress caused by depletion both influenced the overall stress field. We sought to leverage the new state of stress for the purpose of reservoir surveillance. By reinjecting and monitoring for microseismic activity, the locations of the slip events defined the geometry of the depleted region.

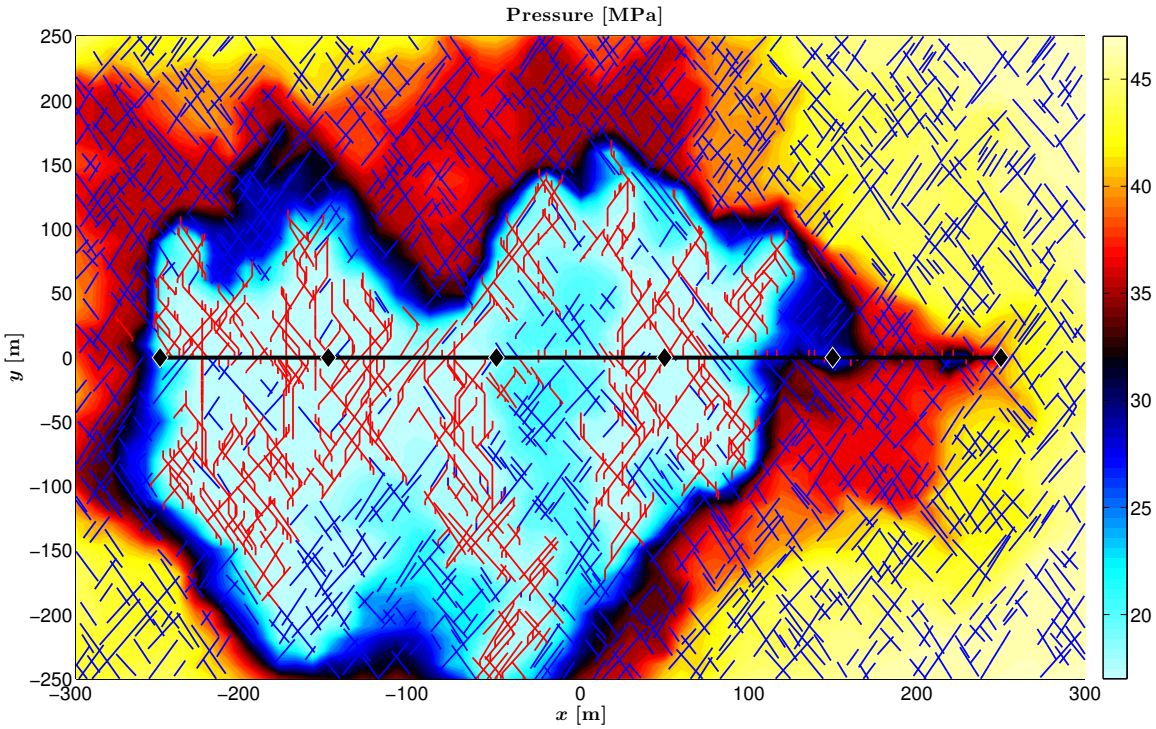

Figure 5.5: Contours of reservoir pressure overlying the stimulated fracture network at the end of one year of production.

Initially, the reservoir was in mechanical equilibrium. In the depleted state, fractures were prone to shear failure at relatively low fluid pressure. Using Eq. 5.11, we estimated the critical fluid pressure that would cause slip in both the initial and depleted states to be $p_0^* = 51.1$ MPa and $p_1^* = 36.5$ MPa, respectively. These calculations assumed that fractures were oriented 30 degrees from the maximum horizontal stress, which was the average orientation of the dominant fracture sets in our synthetic reservoir model. The value of p_1^* was based on the poroelastic stress change given by Eq. 5.10 and neglected any mechanically-induced stress.

We used these preliminary calculations to determine appropriate injection pressures during the MDD test. Water was first injected at a constant pressure of 25 MPa (below p_1^*) for one day. No microseismic events were expected during this period. Then, injection was continued at a pressure of 42 MPa (above p_1^* but below p_0^*) for one additional day. Microseismic activity that occurred at this pressure must correspond to slip on fractures that existed within the depleted zone.

For practical applications, the ability to detect microseismic events accurately can depend on several factors, including the positioning of the microseismic array (horizontal and vertical distance of the sensors from the target injection zone, number and spacing of sensors), uncertainty in the velocity structure of the reservoir, and noise. In addition, the size of the events affect detectability

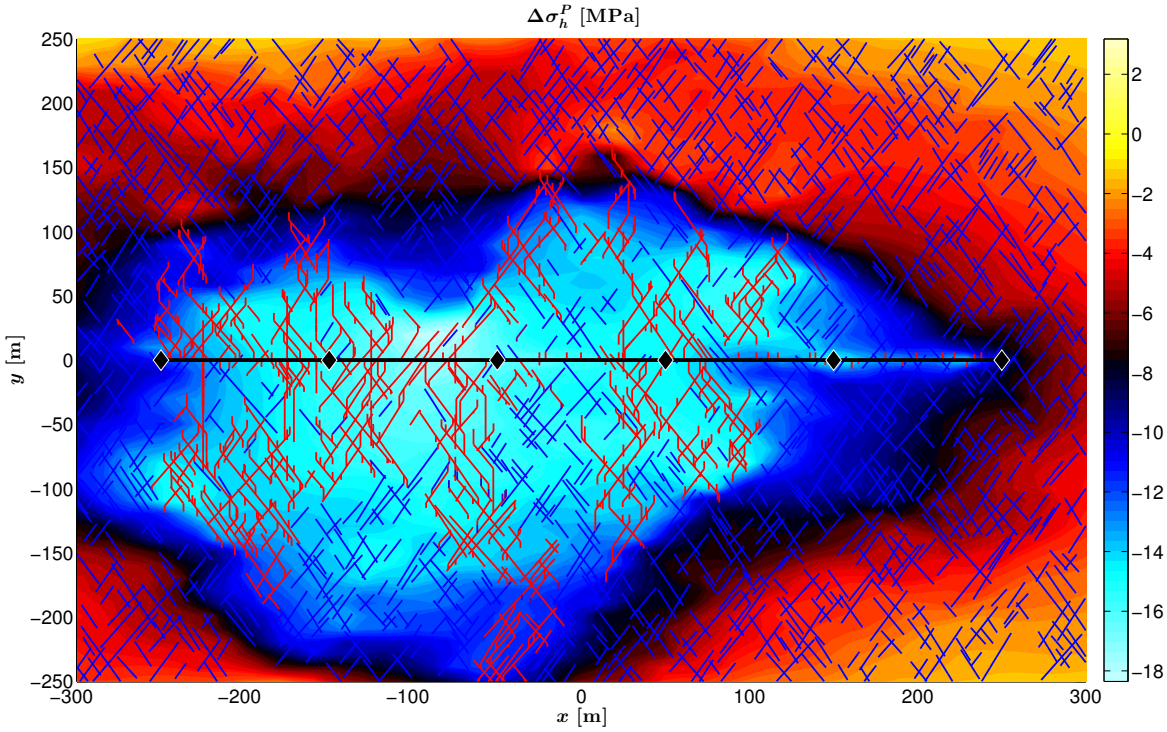

Figure 5.6: Contours of the poroelastic stress change $\Delta\sigma_h$ at the end of one year of production.

significantly and are outside of the engineers' control. When microseismic monitoring programs are designed properly, detectable events have been observed to span several orders of magnitudes with thresholds as low as M -4 (*Warpinski*, 2009).

In the model, injection pressures during the hydraulic stimulation phase exceeded p_1^* (see Fig. 5.4), and so some slip on natural fractures occurred during the initial stimulation. During the MDD reinjection test, we monitored for additional slip that occurred beyond that which had occurred during hydraulic fracturing. The locations of these new slip events were recorded, and were considered as proxies for microseismic events. We defined a detection threshold of one percent of the maximum slip experienced by all fracture elements. In practice, a magnitude detection threshold could be applied analogously. The maximum shear slip during reinjection was 7.8 mm, so fracture elements that slipped less than 0.08 mm did not contribute to the detected microseicmicity.

In Fig. 5.8, we show the injection pressure and the shear slip event rate over the two-day period of reinjection during the MDD test. No events were observed while injecting at 25 MPa, as expected. After injecting for 24 hours, injection pressure was increased quickly until reaching a maximum of 42 MPa. In Fig. 5.8, the *dashed black horizontal line* indicates the value of p_1^*. Very soon after the injection pressure exceeded p_1^*, shear slip events began to occur. This provides additional support for using the uniaxial strain assumption to calculate the poroelastic effect and estimate

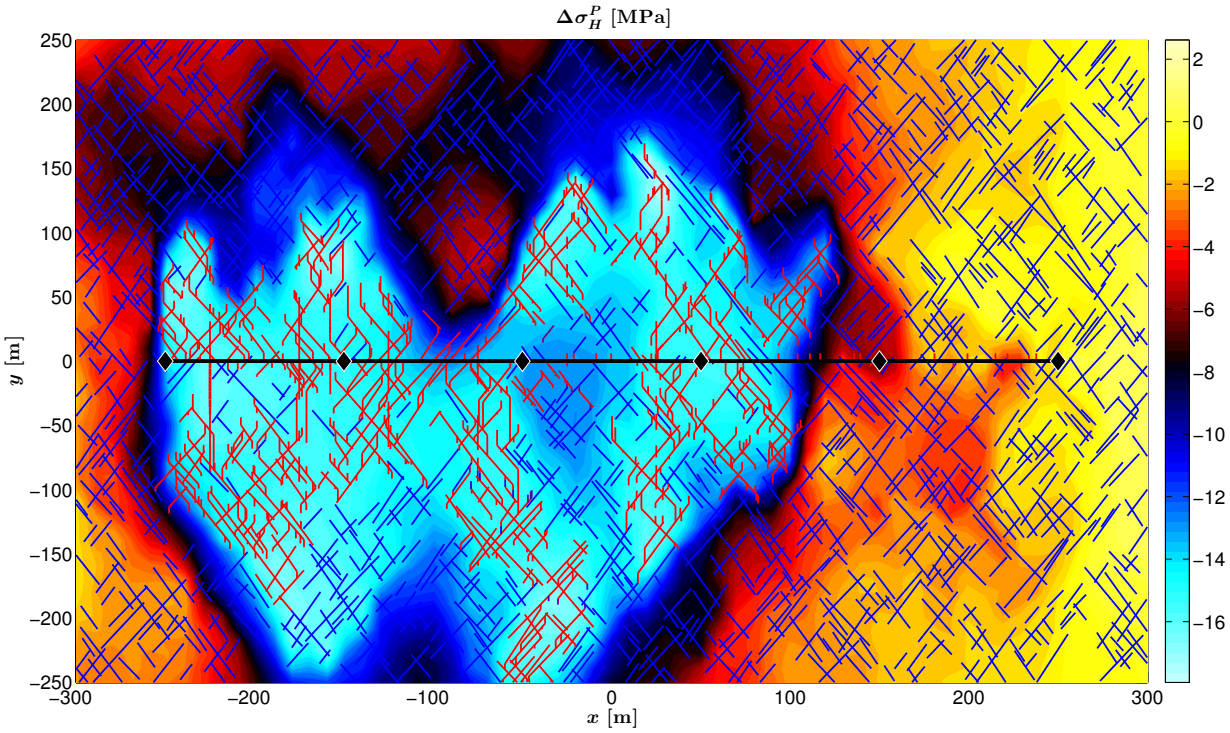

Figure 5.7: Contours of the poroelastic stress change $\Delta\sigma_H$ at the end of one year of production.

the critical injection pressure at the depleted state. Note that the absolute magnitude of the event rate is somewhat arbitrary, given that each natural fracture was discretized into many segments. However, the relative magnitude of each bar is meaningful in terms of understanding the evolution of microseismicity during the MDD test.

In Fig. 5.9, the results of the MDD surveillance test are shown. The filled circles indicate locations where shear slip events occurred during injection at 42 MPa. The color of the circles corresponds to the timing of the individual events. Comparing the locations of the events to the contours of reservoir pressure, the events are able to demarcate the heterogeneous distribution of the depleted zone. Shear slip events did occur in some patches of natural fractures that were not directly stimulated during fracturing, which suggests that MDD can be a useful tool to identify patterns in fracture connectivity. The temporal patterns in seismicity provide additional information that can be used to infer effective flow properties at the reservoir scale. In Figs. 5.10 and 5.11, the shear slip events are shown overlying contours of the poroelastic stress changes. The events were confined to the regions where the stress changes were most significant. The changes in horizontal total stress near regions with microseismicity are very similar in magnitude to the prediction made using Eq. 5.10.

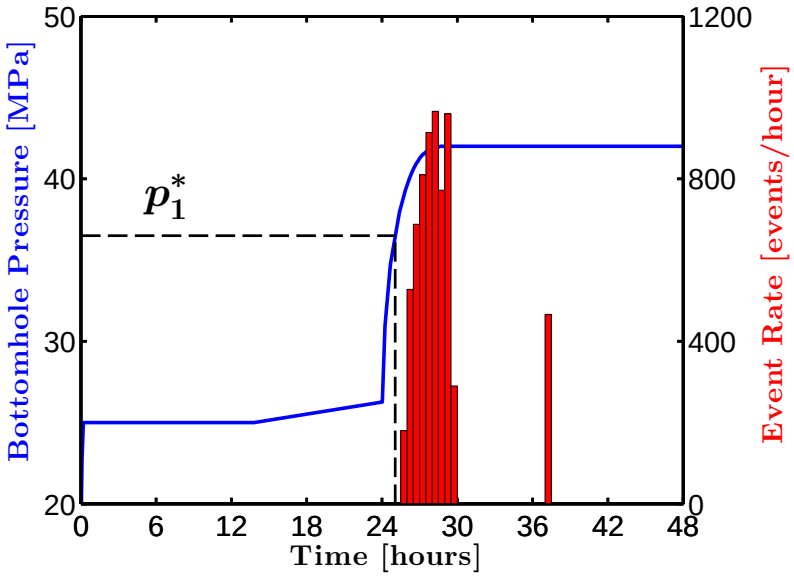

Figure 5.8: Bottomhole pressure and shear slip event rate during the two-day MDD reinjection. No events occurred while injecting at 25 MPa. Events began occurring after the injection pressure exceeded the critical injection pressure at the depleted state, p_1^*.

5.4 Discussion

The numerical simulation results presented in Sect. 5.3 support the hypothesis that MDD can be used as an effective strategy to measure the extent of depletion directly in the field. The main goal when designing a MDD test must be to ensure that the observed microseismic events could only have occurred within the depleted region that has experienced a poroelastic stress change. Ideally, injection pressures during the MDD test should be below the new minimum principal stress at the depleted state to preclude the nucleation and propagation of tensile fractures (i.e., refracturing). However, if refracturing does occur, it does not obviate the MDD results as long as the injection pressure is maintained safely below the critical pressure for shear failure at the undepleted stress state. The best strategy is therefore to perform a controlled experiment by reinjecting fluids into a well that has been on production previously, as opposed to performing hydraulic fracturing treatments on nearby wells while monitoring pressure in the well of interest (as was the case in the field test presented by *Dohmen et al.* (2014)).

Knowledge of the extent of the depleted region near a horizontal well can be used to make several types of important engineering decisions. On an individual well basis, MDD can be used to identify completion stages that did not perform well. By combining this information with hypotheses for the cause of poor performance, strategies for refracturing the well can be developed. On a field basis,

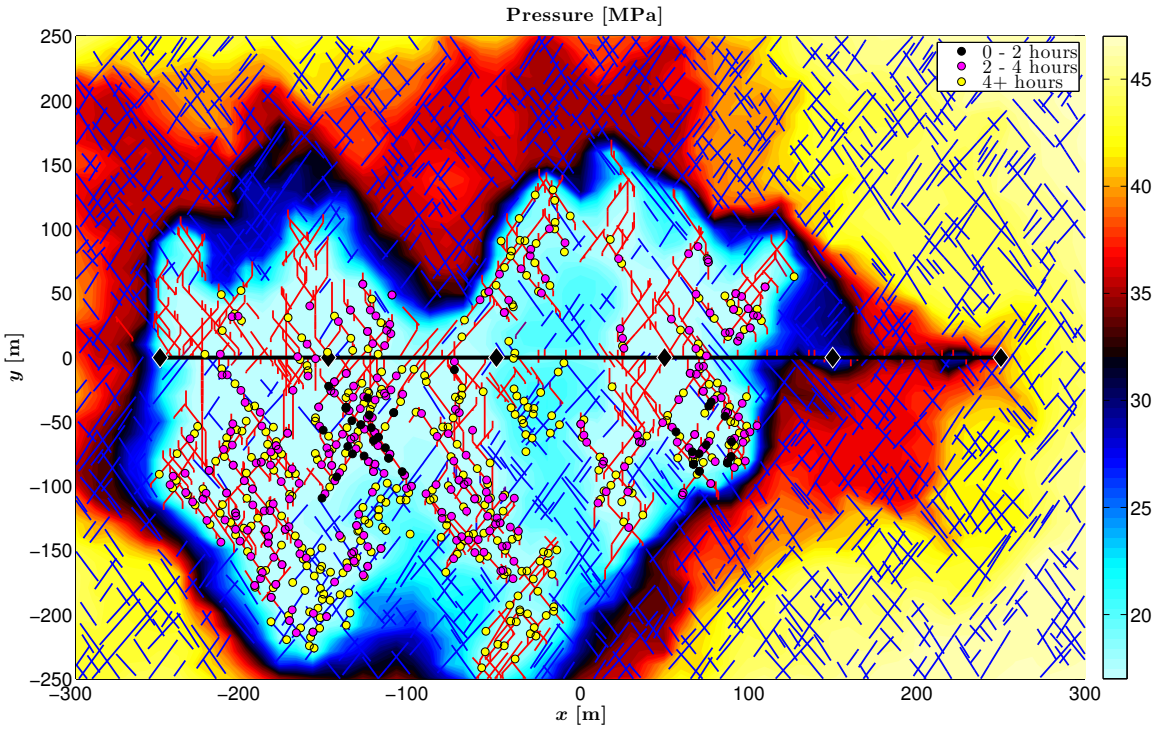

Figure 5.9: Shear slip events (*filled circles*) during the MDD test overlying reservoir pressure contours. The locations of the events demarcate the boundary of the region that experienced significant depletion. The color of each event reflects the timing of the event.

we envision applying the MDD test on multiple wells to gain insight into general field behavior. This information can help to inform engineers to decide on appropriate spacing for infill wells by preventing drilling into areas that have already experienced significant depletion. The MDD field data can help reservoir engineers to determine effective flow properties of the reservoir and evaluate reservoir heterogeneity. This information can be supplied to reservoir simulation models to improve the accuracy of long-term flow predictions.

The modeling approach that we developed can be useful both for designing MDD tests and interpreting results. However, we made several important assumptions in our conceptual reservoir model and numerical model formulation that influenced the results and our interpretations. We address the most important issues here.

The model domain was two-dimensional, so all of the hydraulic fractures and natural fractures had the same height and were oriented vertically. This certainly affected the fracture propagation behavior and overall fracture connectivity pattern exhibited in Fig. 5.3. The hydraulic fractures were assumed to propagate in the direction of the remote maximum principal stress, so local variations in the principal stress orientations that developed during the simulation did not affect the propagation

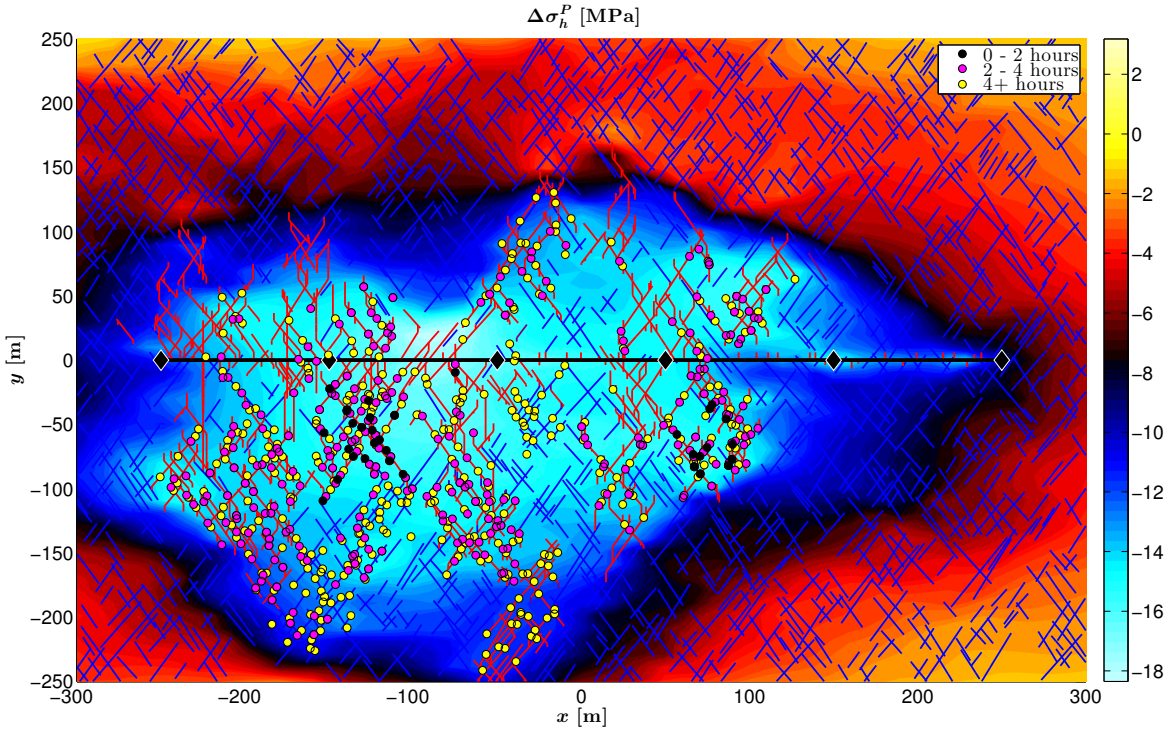

Figure 5.10: Shear slip events (*filled circles*) during the MDD test overlying $\Delta\sigma_h$ contours.

direction. The stimulated fracture network had a significant impact on the outcome of pressure depletion in the reservoir.

We generated the network of natural fractures stochastically by specifying fracture density, average orientation, and average length. In the model, two conjugate fracture sets were oriented at roughly 30 degrees from the direction of the maximum horizontal stress. The orientation of the natural fractures and the magnitude of the differential stress affected the critical pressure to cause shear failure. In practice, it is very difficult to know the statistics of the natural fractures in the reservoir, but this should not deter from performing the MDD test. Taking advantage of the fact that fractures in rock exist over a broad range of length scales and orientations, a limiting case for the critical injection pressure can be determined for the fractures that are most critically-stressed. Of course, it cannot be guaranteed that the full extent of the depleted region will be detected in this case. Increasing injection pressure beyond this limiting critical value will cause misoriented fractures to fail and improve the likelihood of probing the entire depleted region.

The reservoir fluid was single-phase water. The mass balance equations (see Eqs. 5.3 and 5.4) assumed traditional Darcy flow. In reality, flow in unconventional reservoirs consists of water and several hydrocarbon components that can exist in multiple phases. Flow in fractures may deviate from Darcy flow, especially near wells. In low-permeability shales, additional physical mechanisms

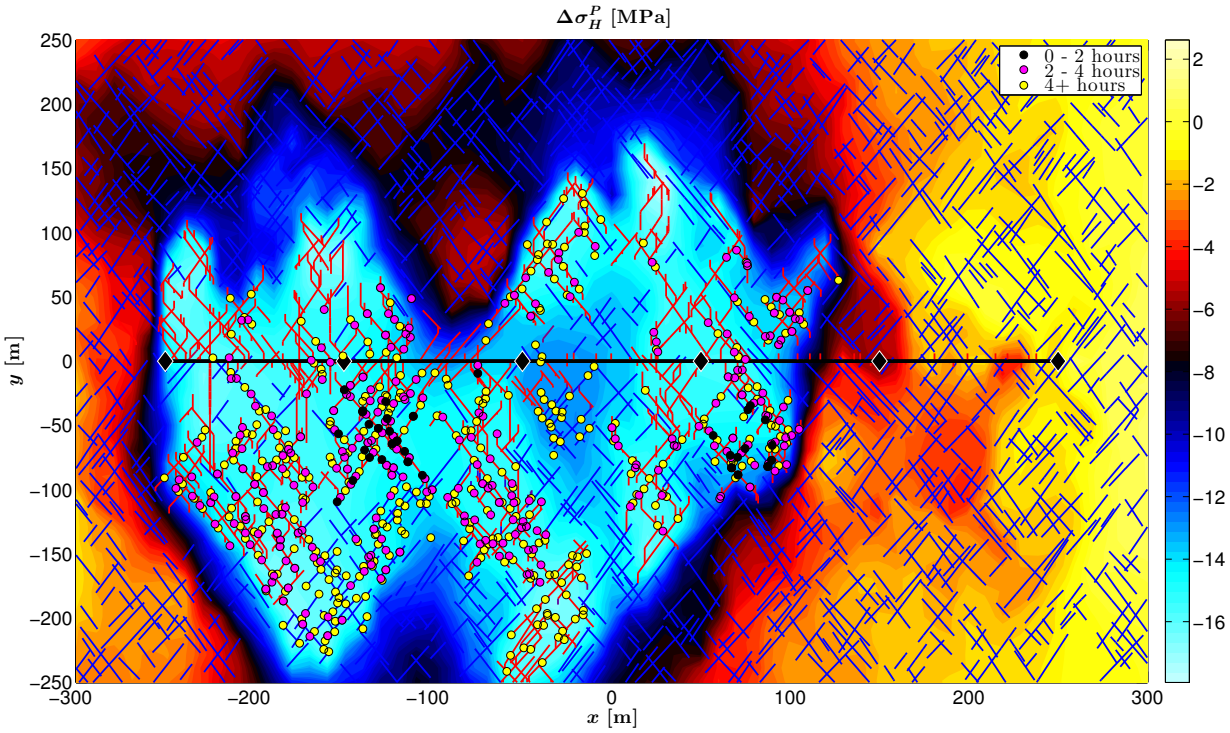

Figure 5.11: Shear slip events (*filled circles*) during the MDD test overlying $\Delta\sigma_H$ contours.

may contribute to flow, such as diffusion or desorbtion (*Heller et al.*, 2014). In more practical applications, these effects should be considered to obtain more accurate estimates of reservoir depletion when modeling the production phase. The embedded fracture modeling approach used in our simulation, which is based on a discrete fracture representation, would be useful in conjunction with improved physics models.

We assumed that the matrix permeability distribution was homogeneous and that matrix permeability was 1×10^{-18} m^2 (1 microdarcy). Experiments performed on multiple samples of rock from the Middle Bakken formation suggest that permeability can vary by up to four orders of magnitude in shale oil reservoirs, depending on mineralogy and the presence of microfractures. (*Kurtoglu et al.*, 2014). In that study, they obtained permeability measurements ranging from 0.01 - 100 microdarcy. In a practical scenario, the influence of matrix heterogeneity on the matrix-fracture interaction is likely to affect the production behavior significantly.

An important concept central to the MDD technique is that a network of hydraulic and natural fractures are connected to the well, and that the overall transmissivity of this network is much larger than the surrounding matrix rock. In reality, the permeability of fractures depends on the state of stress, the fluid pressure, the presence of proppant, and perhaps channels or tortuous pathways. In our model, we neglected the effect of proppant and the fractures were perfectly planar surfaces. In

practice, proppant effects are likely to be important for MDD interpretation, especially as changes during production cause cutoffs to flow pathways. In this study, we did, however, consider permeability to be a nonlinear function of effective stress which had important effects. In particular, the poroelastic effect tended to help keep fractures open longer during production. In Fig. 4, we show production rate during periods of production at constant pressure. Although the production duration was only one year in our study and the fluid was single-phase liquid, the rapid decline followed by a relatively steady tail is similar to behavior observed in many unconventional wells (*Vassilellis et al.*, 2010). The implication is that poroelastic stresses may have significant impacts in long-term production from fractured reservoirs.

The degree of coupling between poroelastic deformation and fluid flow deserves discussion. In our model, changes in matrix fluid pressure caused poroelastic stresses to develop. The poroelastic stresses influenced fracture deformation, which in turn influenced overall flow patterns. However, the poroelastic stresses did not change the matrix porosity. In Fig. 5.4, we observed that the production rate initially declined rapidly, but then tended to sustain flow at relatively low rates. We suggested that the poroelastic stresses had a positive feedback by helping to keep the fractures open to flow. Including the poroelastic stresses in the calculation of matrix porosity will likely impact the production behavior as well.

5.5 Concluding remarks

Determination of appropriate well spacing, especially for infill wells, remains a difficult task related to the economic development of unconventional shale resources. *Dohmen et al.* (2014) proposed a field test, called microseismic depletion delineation (MDD), to measure the extent of the depleted region near horizontal wells that have been produced. The MDD technique takes advantage of a poroelastic stress change that occurs in the reservoir during depletion, and also relies on the assumption that pressure transients will propagate relatively quickly in the network of fractures connected to the well. By reinjecting fluid at a carefully determined pressure while monitoring for microseismic activity, shear failure events on natural fractures will reveal the shape of the depleted zone.

In this work, we used numerical modeling to explore the MDD hypothesis from a fundamental and mechanistic perspective using a fully coupled flow and geomechanics reservoir simulator. We developed a synthetic model of a low-permeability fractured reservoir based loosely on data from a well in the Bakken field. We first modeled a multistage hydraulic fracture treatment of a horizontal well. We then modeled one year of production from the well to cause pressure drawdown in the matrix rock. Finally, we modeled the MDD test by reinjecting fluid at pressures well below the initial reservoir pressure for a short period of time.

During the production phase, poroelastic stresses developed that acted to make the principal stresses less compressive. We found that estimating the magnitude of the poroelastic stresses using

an assumption of uniaxial strain (Eq. 5.10) provided values that were reasonably close to the values calculated numerically. We used a Mohr-Coulomb failure criterion to estimate the critical injection pressure that would cause slip on natural fractures at the depleted stress state in order to design the MDD operational parameters.

In the model, the MDD test began by injecting fluid at a constant pressure below the critical pressure for one day. No shear slip events were observed during this period. Then, fluid pressure was increased until reaching a maximum specified pressure slightly above the critical pressure. Within one hour after the injection pressure exceeded the critical pressure, many shear failure events began to occur. The shear failure events were interpreted as proxies for microseismic events. The locations of the slip events were confined to areas in the reservoir that experienced significant drawdown. The slip events clearly delineated the heterogeneous distribution of reservoir pressure. The vast majority of all seismicity occurred within a six hour window, suggesting that the field test could be performed quickly.

By exploring the physical mechanisms central to the MDD hypothesis, we have shown that it is possible to exploit geomechanical processes that occur during depletion in a reservoir engineering context to learn useful information about the reservoir. The modeling results presented in this study support the application of MDD tests in the field as a reservoir surveillance technique to infer the extent of the depleted region. In practice, the success of a MDD test would depend heavily on developing an appropriate geomechanical model. The ability to interpret results from a MDD test relies on ensuring that observed microseismicity can occur only within the depleted region, so accurate constraints on the reservoir's geologic structure, initial stress state, and the magnitude of the poroelastic effect are critical to the application of microseismic depletion delineation.

Chapter 6

Hydromechanical and Frictional Faulting Response of the 2011 Mw 5.6 Prague, Oklahoma Earthquake Sequence

This work was presented originally in *Norbeck and Horne* (2016c). Mechanisms for the delayed triggering between the M_{w} 4.8 foreshock and M_{w} 5.6 main shock of the 2011 earthquake sequence near Prague, Oklahoma, USA were investigated using a coupled fluid flow and fault mechanics numerical model. Because the stress orientations, stress magnitudes, fault geometry, and earthquake source mechanisms at the Prague site have been well-characterized by previous studies, this particular earthquake sequence offered an opportunity to explore the range of physical processes and in-situ fault properties that might be consistent with the 20 hour delayed triggering effect observed at the site. Our numerical experiments suggest that an initial undrained response resulting from elastic stress transfer from the foreshock followed by transient fluid flow along the fault may have contributed to the earthquake nucleation process. The results of the numerical experiments were used to constrain fault compliance and fault transmissivity for the fault that hosted the M_{w} 5.6 event. Relatively compliant behavior in response to changes in normal stress, corresponding to Skempton pore pressure coefficients near 1, was consistent with the field observations. Fault transmissivity was estimated to range from 10^{-18} to 10^{-15} m^3. This study has implications for understanding hydraulic properties, frictional properties, and faulting behavior of basement faults in Oklahoma that are large enough to host damaging earthquakes.

6.1 Motivation

On 5 November, 2011, a M_w 4.8 earthquake (Event A) occurred near the town of Prague, Oklahoma, USA. The aftershock sequence and regional moment tensor indicated that this event occurred along a previously mapped portion of the Wilzetta Fault (*Keranen et al.*, 2013; *McNamara et al.*, 2015b). Based on recent measurements of the stress orientations and stress magnitudes in the area (*Walsh and Zoback*, 2016), this particular fault segment (Fault A) was oriented at roughly 50 degrees from the direction of maximum principal stress. On the morning of 6 November, 2011, roughly 20 hours after Event A, a M_w 5.6 earthquake (Event B) occurred in very close proximity to the prior event. Detailed analyses of the aftershock sequence and regional moment tensor for Event B indicated that the splay branch (Fault B) off the main Wilzetta Fault that hosted this event was optimally oriented for shear failure. *Keranen et al.* (2013) and *Sumy et al.* (2014) suggested that Event B was triggered by the elastic stress transfer caused by Event A.

In this study, we investigated possible mechanisms for the one-day delayed triggering between Events A and B. The conceptual model we tested involved a strong hydromechanical coupling in which changes in the state of stress along a fault can induce pressure changes and fluid flow within the fault zone. We hypothesized that the delayed triggering of Event B would have been influenced by fluid pressure diffusion along the fault following an initial undrained loading response to Event A as well as a time-dependent impact on fault friction caused by state evolution.

Because the geometry of Faults A and B, the rupture dimension of Event A, and the stress state in the area were reasonably well-characterized based on previous studies, this particular earthquake sequence provided an opportunity to learn about the in-situ properties of basements faults in Oklahoma that are capable of hosting relatively large earthquakes. Ultimately, our goal was to constrain hydraulic and frictional properties of Fault B by exploring the range of scenarios that could explain the observation of the delayed triggering.

It has been recognized that gaining an improved understanding of the interactions between faulting processes and fluid flow along faults will have important implications for analyzing hazard related to injection-induced seismicity (*Ellsworth*, 2013; *McGarr*, 2014; *McGarr et al.*, 2015). For the first time, injection-induced earthquakes have been included in an official one-year seismic hazard forecast for the central and eastern United States (*Petersen et al.*, 2016). However, the seismic hazard model did not relate any injection well operational parameters, such as injection pressure or injection rate, to changes in seismicity. Physics-based models capable of assessing seismic hazard related to induced seismicity, such as those described by *Norbeck et al.* (2016a) and *Király-Proag et al.* (2016), require detailed information about the hydraulic and mechanical properties of the faults that exist in the model. It remains difficult to use traditional reservoir engineering approaches, for example, pressure transient analysis, to measure the in-situ properties of basement faults that would be necessary to inform physics-based models of induced seismicity. Extending behavior observed in

the laboratory for fractured and faulted rocks to large fault structures can be questionable. As a practical alternative, we sought to identify and interpret signatures of hydromechanical behavior that would be useful for inferring properties of the basement faults involved in the Prague earthquake sequence.

The remainder of this chapter is organized as follows. In Section 6.2 we present the hydrogeologic and geomechanical conceptual model used in our study. In Section 6.3, we describe our fluid flow and fault mechanics numerical model. An overview of the theoretical background relevant to analysis of transient flow along faults and rate-and-state friction evolution is provided in Section 6.4. The results of the numerical experiments are provided in Section 6.5. Finally, we discuss the implications of our results for understanding faulting in Oklahoma in Section 6.6 and present several concluding remarks in Section 6.7.

6.2 Hydromechanical conceptual model

During an earthquake rupture, stresses are transferred through the material surrounding the fault. At time scales relevant to the propagation of the earthquake rupture along the fault (on the order of seconds), the extent of the stress transfer is mediated by the elastic wave speed. After an earthquake rupture has arrested, dynamic effects no longer play a role, and the stress change is effectively locked in. A common approach for analyzing the effects of elastic stress transfer induced by large earthquakes on subsequent earthquake activity is to calculate the Coulomb stress change resolved on the fault plane of interest as (*Pollard and Fletcher*, 2005):

$$\Delta\sigma_C = \Delta\tau - f\left(\Delta\sigma - \Delta p\right), \tag{6.1}$$

where τ is shear stress, σ is normal stress, p is fluid pressure within the fault zone, and f is the coefficient of friction. Compressive normal stresses are taken as positive in this sign convention. A positive $\Delta\sigma_C$ indicates the new stress state is more favorable for shear failure.

Sumy et al. (2014) performed a Coulomb stress analysis of the Prague earthquake sequence which suggested that the magnitude of the stress perturbations caused by Event A were sufficient to trigger Event B. However, the one-day delayed triggering implies that some time-dependent process controlled behavior during the sequence. Poroelastic effects, in which stress changes induce pressure changes and fluid flow, have been proposed as a possible physical mechanism for delayed aftershock triggering (*Cocco and Rice*, 2002; *Nur and Booker*, 1972; *Roeloffs*, 1996). As a practical example, *Bosl and Nur* (2002) analyzed the spatial and temporal distributions of aftershocks during the 1992 Landers sequence and illustrated a good correlation between the occurrence of aftershocks and zones of increasing Coulomb stress. Alternatively, some models of fault friction, such as the rate-and-state model, include temporal components that can reproduce realistic aftershock delay behavior (*Dieterich*, 1992, 1994; *Helmstetter and Shaw*, 2009; *Segall*, 2010). *Segall and Lu* (2015)

investigated the combined effects of poroelastic stressing and rate-and-state earthquake nucleation in the framework of a continuum-based semianalytical model and highlighted the interaction between transient fluid flow and friction evolution.

We developed a conceptual model of the Prague earthquake sequence based on interpretations of mapped faults, aftershock sequences, focal mechanisms, and measurements of the regional state of stress. We investigated the relative influence of hydromechanical and friction evolution effects by performing several numerical experiments using a reservoir model that calculated the coupled interaction between fluid flow, fault deformation, and earthquake rupture within a rate-and-state friction framework. The model geometry is illustrated in Fig. 6.1. Here, we provide an overview of the sources of information used to construct the model.

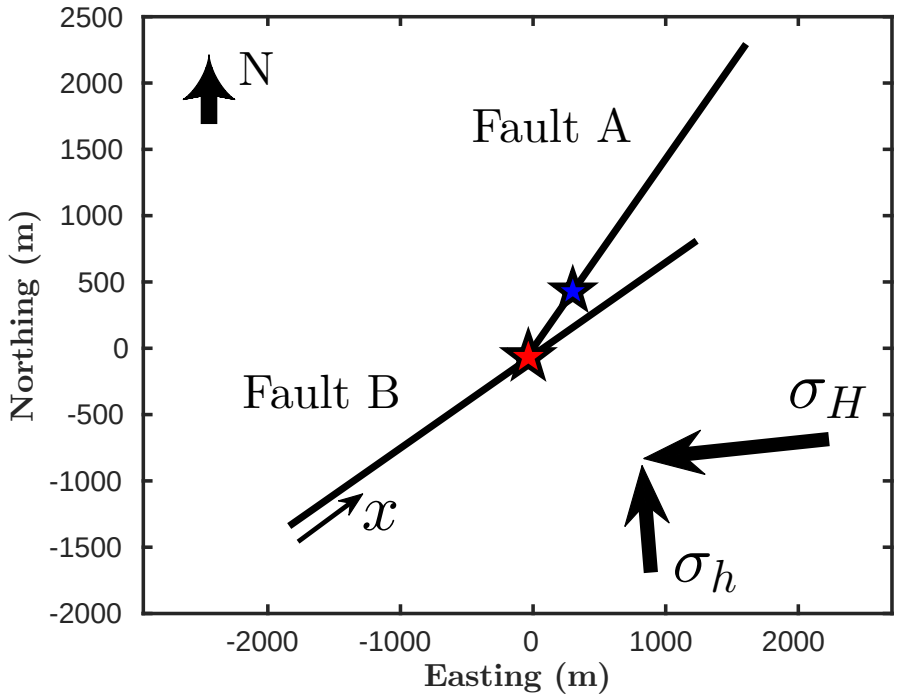

Figure 6.1: Illustration of the two-dimensional fault model geometry. Fault A represents a portion of the Wilzetta Fault that hosted the foreshock, and Fault B represents the splay branch that hosted the main shock. The stress regime in this area of Oklahoma is strike-slip with the maximum horizontal stress oriented at N85°E. The blue and red stars are the modeled epicenters of Event A and Event B, respectively.

6.2.1 Hydrogeology and stress state near Prague

Throughout most of Oklahoma, Precambrian basement rock is overlain directly by a sedimentary aquifer called the Arbuckle formation. *Nelson et al.* (2015) demonstrated how the fluid pressure in aquifers in the midcontinent of the United States is controlled by the elevation at which each unit outcrops. In the area near Prague, Oklahoma, *Nelson et al.* (2015) estimated that the Arbuckle exists in a state of natural underpressure with an equivalent fluid pressure gradient of approximately 9 MPa/km. We assumed that Faults A and B were connected hydraulically with the Arbuckle aquifer because many of the aftershocks from both events were located in the sedimentary sections above the basement (*Keranen et al.*, 2013; *McNamara et al.*, 2015b). *Alt and Zoback* (2014) analyzed wellbore image data for many oil and gas wells in Oklahoma to determine stress orientations and found that the orientation of the maximum horizontal stress in the area near Prague was roughly N85°E. *Walsh and Zoback* (2016) performed stress inversions using a focal mechanism analysis of 15 earthquakes near Prague to determine stress orientations and magnitudes in the area. That analysis assumed an overburden gradient of $\gamma_{\sigma_V} = 25$ MPa/km, a fluid pressure gradient of $\gamma_p = 9$ MPa/km, and a static friction coefficient of $f_S = 0.7$. The stress regime was found to be strike-slip and the orientation of the maximum principal stress was found to be N83°E, in close agreement with *Alt and Zoback* (2014). The minimum and maximum horizontal stress gradients were estimated as $\gamma_{\sigma_h} = 15$ MPa/km and $\gamma_{\sigma_H} = 30$ MPa/km, respectively.

6.2.2 Fault structure geometry

The fault structure geometry for the model used in our numerical experiments (see Fig. 6.1) was based off interpretations of seismic data performed by *Keranen et al.* (2013), *Sumy et al.* (2014), *Sun and Hartzell* (2014), and *McNamara et al.* (2015b). Focal mechanisms from the major earthquakes and many smaller aftershocks indicated that for both Events A and B, slip occurred on near vertical faults with a predominantly strike-slip sense of motion (*McNamara et al.*, 2015b; *NCEDC*, 2014). The focal mechanisms for both events each had a nodal plane orientation that was consistent with the distribution of aftershock locations. The hypocentral depths of Events A and B were recorded as 4.0 km and 7.0 km, respectively, although *McNamara et al.* (2015b) suggested that these depth estimations have large errors associated with them. The inversion performed by *Sun and Hartzell* (2014) suggested that slip on Fault B nucleated at a hypocentral depth of 5 km and was confined initially between depths of 4 to 6 km. In their analysis, *Sumy et al.* (2014) estimated the rupture dimension for Event A as 2.8 km long by 2.9 km deep and for Event B as 8.3 km long by 5.4 km deep based on the distributions of aftershocks. *McNamara et al.* (2015b) estimated the rupture dimension of Event B to be much larger, perhaps as large as 20 km long by 10 km deep.

For our analysis, we modeled Faults A and B as two-dimensional vertical structures within a strike-slip stress regime. The faults were centered at a depth of 5 km, and each had a height of

2.5 km in the vertical direction. The principal stress magnitudes and fluid pressure initially were σ_{H0} = 150 MPa, σ_{h0} = 75 MPa, and p_0 = 45 MPa. Stress and pressure were assumed constant along the vertical dimension of the faults, which is a limitation of our two-dimensional model. Fault A represented a segment along the main Wilzetta Fault, and was modeled as a 2.8 km long segment oriented at N35°E. Fault B represented a splay branch off of the main Wilzetta Fault, and was modeled as a 4.5 km long segment oriented at N55°E. The interpretation provided by *McNamara et al.* (2015b) suggested that Fault B is likely much longer, but because we were only interested in the nucleation phase of Event B and not the full extent of the rupture this did not affect our results significantly. The orientation of σ_H was N85°E, based on the stress indicators provided by *Alt and Zoback* (2014) and *Walsh and Zoback* (2016).

6.3 Numerical model

We performed numerical experiments using a reservoir model that coupled transient fluid flow, fault mechanics, and rate-and-state earthquake rupture. Details of the numerical formulation can be found in *McClure and Horne* (2011), *McClure* (2015), *Norbeck et al.* (2016a), *Norbeck et al.* (2016b), and *Norbeck and Horne* (2016a). The model assumed that the faults were saturated with water and were surrounded by impermeable basement rock. A quasidynamic elasticity formulation was used to model stress transfer along the faults and in the surrounding rock. A two-dimensional displacement discontinuity method was used to relate changes in stress to fault displacement (*Bradley*, 2014). The elastic properties of the rock surrounding the faults were assumed to be homogeneous.

Although our model is able to solve the full set of equations that describe poroelasticity in a continuum sense (e.g., see *Norbeck and Horne* (2015a) and *Norbeck and Horne* (2016a)), it is important to to note that in this study we only considered flow within the fault zone structures. Mass transfer between the faults and the surrounding rock and any associated poroelastic deformation of the host rock was neglected based on the assumption of extremely low permeability of basement rock. Nonetheless, our numerical experiments had the character of poroelasticity due to our choice of a nonlinear fault stiffness constitutive relationship between void volume and changes in effective stress. We use the term hydromechanical deformation to describe the faulting process in order to avoid confusion with more general poroelastic treatments.

The two-dimensional representation of the fault structures was a major simplification in the model that has several important consequences when interpreting the results of our analysis. Both faults were vertical, located at the same depth, and had the same height. Stress and pressure gradients in the vertical direction were neglected. The sense of slip during both major events was predominantly strike-slip which justified the use of vertical faults, but in reality geometrical effects would have contributed to the magnitude and shape of the stress changes along Fault B. The inversion performed by *Sun and Hartzell* (2014) placed the hypocenter of the nucleation site of Event B at 5

km depth. The distribution of aftershocks on both faults existed at similar depths over the range of several kilometers, which suggests that the stress perturbations caused by the foreshock may have affected Fault B at depths near the hypocentral location of Event A. Using a two-dimensional model allowed us to employ a spatial discretization along the faults that was fine enough to ensure numerically-converged solutions for the earthquake nucleation process for values of the characteristic slip-weakening distance as low as $\delta_c = 50 \times 10^{-6}$ m (*Lapusta et al.*, 2000; *Rice and Ben-Zion*, 1996).

6.3.1 Fluid flow along faults

For one-dimensional Darcy flow in the along-fault direction, fluid mass balance can be expressed as (*Norbeck et al.*, 2016a):

$$\frac{\partial}{\partial x}\left(T\frac{\rho}{\mu}\frac{\partial p}{\partial x}\right) = \frac{\partial}{\partial t}\left(\rho E\right), \tag{6.2}$$

where T is fault transmissivity, ρ is water density, μ is water viscosity, and E is fault void aperture. The fault transmissivity can be thought of as the product of permeability and hydraulic aperture (thickness available for flow in the along-fault direction). The void aperture is related to the fault porosity, and in our model was assumed to behave according to a nonlinear fault stiffness relationship (*Bandis et al.*, 1983; *Barton et al.*, 1985; *Willis-Richards et al.*, 1996):

$$E = \frac{E_*}{1 + 9\frac{\bar{\sigma}}{\sigma_*}}, \tag{6.3}$$

where $\bar{\sigma} = \sigma - p$ is the effective normal stress, and the constants E_* and σ_* define the fault stiffness. Hydromechanical coupling arises entirely from the relationship between void volume and effective stress in Eq. 6.3.

6.3.2 Fault mechanics

For the mode-II plane strain quasidynamic elasticity formulation and assuming a Mohr-Coulomb-type shear failure criterion, mechanical equilibrium along the fault can be described as (*Ben-Zion and Rice*, 1997):

$$\tau_0 - \eta V + \Phi = f\bar{\sigma} + s. \tag{6.4}$$

where τ_0 is the initial shear stress due to the tectonic loading, V is the sliding velocity, Φ is the quasistatic stress transfer, η is a material property related to the shear wave speed and density of the host rock, and s is fault cohesion. The friction coefficient was modeled using a rate- and state-dependent constitutive formulation (*Dieterich*, 1992; *Rice et al.*, 2001):

$$f\left(V, \Psi\right) = a \ln \frac{V}{V_*} + \Psi. \tag{6.5}$$

Here, a controls the magnitude of the direct velocity-strengthening effect and Ψ is the state variable. State was assumed to evolve according to the aging law description (*Rojas et al.*, 2009):

$$\frac{\partial \Psi}{\partial t} = -\frac{bV}{\delta_c}\left\{1 - \exp\left[-\frac{f\left(V,\Psi\right) - f_{ss}\left(V\right)}{b}\right]\right\}. \tag{6.6}$$

State evolution occurs over a characteristic slip-weakening distance, δ_c, and evolves towards a steady-state while sliding at constant V, which is defined by a steady-state friction coefficient:

$$f_{ss}\left(V\right) = f_* - \left(b - a\right)\ln\frac{V}{V_*}. \tag{6.7}$$

In Eqs. 6.6 and 6.7, b controls the magnitude of the state evolution effect. *Linker and Dieterich* (1992) demonstrated through laboratory experiments that $\partial\Psi/\partial t$ may also have a dependence on changes in $\bar{\sigma}$. We neglected that effect in this study, but it may be worthwhile to investigate in future studies. Equations 6.2 and 6.4 were solved numerically in a fully-coupled framework.

6.4 Theoretical framework

In this section, we present a brief description of the relevant physical processes considered in our numerical experiments. The range of each model parameter tested in the study was guided by this theoretical framework.

6.4.1 Static stress change caused by Event A

We modeled Event A as a M_{w} 4.8 event resulting from a uniform stress drop of roughly 1.7 MPa over a 2.8 km by 2.5 km rupture surface. The spatial distributions of the Coulomb stress changes induced by Event A (as resolved along Fault B) are shown in Figs. 6.2 and 6.3. The largest changes in Coulomb stress did not occur near the epicenter of Event A, but rather near the crack tips of the rupture patch. The distribution of the induced stresses resolved along Fault B are shown in Fig. 6.4. The stress concentrations were large in the vicinity of the tip of Fault A, but fell off to the background levels over distances of several hundred meters. The largest induced shear stress and largest reduction in normal stress were both on the order of 2 – 3 MPa. Based on the initial state of stress and a static friction coefficient of $f_S \approx 0.7$, the critical change in Coulomb stress to initiate slip, $\Delta\sigma_{C,crit} = f_S\bar{\sigma}_0 + s - \tau_0$, was calculated to be 2.15 MPa.

6.4.2 Undrained response and fault compliance

Following *Segall* (2010), the change in fluid mass in a fault zone control volume in response to perturbations Δp and $\Delta\sigma$ is:

$$\Delta m = \Delta\left(\rho E\right) = E_0\Delta\rho + \rho_0\Delta E, \tag{6.8}$$

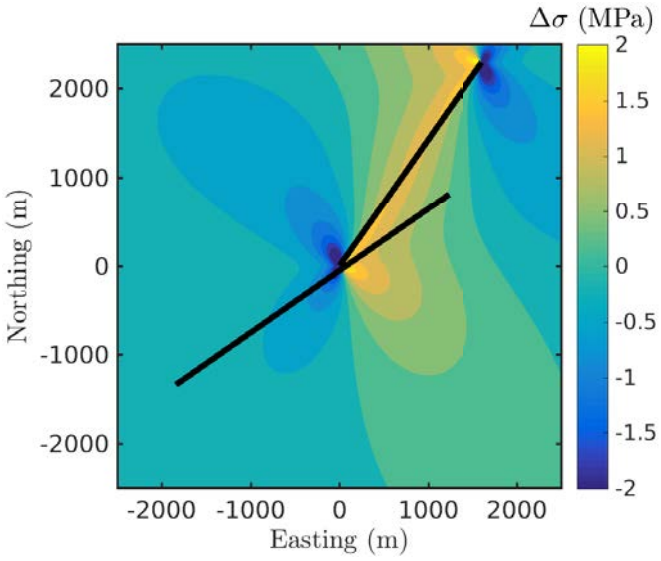

Figure 6.2: The distribution of the static stress change caused by Event A. This figure shows the normal stress component of the Coulomb stress change resolved in the orientation of Fault B. Increased compressive stresses were generated behind the rupture front, whereas decreased compressive stresses were generated ahead of the rupture patch.

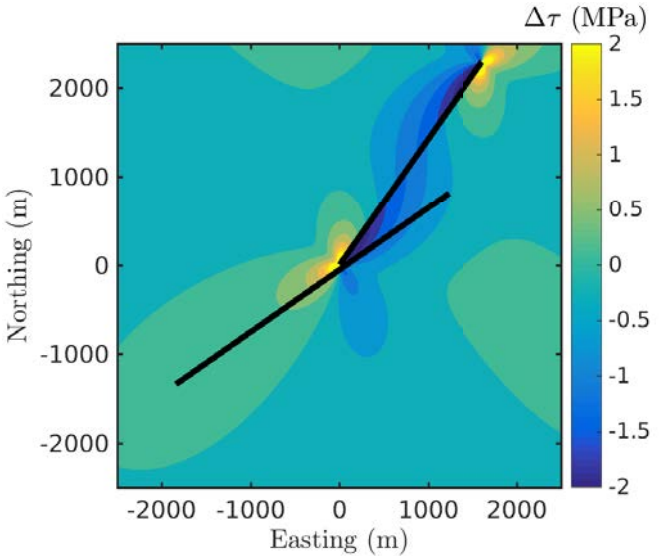

Figure 6.3: The distribution of the static stress change caused by Event A. This figure shows the shear stress component of the Coulomb stress change resolved in the orientation of Fault B. A reduction in shear stress occurred behind the rupture patch, and concentrations of increased shear stress occurred ahead of the rupture patch.

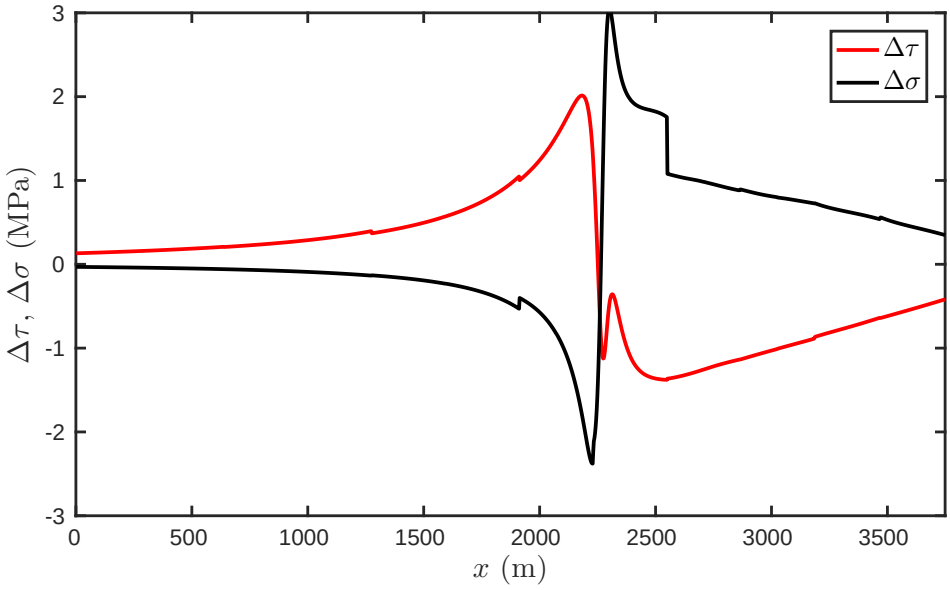

Figure 6.4: Distributions of the changes in shear and normal stresses along Fault B resulting from the elastic stress transfer caused by slip on Fault A.

where E_0 and ρ_0 are the void aperture and water density at a reference state. Water compressibility is defined as $\beta_\varphi = (1/\rho)(\partial\rho/\partial p)$. The nonlinear stiffness relationship used in our model (Eq. 6.3) can be used to define fault compressibility as $\beta_f = (1/E)(\partial E/\partial p) = -(1/E)(\partial E/\partial\sigma)$. Note that the fault compressibility is related directly to the mode-I fault compliance, which is usually defined as $\partial E/\partial\sigma$, so we use the terms interchangeably in this paper.

In the undrained limit, the flux term in Eq. 6.2 must vanish, so the change in fluid mass content in the fault control volume can be expressed as:

$$\frac{\Delta m}{\rho_0 E_0} = (\beta_f + \beta_\varphi)\,\Delta p - \beta_f \Delta\sigma \equiv 0. \tag{6.9}$$

The instantaneous change in fluid pressure in the fault zone with respect to the static stress change caused by a nearby earthquake is:

$$B = \frac{\Delta p}{\Delta\sigma} = \frac{\beta_f}{\beta_f + \beta_\varphi}. \tag{6.10}$$

The parameter B is analogous conceptually to the Skempton coefficient in poroelasticity. Laboratory measurements suggest that the Skempton coefficient for rocks ranges from 0.4 to 1 (*Lockner and Stanchits*, 2002; *Roeloffs*, 1996).

In the earthquake aftershock triggering process, the instantaneous undrained response acts to negate changes in normal stress at early time. In Figs. 6.5 and 6.6 we compare the change in Coulomb

stress along Fault B for stiff and compliant responses, respectively. Separating the relative influence of the different terms affecting $\Delta\sigma_C$ in Eq. 6.1 illustrates that $\Delta\tau$ dominates the immediate response as $B \to 1$.

It is important to recognize the differences between the hydromechanical model applied in this work and traditional poroelastic theory. We used the displacement discontinuity method to perform fault deformation calculations, therefore the faults were represented mathematically as infinitely thin surfaces. A limitation of the model is that were were unable to resolve mechanical processes within the fault zone material itself. In poroelastic theory, the fault pore volume deforms subject to changes in mean stress (*Segall*, 2010). In contrast, the pore volume of the faults in our model deforms subject to the nonlinear stiffness relation (see Eq. 6.3) which is affected only by the normal stress acting on the fault. *Cocco and Rice* (2002) investigated poroelastic response to stress changes resulting from earthquakes and demonstrated that if the rigidity of the fault zone material is significantly less than that of the intact rock surrounding the fault, then the change in fluid pressure within the fault zone is dominated by changes in the normal stress component (i.e., it is unnecessary to resolve the mean stress within the fault zone). The argument of rigidity contrast effects proposed by *Cocco and Rice* (2002) supports the use of constitutive relationships such as the one used in this study. Another simplification in our model is that the empirical nature of Eq. 6.3 implicitly assumes that the rock grain compressibility is negligible, which is why Eq. 6.10 appears slightly different from that derived by *Zimmerman* (1992).

The stiffness relationship used in our model (Eq. 6.3) was developed for open fractures or joints, and it is not clear if it is directly applicable to fault structures. Fault zones are often believed to contain a low-permeability, stiff inner core surrounded by a more permeable, more compliant fractured damage zone. *McClure et al.* (2016b) used field data from diagnostic fracture injection tests to constrain the stiffness parameters in Eq. 6.3 for hydraulic fractures during fracture closure and observed relatively compliant behavior. In this case, $\beta_f \gg \beta_\varphi$ and $B \to 1$. For a narrow damage zone comprised of many fractures, the mechanical interactions between the individual fractures results in an overall stiffer response than for a single fracture, so it is likely that the stiffness values provided by *McClure et al.* (2016b) are lower-bounds for faults. When β_f is taken as the pore compressibility of intact rock, B can be lower. In our analysis we tested a range of scenarios where $B = 0$, $B = 0.5$, and $B = 1$.

6.4.3 Transient flow and fault transmissivity

Following the arrest of Event A, the total normal stress along Fault B remained fixed so that changes in void volume occurred only from pressure changes. Assuming that the fault transmissivity is

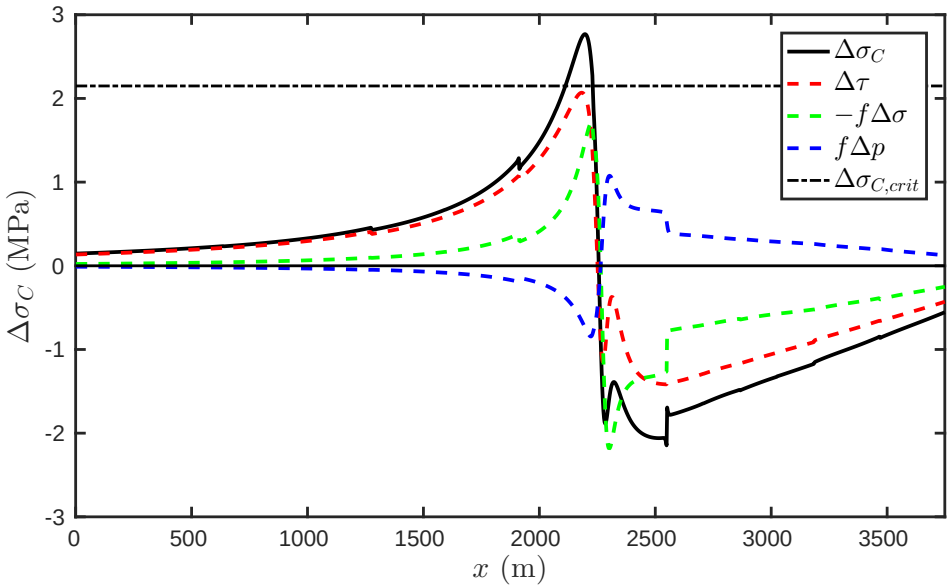

Figure 6.5: Change in Coulomb stress following an instantaneous undrained response along Fault B for a stiff fault with $B = 0.5$.

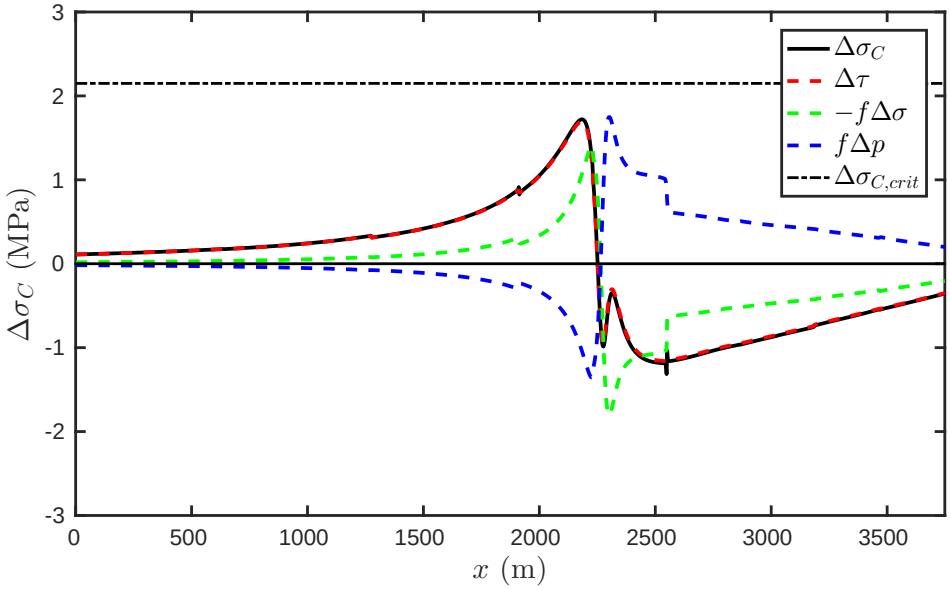

Figure 6.6: Change in Coulomb stress following an instantaneous undrained response along Fault B for a compliant fault with $B = 1$.

constant for small pressure changes and before slip begins to occur, Eq. 6.2 can be linearized as:

$$\frac{T}{\mu}\frac{\partial^2 p}{\partial x^2} = E_0\left(\beta_f + \beta_\varphi\right)\frac{\partial p}{\partial t}. \tag{6.11}$$

The hydraulic diffusivity for fluid flow along faults, $D_H = T/\left[E_0\left(\beta_f + \beta_\varphi\right)\mu\right]$, can be introduced to simplify the appearance of Eq. 6.11:

$$D_H\frac{\partial^2 p}{\partial x^2} = \frac{\partial p}{\partial t}. \tag{6.12}$$

Pressure transients will occur across characteristic temporal and length scales (t_c and x_c) according to:

$$\frac{x_c^2}{t_c} \sim D_H \sim \frac{T}{E_0\left(\beta_f + \beta_\varphi\right)\mu}. \tag{6.13}$$

The functional form of hydraulic diffusivity given in Eq. 6.13 is distinct from the traditional form used to analyze flow in porous media and is particularly useful for understanding flow along fault zone structures. In particular, we are able to acknowledge, using this form of D_H, many of the complexities and epistemic uncertainties associated with natural faults. Instead of emphasizing permeability, this form of D_H emphasizes fault transmissivity in order to recognize that the physical thickness of the fault zone and connectivity of the fractured damage zone can be difficult to measure in practice. The void aperture of the fault zone material may involve contributions from both connected and unconnected fracture porosity as well as porosity of the intact rock.

In our numerical experiments, we assumed that the fluid pressure distribution in the fault was spatially uniform at the initial condition. The instantaneous changes in fluid pressure for faults subjected to changes in normal stress is controlled by the fault compliance, as described by Eq. 6.10. In our model, stress concentrations were largest in the vicinity of where the two fault surfaces met because the Event A rupture was assumed to have arrested at that location based on the distribution of aftershocks (*McNamara et al.*, 2015b). In Figs. 6.2 and 6.4, it is observed that the changes in normal stress resolved on Fault B transitioned from decreased compression (unclamping) to increased compression (clamping) across the intersection with the Fault A crack tip.

In Fig. 6.7, a typical simulation result for the transient pressure response along the fault is illustrated. During the initial undrained response, a significant pressure change was induced along Fault B both ahead of and behind the crack tip of Fault A. Pressure gradients induced fluid flow along the fault, and the pressure eventually equilibrated back toward the initial condition. Meanwhile, the total normal stress along Fault B remained constant, so the changes in fluid pressure over time resulted in a transient loading mechanism that influenced the nucleation process.

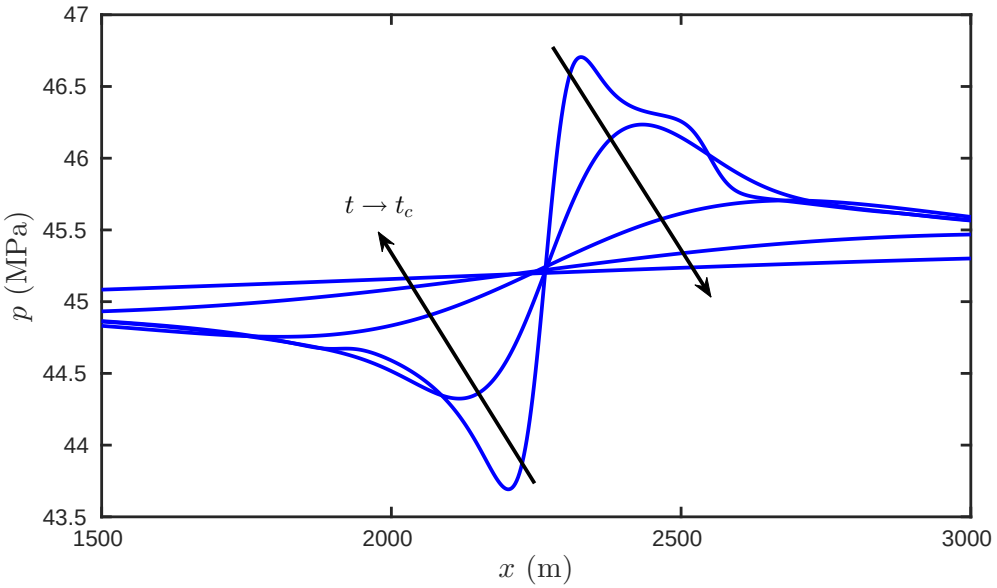

Figure 6.7: Distribution of fluid pressure along Fault B at several snapshots in time following the arrest of Event A corresponding to $t/t_c = 0$, 0.05, 0.1, 0.2, and 1. Following an instantaneous undrained response the pressure in the fault began to equilibrate, effectively bringing part of the fault closer to failure.

6.4.4 Time to instability

During the nucleation phase of an earthquake while the sliding velocities are still small, the inertial term in Eq. 6.4, ηV, can be neglected. In an idealized spring-slider faulting model, the stress drop along the fault can be approximated as the product of the mode-II fault stiffness and some average slip quantity, i.e., $\Phi \approx -k \langle \delta \rangle$. Taking the time derivative of both sides of Eq. 6.4 gives:

$$\frac{\partial \tau}{\partial t} = -kV = \bar{\sigma} \left(\frac{a}{V} \frac{\partial V}{\partial t} + \frac{\partial \Psi}{\partial t} \right) + f \frac{\partial \bar{\sigma}}{\partial t}. \tag{6.14}$$

We can define a characteristic stiffness as $k_c = -(\bar{\sigma}/V)(\partial \Psi / \partial t)$. Rearranging Eq. 6.14 yields a partial differential equation that describes the evolution of the sliding velocity:

$$\frac{\partial V}{\partial t} = \frac{(k_c - k)}{a\bar{\sigma}} V^2 + \frac{f}{a\bar{\sigma}} \frac{\partial p}{\partial t} V. \tag{6.15}$$

We recognize that $k_c \sim (f - f_{ss})$ is a weak function of V and friction is approximately constant at the static friction level during nucleation (i.e., $f \approx f_S$). In general, $\partial p / \partial t$ is not constant during transient flow, but here we assume it to be so for the sake of obtaining a tractable solution. Following

Dieterich (1994), Eq. 6.15 can be integrated to solve for V:

$$V = \frac{V_0}{1 - \dfrac{t}{a\bar{\sigma}/\left[(k_c - k)\, V_0\right]}}, \quad \frac{\partial p}{\partial t} = 0, \tag{6.16}$$

$$V = \left\{ \left[\frac{1}{V_0} + \frac{f_S}{(k_c - k)\left(\frac{\partial p}{\partial t}\right)} \right] \exp\left[-\left(\frac{f_S}{a\bar{\sigma}}\right)\left(\frac{\partial p}{\partial t}\right) t \right] - \frac{f_S}{(k_c - k)\left(\frac{\partial p}{\partial t}\right)} \right\}^{-1}, \quad \frac{\partial p}{\partial t} \neq 0. \tag{6.17}$$

Setting $1/V = 0$ in Eqs. 6.16 and 6.17 and solving for t yields a good approximation for the time to instability:

$$t_i = \frac{a\bar{\sigma}}{(k_c - k)\, V_0}, \quad \frac{\partial p}{\partial t} = 0, \tag{6.18}$$

$$t_i = \frac{a\bar{\sigma}}{f_s\,(\partial p/\partial t)} \ln\left[\frac{f_S\,(\partial p/\partial t)}{(k_c - k)\, V_0} + 1 \right], \quad \frac{\partial p}{\partial t} \neq 0. \tag{6.19}$$

These expressions are useful for understanding how each parameter influences the time to instability.

In Fig. 6.8, we show a representative history of sliding velocity along Fault B following the end of the foreshock obtained from the numerical experiments. As Event A died out, the elastic stress transfer effectively loaded the fault with a step change in Coulomb stress. *Dieterich* (1994) showed that the velocity response to step changes in normal and shear stress is (here, neglecting the *Linker and Dieterich* (1992) effect):

$$V = V_0 \exp\left(\frac{\tau}{a\bar{\sigma}} - \frac{\tau_0}{a\bar{\sigma}_0} \right). \tag{6.20}$$

This effect acted to increase the sliding velocity to a new value. Following the initial loading by elastic stress transfer, fluid flow along the fault acted as a transient loading mechanism. This contributed to additional velocity increase as described by Eq. 6.20, which in turn increased the rate of state evolution. Finally, rapid acceleration occurred. Event B nucleated and began to propagate as a sustained rupture.

6.5 Numerical experiments

The purpose of the numerical experiments was to determine whether transient effects related to rate-and-state friction evolution and hydromechanical coupling could plausibly explain the 20 hour delay between Events A and B. Both the hydromechanical processes (see Eqs. 6.10 and 6.13) as well as frictional processes (see Eqs. 6.18 and 6.19) involve combinations of parameters that can lead to nonunique interpretations of the behavior. It was necessary to specify a realistic set of parameters around which perturbations were made to investigate the relative influence of each physical property.

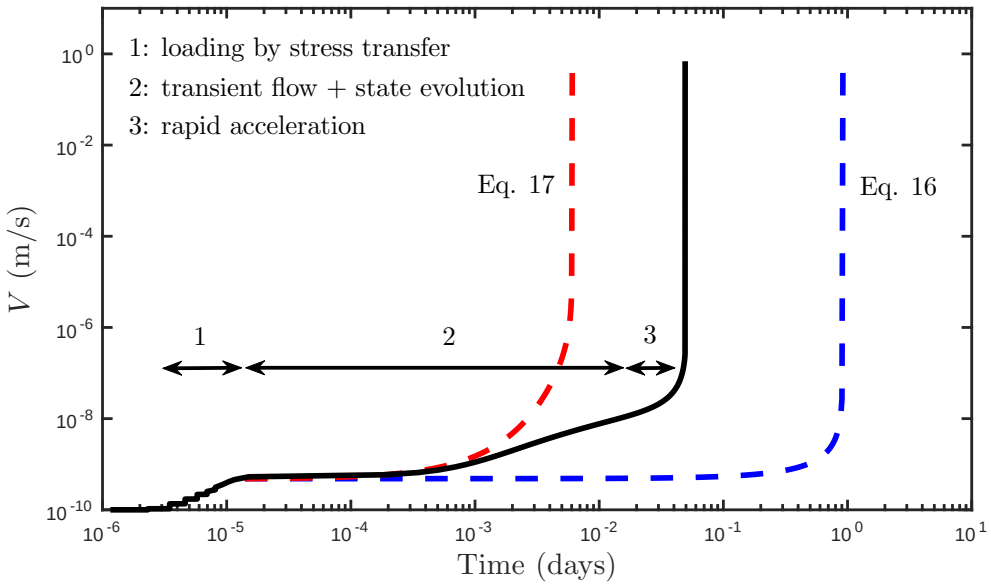

Figure 6.8: A typical profile for the evolution of sliding velocity at the nucleation site on Fault B following the end of the foreshock. The initial stress transfer loading caused a jump in the sliding velocity according to Eq. 6.20. Next, a gradual loading from transient flow combined with state evolution effects (see Eq. 6.15) caused a mild increase in velocity. Finally, nucleation became inevitable as rapid acceleration occurred. The black line is the result of a numerical simulation. The blue and red dashed lines show the velocity evolution described by Eqs. 6.16 and 6.17, respectively, for the same properties used in the simulation.

The rate-and-state frictional properties used in the numerical experiments were based on laboratory friction experiments performed on granite samples with gouge (*Dieterich*, 1981; *Marone and Kilgore*, 1993; *Marone*, 1998). It has been recognized that the values of the rate-and-state parameters, a and b, do not vary largely across different experiments, however, it has been speculated that the characteristic slip-weakening distance, δ_c, may depend on fault roughness and may be scale-dependent (*Dieterich*, 1981; *Marone and Kilgore*, 1993). In the expression for time to instability (see Eq. 6.18), the time to instability scales with the direct-effect parameter as $t_i \sim a$ and with the initial sliding velocity as $t_i \sim 1/V_0$. In our experiments, we tested a range of $0.005 \leq a \leq 0.02$ while holding $(b - a) = 0.004$ constant. The initial sliding velocity was held the same in each simulation and was prescribed to be $V_0 = 10^{-12}$ m $\cdot$ s^{-1}. This value was relatively arbitrary because there are not good constraints on the background sliding velocity of inactive faults in Oklahoma, other than they must be sliding very slowly given that there have not been any large earthquakes in recent history. The slip-weakening distance was fixed to a value of $\delta_c = 50 \times 10^{-6}$ m, consistent with laboratory friction measurements (*Dieterich*, 1981). The initial value of the state variable, Ψ_0, was defined by the initial sliding velocity and the initial stress conditions along the fault to be

$\Psi_0 = \tau_0/\bar{\sigma}_0 - a \ln (V_0/V_*)$.

One of the primary goals of this work was to develop constraints on the in-situ hydraulic properties of fault structures that are capable of hosting large earthquakes. To arrive at a first estimate of the hydraulic properties, the hydraulic diffusivity of the fault was estimated based on the assumption that hydromechanical effects were the dominant triggering mechanism. The characteristic diffusion time of interest was $t_c \approx 1$ day. Based on the modeled Coulomb stress changes illustrated in Figs. 6.5 and 6.6, the diffusive length scale of interest (i.e., the distance over which $\Delta\sigma_C > \Delta\sigma_{C,crit}$) was approximately $x_c \approx 100$ m. A first-order estimate of hydraulic diffusivity was calculated as $D_H \sim x_c^2/t_c \approx 0.1$ m$^2 \cdot$ s^{-1}. *Shapiro et al.* (2005) estimated the hydraulic diffusivity of a fractured granite geothermal reservoir to be $D_H = 0.16$ m$^2 \cdot$ s^{-1}, which is the same order of magnitude as our first-order estimate for the Prague fault. *Xue et al.* (2013) measured the hydraulic properties of a large fault structure based on tidal fluctuations in a borehole and estimated the diffusivity to be roughly $D_H = 0.024$ m$^2 \cdot$ s^{-1}, which is roughly four times lower than our first-order estimate for the Prague fault. Note that the field measurements performed by *Xue et al.* (2013) did not interrogate the highly damaged zone close to the major slip plane directly, but rather a broader damage zone encompassing several hundred meters surrounding the major slip plane, so their estimate of D_H may be a lower-bound. Compared to measurements of fault zone diffusivity, our first-order estimate of D_H provided a reasonable basis around which to vary parameters in this study.

The hydraulic diffusivity is the ratio of transmissivity to storativity (i.e., $D_H = T/S = T/\left[E_0 \left(\beta_f + \beta_\varphi\right) \mu\right]$). To arrive at a first-order estimate of the storativity of the fault zone we assumed that most of the storage volume was located within the densely fractured damage zone, because fracture density typically exhibits a power-law decay with distance away from the slip plane (*Faulkner et al.*, 2010). Assuming a 5 m thick damage zone with a porosity of 1% gives an estimate for the fault void volume as $E_0 = 0.05$ m. This value of E_0 was held constant in each numerical experiment. The fault zone compressibility influences the storativity of the fault as well as the magnitude of the undrained pressure response. The compressibility of porous rock can vary from an order of magnitude less than water to an order of magnitude greater than water (*Horne*, 1995; *Townend and Zoback*, 2000). As described in Sect. 6.4.2, the compressibility of individual fractures can be several orders of magnitude larger than water (*McClure et al.*, 2016b). As a first-order estimate of the fault zone compressibility, we took $\beta_f = \beta_\varphi$. In the numerical simulations, we tested variable fault compressibility values over the range of $\beta_\varphi/9 \leq \beta_f \leq 9\beta_\varphi$, which corresponded to Skempton coefficients ranging from $0.1 \leq B \leq 0.9$. Fluid properties were taken to reflect those of water at 45 MPa and 150 °C (*Lemmon et al.*, 2016), giving $\beta_\varphi = 5 \times 10^{-10}$ Pa^{-1}, $\rho_0 = 940.3$ kg $\cdot$ m^{-3}, and $\mu = 2 \times 10^{-4}$ Pa $\cdot$ s. Based on these values, first-order estimates of fault storativity and transmissivity were calculated to be $S = 10^{-14}$ m $\cdot$ s and $T = 10^{-15}$ m^3, respectively. In the numerical experiments, we varied transmissivity over six orders of magnitude ranging from $10^{-18} \leq T \leq 10^{-12}$ m^3.

We tested three different scenarios (Cases 1 through 3) to determine which types of physical processes and groups of fault properties could explain the one day delayed triggering between Events A and B (see Table 6.1 for a description of each case). The model properties used in the numerical experiments are listed in Table 6.2. The main comparison metric was the time to instability, t_i, of Event B.

Table 6.1: Description of the four sets of numerical experiments.

	Description
Case 1	Variable fault compliance ($0.1 \leq B \leq 0.9$) Transmissivity held constant ($T = 10^{-15}$ m^3)
Case 2a	Relatively stiff fault (B = 0.5) Variable transmissivity (10^{-18} m^3 $\leq T \leq 10^{-12}$ m^3)
Case 2b	Relatively stiff fault (B = 0.9) Variable transmissivity (10^{-18} m^3 $\leq T \leq 10^{-12}$ m^3)
Case 3	Negligible hydromechanical effects ($B = 0$ and $T = 0$) Variable direct-effect parameter ($0.005 \leq a \leq 0.02$)

Table 6.2: Model properties used in the numerical experiments.

Parameter	Value	Unit
Depth	5	km
σ_{H0}	150	MPa
σ_{h0}	75	MPa
p_0	45	MPa
θ_{σ_H}	N85°E	-
θ_A	N35°E	-
θ_B	N55°E	-
μ	2×10^{-4}	Pa · s
ρ_0	940.3	kg · m^{-3}
β_φ	5×10^{-10}	Pa^{-1}
G	15	GPa
ν	0.25	-
η	3	MPa · s · m^{-1}
E_0	0.05	m
β_f	$\beta_\varphi/9$ – $9\beta_\varphi$	Pa^{-1}
T	10^{-18} – 10^{-12}	m^3
f_*	0.7	-
V_*	1×10^{-12}	m · s^{-1}
a	0.005 – 0.02	-
$(b - a)$	0.004	-
s	0.5	MPa

6.5.1 Case 1: Fault compliance

The compressibility or compliance of the fault zone material influenced the magnitude of the undrained loading response to changes in normal stress. In Eq. 6.10, larger β_f and larger B allow for larger pressure perturbations in the undrained loading response. Because the pressure perturbations act to negate the changes in total normal stress, this mechanism dampens the initial Coulomb stress change and tends to discourage shear failure. In Case 1, we investigated the influence of fault zone compliance on the time to instability of the main earthquake (Event B). The fault zone compressibility was varied over the range of $\beta_\varphi/9 \leq \beta_f \leq 9\beta_\varphi$, which corresponded to Skempton coefficient values ranging from $0.1 \leq B \leq 0.9$. In each case, the fault zone transmissivity was held constant at $T = 10^{-15}$ m^3.

In Fig. 6.9, the sliding velocity histories at the Event B nucleation site for Case 1 are shown. The fault zone compliance affected the time to instability most notably through the initial rise in sliding velocity, which was influenced by the magnitude of $\Delta\sigma_C$ experienced by Fault B during the foreshock. For the fault with the lowest compliance ($B = 0.1$), nearly the full static stress change was realized immediately, driving the fault to rupture only 52 minutes following the arrest of Event A. For the scenarios where $B = 0.5$ and $B = 0.9$, the effect of the Coulomb stress dampening was to delay the onset of instability, which resulted in times to instability of 3.5 hours and 14.3 hours, respectively. The results of this numerical experiment demonstrate that hydromechanical coupling, in particular, the undrained loading response, can influence the earthquake nucleation process significantly.

6.5.2 Case 2: Fault transmissivity

In our numerical experiments, the undrained loading response resulted in significant fluid pressure perturbations within the fault zone. Fluid flow occurred along the fault structure in response to the pressure gradients that developed, ultimately driving the fluid pressure distribution in the fault back toward equilibrium. Because the change in total normal stress caused by the foreshock remained constant, the transient flow period acted as a loading mechanism by gradually reducing the effective normal stress acting over some parts of the fault (see Fig. 6.7). The transmissivity of the fault controlled the time scales over which the transient loading occurred. Laboratory and field experiments have indicated that fault transmissivity can vary over many orders of magnitude. In Case 2, we performed two sets of numerical experiments to investigate the effect of the fault transmissivity by varying transmissivity over the range of $10^{-18} \leq T \leq 10^{-12}$ m^3. In Case 2a relatively stiff behavior was tested ($B = 0.5$), and in Case 2b relatively compliant behavior was tested ($B = 0.9$).

The sliding velocity profiles for Cases 2a and 2b are shown in Figs. 6.10 and 6.11, respectively. In both cases, the scenarios with the largest transmissivity underestimated the time to instability by nearly two orders of magnitude. The scenarios with medium and low transmissivity estimated the

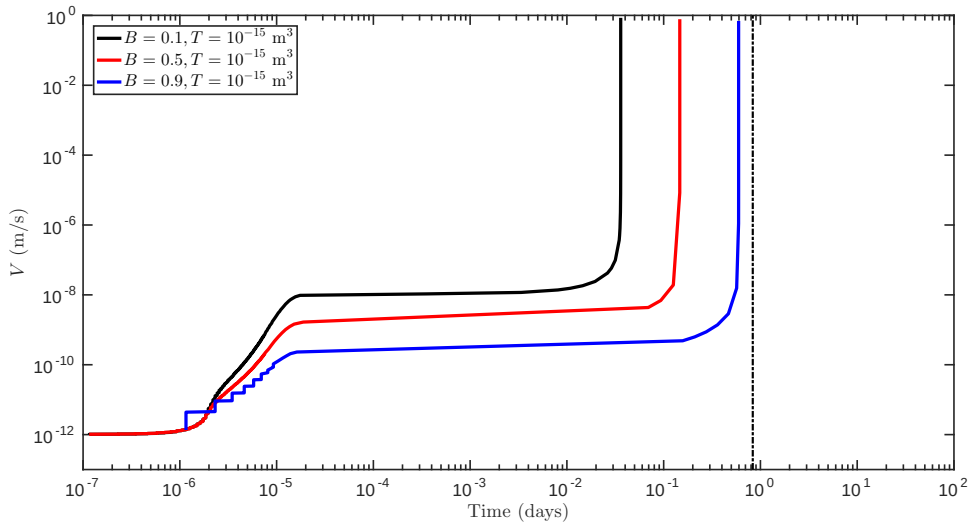

Figure 6.9: Sliding velocity history at the Event B nucleation site for Case 1. The actual timing of Event B is shown as the vertical dashed line. The fault zone compressibility was varied from $\beta_\varphi/9 \leq \beta_f \leq 9\beta_\varphi$, which corresponded to Skempton coefficients that varied over the range of $0.1 \leq B \leq 0.9$. For larger fault compressibility, the undrained loading effect that acted to dampen the Coulomb stress change temporarily was more pronounced, which increased the time to instability. For the lowest fault compressibility tested, the time to instability was underestimated by over an order of magnitude.

time to instability within the same order of magnitude compared to the actual event timing. The combination of fault properties that resulted in the closest match were characterized by relatively high compliance ($B = 0.9$) and low to medium transmissivity ($T = 10^{-18}$ to $T = 10^{-15}$ m^3).

6.5.3 Case 3: Neglecting hydromechanical coupling

The rate-and-state friction framework involves many fault properties that bear substantial uncertainty. In Case 3, we investigated whether the timing of the main shock could be described purely by rate-and-state effects by neglecting hydromechanical coupling completely. By neglecting the undrained loading effect, the full static stress change was realized instantaneously. In this set of numerical experiments, the fault hydraulic properties were $B = 0$ and $T = 0$, and the rate-and-state direct effect parameter was varied over the range of $0.005 \leq a \leq 0.02$. For reference, note that in Case 1 and Case 2 the fault was assigned $a = 0.007$. In each scenario, the magnitude of velocity weakening was maintained constant by holding $(b - a) = 0.004$ constant.

The sliding velocity profiles for Case 3 are shown in Fig. 6.12. Each of the scenarios tested exhibited the same qualitative behavior. An initial jump in sliding velocity was followed by an extended period of time where velocity remained relatively constant. In contrast to the scenarios

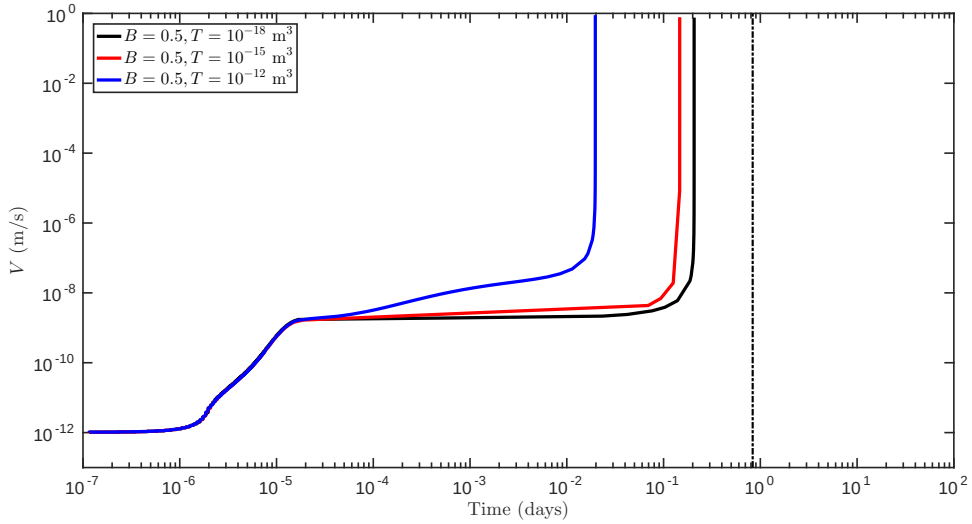

Figure 6.10: Sliding velocity history at the Event B nucleation site for Case 2a. The actual timing of Event B is shown as the vertical dashed line. The fault zone compressibility was held constant to achieve $B = 0.5$, and the fault transmissivity was varied over the range of $10^{-18} \leq T \leq 10^{-12}$ m^3. In these scenarios with relatively stiff fault compliance, the time to instability was underestimated even for the lowest transmissivity fault.

in Case 2 that showed strong transient loading effects, the onset of rapid acceleration occurred in a manner predicted by Eq. 6.18. In this set of experiments, a significant variation in t_i was observed, with values ranging from $t_i = 2$ minutes (for the scenario with $a = 0.005$) to $t_i = 5$ days (for the scenario with $a = 0.02$). The predominant influence of a was on the magnitude of the rise in sliding velocity caused by the static stress change (see Eq. 6.20). The value of a also influenced the time to instability through state evolution effects (see Eq. 6.18). Interpolating between these results, it is evident that using a value for the direct-effect parameter between $a = 0.01$ and $a = 0.02$ would have been able to match the 20 hour delay period.

6.6 Discussion

It is evident from Eqs. 6.2 through 6.6 that stress and friction along a fault can be influenced by transient processes including both fluid flow and state evolution. Using a simple "static" description of fault friction, a poroelastic response and subsequent pressure relaxation provides a physics-based explanation of delayed triggering and aftershock decay (*Cocco and Rice*, 2002; *Nur and Booker*, 1972; *Roeloffs*, 1996). Using a rate-and-state description of friction, *Dieterich* (1994) investigated how step changes in shear and normal stress can influence the earthquake nucleation process. The results of that study demonstrated a delayed triggering process between earthquakes and subsequent

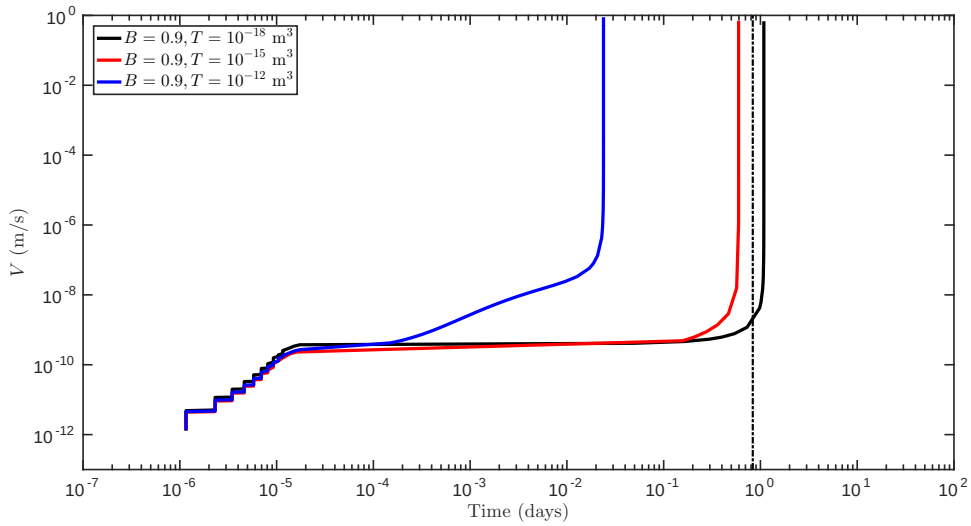

Figure 6.11: Sliding velocity history at the Event B nucleation site for Case 2b. The actual timing of Event B is shown as the vertical dashed line. The fault zone compressibility was held constant to achieve $B = 0.9$, and the fault transmissivity was varied over the range of $10^{-18} \leq T \leq 10^{-12}$ m^3. In these scenarios with relatively compliant behavior, the time to instability was delayed to achieve a timing consistent with the field observation for the faults with medium and low transmissivity.

aftershocks even for loading that remained constant in time. *Segall and Lu* (2015) extended that analysis to incorporate the effects of transient fluid flow and associated poroelastic stressing in the earthquake nucleation process in a semianalytical model.

In this study, we sought to identify whether hydromechanical effects were necessary to explain the 20 hour delay between Events A and B in the Prague earthquake sequence and, in doing so, learn about the in-situ properties of basement faults in Oklahoma. The study was informed by previous work that enabled characterization of the stress orientations, reservoir fluid pressure, fault geometry, and earthquake source mechanisms (*Alt and Zoback*, 2014; *Keranen et al.*, 2013; *McNamara et al.*, 2015b; *Nelson et al.*, 2015; *Sumy et al.*, 2014; *Sun and Hartzell*, 2014). Estimates of the stress magnitudes at depth in the area near Prague, Oklahoma were provided by *Walsh and Zoback* (2016). Assimilation of these sources of information enabled accurate modeling of the stress change caused by Event A resolved along Fault B and provided constraints on Fault B's initial proximity to failure. We performed experiments using a fully-coupled fluid flow and fault mechanics numerical model that performed earthquake rupture calculations within the context of rate-and-sate friction.

The results of our numerical experiments suggested that several different scenarios could explain the delayed triggering. This reflects the nonunique combinations of parameters that can influence earthquake nucleation. The exact nature of the physical processes that led to the delay between the foreshock and main shock at Prague remain ambiguous. Nonetheless, this study demonstrated

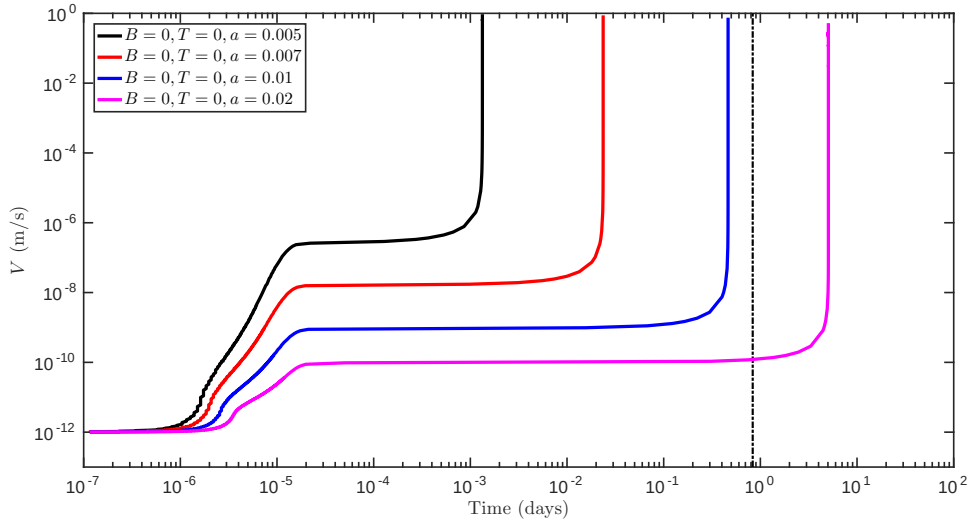

Figure 6.12: Sliding velocity history at the Event B nucleation site for Case 3. The actual timing of Event B is shown as the vertical dashed line. In this case, hydromechanical effects were neglected (i.e., $B = 0$ and $T = 0$), and the rate-and-state direct effect parameter was varied over the range of $0.005 \leq a \leq 0.02$. The value of a influenced the time to instability predominantly by affecting the magnitude of the initial rise in sliding velocity and also through state evolution effects.

that for specific circumstances it was possible to set useful bounds on fault transmissivity, fault compliance, and rate-and-state frictional properties. Here, we review the major conclusions drawn from our study.

In Cases 1 and 2, we investigated the roles of various hydromechanical processes in the earthquake nucleation process, including pressure changes during undrained loading conditions and transient changes in effective stress caused by flow along faults. In our numerical experiments, varying the hydraulic properties of the fault influenced the timing of Event B significantly. A competition existed between a damped static stress change caused by fault compliance, which tended to delay rupture, and a loading mechanism caused by transient fluid flow, which tended to encourage rupture. Our results suggested that relatively compliant behavior ($B = 0.9$) combined with medium to low transmissivity ($T = 10^{-18}$ to 10^{-15} m^3) was consistent with the earthquake timing from the field observations.

Comparing Figs. 6.10 and 6.11, it was observed that the time to instability for the highly transmissive faults was insensitive to fault compliance (t_i in these two scenarios was nearly identical, even though B was significantly different). Although the theory presented in Sect. 6.4.4 was developed for idealized cases (e.g., constant loading rate), we can apply those principles to aid in the interpretation of the behavior observed in the numerical experiments. In general, step changes in $\Delta\sigma_C$ act to bring the fault to a new "initial" sliding velocity through a rate-strengthening process described

by Eq. 6.20. For faults with very low transmissivity there should be no transient loading mechanism (i.e., $\partial p/\partial t \approx 0$), and the time to instability scales as $t_i \sim V_0^{-1}$ (see Eq. 6.18). However, when the transient loading mechanism is nonnegligible, Eq. 6.19 indicates that the transient loading term can dominate ($t_i \sim \partial p/\partial t$), and the influence of the initial sliding velocity is reduced to a logarithmic dependence ($t_i \sim \ln V_0^{-1}$). Recent field experiments, such as the one described by *Guglielmi et al.* (2015), have equipped wells with strain gauges to measure slip across faults that intersect the wellbore. With this type of technology, it could be possible to measure the evolution of the sliding velocity at the nucleation site of an earthquake. The numerical modeling analysis performed in the present study would be useful for informing future field studies related to injection-induced earthquakes and earthquake nucleation.

In Case 3, we neglected the hydromechanical response altogether, and nucleation was driven purely by state evolution effects. In this set of experiments, the timing of Event B was underestimated by 1 to 3 orders of magnitude (relative to the actual timing observed in the Prague earthquake sequence) for $a \leq 0.007$ (see Fig. 6.12). For $0.01 \leq a \leq 0.02$, the time to instability was on the same order of magnitude as the field observations. Laboratory friction experiments on granite rock with simulated gouge typically show measurements of the direct-effect parameter ranging from $0.005 < a < 0.015$ (*Blanpied et al.*, 1991; *Dieterich and Kilgore*, 1996; *Marone and Kilgore*, 1993; *Marone*, 1998). The range of a values that led to aftershock timings consistent with the field observations were on the high end of the values measured in the laboratory, but were certainly within a realistic range. Thus, the possibility that the nucleation phase of the Prague main shock may have been influenced exclusively by rate-and-state friction effects cannot be precluded.

Further investigation within the context of the conceptual model proposed in this study is justified. In the rate-and-state friction framework, the time to instability for earthquake nucleation is extremely sensitive to the initial sliding velocity prescribed to the fault as well as the state evolution law. In this work, we assumed a relatively arbitrary value for the initial sliding velocity of $V_0 = 10^{-12}$ $\mathrm{m} \cdot \mathrm{s}^{-1}$ due to the epistemic uncertainty associated with the background sliding velocity of inactive faults in Oklahoma. It is arguable that the sliding velocity may have been significantly lower based on the observation that there have been no significant earthquakes on this fault in recent geologic history. Alternatively, one may argue that if the fault had been influenced by nearby fluid injection, then it is plausible that the fault was at an elevated state of sliding just prior to the foreshock. We tested only the aging law form of state evolution. It would be worthwhile to test the slip law, in which state can only evolve during sliding. Furthermore, based on the hypothesis that the Prague sequence was induced by fluid injection, application of a form of the slip law that is coupled with the variable normal stress mechanism proposed by *Linker and Dieterich* (1992) may provide new insight into the manner in which seemingly inactive faults become excited by changes in fluid pressure.

In future studies of the Prague earthquake sequence, it would be worthwhile to investigate alternative conceptual models other than Coulomb stress triggering. For example, if it is assumed that

the foreshock and main shock were fluid-injection-induced earthquakes, then a major inconsistency that must be overcome is that, based on the stress measurements, the foreshock likely occurred on a fault segment (Fault A) that was much more poorly oriented for shear failure than the fault that hosted the main shock (Fault B). One possible explanation is that initially Fault A was connected hydraulically to the injection aquifer, and Fault B was not connected hydraulically to either Fault A or the injection aquifer. Following the foreshock, a permeable pathway connecting the two faults could have been created allowing pressure to build along Fault B, ultimately triggering the event. Shear-enhanced permeability along faults has been observed during hydraulic stimulation treatments in geothermal reservoirs (*Dempsey et al.*, 2015; *Häring et al.*, 2008), and has also been argued to control fluid migration in natural geologic processes (*Sibson*, 2014).

6.7 Concluding remarks

We investigated several potential mechanisms for the one day delayed triggering between the M_{w} 4.8 foreshock and the M_{w} 5.6 main shock during the 2011 Prague, Oklahoma earthquake sequence. We performed three sets of numerical experiments to isolate the effects of different physical processes, including the instantaneous undrained response to changes in normal stress, transient fluid flow along the fault, and the evolution of the state variable and its influence on fault friction. The purpose of the study was to take advantage of the well characterized state of stress, fault geometry, and earthquake source mechanisms combined with the observation of the time delay between events in order to set constraints on the in-situ properties of basement faults in Oklahoma. The main conclusions drawn from the results of the numerical experiments were:

- A coupling between transient hydromechanical loading and transient friction evolution can plausibly explain the timing of the main shock.
- Relatively compliant behavior in response to changes in normal stress, corresponding to a Skempton pore pressure coefficient near 1, was consistent with the field observations.
- The fault transmissivity was estimated to range from 10^{-18} to 10^{-15} m^3.

Due to the nonunique combination of fault properties and stress conditions that influence the earthquake nucleation process, it was not possible to identify the exact physical process that led to the 20 hour delay between the foreshock and main shock in the Prague sequence. However, this study provided insight into the coupled interactions between elastic stress transfer, hydromechanical response, and the transient evolution of fault friction that may have occurred during the earthquake sequence. The analysis ultimately yielded useful constraints on in-situ fault properties within the context of the hypothesis tested in this study, which has broad implications for understanding faulting behavior for other large-scale basement faults in Oklahoma and the rest of the central and eastern United States

if the properties can be extrapolated elsewhere. The range of fault properties inferred from this study will provide a basis for physics-based seismic hazard models of injection-induced seismicity.

Chapter 7

Wastewater Disposal and Induced Seismicity

The central and eastern United States (CEUS) is an intraplate region that historically has remained relatively aseismic. The average rate of earthquakes with $M_w \geq 3$ in the CEUS between 1967 through 2000 was observed to be 21 events per year (*Ellsworth*, 2013). *Ellsworth* (2013) documented an unprecedented increase in the seismicity rate starting in about 2001 and accelerating again in about 2009. In 2014, there were more earthquakes with $M_w \geq 3$ in Oklahoma than in California for the first time in recorded history (*McGarr et al.*, 2015). Several case studies of relatively large earthquake events ($M_w \geq 4$) in the CEUS suggested that the increased rate of seismicity may have been related to oil and gas activities in the area, in particular, the disposal of large volumes of saltwater into deep subsurface aquifers (*Frohlich et al.*, 2011; *Horton*, 2012; *Hornbach et al.*, 2015; *Keranen et al.*, 2013; *Kim*, 2013).

In the United States, wastewater disposal wells are regulated as class-II underground injection control (UIC) wells. Wells used for the purposes of waterflooding and enhanced oil recovery (EOR) are also regulated as class-II UIC wells. There are over 140,000 wells permitted for deep injection in the United States, and over 30,000 of those wells are permitted specifically for the purpose of wastewater disposal (*Ellsworth*, 2013). *Walsh and Zoback* (2015) analyzed injection well data reported by the operators to the state regulatory body for all wells operating in Oklahoma. *Walsh and Zoback* (2015) demonstrated that in three study areas within the state where the majority of the recent seismicity was observed, the increased rate of seismicity followed significant increases (5- to 10-fold) in rates of wastewater disposal. In areas where no significant operational changes occurred, the seismicity rate was observed to remain unchanged from the background levels (*Walsh and Zoback*, 2015). Furthermore, the analysis of *Walsh and Zoback* (2015) found that in Oklahoma, the vast majority of the disposal fluid was comprised of saltwater coproduced from conventional oil

fields rather than flowback water from hydraulic fracturing operations. An analysis performed by *Weingarten et al.* (2015) suggested that seismicity occurred preferentially near wells that disposed fluid at high injection rates (> 300,000 barrels per month). In this work, we investigated injection-induced seismicity in geologic and operational settings relevant to wastewater disposal into deep aquifers overlying basement rock.

7.1 Motivation

Disposal of wastewater associated with oil and gas operations by injection into the subsurface is a common practice in the petroleum industry. Changes in the state of stress at depth caused by fluid injection have reportedly generated significant levels of seismic activity near Underground Injection Control (UIC) class-II wells in several instances (*Healy et al.*, 1968; *Frohlich et al.*, 2011; *Frohlich*, 2012; *Horton*, 2012; *Kim*, 2013; *Frohlich et al.*, 2014; *Keranen et al.*, 2014; *Rubinstein et al.*, 2014; *Hornbach et al.*, 2015). In order to determine the seismic hazard risk for a site it is important to estimate parameters in probabilistic seismic hazard assessment models, such as the expected maximum earthquake magnitude and the occurrence rate of a given-magnitude earthquake (*Ellsworth et al.*, 2015). Understanding how the interaction between injection well operational parameters and natural geologic setting affects the behavior of induced earthquakes is difficult to quantify and has, so far, remained unresolved (*Ellsworth*, 2013; *McGarr*, 2014; *McGarr et al.*, 2015).

Wastewater injection wells target injection horizons within naturally permeable brine aquifers, which are usually composed of sedimentary rocks. In most cases where relatively large earthquakes have been attributed to fluid injection, the earthquake hypocenters were located beneath the target aquifers along faults that exist within igneous basement rocks (*Horton*, 2012; *Kim*, 2013; *Keranen et al.*, 2014; *Hornbach et al.*, 2015). It has been suggested previously that basement faults may sometimes extend into overlying formations, providing a necessary hydraulic connection for pressure communication (*Hornbach et al.*, 2015; *Ellsworth*, 2013; *McGarr*, 2014; *Göbel*, 2015; *Göbel et al.*, 2016). If the fluid pressure within a fault zone increases due to injection, the effective normal compressive stresses that provide resistance for shear slip are reduced, thereby bringing the state of stress on the fault closer to failure conditions (*Ellsworth*, 2013; *Jaeger et al.*, 2007; *Raleigh et al.*, 1976; *Zoback*, 2007).

Apart from ground motion estimates, the most influential parameters in earthquake hazard analysis are the seismicity rate, recurrence rate of a given-magnitude earthquake, the Gutenberg-Richter (GR) b-value, and the maximum earthquake magnitude (*Petersen et al.*, 2014). If these earthquake statistics can be quantified accurately, then the data can be combined to develop a probabilistic estimate of earthquake hazard for a particular area. In a recent study, *van der Elst et al.* (2016) found that the maximum magnitude earthquake events observed in 21 separate cases of injection-induced seismicity were each as large as expected statistically based on the local earthquake

catalogs. Characterization of the hydromechanical reservoir response to fluid injection must therefore be cast in terms of understanding how these types of earthquake statistics can be expected to change due to injection operations.

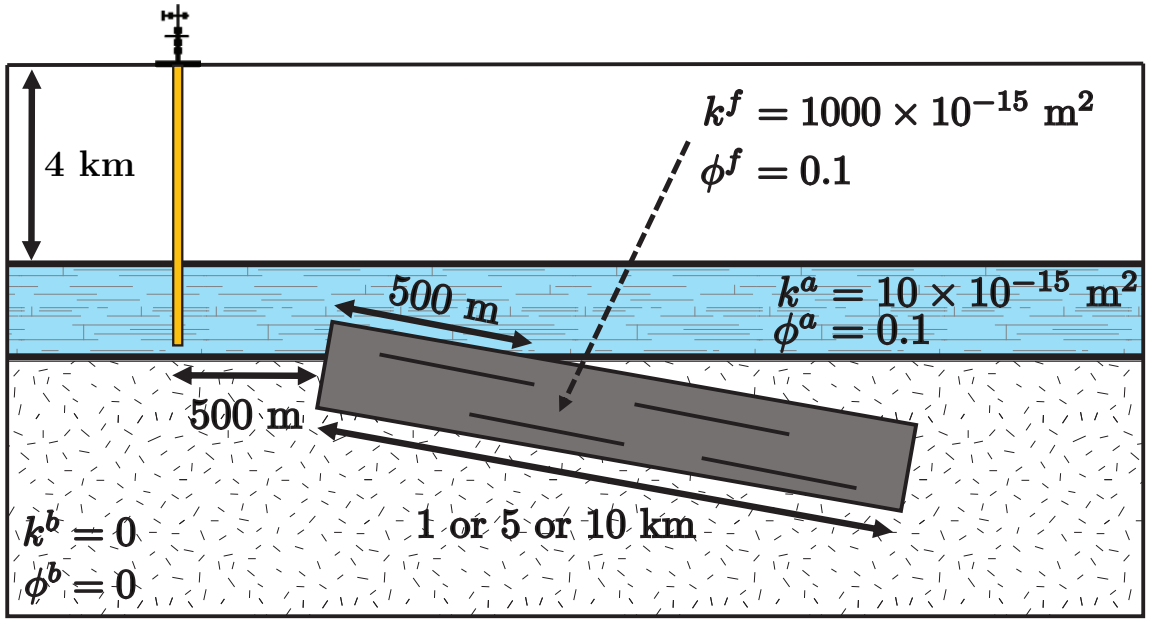

Figure 7.1: Conceptual reservoir model used to design the numerical modeling experiments. A permeable basement fault extended slightly into a saline aquifer, allowing for pressure communication during fluid injection.

7.2 Maximum magnitude of injection-induced earthquakes

McGarr (2014) used a combination of physical arguments and earthquake statistics to develop an expression for a theoretical upper bound on earthquake magnitude that was related linearly to the cumulative volume of fluid injected. An implicit assumption was made that earthquakes are confined to regions that experience pressure change. In that study, it was concluded that data collected from 18 different case studies of injection-induced seismicity supported the proposed relationship between maximum magnitude and injection volume. In this perspective, the size of an earthquake is related closely to the injection well operations. *Göbel* (2015) presented a comparison between Oklahoma and California based on regional-scale statistics of earthquakes, injection rates, and injection pressures. In that study, it was concluded that differences in the geologic setting likely played the primary role in how injection-triggered seismicity has evolved in those study areas over the past two decades, and the influence of injection well operations was of secondary importance.

In reservoir engineering, the "distance of investigation" has been used to describe the location

in the reservoir where pressure has changed by a prescribed magnitude and is often interpreted as a pressure front (*Horne*, 1995). It is intuitive to understand that the likelihood of interacting with hydraulic connections to basement faults increases as injection continues and the pressure front migrates further from the well. However, does this length scale set a bound on the dimension of an earthquake rupture and, ultimately, the earthquake magnitude?

In the present study, we addressed this question by applying a numerical model that couples fluid flow in porous media, fluid flow in faults, and earthquake rupture physics. We modeled a scenario where fluid was injected into a permeable aquifer overlying impermeable basement rock. A strike-slip fault zone in the vicinity of the well was located mostly within the basement rock, but a portion of the fault extended into the aquifer (see Fig. 7.1). The conceptual model was similar to other recent case studies and numerical modeling studies of induced seismicity (*Göbel et al.*, 2016; *Hornbach et al.*, 2015; *Horton*, 2012; *Keranen et al.*, 2014; *Kim*, 2013; *McGarr*, 2014). Two important differences were that we modeled the hydraulic interaction between the aquifer and the fault explicitly, and we considered a rigorous treatment of the earthquake rupture process within the framework of rate-and-state friction theory.

We observed that in some cases the earthquake ruptures were indeed constrained to occur within the zone of the fault that experienced significant pressure change, however, this was not unequivocally true. In some instances, the earthquake ruptures nucleated initially within the pressurized region, and then continued to propagate in a sustained manner well beyond the pressure front. Earthquake magnitudes tended to be constrained by the extent of the pressure front in the former case, and by the size of the fault in the latter case. Here, we introduce a criterion for determining the transition between these two types of behavior. From a practical perspective, this has important implications for assessing whether induced seismicity can be expected to be controllable by moderating injection well operations.

7.2.1 Faulting criterion

We propose classifying faulting behavior into two separate categories:

- Type A: **pressure-constrained ruptures** are limited by the extent of the pressure perturbation along the fault.
- Type B: **runaway ruptures** are controlled by traditional tectonic factors such as fault geometry.

This is a useful distinction because pressure-constrained behavior can be considered more stable, and so parameters that affect the seismic hazard assessment, like the maximum earthquake magnitude or earthquake recurrence interval, could be influenced by injection well operational parameters. For example, the maximum earthquake magnitude might be expected to grow over time in a systematic manner as larger patches of the fault are exposed to significant pressure changes. For Type B

behavior, although fluid injection may be ultimately responsible for causing earthquakes to nucleate, the seismicity might depend more closely on characteristics of the natural geology, such as the size of the fault.

We propose a faulting criterion, C, to separate the two categories of behavior:

$$C = \frac{f_0}{f_D}, \tag{7.1}$$

where f_D is the dynamic friction coefficient and $f_0 = \tau_0/\bar{\sigma}_0$ is the ratio of shear stress, τ_0, to effective normal stress, $\bar{\sigma}_0$, acting on the fault before injection begins (i.e., the prestress ratio). For $C < 1$, Type A behavior occurs, and for $C > 1$, Type B behavior occurs.

The parameter f_D can be estimated from rate-and-state friction laboratory experiments. The parameter f_0 embodies the initial state of stress, the initial fluid pressure, and the orientation of the fault. In the numerical experiments we performed, the value of the faulting criterion in Eq. 7.1 was observed to be a good indicator of whether earthquake ruptures would arrest within the pressure-perturbed region or propagate in a sustained manner beyond the pressure front.

7.2.2 Description of numerical experiments

We explored a wastewater disposal setting in which a basement fault was connected hydraulically to an overlying aquifer. In this study, it was essential to model the interaction between flow in the aquifer and flow in the fault explicitly. Faults that are able to host induced earthquakes of significant magnitude are not likely to exist entirely within the target injection aquifer, are on the scale of tens of kilometers long, and have finite transmissivity (*Aydin*, 2000; *Zoback and Gorelick*, 2012). The transient nature of pressure diffusion along the fault influenced the earthquake nucleation, rupture, and arrest processes significantly.

We modeled three separate cases to test conditions spanning a broad range of C values:

- Case 1: varied orientation of the fault
- Case 2: varied magnitude of the least principal stress
- Case 3: varied b in the rate-and-state model to influence dynamic friction

In each case, 1 km, 5 km, and 10 km faults were considered. Tables 7.1 though 7.7 list important parameters for each specific scenario that was modeled.

Model geometry and physical properties

The conceptual reservoir model used in this study was motivated by recent case studies of injection-induced seismicity (*Horton*, 2012; *Kim*, 2013) and is illustrated in Fig. 7.1. In the model, water was injected into a 4 km deep saline aquifer at a constant rate of 10 kg/s (roughly 165,000 bbl/month)

over a period of three years. This is representative of a relatively high-rate wastewater disposal well for the state of Oklahoma (*Walsh and Zoback*, 2015; *Weingarten et al.*, 2015). Flow was two-dimensional in the aquifer and one-dimensional along the length of the fault. We considered a purely mode-II shear problem and assumed plane strain along the vertical dimension of the fault. The state of stress and frictional properties were homogeneous. Under these assumptions, fault properties (fluid pressure, effective stress, slip, etc.) were constant along the vertical dimension of the fault, but could vary along the length of the fault.

The aquifer was modeled as a wide channel. The aquifer was 100 m thick, 1 km wide, and 25 km long. This situation could represent a scenario in which the injection well is bounded on two sides by impermeable geologic structures or perhaps other wells. The edge of the basement fault existed 500 m away from the injection well in the center of the channel aquifer. The orientation of the aquifer paralleled the strike of the fault. The fault was in direct contact with the aquifer for 500 m, and was assumed to be surrounded completely by impermeable basement rock for the remaining extent of the fault. The aquifer-fault mass transfer terms (see Eq. 2.7) were calculated for elements within the first 500 m of the fault, assuming that the entire surface area of each fault element was embedded in the aquifer domain. From the perspective of the fault, this scenario could be interpreted as a series of constant pressure source terms for the elements within first 500 m and a no-flow boundary condition along the rest of the fault. The initial fluid pressure in the aquifer and fault were both $p_0 = 40$ MPa, approximately equal to hydrostatic pressure at a depth of 4 km.

The permeability of the aquifer was $k^m = 10 \times 10^{-15}$ m^2 (10 md) and the porosity of the aquifer was $\phi^m = 0.1$. The aquifer overlaid impermeable basement rock. The transmissivity of the fault was $T = 3.5 \times 10^{-18}$ m^3. Rate-and-state friction properties used in the model were consistent with values obtained from laboratory experiments on granitic rocks (*Blanpied et al.*, 1991, 1995). Additional important model parameters are listed in Tables 7.1 through 7.4.

Numerical discretization

We used an embedded fracture modeling strategy to couple flow in the fault and flow in the aquifer, so the aquifer discretization did not conform to the fault discretization (*Norbeck et al.*, 2016a). Taking advantage of symmetry, only half of the aquifer was modeled. The aquifer was discretized into a nonuniform structured mesh with a total of 1000 x 3 x 1 grid blocks. The grid block spacing along the length of the aquifer was constant out to a distance of 6.5 km from the well then increased exponentially to the edge of the domain. No-flow boundaries were enforced on the top and bottom of the aquifer. A no-flow boundary was also enforced at the edge of the aquifer, but the pressure front did not reach this boundary in any of the simulations. The fault was discretized into discrete elements along the length of the fault. Each fault element was 1.0 m long, much less than L_c for all scenarios ensuring minimal discretization dependence.

Table 7.1: Model geometry for the study of maximum magnitude of injection-induced earthquakes.

Parameter	Value	Unit	Description
L^f	1 or 5 or 10	km	fault length
H^f	50	m	fault height
W^f	0.1	m	fault width
L^m	25	km	aquifer length
W^m	1	km	aquifer width
H^m	100	m	aquifer height

Table 7.2: Aquifer and fault hydraulic properties for the study of maximum magnitude of injection-induced earthquakes.

Parameter	Value	Unit	Description
k^f	1×10^{-12}	m^2	fault permeability
ϕ_*^f	0.1	-	fault porosity
c_ϕ^f	0	Pa^{-1}	fault pore compressibility
k^m	1×10^{-14}	m^2	aquifer permeability
ϕ_0^m	0.1	-	aquifer porosity
c_ϕ^m	4.4×10^{-10}	Pa^{-1}	fault pore compressibility
$p_{\phi *}$	40	MPa	porosity reference pressure

Table 7.3: Fluid properties for the study of maximum magnitude of injection-induced earthquakes.

Parameter	Value	Unit	Description
λ^{-1}	0.7×10^{-3}	$Pa \cdot s$	water viscosity
ρ_*	1000	$kg \cdot m^{-3}$	reference water density
c_w	4.4×10^{-10}	Pa^{-1}	water compressibility
$p_{\rho *}$	0.1013	MPa	density reference pressure

Table 7.4: Rate-and-state friction and elastic properties for the study of maximum magnitude of injection-induced earthquakes.

Parameter	Value	Unit	Description
a	0.0100	-	direct effect constant
b	0.0110 to 0.0175	-	state evolution constant
δ_c	50×10^{-6}	m	state evolution characteristic length
f_*	0.6	-	steady-state friction constant
V_*	1×10^{-9}	$m \cdot s^{-1}$	steady-state velocity constant
G	30	GPa	shear modulus
ν	0.25	-	Poisson's ratio
η	3.15	$MPa \cdot s \cdot m^{-1}$	radiation damping parameter

Table 7.5: Summary of each scenario for Case 1. The fault orientation was varied while holding the stress state and frictional properties constant.

Label	α [deg]	τ_0 [MPa]	$\bar{\sigma}_0$ [MPa]	f_0 [-]	b [-]	f_D [-]	C [-]	$\Delta p_{c,S}$ [MPa]	L_c [m]
1-1	45	15.0	30.0	0.500	0.0140	0.526	0.950	5.0	79
1-2	35	14.1	24.9	0.567	0.0140	0.526	1.077	1.4	95
1-3	30	13.0	22.5	0.577	0.0140	0.526	1.097	0.9	105
1-4	25	11.5	20.4	0.564	0.0140	0.526	1.072	1.2	116
1-5	20	9.6	18.5	0.521	0.0140	0.526	0.990	2.4	127
1-6	15	7.5	17.0	0.441	0.0140	0.526	0.838	4.5	139

Table 7.6: Summary of each scenario for Case 2. The state of stress was varied while holding fault orientation and frictional properties constant.

Label	α [deg]	τ_0 [MPa]	$\bar{\sigma}_0$ [MPa]	f_0 [-]	b [-]	f_D [-]	C [-]	$\Delta p_{c,S}$ [MPa]	L_c [m]
2-1	30	13.0	22.5	0.577	0.0140	0.526	1.097	0.8	105
2-2	30	12.8	22.9	0.558	0.0140	0.526	1.061	1.6	103
2-3	30	12.6	23.3	0.540	0.0140	0.526	1.026	2.3	101
2-4	30	12.3	23.6	0.522	0.0140	0.526	0.992	3.1	100
2-5	30	12.1	24.0	0.505	0.0140	0.526	0.960	3.8	98
2-6	30	10.8	26.3	0.412	0.0140	0.526	0.784	8.2	90

Table 7.7: Summary of each scenario for Case 3. The value of b in the rate and state friction constitutive model was varied while holding fault orientation and the state of stress constant.

Label	α [deg]	τ_0 [MPa]	$\bar{\sigma}_0$ [MPa]	f_0 [-]	b [-]	f_D [-]	C [-]	$\Delta p_{c,S}$ [MPa]	L_c [m]
3-1	25	11.5	20.4	0.564	0.0115	0.572	0.986	1.2	309
3-2	25	11.5	20.4	0.564	0.0125	0.554	1.019	1.2	185
3-3	25	11.5	20.4	0.564	0.0135	0.536	1.054	1.2	132
3-4	25	11.5	20.4	0.564	0.0145	0.517	1.092	1.2	103
3-5	25	11.5	20.4	0.564	0.0155	0.499	1.132	1.2	84
3-6	43	15.0	29.0	0.517	0.0125	0.554	0.933	4.0	130
3-7	43	15.0	29.0	0.517	0.0135	0.536	0.965	4.0	93
3-8	43	15.0	29.0	0.517	0.0145	0.517	0.999	4.0	72
3-9	43	15.0	29.0	0.517	0.0155	0.499	1.036	4.0	59
3-10	43	15.0	29.0	0.517	0.0165	0.480	1.076	4.0	50
3-11	43	15.0	29.0	0.517	0.0175	0.462	1.119	4.0	43

7.2.3 Injection-induced earthquake rupture behavior

Subsurface fluid injection can cause a change in reservoir pressure, Δp, which can be transmitted within a fault zone if there is a hydraulic connection between a well and a fault. Assuming a Mohr-Coulomb shear failure criterion, a fault can be expected to begin to fail if the frictional resistance to slip is reduced to the level of shear stress acting on the fault, i.e., $f_S\left(\bar{\sigma}_0 - \Delta p\right) = \tau_0$, where f_S is the static friction coefficient of the fault (*Zoback*, 2007). This failure criterion implies there is a critical pressure perturbation that is required to initiate slip on a fault, $\Delta p_{c,S}$:

$$\Delta p_{c,S} = \bar{\sigma}_0 - \frac{\tau_0}{f_S}. \tag{7.2}$$

In rate-and-state friction theory, earthquake nucleation occurs when slip accumulates over a sufficiently large coherent patch of the fault (*Ampuero and Rubin*, 2008; *Rice*, 1980; *Rice and Ruina*, 1983; *Rice et al.*, 2001). In the context of injection-induced seismicity, this requires that a pressure perturbation of at least $\Delta p_{c,S}$ must diffuse over this critical length-scale of the fault before an earthquake can nucleate, otherwise slip will be purely aseismic. Aseismic behavior over the entire three-year injection duration was a common outcome in many scenarios we modeled. This depended mostly on the initial proximity to failure of the fault.

For scenarios in which seismicity did occur, two general patterns of earthquake rupture behavior emerged: a) earthquake ruptures that were confined within pressurized regions of the fault (Type A), and b) earthquake ruptures that propagated beyond the pressure front and were limited by the size of the fault (Type B). Here, we provide examples of model results to illustrate each type of behavior.

Figures 7.2 and 7.3 show profiles of fault properties during typical Type A and Type B earthquake events on 5 km long faults, respectively. These two faults had the same orientation and stress state, but had different dynamic friction values. The earthquake events occurred at similar times (285 and 310 days after injection began, respectively). The pressure and effective stress distributions developed because the faults were relatively large and had finite permeability and storativity. The location along the fault at which the pressure changed by 0.1 MPa was taken as the pressure front. The pressure distribution was effectively constant during each earthquake event because the earthquake ruptures occurred very quickly relative to pressure diffusion time scales and fault permeability was assumed to be constant. In between subsequent events, the pressure front migrated along the fault.

In Figs. 7.2 and 7.3, the earthquake rupture front can be identified as the location along the fault where slip velocity, shear stress, and friction are at their maximum. Ahead of the rupture front, the cumulative shear slip is zero. During an earthquake, the value of friction behind the rupture front represents the dynamic friction, f_D, and the value well ahead of the rupture front represents f_0. The relative magnitude of these two values is described by the faulting criterion in Eq. 7.1, and was

the most influential factor governing earthquake behavior in these experiments.

For the Type A earthquake event, shown in Fig. 7.2, the rupture died out before reaching the pressure front so that only a small incremental accumulation of shear slip occurred during the earthquake. The magnitude of this earthquake was calculated as Mw 2.8. The Type B event shown in Fig. 7.3 displayed markedly different behavior. Friction behind the rupture front was below f_0 which enabled a stress drop to occur outside of the pressurized region, providing the necessary energy to drive the rupture a significant distance beyond the pressure front. Slip was able to accumulate over the entire fault surface area which produced a correspondingly large seismic moment release. The magnitude of this earthquake was calculated as Mw 4.0.

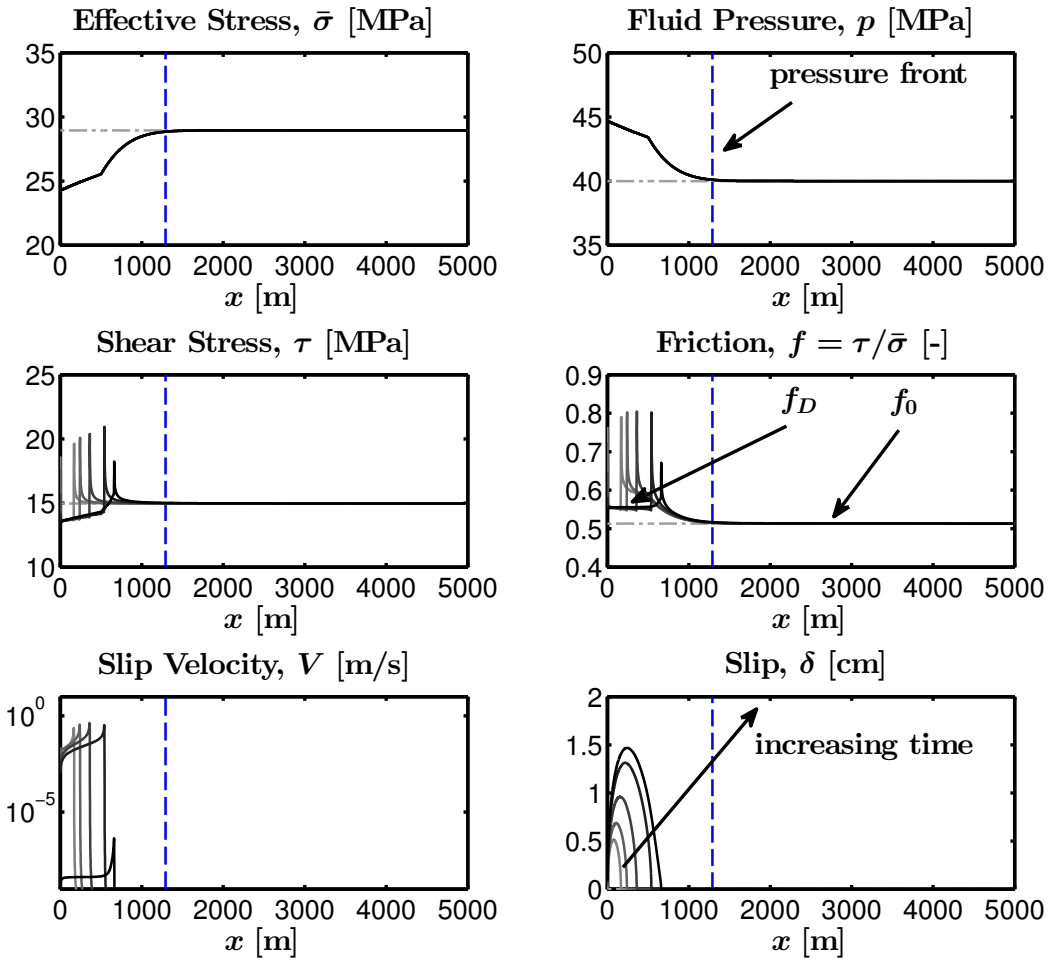

Figure 7.2: Earthquake rupture profiles during a typical pressure-constrained rupture event (Type A). The location of the pressure front is indicated by the *blue dashed line*. The earthquake rupture was confined to the pressurized region.

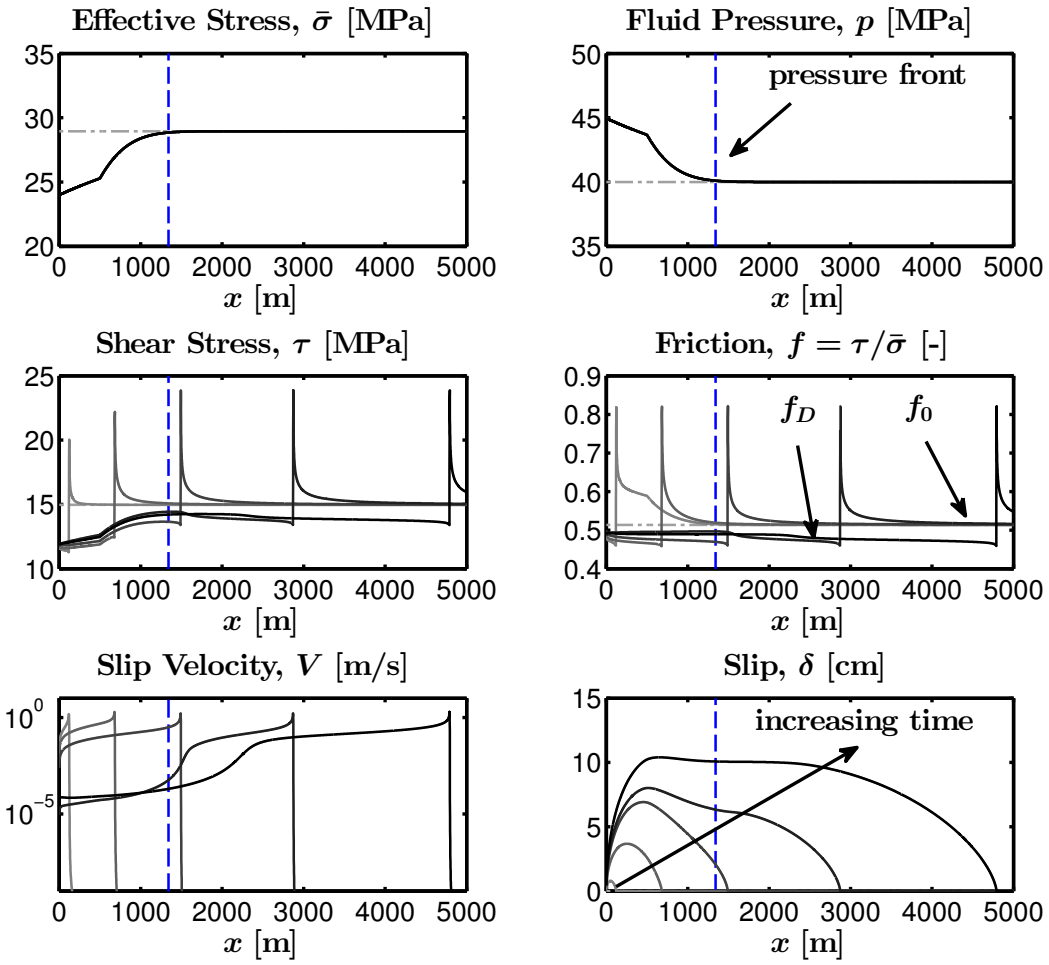

Figure 7.3: Earthquake rupture profiles during a typical runaway rupture event (Type B). The location of the pressure front is indicated by the *blue dashed line*. The earthquake rupture propagated beyond the pressure front and ultimately arrested after reaching the fault boundary.

7.2.4 Critical pressure perturbation for sustained rupture

Although the faulting criterion proposed in Eq. 7.1 was based on observations from numerical experiments, it can also be interpreted within the theory of earthquake rupture dynamics as a limiting case of an earthquake energy balance. The rupture and arrest processes are governed by a competition between fracture energy, Γ, and energy release rate, G_c (*Ampuero and Rubin*, 2008; *Rice*, 1980). In the limit that $\Gamma \to 0$, then $G_c > 0$ will cause instability leading to earthquake rupture. The energy release rate scales with the stress intensity factor, K, as $G_c \sim K^2$ (*Rice*, 1980). In turn, $K \sim \Delta\tau$

depends on the stress drop behind the rupture front, $\Delta\tau$ (*Rice*, 1980):

$$\Delta\tau = \tau_0 - f_D\bar{\sigma}_0 + f_D\Delta p. \tag{7.3}$$

In the case that $(\tau_0 - f_D\bar{\sigma}_0) < 0$ (or, equivalently, $C < 1$) it is possible for a stress drop to occur only over the region that has been pressurized, so the rupture will be constrained by the pressure front.

If we relax the criterion proposed in Eq. 7.1 and now allow C to be a function of fluid pressure during injection, then Eq. 7.3 can be used to determine the pressure change at the transition point along the fault where $C = 1$. This critical pressure perturbation, $\Delta p_{c,D}$, depends on the dynamic friction coefficient:

$$\Delta p_{c,D} = \bar{\sigma}_o - \frac{\tau_0}{f_D}. \tag{7.4}$$

For faults that exhibit pressure-constrained behavior (Type A), $\Delta p_{c,D}$ can be used to define a nonarbitrary pressure front that represents approximately the distance at which earthquake ruptures will arrest. Portions of the fault that have experienced a pressure change of at least $\Delta p_{c,D}$ are able to host sustained earthquake ruptures. The apparent similarity between Eqs. 7.2 and 7.4 is encouraging, because it suggests that Eq. 7.4 can be applied in a manner analogous to the Mohr-Coulomb failure criterion as a method for estimating the maximum extent of induced earthquake ruptures.

We demonstrate this principle in Fig. 7.4. The location along the fault at which the faulting criterion transitions across $C = 1$ is now taken as the critical pressure front. In this case, this critical pressure front corresponded with the rupture arrest location extremely accurately. In general, the extent of the critical pressure front defined using Eq. 7.4 represents the approximate location of rupture arrest accurately.

7.2.5 Results of parametric study

We performed three sets of numerical experiments to assess the validity of the proposed faulting criterion and to isolate the effect of different parameters that influence the value of C. In Case 1, the effect of fault orientation was investigated. In Case 2, the principal stress ratio was varied. In Case 3, dynamic friction of the fault was varied. The state of stress, fault orientation, and frictional properties of the fault for each scenario are illustrated as Mohr circle representations in Fig. 7.5 and are also summarized in Tables 7.5 though 7.7. For each case, we examined three different fault sizes: 1 km, 5 km, and 10 km long.

In all scenarios, a sequence of earthquakes developed along the fault over the three year duration of injection. We compared different scenarios by normalizing seismic moment, M_0, by the cumulative volume of fluid injected up until the earthquake was induced, Q. The seismic moment was calculated

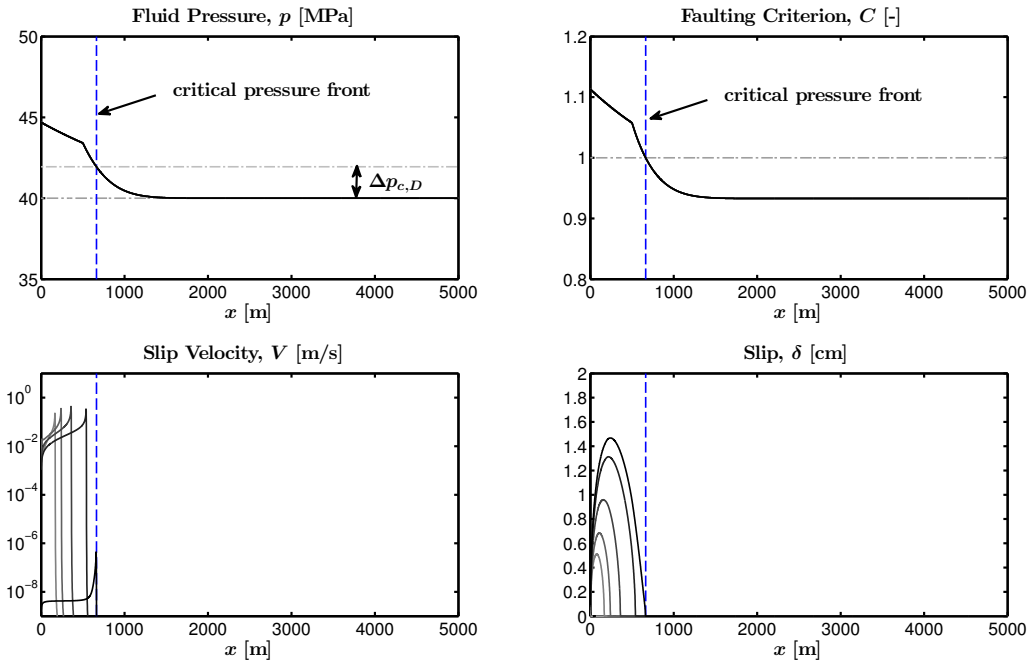

Figure 7.4: The faulting criterion (Eq. 7.1) was applied to identify the maximum extent of rupture propagation for pressure-constrained ruptures. The critical pressure front where pressure changed by at least $\Delta p_{c,D}$ is represented by the *dashed blue line*. Alternatively, the critical pressure front location can be identified as the point along the fault where the faulting criterion transitioned across $C = 1$. This location corresponded to the rupture arrest location.

as:

$$M_0 = G \int_A \Delta\delta \, dA, \tag{7.5}$$

where $\Delta\delta$ is the shear slip accumulated during an individual earthquake rupture, and A is the surface area of the fault. We used Q as a proxy for the distance of the pressure front because it is a tangible operational parameter. We are not attempting to demonstrate a direct relationship between M_0 and Q. In Fig. 7.6, we show M_0/Q for different faults. The data presented represent the average value of M_0/Q for earthquake sequences over the three year injection duration.

The results from the Case 1 experiments, shown in Fig. 7.6(a), demonstrate the marked contrast in behavior depending on the value of the faulting criterion, C, calculated using Eq. 7.1. For faults with $C < 1$ the normalized seismic moment did not depend on the size of the fault. This is because the dimension of the earthquake rupture was dictated by the pressure front. The earthquake magnitude of subsequent earthquakes increased as the pressure perturbed larger zones of the fault. For faults with $C > 1$, the normalized seismic moment tended to be one to three orders of magnitude larger and was dependent predominantly on the size of the fault. In these types of earthquakes, once

an event nucleated it was able to propagate in a sustained manner far beyond the pressure front, which resulted in relatively large earthquakes.

Previous numerical modeling studies have also proposed a distinction between Type A and Type B faulting behavior. *Gischig* (2015) modeled quasidynamic earthquake rupture on one-dimensional fault planes with a homogeneous shear stress distribution. *Dieterich et al.* (2015) modeled quasi-dynamic earthquake rupture on two-dimensional fault planes with heterogeneous shear stress distributions. In both of these studies, the distinction between the two behaviors was observed, and it was reported that τ_0 influenced the transition between behaviors. By introducing Eq. 7.1, it is recognized that the transition between faulting behaviors is more fully characterized by considering relative magnitudes of the prestress ratio, $f_0 = \tau_0/\bar{\sigma}_0$, and the dynamic friction, f_D.

The results from the Case 2 and Case 3 experiments, shown in Figs. 7.6(b) and 7.6(c), further demonstrate the two distinct earthquake behaviors over broader ranges of parameter space. It was observed that the transition between the Type A and Type B behavior did not occur strictly at $C = 1$. For faults with C slightly greater than one, Type A behavior tended to occur. In the models, the fault had a finite fracture energy. In the energy balance referenced in the discussion of Eq. 7.3, the effect of a finite fracture energy is to require $G_c > \Gamma$, which explains why Type B behavior required C slightly greater than one in our numerical experiments.

We modeled earthquake behavior along planar faults in a homogeneous state of stress and with homogeneous frictional properties. The coupled interaction between fluid flow and earthquake rupture processes for more realistic faults will have a strong influence on the evolution of earthquake sequences along faults. *Fang and Dunham* (2013) performed dynamic earthquake rupture simulations on rough faults, and observed that nonplanar geometries tended to prevent earthquakes from rupturing the entire fault. In the presence of heterogeneity, the pressure-constrained and surface-area-constrained rupture dimensions discussed in this study likely represent upper-bounds for Type A and Type B earthquakes, respectively.

7.2.6 Discussion

Many of the largest injection-induced earthquakes have occurred along faults in basement rock beneath the target injection aquifers (*Hornbach et al.*, 2015; *Horton*, 2012; *Keranen et al.*, 2014; *Kim*, 2013). During injection a pressure front exists within the aquifer, and a separate pressure front can exist within the fault zone. The critical pressure perturbations given in Eqs. 7.2 and 7.4 are useful from a reservoir engineering perspective to define pressure fronts that dictate where earthquakes can be expected to nucleate and arrest, respectively. In the limit of infinite fault permeability, the aquifer pressure would be transmitted instantaneously along the entire fault zone, which would effectively increase f_0 and promote Type B faulting behavior. Given this emerging understanding of the issue, the importance of characterizing the hydraulic interaction between aquifers and fault zones in-situ cannot be understated. In practice, ensuring that a bottom seal exists to provide a hydraulic barrier

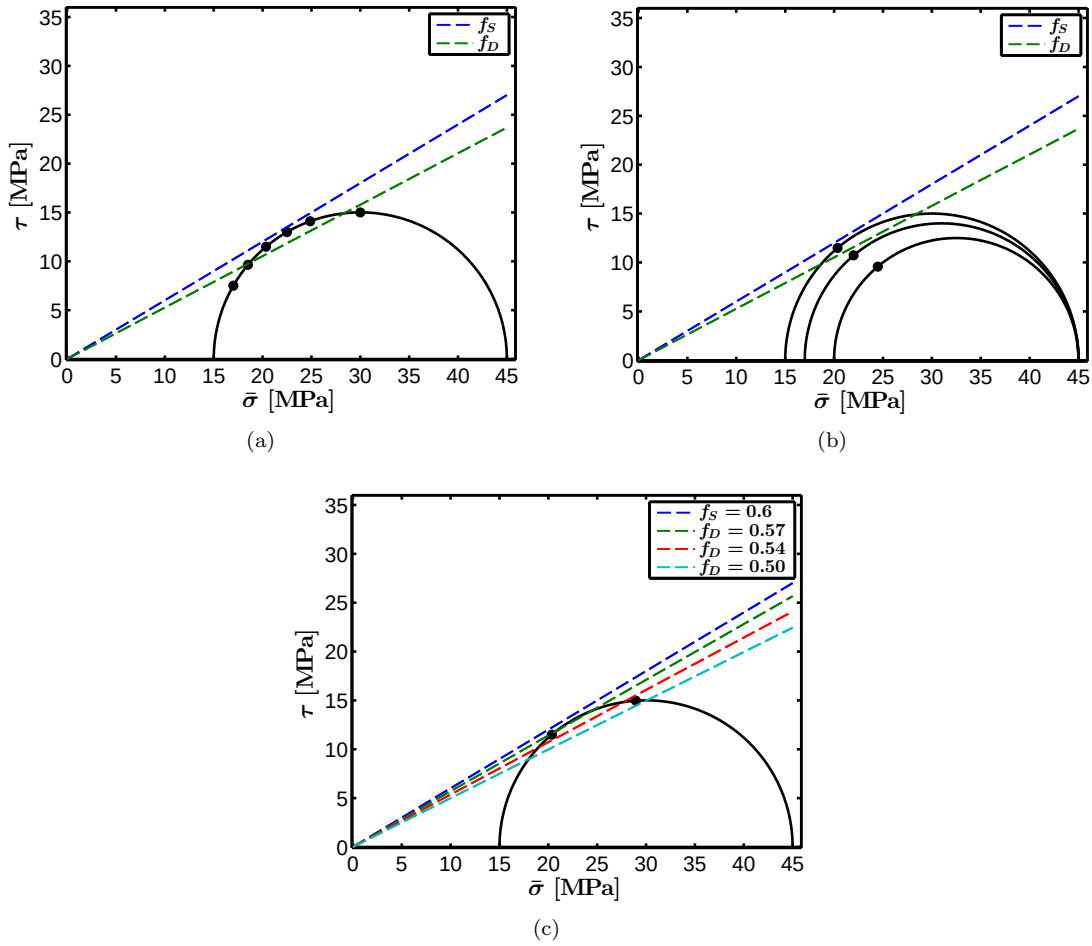

Figure 7.5: Mohr circle representations of the state of stress (black semicircles), fault orientation (black dots), and friction coefficients (colored dashed lines) for scenarios with variable C values. (a) In Case 1, the fault orientation was varied while holding the stress state and frictional properties of the fault constant. (b) In Case 2, the state of stress was varied. (c) In Case 3, the dynamic friction coefficient was varied.

between the injection aquifer and the basement rock would likely help to prevent pressurization of basement faults. However, it is difficult to guarantee that a basement seal will be extensive enough laterally to preclude hydraulic communication.

Assessing the manner in which faults are likely to respond to pressure perturbations caused by fluid injection is important for developing management strategies and to characterize hazard for wastewater disposal wells. In general, seismicity is not an inherent outcome as a response to fluid injection, as evidenced by the vast number of currently operating UIC class-II wells that have not been associated with seismicity (*Ellsworth*, 2013). The results from the numerical experiments

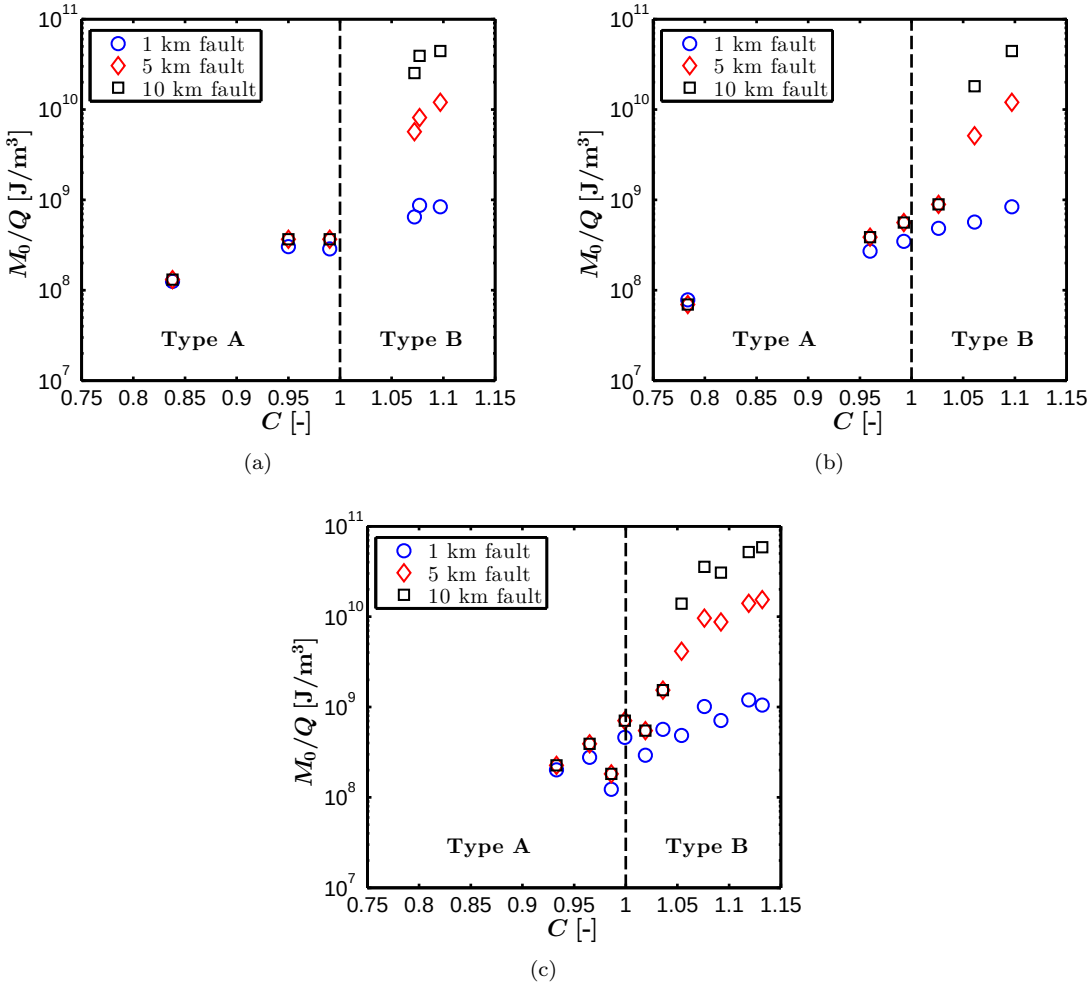

Figure 7.6: Seismic moment, M_0, normalized by cumulative volume of fluid injected, Q for (a) Case 1, (b), Case 2, and (c), Case 3. The parameter M_0/Q did not depend on fault size for $C < 1$ because the earthquake ruptures were limited by the pressure front (Type A behavior). In contrast, M_0/Q depended strongly on fault size for $C > 1$ because the ruptures propagated beyond the pressure front and arrested at the edge of the fault (Type B behavior).

performed in this study indicate that when fluid injection does induce seismicity, there exist two distinct types of faulting behavior that may emerge: a) earthquake ruptures that are confined to the pressurized region of the fault and b) sustained earthquake ruptures that propagate far beyond the pressure front. Through the experiments, we observed that Eq. 7.1 can be used effectively as a faulting criterion to evaluate whether or not the extent of the pressure front sets a limit on the earthquake rupture dimension for a given fault. With practical utility in mind, the proposed criterion strikes a balance between incorporating a rigorous treatment of the earthquake rupture process while

at the same time simplifying the problem so that making estimates of important parameters at a field site remains tractable. Nonetheless, practical application of the faulting criterion remains a challenging task.

Methods to constrain the state of stress and fluid pressure in the subsurface are well established (*Zoback*, 2007), but it may be difficult to extrapolate stress measurements made in the injection aquifers to greater depths. The locations and orientations of basements faults are difficult to determine before injection begins, but could potentially be determined if sufficient monitoring is performed. For example, at Guy, Arkansas a three-station seismic array was installed after several relatively small earthquakes were observed ($M_w < 3$), which allowed for accurate determination of event hypocenters that defined a previously unknown fault (*Horton*, 2012). Although it may be difficult to bridge the gap between the laboratory and field scales confidently, laboratory measurements of frictional properties of rock can provide a basis for appropriate friction models. Alternatively, the field experiments performed by *Guglielmi et al.* (2015), where fluid was injected into a natural fault, demonstrated an ability to obtain direct in-situ measurements of the frictional properties of real faults. After obtaining appropriate information and acknowledging the uncertainty associated with the field data, one could use the criterion proposed in this study to assess expected faulting behavior near a wastewater disposal site.

7.3 Fault heterogeneity as a mechanism for controlling frequency - magnitude behavior

Numerical reservoir models are useful tools for investigating how natural geologic and injection conditions can affect seismicity, but it can often be difficult to generate realistic earthquake sequences using physics-based seismicity models. Rate-and-state simulations on planar faults with homogeneous frictional properties and stress conditions typically yield single event sequences with a single earthquake magnitude characteristic of the size of the fault. In their investigation of injection-induced seismicity, *McClure and Horne* (2011) observed sequences of events with magnitudes that increased over time as pressure moved along the fault. In reality, earthquake sequences have been observed to follow a Gutenberg-Richter-type frequency magnitude distribution. Gutenberg-Richter (GR) earthquake sequences can be characterized by two parameters that define the rate of earthquake activity, a_{GR}, and the power-law scaling behavior of earthquake magnitudes, b_{GR}:

$$\log_{10} N_{M \geq m} = a_{GR} - b_{GR} m, \tag{7.6}$$

where $N_{M \geq m}$ is the number of events observed in some time period with magnitude M that is greater than or equal to a threshold magnitude m. In this work, we modeled sequences of induced earthquakes along a large basement fault. The a_{GR} and b_{GR} are important components of earthquake

hazard analyses. The purpose of this study was to determine how fault heterogeneity can affect the frequency-magnitude distribution of simulated earthquake events.

The significance of heterogeneous properties in terms of understanding the hydromechanical behavior of fractures and faults have been highlighted in many previous theoretical, laboratory, and field studies. *Andrews* (1980) argued that stress heterogeneity over a range of spatial scales contributed to the power law form of the commonly observed Gutenberg-Richter-type frequency-magnitude distribution of earthquake events. *Okubo and Aki* (1987) measured the roughness of the trace of the San Andreas Fault, and observed that it could be described as a fractal pattern. *Ishibashi et al.* (2014) performed laboratory flow experiments on samples of granitic rocks in order to investigate how fracture surface roughness affected fluid flow for joints and sheared fractures at several different confining pressures and over several different length scales. In that study, it was observed that the heterogeneous fracture aperture distribution caused flow channeling to occur, and it was suggested that these effects could have significant impacts in terms of mass transport or heat transfer. Moreover, both the fracture aperture distributions and the effective fracture surface area were found to be scale-invariant (fractal). *Mai and Beroza* (2002) analyzed coseismic slip distributions of real earthquakes using finite source models, and found that the slip patterns could be well characterized by a fractal decay model. *Ripperger et al.* (2007) performed quasidynamic earthquake rupture simulations with slip-weakening friction on faults with fractal shear stress distributions and found that the frequency-magnitude statistics of a collective series of random realizations was influenced by the heterogeneity. In this work, we applied a spatial random field model to generate heterogeneous, spatially correlated distributions of fault properties and performed quasidynamic earthquake rupture simulations with rate-and-state friction.

In the three-dimensional version of the present model, fractures and faults are represented as two-dimensional surfaces and discretized into rectangular elements. Each of the rate-and-state parameters $(a, b, \delta_c, f_*, V_*)$ can be heterogeneous over the fault surface. Hydraulic and void aperture (e and E) can also be considered heterogeneous fault properties. Finally, one of the most important aspects of this model is its ability to handle spatially and temporally variable stress states while enforcing mechanical equilibrium rigorously, so it is clear that stress can also be considered a heterogeneous fault property.

7.3.1 Spatial random field model

The spatial random field model we used was similar to the models used in other previous investigations of fault heterogeneity and earthquake rupture (*Dempsey and Suckale*, 2016; *Dempsey et al.*, 2016; *Mai and Beroza*, 2002; *Ripperger et al.*, 2007). For a two-dimensional fault plane, the power spectral density, $P(K_s, K_d)$ is a function of the spatial wave numbers in the strike- and dip-directions

and follows a power law decay that is related to the fractal dimension, D (*Saupe*, 1988):

$$P\left(K_s, K_d\right) \sim \frac{1}{\left(K_s^2 + K_d^2\right)^{4-D}} \tag{7.7}$$

In the spatial random field model, P controls the amplitude of the perturbation about the mean value. For application to earthquake rupture numerical models, the practical range of wave number depends on the size of the model fault and the size of a discretized fault element. Equation 7.7 was used to define P over the practical wave number range and fractal dimension of interest, random phase angles were applied to perturb P in the Fourier domain to create a unique pattern, and then P was inverted into the real space domain, as described in Chapter 2 of *Saupe* (1988). Higher values of D yielded a more random, less spatially correlated pattern. For example, filtering the same random field for different fractal dimensions ranging from $2 \leq D \leq 3$ yielded the distributions shown in Fig. 7.7.

It was recognized that perturbations in shear stress, normal stress, and fault friction can each have a unique impact on the earthquake rupture process. We attempted to achieve consistency between cases involving different fault properties by controlling the magnitude of the perturbations based on their expected impact in stress drop during an individual earthquake rupture. The stress drop during an earthquake, $\Delta\tau$, is the difference between the background initial shear stress acting on the fault well ahead of the rupture front, τ^R, and the stress level behind the rupture front during sliding, τ_D:

$$\Delta\tau = \tau^R - \tau_D. \tag{7.8}$$

We used the spatial random fields to alter the state of stress or frictional properties by adding perturbations to background (average) values of shear stress, $\delta\tau$, normal stress, $\delta\sigma$, or b in the rate-and-state friction model (which affects dynamic friction), δb. Comparing their impact on the stress drop:

$$\tau^R + \delta\tau - f_D\bar{\sigma}_n^R \sim \tau^R - f_D\left(\bar{\sigma}_n^R - \delta\sigma\right) \sim \tau^R - \left[f_* - (b + \delta b - a)\ln\frac{V_{max}}{V_*}\right]\bar{\sigma}_n^R, \tag{7.9}$$

it is apparent that the following scaling relationships provide an appropriate basis for comparing the influence of spatial random fields of different fault properties:

$$\delta\tau \sim f_D\delta\sigma \sim \bar{\sigma}_n^R \ln\frac{V_{max}}{V_*}\delta b. \tag{7.10}$$

The spatial random fields we generated had a mean values of zero and a standard deviation χ. We normalized the spatial random fields such that the perturbation at one standard deviation from the mean corresponded to a specified fraction, α, of the initial shear stress (i.e., $\delta\tau^{1\chi} = \alpha\tau^R$).

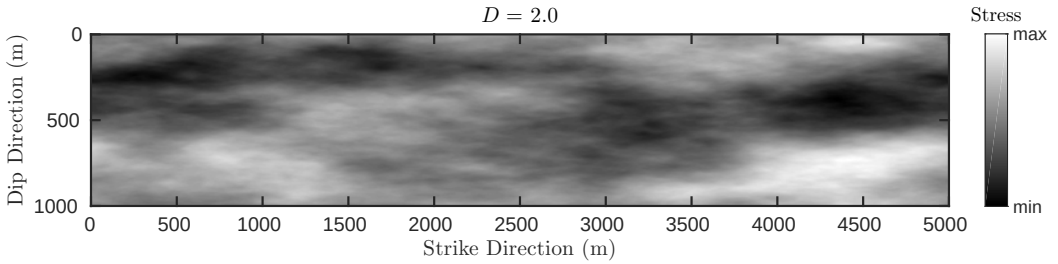

(a)

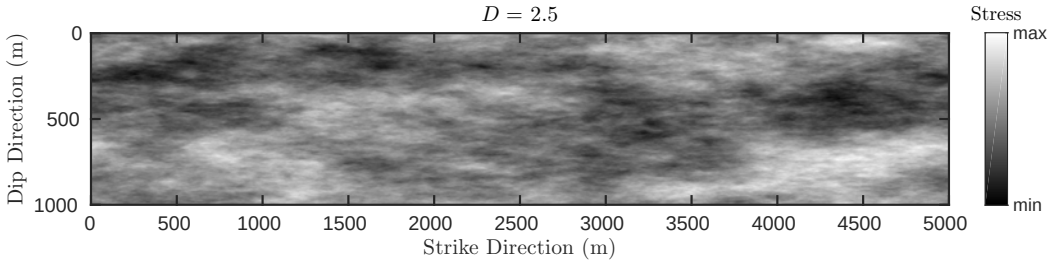

(b)

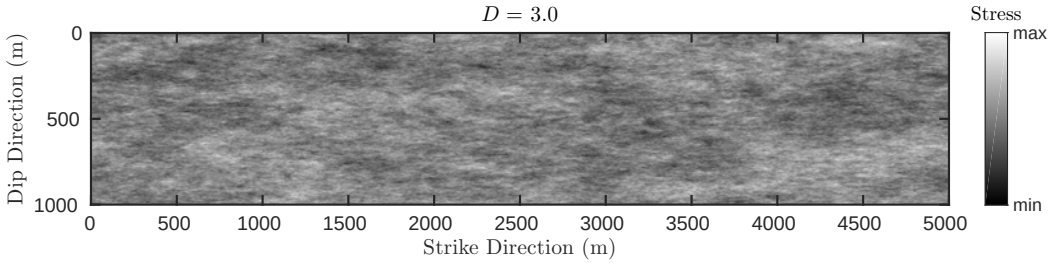

(c)

Figure 7.7: Example of the heterogeneous stress distributions generated using the spatial random field model. The same realization of the random field was filtered at different fractal dimensions: (a) $D = 2$, (b) $D = 2.5$, and (c) $D = 3$. The fractal dimension controlled the rate of power-law decay of the amplitude of the stress perturbations in the wave number domain. The random fields were normalized such that the amplitude of the stress perturbation at one standard deviation from the mean was equal to some fraction, α, of the remote shear stress (i.e., $\delta\tau^{1\chi} = \alpha\tau^{R}$).

7.3.2 Injection-induced earthquake sequences on planar three-dimensional rate-and-state faults with heterogeneous stress distributions

We performed simulations that coupled fluid flow along the fault with the earthquake rupture process within a rate-and-state friction framework. Equation 7.7 was used to generate stochastic realizations of heterogeneous, spatially correlated stress distributions along two-dimensional fault surfaces.

Because we modeled the two-dimensional fault surface as a planar feature, stress heterogeneity was considered to be a proxy for modeling the roughness of real faults (*Andrews*, 1980; *Andrews and Barall*, 2011; *Okubo and Aki*, 1987; *Dempsey and Suckale*, 2016). The purpose of introducing stress heterogeneity was to attempt to generate realistic earthquake distributions using the rate-and-state model. For the purposes of this study, a realistic earthquake sequence means one that hosts multiple events of different magnitudes and which exhibits Gutenberg-Richter-type power-law scaling of the frequency-magnitude distribution.

In this study, flow in the aquifer was not modeled numerically. The analytical solution for radial flow in an aquifer was used to generate a temporal history of pressure evolution at a point assumed to be 500 m away from the well. In our conceptual model, a 5 km by 1 km vertical strike-slip fault existed entirely within impermeable basement rock. Several smaller fractures connected the fault to the aquifer. A pressure boundary condition based on the radial flow solution was prescribed to each of the smaller fractures, which allowed for mass flux into the main fault zone. A five year period of injection was modeled.

The fault was initialized with heterogeneous distributions of both shear and normal stress. The rate-and-state frictional properties were homogeneous. The initial sliding velocity was constant across the fault. Stress gradients in the vertical direction and pressure gradients due to gravity were neglected. The stress transfer calculations were performed using the *Okada* (1992) Green's functions for rectangular loads in a half-space. A quasidynamic elasticity formulation was used. Important model parameters are listed in Table 7.8.

In this study, careful consideration was taken to avoid well-known numerical discretization issues related to the rate-and-state friction formulation. In discretization refinement studies performed using our model, it was found that an appropriately refined grid required roughly 20 x 20 elements to resolve the nucleation patch. For the parameters listed in Table 7.8, the critical length scale for nucleation was $L_c = \pi G \delta_c / \left[\bar{\sigma}_n (b-a)(1-\nu)\right] = 322$ m. In this study, the 5 km by 1 km fault was discretized into square elements that were each 10 m by 10 m, yielding a total of 50,000 elements.

In the simulations, earthquake ruptures were triggered as pressure perturbations migrated along the fault. Multiple earthquake ruptures of various magnitude were triggered throughout the simulation. Two examples of typical earthquake ruptures are illustrate in Figs. 7.8 and 7.9 (the stress patterns for the simulations shown in these figures were generated with $D = 2.5$ and $\alpha = 0.2$). Upon nucleation, the ruptures tended to be guided by the stress patterns. Rupture arrest was caused by propagation into low stress areas as well as a result of the rupture reaching the fault boundaries. Rupture arrest was observed to be influenced mostly by the large wavelength fluctuations in stress, and tended to propagate though relatively small fluctuations with ease.

In our simulations, earthquakes tended to be influenced by the stress distribution from prior events. In simulations not shown here, if a homogeneous distribution of initial normal stress was used, constant shear stress behind the rupture fronts tended to result. In the simulation results

shown in Figs. 7.8 and 7.9, the heterogeneous distribution of shear stress left behind the rupture front is a result of the combination of heterogeneous normal stress and constant dynamic coefficient of friction.

Table 7.8: Model properties for study of frequency-magnitude scaling relationship for heterogeneous faults.

Parameter	Value	Unit
Depth	5	km
σ_n^R	93.75	MPa
τ^R	27.5	MPa
p_0	45	MPa
G	15	GPa
ν	0.25	-
η	3.15	MPa $\cdot$ s $\cdot$ m^{-1}
e_*	0.0001	m
E_*	0.001	m
σ_{e*}	100	MPa
σ_{E*}	100	MPa
f_*	0.7	-
V_*	1×10^{-10}	m $\cdot$ s^{-1}
a	0.01	-
b	0.012	-
δ_c	5×10^{-4}	m
s	0.5	MPa
k^m	20×10^{-15}	m^2
ϕ^m	0.2	-
λ^{-1}	0.7×10^{-9}	MPa $\cdot$ s
ρ_0	1000	kg $\cdot$ m^{-3}
$\beta_\varphi + \beta_r$	2×10^{-3}	MPa^{-1}
H^m	200	m
q_i	0.018	m$^3\cdot$ s^{-1}

7.3.3 Power-law scaling behavior of earthquake sequences

For each individual realization, the number of observed earthquakes ranged from roughly 1 to 10 over the five year simulation duration. This was determined to be insufficient for understanding the effect of the stress heterogeneity on the frequency-magnitude behavior. We followed the approach used by *Ripperger et al.* (2007), in which the collective properties of simulations using many realizations of stochastic stress patters were analyzed. We performed two sensitivity studies. In Case 1, a fractal dimension of $D = 2.5$ was used to generate the spatial random fields, and the stress amplitude scaling factor was varied over the range of $0.05 \leq \alpha \leq 0.2$. In Case 2, we used $\alpha = 0.2$ and varied the fractal dimension over the range of $2 \leq D \leq 3$. For each scenario, 90 realizations were simulated. We constructed frequency-magnitude distributions (FMD) for each scenario. In the FMD plots shown

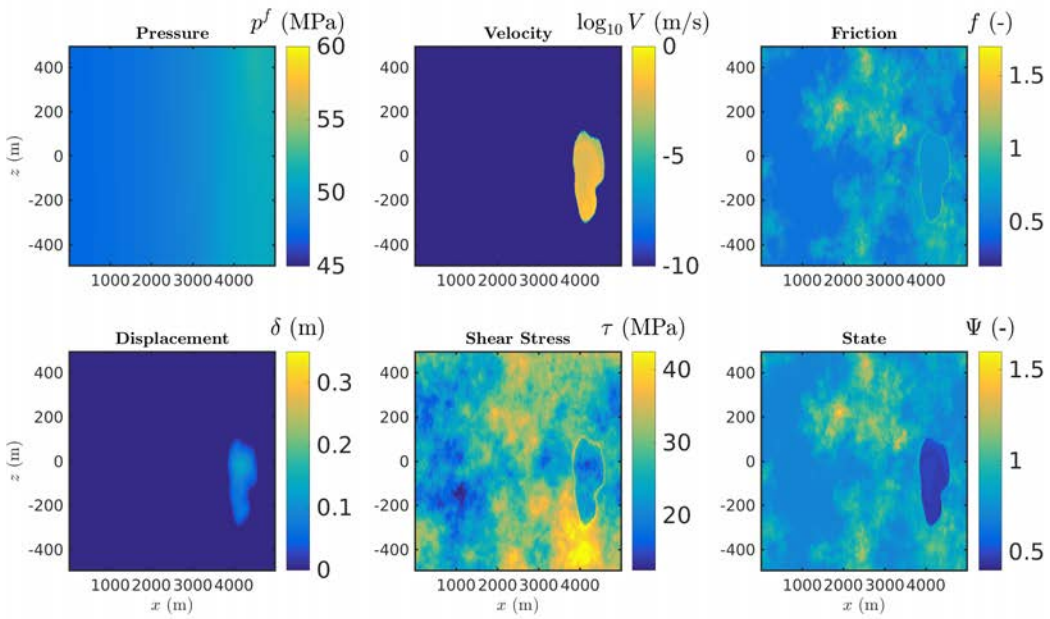
Pressure
p^f (MPa)
60
55
50
45
Velocity
$\log_{10} V$ (m/s)
0
-5
-10
Friction
f (-)
1.5
1
0.5
Displacement
δ (m)
0.3
0.2
0.1
0
Shear Stress
τ (MPa)
40
30
20
State
Ψ (-)
1.5
1
0.5
z (m)
400
200
0
-200
-400
1000 2000 3000 4000
x (m)

(a)

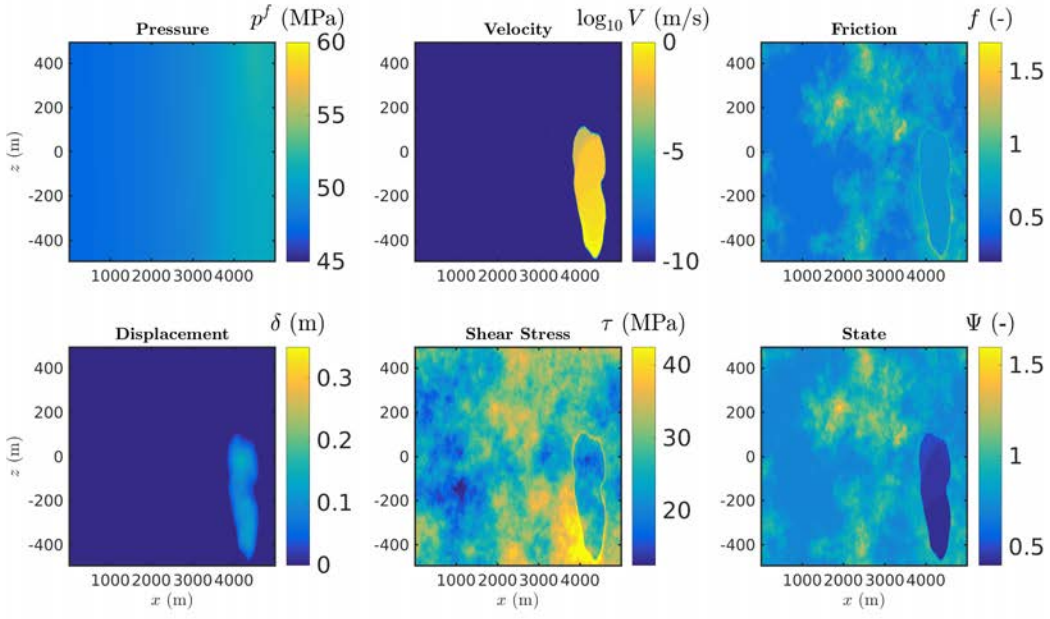
Pressure
p^f (MPa)
60
55
50
45
Velocity
$\log_{10} V$ (m/s)
0
-5
-10
Friction
f (-)
1.5
1
0.5
Displacement
δ (m)
0.3
0.2
0.1
0
Shear Stress
τ (MPa)
40
30
20
State
Ψ (-)
1.5
1
0.5
z (m)
400
200
0
-200
-400
1000 2000 3000 4000
x (m)

(b)

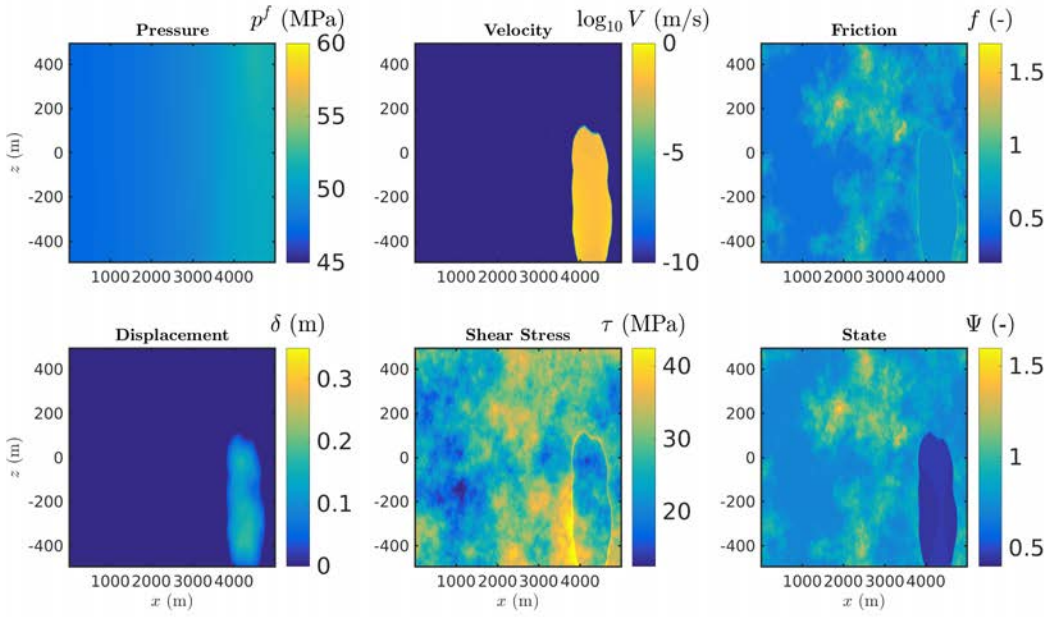

(c)

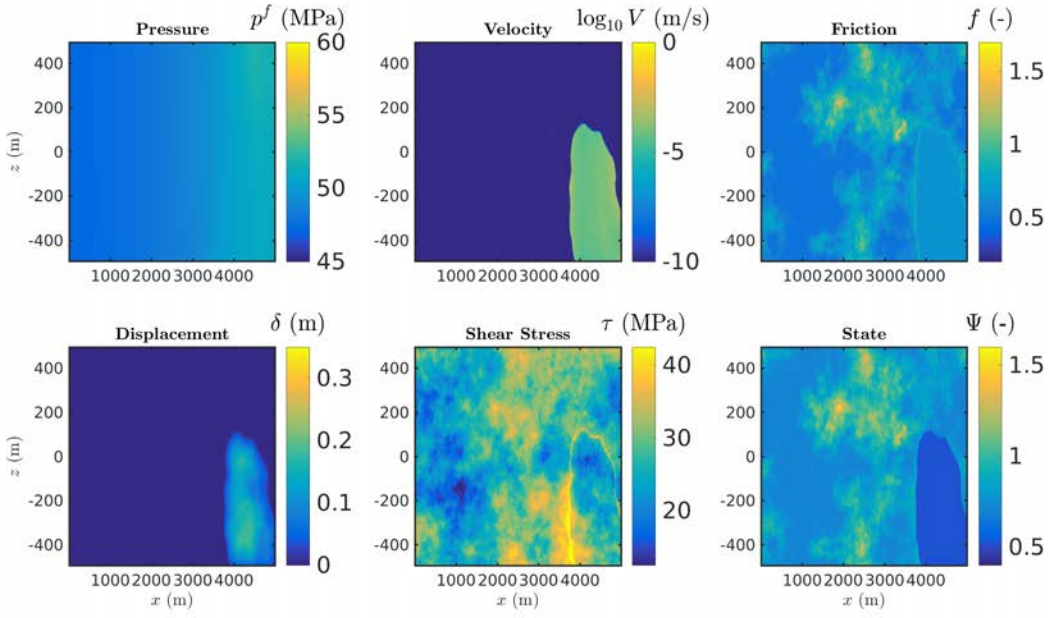

(d)

Figure 7.8: A typical earthquake rupture on a fault with heterogeneous distributions of shear and normal stress. Subfigures (a) through (d) show the propagation of the rupture at several points during the rupture process. The rupture was triggered by pressure diffusion along the fault.

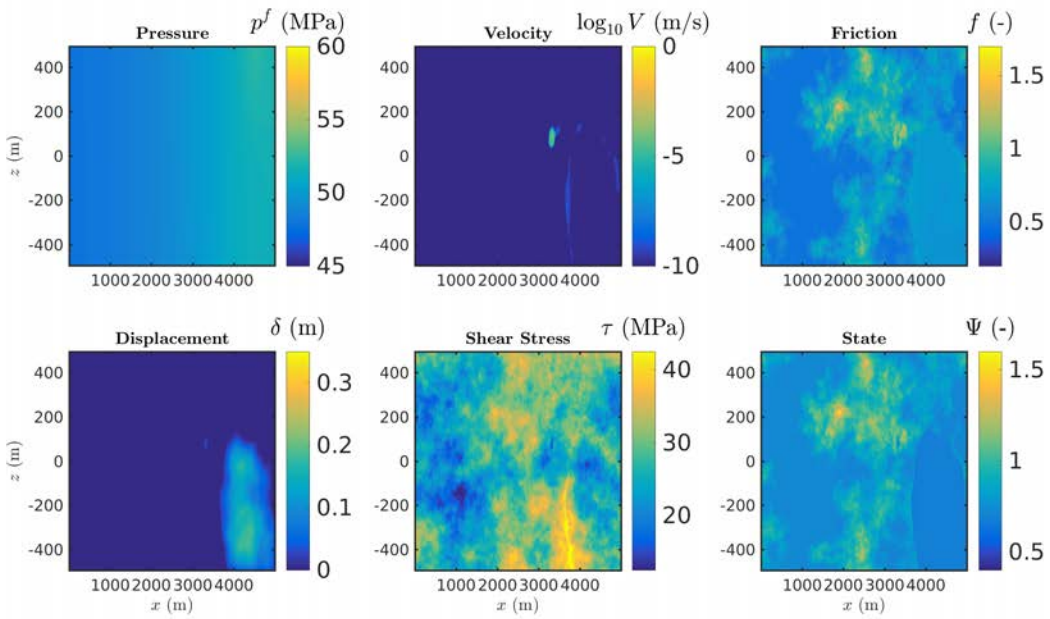
Pressure
p^f (MPa)
60
55
50
45
Velocity
$\log_{10} V$ (m/s)
0
-5
-10
Friction
f (-)
1.5
1
0.5
Displacement
δ (m)
0.3
0.2
0.1
0
Shear Stress
τ (MPa)
40
30
20
State
Ψ (-)
1.5
1
0.5
z (m)
400
200
0
-200
-400
1000 2000 3000 4000
x (m)

(a)

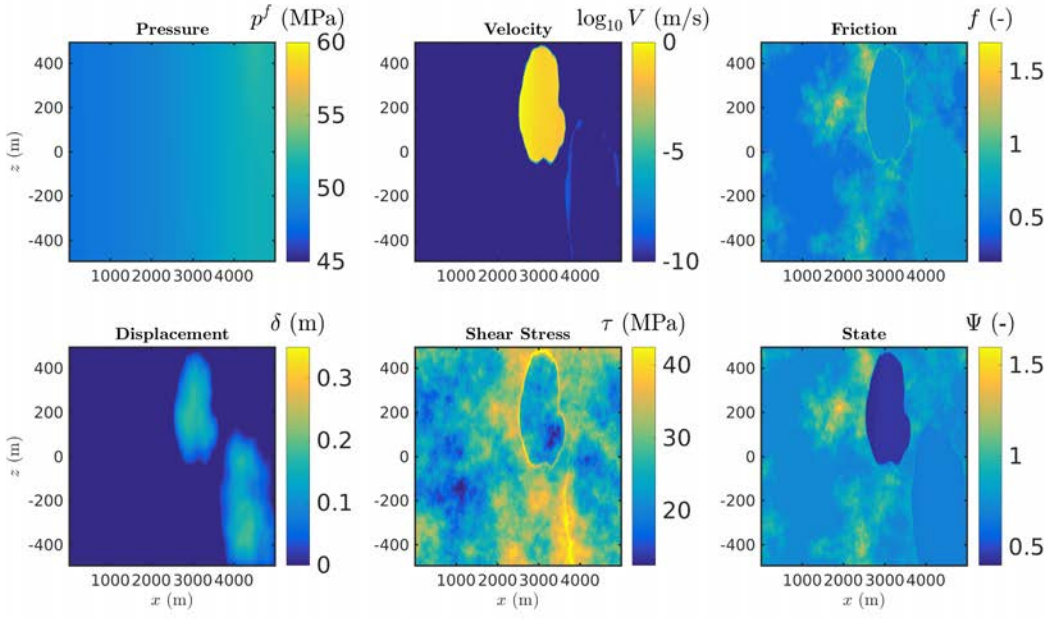
Pressure
p^f (MPa)
60
55
50
45
Velocity
$\log_{10} V$ (m/s)
0
-5
-10
Friction
f (-)
1.5
1
0.5
Displacement
δ (m)
0.3
0.2
0.1
0
Shear Stress
τ (MPa)
40
30
20
State
Ψ (-)
1.5
1
0.5
z (m)
400
200
0
-200
-400
1000 2000 3000 4000
x (m)

(b)

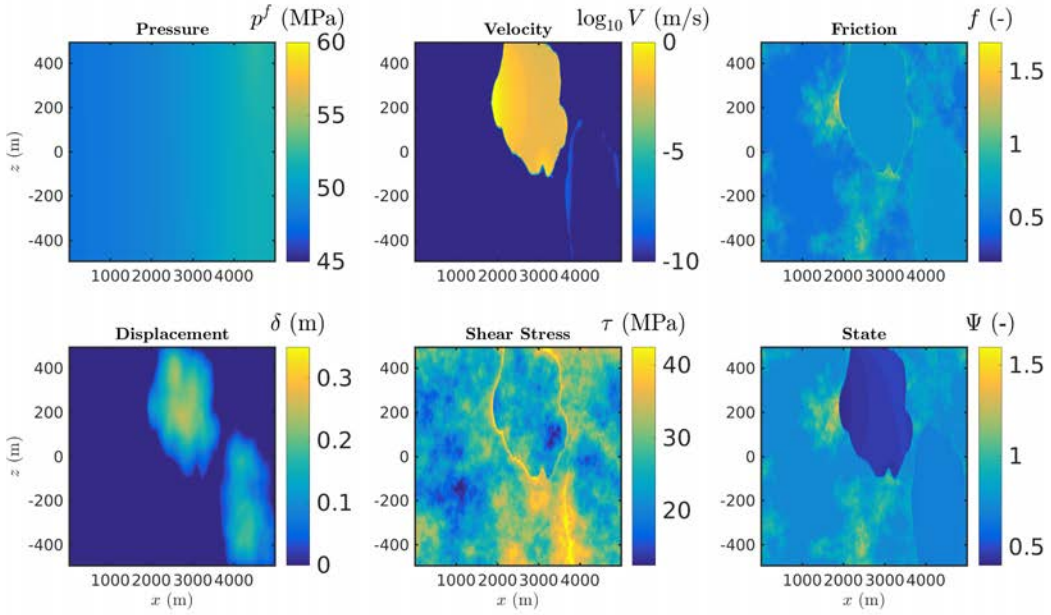

(c)

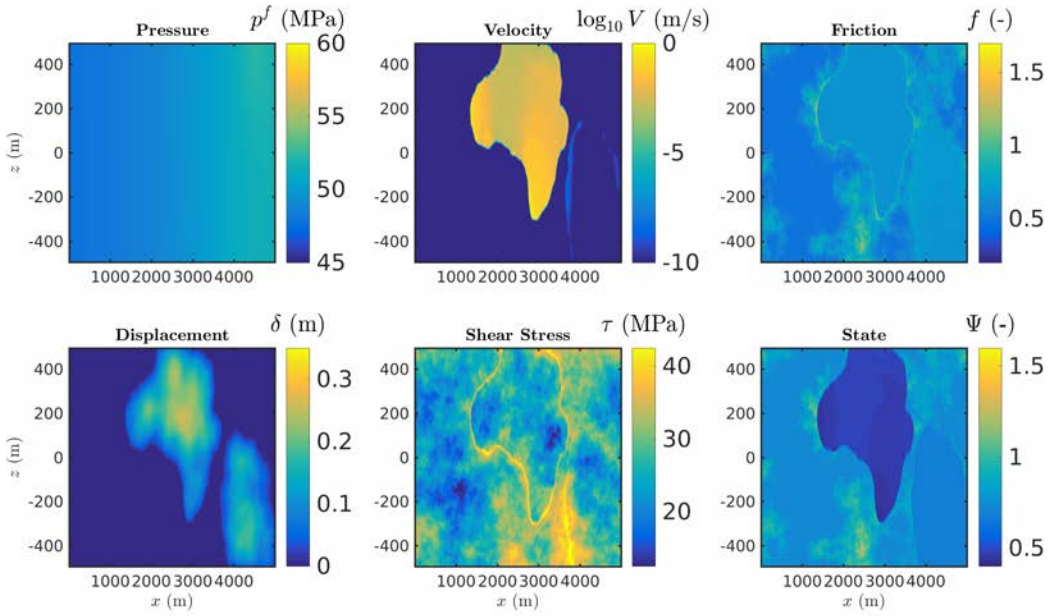

(d)

Figure 7.9: A typical earthquake rupture on a fault with heterogeneous distributions of shear and normal stress. Subfigures (a) through (d) show the propagation of the rupture at several points during the rupture process. The rupture propagate along high stress pathways and was arrested by low stress areas and the fault boundary.

in this section, the values of $N_{M \geq m}$ were normalized by the total number of events that occurred across all realizations. This normalization was performed because some of the simulations failed to run to the total simulation time due to convergence issues.

We observed earthquakes ranging from roughly M 2 up to a maximum magnitude of M 4.6, which was characteristic of the size of the fault. The frequency-magnitude distributions (FMD) for the scenarios tested in Case 1 are shown in Fig. 7.10. For the scenario where $\alpha = 0.05$, which represented a relatively uniform stress distribution, the FMD was almost flat. This indicates that as $\alpha \rightarrow 0$, the ruptures tended to propagate across the entire fault. For the scenarios with $\alpha > 0.05$, the FMD's were similar to each other. This suggests that increasing the amplitude of the stress perturbation beyond a certain threshold did not affect the rupture arrest behavior significantly. Although a weak power-law scaling was observed, the slope of the power-law decay was not observed to follow the behavior of natural earthquakes.

In Fig. 7.11, the FMD's for collections of simulations with different fractal dimension are shown (Case 2). In Case 2, a wider range of power-law decay slopes were observed. For the scenario with the largest fractal dimension tested ($D = 3$), the slope was found to be slightly larger than $b_{GR} = 0.5$. This was an encouraging result, because the FMD slope was more similar to natural earthquakes than in Case 1. These results suggest that perhaps the fractal dimension of the stress distribution, which controls the texture of the pattern, may be important for controlling the Gutenberg-Richter behavior of earthquake sequences.

7.3.4 Discussion

The purpose of this study was to generate earthquake sequences using a rate-and-state friction earthquake simulator that exhibited Gutenberg-Richter-type behavior in their frequency-magnitude statistics. Previous work has demonstrated that rate-and-state simulations of earthquake ruptures on planar faults with homogeneous stress and frictional properties tend to generate sequences of events with a single magnitude characteristic of the size of the fault. In this study, we introduced stress heterogeneity as a proxy for modeling the rough geometric texture of real faults. A fractal distribution of stress, in which the amplitudes of the stress perturbations vary with scale, has been suggested previously as a mechanism for causing power-law frequency-magnitude distributions.

In order to simulate a Gutenberg-Richter-type FMD, the size of the earthquakes must span several orders of magnitude. The maximum earthquake magnitude is dictated predominantly by the size of the model fault. The minimum earthquake magnitude is controlled by the critical distance for nucleation, L_c. In order to preclude discretization error, a sufficient number of grid blocks must be used to resolve the nucleation patch. Therefore, there is an unavoidable interplay between resolving the smallest events possible while still modeling a fault that is large enough to provide an ample range of earthquake magnitudes to sample. Theoretically, these issues promote questions surrounding the scaling of laboratory-derived friction properties to real faults and how to adequately conceptualize

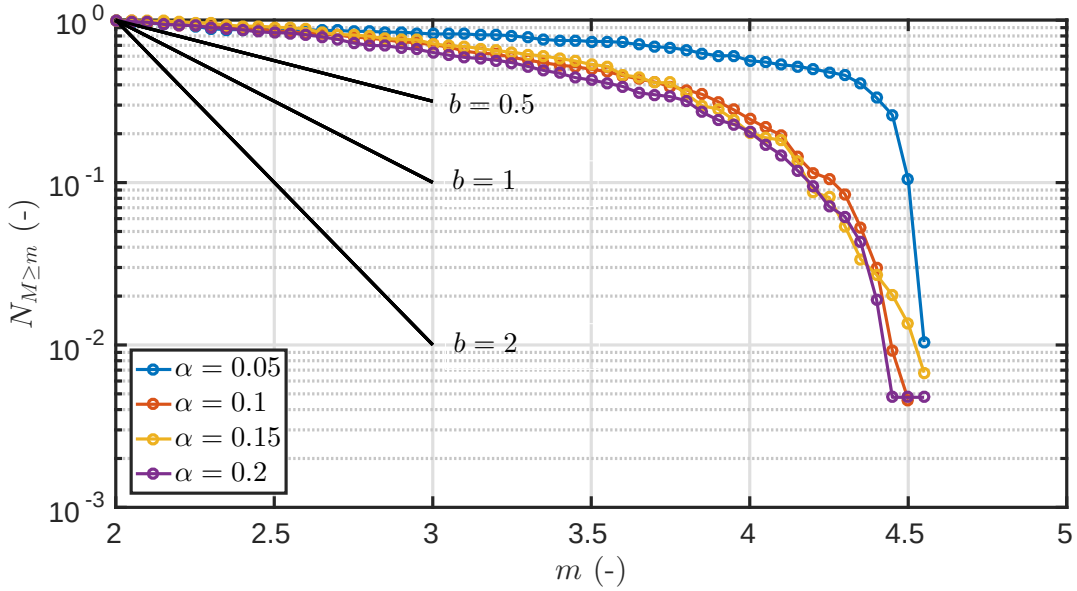

Figure 7.10: Frequency-magnitude distributions for several collections of simulations in which the heterogeneous stress distributions were obtained using different stress amplitude scaling factors ($0.05 \leq \alpha \leq 0.2$). The fractal dimension was the same for each case ($D = 2.5$). For each case (containing 90 realizations each), $N_{M\geq m}$ was normalized by the total number of events that occurred across all realizations. The *black lines* represent Gutenberg-Richter b-value slopes ranging from $0.5 \leq b \leq 2$.

the multiscale nature of large fault structures. Practically, this is simply an issue of computational performance.

In our study, we observed earthquake magnitudes ranging from roughly $2 \leq \mathrm{M} \leq 4.6$. This is perhaps a lower bound on an adequate range of magnitudes to observe power-law scaling behavior. In general, the stress heterogeneity did promote power-law scaling FMD's. However, the power-law decay was observed to be too weak compared to natural earthquakes. This suggests that rupture arrest was not controlled by the short wavelength stress perturbations. It would be useful to test this method further by investigating a broader range of initial stress states and frictional property values as well as further discretization refinement studies. However, based on the results of this study, we conclude that the fractal stress patterns were not sufficient to generate realistic Gutenberg-Richter-type behavior using the model. It may be necessary to resolve the true geometrical roughness in order to reproduce natural frequency-magnitude distributions.

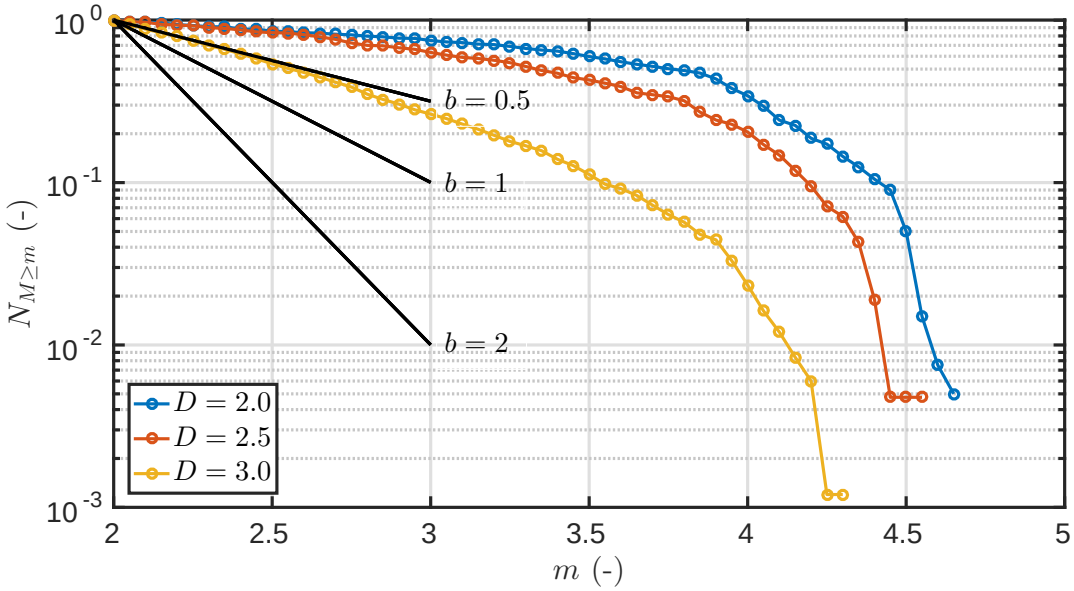

Figure 7.11: Frequency-magnitude distributions for several collections of simulations in which the heterogeneous stress distributions were obtained using different fractal dimensions ($2.0 \leq D \leq 3.0$). The stress amplitude scaling factor was the same for each case ($\alpha = 0.2$). For each case (containing 90 realizations each), $N_{M\geq m}$ was normalized by the total number of events that occurred across all realizations. The *black lines* represent Gutenberg-Richter b-value slopes ranging from $0.5 \leq b \leq 2$.

7.4 Concluding remarks

Seismic hazard analysis relies on statistical methods to arrive at hazard forecasts. Important earthquake statistics include the maximum expected earthquake magnitude, the seismicity rate, and the frequency-magnitude scaling relationship. Given these three statistical parameters, it is possible to calculate the probability of experiencing a magnitude of a given threshold within a specified time period. Typically, these parameters are considered to be stationary. Because injection-induced earthquakes are triggered by fluid injection operations, it is important to understand how the earthquake statistics may vary with operations. In this work, we applied numerical modeling to investigate fundamental physical processes that relate fluid flow through faulted porous media and earthquake rupture mechanics.

We developed a faulting criterion that can be applied in order to assess whether the maximum expected earthquake magnitude will be controlled by injection operations or purely by tectonic conditions. The faulting criterion depended on the state of stress, orientation of the fault, hydraulic properties of the fault, and frictional properties of the fault. In practice, there is considerable uncertainty in many of the parameters that influence the faulting criterion. Nonetheless, the criterion provides a basis for assessing which properties are most important to consider when performing site

characterization.

Previous work has demonstrated that it is difficult to simulate earthquake sequences with Gutenberg-Richter-type frequency-magnitude behavior using rate-and-state friction models on planar faults with homogeneous stress conditions and frictional properties. We applied a spatial random field model to generate heterogeneous, spatially correlated stress distributions and modeled sequences of injection-induced earthquakes on two-dimensional fault surfaces. The stress heterogeneity was introduced as a proxy for the geometrical complexity of real faults. Power-law scaling of the frequency magnitude distributions was observed for collections of many realizations. However, the power-law decay was found to be significantly weaker than observed for natural earthquake sequences. It may be important to resolve the geometrical complexity to obtain more realistic frequency-magnitude statistics from numerical earthquake rupture models.

Chapter 8

Concluding Remarks

The work described in the preceding chapters encompassed a variety of topics in computational physics, reservoir engineering, geomechanics, and earthquake rupture mechanics. The numerical model developed in this work was applied to aid interpretation of the hydromechanical and frictional faulting behavior of injection-induced earthquakes in a variety of geological and operational settings. Scenarios that were investigated include hydraulic stimulation in a geothermal reservoir, microseismic monitoring in a shale oil reservoir, and seismicity along large basements faults in hydraulic communication with overlying aquifers targeted for wastewater disposal. In Sect. 8.1, a summary is provided for each chapter. In Sect. 8.2, several suggestions are provided to encourage further research in the area of injection-induced seismicity.

8.1 Summary

Enhanced geothermal systems have not reached their full potential in large part due to technical challenges associated with generating significant reservoir permeability to achieve commercially viable fluid circulation rates. In Chapter 4, we performed an investigation of the Fenton Hill, New Mexico, USA Enhanced Geothermal System test site. Our goal was to develop an improved understanding of the geologic structure and hydromechanical behavior of fractured geothermal reservoirs. Using interpretations of the data sets recorded during several field experiments at Fenton Hill, we designed a conceptual model of the geologic structure and stimulation mechanism at the site. We hypothesized that stimulation (i.e., permeability enhancement) occurred though a mixed-mechanism process caused by mechanical opening of natural fractures and propagation of hydraulic splay fractures. We applied a numerical model that coupled fluid flow, heat transfer, elasticity, and fracture propagation in order to validate the hypothesis. Our numerical results were consistent with several distinct behavioral traits of the Fenton Hill experiments, which lends credit to our proposed conceptual model of the reservoir geologic structure and stimulation mechanism. In particular, the

results demonstrate that the mixed-mechanism hypothesis provides a cohesive explanation for two apparently contradictory observations: 1) injection occurred at fluid pressures significantly above the fracturing pressure, and 2) the locations of microseismic events migrated consistently in a direction that was not aligned with the orientation of the maximum principal stress. Recognition of the possiblitiy for mixed-mechanism stimulation will inform design of future enhanced geothermal systems.

Determination of appropriate well spacing, especially for horizontal infill wells, remains a difficult task related to the economic development of unconventional shale resources. In Chapter 5, we investigated a novel field test, called microseismic depletion delineation, that has been proposed previously as a useful method for assessing production trends near horizontal wells. The microseismic depletion delineation technique takes advantage of a poroelastic stress change that occurs in the reservoir during depletion, and also relies on the assumption that pressure transients will propagate relatively quickly in the network of fractures connected to the well. By reinjecting fluid at a carefully determined pressure while monitoring for microseismic activity, shear failure events on natural fractures will reveal the shape of the depleted zone.

In order to inform physics-based hazard models of induced seismicity related to wastewater disposal operations, it is necessary to determine appropriate hydraulic and frictional properties of large-scale basement faults that are able to host damaging earthquakes. Traditional reservoir engineering analyses, such as pressure transient testing, are unable to measure fault properties directly. It is also uncertain whether it is possible to extrapolate laboratory-scale measurements of fault properties to the field scale. In Chapter 6, we investigated the 2011 M_w 5.6 earthquake sequence that occurred near Prague, Oklahoma, USA, which is the largest earthquake that has been associated with wastewater disposal to date. Because the stress orientations, stress magnitudes, fault geometry, and earthquake source mechanisms at the Prague site have been well-characterized by previous studies, this particular earthquake sequence offered an opportunity to explore the range of physical processes and in-situ fault properties that could explain the 20 hour delayed triggering effect observed at the site. Our numerical experiments suggest that an initial undrained response resulting from elastic stress transfer from the foreshock followed by transient fluid flow along the fault may have contributed to the earthquake nucleation process. The results of the numerical experiments were used to constrain fault compliance and fault transmissivity for the fault that hosted the M_w 5.6 event. Fault zone compliance was found to be relatively large, tending towards values representative of a Skempton pore pressure coefficient near 1. Fault transmissivity was estimated to range from 10^{-18} to 10^{-15} m^3. This study has implications for understanding hydraulic properties, frictional properties, and faulting behavior of basement faults in Oklahoma that are large enough to host damaging earthquakes.

Seismic hazard analysis relies on statistical methods to arrive at hazard forecasts. Important earthquake statistics include the maximum expected earthquake magnitude, the seismicity rate, and

the frequency-magnitude scaling relationship. Given these three statistical parameters, it is possible to calculate the probability of experiencing a magnitude of a given threshold within a specified time period. Typically, these parameters are considered to be stationary. Because injection-induced earthquakes are triggered inherently by fluid injection operations, it is important to understand how the earthquake statistics may vary with operations. In this work, we applied numerical modeling to investigate fundamental physical processes that relate fluid flow through faulted porous media and earthquake rupture mechanics. We developed a faulting criterion that can be applied in order to assess whether the maximum expected earthquake magnitude will be controlled by injection operations or purely by tectonic conditions. We applied a spatial random field model to generate heterogeneous, spatially correlated stress distributions and modeled sequences of injection-induced earthquakes on two-dimensional fault surfaces. The stress heterogeneity was introduced as a proxy for the geometrical complexity of real faults. Power-law scaling of the frequency magnitude distributions was observed for collections of many realizations. However, the power-law decay was found to be significantly weaker than observed for natural earthquake sequences. It may be important to resolve the geometrical complexity to obtain more realistic frequency-magnitude statistics from numerical earthquake rupture models.

8.2 Recommendations for future work

The fundamental mechanism of injection-induced earthquakes, whereby a reduction in effective normal stress and the associated reduction in frictional strength triggers the earthquake nucleation process, has been well established for several decades. Nonetheless, significant scientific contributions to the field of induced seismicity remain possible. The work presented in this dissertation involved a combination of advanced numerical modeling, interpretation of field observations, and theoretical investigations. Here, several suggestions are provided to encourage further research in each of these areas.

The numerical model applied in this work relied on a boundary element method to solve the fault mechanics problem. In the boundary element method, faults are represented mathematically as infinitely thin surfaces. In this approach, a question of scale emerges. Large faults that are capable of hosting damaging earthquakes are known to encompass structural complexity over a range of length scales, and can be comprised of a core of fine-grained, stiff, low-permeability material surrounded by a damage zone of fractured rock. The extent of the fault zone thickness is difficult to measure in practice, and can have several different conceptual interpretations. A significant limitation of the model was that it was unable to account for mechanical processes that may occur at scales on the order of the fault zone thickness. For example, because fault zone material can include a combination of porous rock and fractures, poroelastic effects related to changes in fluid pressure in the pores and fractures may affect the local state of stress within the fault zone. It may be possible

to resolve this type of behavior with a coupled fracture mechanics and poroelasticity model such as the one described in Sect. 2.3, but this approach would likely require a significant increase in the computational burden which may obviate the model's utility. Therefore, it is worthwhile to pursue the development of numerical methods that are able to incorporate the effects of fault-zone-scale mechanical processes yet maintain the computational efficiency of the boundary element approach.

In our model, fluid flow and storage in fault zone structures was characterized by empirical models that related hydraulic aperture, void aperture, and transmissivity to fault deformation. Hydraulic and void aperture were assumed to behave according to the nonlinear joint stiffness equation provided by *Willis-Richards et al.* (1996). Along-fault transmissivity was related to the hydraulic aperture through a model for flow between parallel plates (*Witherspoon et al.*, 1980). These empirical models were developed originally to describe the behavior of individual fractures and were based on laboratory experiments. Because fault zones are comprised of many individual fractures it is reasonable to apply these types of models to study the interaction between fluid flow and earthquake mechanics, however, their application to natural faults must be approached with some skepticism. In Chapter 6, we applied our numerical model to reproduce behavior observed during the 2011 Prague, Oklahoma earthquake sequence which involved a fault that was on the order of 5 to 20 km long. Based on the modeling results and a few plausible assumptions, we provided ranges of estimates for in-situ fault compliance and transmissivity in the context of our preferred empirical constitutive models. Research that aims to bridge the gap between characterizing behavior that can be quantified at the laboratory-scale with the behavior that can be expected to occur on large faults will be invaluable for informing physics-based numerical models. Emphasis should be placed on developing empirical models that can be tested and validated using field-scale observations.

Physics-based numerical models of induced seismicity have several applications to seismic hazard analysis. From a theoretical perspective, it will be useful to perform further studies that are similar to those presented in Chapter 7 to determine whether a relationship exists between injection well operational controls, such as injection rate or injection pressure, and the earthquake statistics that many seismic hazard analyses rely upon, such as the rate of earthquake productivity or the frequency-magnitude scaling relationship. To date, most hazard analyses assume stationarity in the earthquake statistics, and therefore are not able to forecast changes in seismic hazard that may result as a consequence of a change in operational strategy (i.e., changing the location of significant fluid injection). From a practical perspective, physics-based models such as the one presented in this work could be applied at particular field sites to characterize seismic hazard. In this application, it would be useful to develop possible conceptual models of subsurface geologic structure, develop constraints on the geomechanical properties and state of stress at depth, and then generate a series of stochastic realizations. In that manner, the analysis is informed by the underlying physical processes that govern seismicity and the hazard is quantified within a probabilistic framework.

List of References

Abate, J., and W. Whitt (2006), A unified framework for numerically inverting Laplace transforms, *INFORMS Journal on Computing*, **18**(4), 408–421, doi:10.1287/ijoc.1050.0137.

Addis, M. (1997), The Stress-Depletion Response Of Reservoirs, in *SPE Annual Technical Conference and Exhibition*, San Antonio, Texas, USA, doi:10.2118/38720-MS.

Alberty, M., and M. McLean (2001), Fracture gradients in depleted reservoirs-drilling wells in late reservoir life, in *SPE/IADC Drilling Conference*, Amsterdam, The Netherlands, doi:10.2118/67740-MS.

Alt, R., and M. Zoback (2014), Development of a detailed stress map of Oklahoma for avoidance of potentially active faults when siting wastewater injection wells, in *AGU Fall Meeting*, San Francisco, California, USA.

Ampuero, J.-P., and A. Rubin (2008), Earthquake nucleation on rate and state faults - Aging and slip laws, *Journal of Geophysical Research*, **113**(August 2007), 1–61, doi:10.1029/2007JB005082.

Andrews, D. (1980), A stochastic fault model, 1. Static case, *Journal of Geophysical Research*, **85**(B7), 3867–3877, doi:10.1029/JB085iB07p03867.

Andrews, D., and M. Barall (2011), Specifying initial stress for dynamic heterogeneous earthquake source models, *Bulletin of the Seismological Society of America*, **101**(5), 2408–2417, doi:10.1785/0120110012.

Atkinson, G., D. Eaton, H. Ghofrani, D. Walker, B. Cheadle, R. Schultz, R. Shcherbakov, K. Tiampo, J. Gu, R. Harrington, Y. Liu, M. van der Baan, and H. Kao (2016), Hydraulic Fracturing and Seismicity in the Western Canada Sedimentary Basin, *Seismological Research Letters*, **87**(3), 631–647, doi:10.1785/0220150263.

Aydin, A. (2000), Fractures, faults, and hydrocarbon entrapment, migration and flow, *Marine and Petroleum Geology*, **17**(7), 797–814, doi:10.1016/S0264-8172(00)00020-9.

Aziz, K., and A. Settari (1979), *Petroleum Reservoir Simulation*, Khalid Aziz and Antonin Settari.

Baisch, S., E. Rothert, H. Stang, R. Voros, C. Koch, and A. McMahon (2015), Continued geothermal reservoir stimulation experiments in the Cooper Basin (Australia), *Bulletin of the Seismological Society of America*, **105**(1), 1–12, doi:10.1785/0120140208.

Bandis, S., A. Lumsden, and N. Barton (1983), Fundamentals of rock joint deformation, *Int. J. Rock Mech. Min. Sci. & Geomech. Abstr.*, **20**(6), 249–268, doi:10.1016/0148-9062(83)90595-8.

Barton, C., M. Zoback, and K. Burns (1988), In-situ stress orientations and magnitude at the Fenton Hill geothermal site, New Mexico, determined from wellbore breakouts, *Geophysical Research Letters*, **15**(5), 467–470, doi:10.1029/GL015i005p00467.

Barton, N., S. Bandis, and K. Bakhtar (1985), Strength, deformation and conductivity coupling of rock joints, *Int. J. Rock Mech. Min. Sci. & Geomech. Abstr.*, **22**(3), 121–140, doi:10.1016/0148-9062(85)93227-9.

Baumgartner, J., and M. Zoback (1989), Interpretation of Hydraulic Fracturing Pressure-Time Records Using Interactive Analysis Methods, *Int. J. Rock Mech. Min. Sci. & Geomech. Abstr.*, **26**(6), 461–469, doi:http://dx.doi.org/10.1016/0148-9062(89)91422-8.

Beeler, N., T. Tullis, and D. Goldsby (2008), Constitutive relationships and physical basis of fault strength due to flash heating, *Journal of Geophysical Research: Solid Earth*, **113**(1), 1–12, doi:10.1029/2007JB004988.

Ben-Zion, Y., and J. Rice (1995), Slip patterns and earthquake populations along different classes of faults in elastic solids, *Journal of Geophysical Research*, **100**, 12,959–12,983, doi:10.1029/94JB03037.

Ben-Zion, Y., and J. Rice (1997), Dynamic simulations of slip on a smooth fault in an elastic solid, *Journal of Geophysical Research: Solid Earth*, **102**(B8), 17,771–17,784, doi:10.1029/97JB01341.

Blanpied, M., D. Lockner, and J. Byerlee (1991), Fault stability inferred from grainte sliding experiments at hydrothermal conditions, *Geophysical Research Letters*, **18**(4), 609–612, doi:10.1029/91GL00469.

Blanpied, M., D. Lockner, and J. Byerlee (1995), Frictional slip of granite at hydrothermal conditions, *Journal of Geophysical Research*, **100**(B7), 13,045–13,064, doi:10.1029/95JB00862.

Bommer, J., S. Oates, J. Cepeda, C. Lindholm, J. Bird, R. Torres, G. Marroquin, and J. Rivas (2006), Control of hazard due to seismicity induced by a hot fractured rock geothermal project, *Engineering Geology*, **83**(4), 287–306, doi:10.1016/j.enggeo.2005.11.002.

Bosl, W., and A. Nur (2002), Aftershocks and pore fluid diffusion following the 1992 Landers earthquake, *Journal of Geophysical Research*, **107**(B12), 2366, doi:10.1029/2001JB000155.

Bradford, J., M. Ohren, W. Osborn, J. McLennan, J. Moore, and R. Podgorney (2014), Thermal Stimulation and Injectivity Testing at Raft River, ID EGS Site, in *39th Workshop on Geothermal Reservoir Engineering*, Stanford, California, USA.

Bradley, A. (2014), Software for Efficient Static Dislocation Traction Calculations in Fault Simulators, *Seismological Research Letters*, **85**(6), 1–8, doi:10.1785/0220140092.

Brown, D. (1989), The potential for large errors in the inferred minimum earth stress when using incomplete hydraulic fracturing results, *Int. J. Rock Mech. Min. Sci. & Geomech. Abstr.*, **26**(6), 573–577, doi:10.1016/0148-9062(89)91437-X.

Brown, D., D. Duchane, G. Heiken, and V. Hriscu (2012), *Mining the Earth's Heat: Hot Dry Rock Geothermal Energy*, Springer, doi:10.1007/978-3-540-68910-2.

Carder, D. (1945), Seismic Investigations in the Boulder Dam Area, 1940-1944, and the Influence of Reservoir Loading on Local Earthquake Activity, *Bulletin of the Seismological Society of America*, **35**(4), 1940–1944.

Carslaw, H., and J. Jaeger (1959), *Conduction of Heat in Solids*, Oxford University Press, Oxford.

Charoenwongsa, S., H. Kazemi, J. Miskimins, and P. Fakcharoenphol (2010), A Fully-Coupled Geomechanics and Flow Model for Hydraulic Fracturing and Reservoir Engineering Applications, in *Canadian Unconventional Resources & International Petroleum Conference*, vol. 6, Calgary, Alberta, Canada.

Cocco, M., and J. Rice (2002), Pore pressure and poroelasticity effects in Coulomb stress analysis of earthquake interactions, *Journal of Geophysical Research*, **107**(B2), ESE.2.1–ESE.2.17, doi:10.1029/2000JB000138.

Cornet, F. H., and R. H. Morin (1997), Evaluation of hydromechanical coupling in a granite rock mass from a high-volume high-pressure injection experiment: Le Mayet de Montagne, France, *International Journal of Rock Mechanics and Mining Sciences & Geomechanics Abstracts*, **34**(3-4), 207.e1–207.e14, doi:10.1016/S1365-1609(97)00185-8.

Coussy, O. (2004), *Poromechanics*, John Wiley & Sons, Ltd., Chichester, doi:10.1007/s13398-014-0173-7.2.

Crouch, S. (1976), Solution of plane elasticity problems by the displacement discontinuity method, *International Journal for Numerical Methods in Engineering*, **10**(2), 301–343, doi:10.1002/nme.1620100206.

Crouch, S., and A. Starfield (1983), *Boundary Element Methods in Solid Mechanics*, Allen and Unwin, London.

Davis, S., and C. Frohlich (1993), Did (or will) fluid injection cause earthquakes? - Criteria for a rational assessment, *Seismological Research Letters*, **64**(3-4), 207–224, doi:10.1017/CBO9781107415324.004.

de Pater, C., and S. Baisch (2011), Geomechanical Study of Bowland Shale Seismicity, *Tech. Rep. November*, Prepared for Cuadrilla Resources.

Dempsey, D., and J. Suckale (2016), Collective properties of injection-induced earthquake sequences: 1. Model description and directivity bias, *Journal of Geophysical Research: Solid Earth*, **121**(5), 3609–3637, doi:10.1002/2015JB012550.

Dempsey, D., S. Kelkar, N. Davatzes, S. Hickman, and D. Moos (2015), Numerical modeling of injection, stress and permeability enhancement during shear stimulation at the Desert Peak Enhanced Geothermal System, *International Journal of Rock Mechanics and Mining Sciences*, **78**, 190–206, doi:10.1016/j.ijrmms.2015.06.003.

Dempsey, D., J. Suckale, and Y. Huang (2016), Collective properties of injection-induced earthquake sequences: 2. Spatiotemporal evolution and magnitude frequency distributions, *Journal of Gephysical Research: Solid Earth*, **121**(5), 3638–3665, doi:10.1002/2015JB12550.

Detournay, E., and A.-D. Cheng (1987), Poroelastic Solution of a Plane Strain Point Displacement Discontinuity, *Journal of Applied Mechanics*, **54**, 783–787, doi:10.1115/1.3173117.

Dieterich, J. (1992), Earthquake nucleation on faults with rate- and state-dependent friction, *Tectonophysics*, **211**(1–4), 115–134, doi:10.1016/0040-1951(92)90055-B.

Dieterich, J. (1994), A constitutive law for rate of earthquake production and its application to earthquake clustering, *Journal of Geophysical Research: Solid Earth*, **99**(B2), 2601–2618, doi:10.1029/93JB02581.

Dieterich, J., and B. Kilgore (1996), Implications of fault constitutive properties for earthquake prediction., *Proceedings of the National Academy of Sciences of the United States of America*, **93**(9), 3787–3794, doi:10.1073/pnas.93.9.3787.

Dieterich, J., K. Richards-Dinger, and K. Kroll (2015), Modeling Injection-Induced Seismicity with the Physics-Based Earthquake Simulator RSQSim, *Seismological Research Letters*, **86**(4), 1102–1109, doi:10.1785/0220150057.

Dieterich, J. H. (1981), Constitutive properties of faults with simulated gouge, *Mechanical Behavior of Crustal Rocks*, **24**, 103–120, doi:10.1029/GM024p0103.

Ding, D., Y. Wu, and L. Jeannin (2014), Efficient simulation of hydraulic fractured wells in unconventional reservoirs, *Journal of Petroleum Science and Engineering*, **122**, 631–642, doi:10.1016/j.petrol.2014.09.005.

Dohmen, T., J. Zhang, C. Li, J. Blangy, K. Simon, J. D. Valleau, S. Morton, and S. Checkles (2013), A new surveillance method for delineation of depletion using microseismic and its application to development of unconventional reservoirs, in *SPE Annual Technical Conference and Exhibition*, New Orleans, Louisiana, USA, doi:10.2118/166274-MS.

Dohmen, T., J.-P. Blangy, and J. Zhang (2014), Microseismic depletion delineation, *Interpretation*, **2**(3), SG1–SG13, doi:10.1190/INT-2013-0164.1.

Dunham, E., and J. Rice (2008), Earthquake slip between dissimilar poroelastic materials, *Journal of Geophysical Research: Solid Earth*, **113**(B09304), 1–20, doi:10.1029/2007JB005405.

Dunham, E. M. (2008), MDSBI: Multi-Dimensional Spectral Boundary Integral Code, Version 4.1.7, *Tech. Rep. September*, Stanford University.

Dunham, E. M., D. Belanger, L. Cong, and J. E. Kozdon (2011), Earthquake Ruptures with Strongly Rate-Weakening Friction and Off-Fault Plasticity, Part 1: Planar Faults, *Bulletin of the Seismological Society of America*, **101**(5), 2296–2307, doi:10.1785/0120100075.

Economides, M., and K. Nolte (2000), *Reservoir Stimulation*, 3rd ed., Wiley.

Ellsworth, W., A. Llenos, A. McGarr, A. Michael, J. Rubinstein, C. Mueller, M. Petersen, and E. Calais (2015), Increasing seismicity in the U.S. midcontinent: Implications for earthquake hazard, *The Leading Edge*, **34**(6), 618–626, doi:10.1190/tle34060618.1.

Ellsworth, W. L. (2013), Injection-Induced Earthquakes, *Science*, **341**, doi:10.1785/gssrl.83.2.250.

Fang, Z., and E. Dunham (2013), Additional shear resistance from fault roughness and stress levels on geometrically complex faults, *Journal of Geophysical Research: Solid Earth*, **118**, 3642–3654, doi:10.1002/jgrb.50262.

Faulkner, D., C. Jackson, R. Lunn, R. Schlische, Z. Shipton, C. Wibberley, and M. Withjack (2010), A review of recent developments concerning the structure, mechanics and fluid flow properties of fault zones, *Journal of Structural Geology*, **32**(11), 1557–1575, doi:10.1016/j.jsg.2010.06.009.

Fehler, M. (1989), Stress control of seismicity patterns observed during hydraulic fracturing experiments at the Fenton Hill hot dry rock geothermal energy site, New Mexico, *International Journal of Rock Mechanics and Mining Sciences and*, **26**(3-4), 211–219, doi:10.1016/0148-9062(89)91971-2.

Fehler, M., L. House, and H. Kaieda (1987), Determining planes along which earthquakes occur: Method and application to earthquakes accompanying hydraulic fracturing, *Journal of Geophysical Research*, **92**(B9), 9407–9414, doi:10.1029/JB092iB09p09407.

Friberg, P., G. Besana-Ostman, and I. Dricker (2014), Characterization of an Earthquake Sequence Triggered by Hydraulic Fracturing in Harrison County, Ohio, *Seismological Research Letters*, **85**(6), 1295–1307, doi:10.1785/0220140127.

Frigo, M., and S. G. Johnson (2005), The design and implementation of FFTW3, *Proceedings of the IEEE*, **93**(2), 216–231, doi:10.1109/JPROC.2004.840301.

Frohlich, C. (2012), Two-year survey comparing earthquake activity and injection-well locations in the Barnett Shale, Texas., *Proceedings of the National Academy of Sciences of the United States of America*, **109**(35), 13,934–13,938, doi:10.1073/pnas.1207728109.

Frohlich, C., C. Hayward, B. Stump, and E. Potter (2011), The Dallas-Fort Worth Earthquake Sequence: October 2008 through May 2009, *Bulletin of the Seismological Society of America*, **101**(1), 327–340, doi:10.1785/0120100131.

Frohlich, C., W. Ellsworth, W. Brown, M. Brunt, J. Luetgert, T. MacDonald, and S. Walter (2014), The 17 May 2012 M4.8 earthquake near Timpson, East Texas: An event possibly triggered by fluid injection, *Journal of Geophysical Research: Solid Earth*, **119**, 581–593, doi:10.1002/2013JB010755.

Garipov, T., M. Karimi-Fard, and H. Tchelepi (2016), Discrete fracture model for coupled flow and geomechanics, *Computational Geosciences*, **20**, 149–160, doi:10.1007/s10596-015-9554-z.

Ge, S., M. Liu, N. Lu, J. Godt, and G. Luo (2009), Did the Zipingpu Reservoir trigger the 2008 Wenchuan earthquake?, *Geophysical Research Letters*, **36**(20), 3–7, doi:10.1029/2009GL040349.

Geertsma, J., and F. de Klerk (1969), A Rapid Method of Predicting Width and Extent of Hydraulically Induced Fractures, *Journal of Petroleum Technology*, **21**(12), 1571–1581, doi:10.2118/2458-PA.

Ghassemi, A., A. Nygren, and A. Cheng (2008), Effects of heat extraction on fracture aperture: A porothermoelastic analysis, *Geothermics*, **37**(5), 525–539, doi:10.1016/j.geothermics.2008.06.001.

Ghassemi, A., S. Kelkar, and M. McClure (2015), Influence of Fracture Shearing on Fluid Flow and Thermal Behavior of an EGS Reservoir - Geothermal Code Comparison Study, in *Fourtieth Workshop on Geothermal Reservoir Engineering*, pp. 1–14, Stanford, California, USA.

Gidley, J., S. Holditch, D. Nierode, and R. Veatch Jr. (1990), Recent Advances in Hydraulic Fracturing, in *SPE Monograph Series, Vol. 12*, Society of Petroleum Engineers, Richardson, Texas, USA.

Gischig, V. (2015), Rupture propagation behavior and the largest possible earthquake induced by fluid injection into deep reservoirs, *Geophysical Research Letters*, **42**(18), 7420–7428, doi:10.1002/2015GL065072.

Göbel, T. (2015), A comparison of seismicity rates and fluid-injection operations in Oklahoma and California: Implications for crustal stresses, *The Leading Edge*, **34**(6), 640–648, doi:10.1190/tle34060640.1.

Göbel, T., S. Hosseini, F. Cappa, E. Hauksson, J. Ampuero, F. Aminzadeh, and J. Saleeby (2016), Wastewater disposal and earthquake swarm activity at the southern end of the Central Valley, California, *Geophysical Research Letters*, **43**(3), 1092–1099, doi:10.1002/2015GL066948.

Griffiths, D., and I. Smith (2006), *Numerical Methods for Engineers*, 2nd ed., CRC Press.

Gringarten, A., H. Ramey, and R. Raghavan (1974), Unsteady-State Pressure Distributions Created by a Well With a Single Infinite-Conductivity Vertical Fracture, *SPE Journal*, **14**(04), 347–360, doi:10.2118/4051-PA.

Gringarten, A., P. Witherspoon, and Y. Ohnishi (1975), Theory of Heat Extraction From Fractured Hot Dry Rock, *Journal of Geophysical Research*, **80**(8), 1120–1124, doi:10.1029/JB080i008p01120.

Guglielmi, Y., F. Cappa, J.-P. Avouac, P. Henry, and D. Elsworth (2015), Seismicity triggered by fluid injection induced aseismic slip, *Science*, **348**(6240), 1224–1227, doi:10.1126/science.aab0476.

Hajibeygi, H., D. Karvounis, and P. Jenny (2011), A hierarchical fracture model for the iterative multiscale finite volume method, *Journal of Computational Physics*, **230**(24), 8729–8743, doi:10.1016/j.jcp.2011.08.021.

Häring, M., U. Schanz, F. Ladner, and B. Dyer (2008), Characterisation of the Basel 1 Enhanced Geothermal System, *Geothermics*, **37**(5), 469–495, doi:10.1016/j.geothermics.2008.06.002.

Healy, J., W. Rubey, D. Griggs, and C. Raleigh (1968), The Denver earthquakes, *Science*, **161**(3848), 1301–1310, doi:10.1126/science.161.3848.1301.

Heller, R., J. Vermylen, and M. Zoback (2014), Experimental investigation of matrix permeability of gas shales, *AAPG Bulletin*, **98**(5), 975–995, doi:10.1306/09231313023.

Helmstetter, A., and B. Shaw (2009), Afterslip and aftershocks in the rate-and-state friction law, *Journal of Geophysical Research: Solid Earth*, **114**(B01308), 1–24, doi:10.1029/2007JB005077.

Holl, H.-G., and C. Barton (2015), Habanero Field - Structure and State of Stress, in *World Geothermal Congress*, April, pp. 1–8, Melbourne, Australia.

Holland, A. (2013), Earthquakes triggered by hydraulic fracturing in south-central Oklahoma, *Bulletin of the Seismological Society of America*, **103**(3), 1784–1792, doi:10.1785/0120120109.

Hornbach, M., H. DeShon, W. Ellsworth, B. Stump, C. Hayward, C. Frohlich, H. Oldham, J. Olson, M. Magnani, C. Brokaw, and J. Luetgert (2015), Causal factors for seismicity near Azle, Texas, *Nature Communications*, **6**(6728), doi:10.1038/ncomms7728.

Horne, R. (1995), *Modern Well Test Analysis: A Computer-Aided Approach*, 2nd ed., Petroway, Inc., Palo Alto, California, USA.

Horne, R., and J. Tester (2014), Geothermal energy: An emerging option for heat and power, *The Bridge*, **44**(1), 7–15.

Horton, S. (2012), Disposal of Hydrofracking Waste Fluid by Injection into Subsurface Aquifers Triggers Earthquake Swarm in Central Arkansas with Potential for Damaging Earthquake, *Seismological Research Letters*, **83**(2), 250–260, doi:10.1785/gssrl.83.2.250.

House, L., H. Keppler, and H. Kaieda (1985), Seismic studies of a massive hydraulic fracturing experiment, in *Geothermal Resources Council Transactions*, vol. 9, Davis, California, USA.

Howard, G., and C. R. Fast (1957), Optimum Fluid Characteristics for Fracture Extension?, in *Proceedings of the American Petroleum Institute*, pp. 261–270, New York, New York, USA.

Hsieh, P., and J. Bredehoeft (1981), A reservoir analysis of the Denver earthquakes: A case of induced seismicity, *Journal of Geophysical Research*, **86**(B2), 903–920, doi:10.1029/JB086iB02p00903.

Hunsweck, M., Y. Shen, and A. Lew (2008), A finite element approach to the simulation of hydraulic fractures with lag, *International Journal for Numerical and Analytical Methods in Geomechanics*, **32**, 189–213, doi:10.1002/nag.1131.

Ishibashi, T., N. Watanabe, N. Hirano, A. Okamoto, and N. Tsuchiya (2014), Beyond-laboratory-scale prediction for channeling flows through subsurface rock fractures with heterogeneous aperture distributions revealed by laboratory evaluation, *Journal of Geophysical Research: Solid Earth*, **120**(1), 106–124, doi:10.1002/2014JB011555.

Jaeger, J., N. Cook, and R. Zimmerman (2007), *Fundamentals of Rock Mechanics*, 4th ed., Blackwell Publishing Ltd., Oxford.

Juliusson, E. (2012), Characterization of Fractured Geothermal Reservoirs Based on Production Data, Ph.D. thesis, Stanford University.

Karimi-Fard, M., L. Durlofsky, and K. Aziz (2004), An Efficient Discrete-Fracture Model Applicable for General-Purpose Reservoir Simulators, *SPE Journal*, **9**(02), 227–236, doi:10.2118/88812-PA.

Karvounis, D. (2013), Simulations of Enhanced Geothermal Systems with an Adaptive Hierarchical Fracture Representation, Ph.D. thesis, ETH Zurich, doi:10.3929/ethz-a-009967366.

Karvounis, D., and P. Jenny (2016), Adaptive hierarchical fracture model for enhanced geothermal systems, *SIAM*, **14**(1), 207–231, doi:10.1137/140983987.

Karvounis, D., V. Gischig, and S. Wiemer (2014), EGS Probabilistic Seismic Hazard Assessment with 3-D Discrete Fracture Modeling, in *Thirty-Ninth Workshop on Geothermal Reservoir Engineering*, pp. 1–9, Stanford, California, USA.

Kaven, J., S. Hickman, A. McGarr, and W. Ellsworth (2015), Surface Monitoring of Microseismicity at the Decatur, Illinois, CO2 Sequestration Demonstration Site, *Seismological Research Letters*, **86**(4), 1096–1101, doi:10.1785/0220150062.

Kazemi, H. (1969), Pressure Transient Analysis of Naturally Fractured Reservoirs with Uniform Fracture Distribution, *SPE Journal*, **9**(04), 451 – 462, doi:10.2118/2156-A.

Kelkar, S., H. Murphy, and Z. Dash (1986), Earth stress measurements in deep granitic rock, in *27th US Symposium on Rock Mechanics*, Tuscaloosa, Alabama, USA.

Kelkar, S., D. Danko, D. Bahrami, K. Chiu, D. Elsworth, Y. Fang, P. Fu, J. Furtney, Q. Gao, A. Ghassemi, B. Guo, K. Im, M. McClure, R. Podgorney, J. Rutqvist, M. Sarai, M. White, S. White, and Y. Xia (2016), Numerical simulators for enhanced geothermal systems : Benchmark problems of multi-dimensional coupled thermal-hydrologic-mechanical processes (Problems 2 and 4), *Computational Geosciences*, **submitted.**

Keranen, K., H. Savage, G. Abers, and E. Cochran (2013), Potentially induced earthquakes in Oklahoma, USA: Links between wastewater injection and the 2011 Mw 5.7 earthquake sequence, *Geology*, **41**(6), 699–702, doi:10.1130/G34045.1.

Keranen, K., M. Weingarten, G. Abers, B. Bekins, and S. Ge (2014), Sharp increase in central Oklahoma seismicity since 2008 induced by massive wastewater injection., *Science*, **448**(6195), 448–451, doi:10.1126/science.1255802.

Kikani, J. (1989), Application of Boundary Element Method to Streamline Generation and Pressure Transient Testing, Ph.D. thesis, Stanford University.

Kim, J., H. Tchelepi, and R. Juanes (2011), Stability , Accuracy , and Efficiency of Sequential Methods for Coupled Flow and Geomechanics, *SPE Journal*, **16**(02), 249–262, doi:10.2118/119084-PA.

Kim, W.-Y. (2013), Induced seismicity associated with fluid injection into a deep well in Youngstown, Ohio, *Journal of Geophysical Research: Solid Earth*, **118**(7), 3506–3518, doi:10.1002/jgrb.50247.

King, G. (2012), Hydraulic Fracturing 101: What Every Representative, Environmentalist, Regulator, Reporter, Investor, University Researcher, Neighbor and Engineer Should Know About Estimating Frac Risk and Improving Frac Performance in Unconventional Gas and Oil Wells, in *SPE Hydraulic Fracturing Technology Conference*, The Woodlands, Texas, USA, doi:10.2118/152596-MS.

Király-Proag, E., J. Zechar, V. Gischig, S. Wiemer, D. Karvounis, and J. Doetsch (2016), Validating induced seismicity forecast models - Induced Seismicity Test Bench, *Journal of Geophysical Research: Solid Earth*, **121**(8), 6009–6029, doi:10.1002/2016JB013236.

Kurtoglu, B., H. Kazemi, R. Rosen, W. Mickelson, and T. Kosanke (2014), A rock and fluid study of Middle Bakken Formation: Key to enhanced oil recovery, in *SPE/CSUR Unconventional Resources Conference - Canada*, Calgary, Alberta, Canada, doi:10.2118/171668-MS.

Langenbruch, C., and S. Shapiro (2010), Decay rate of fluid-induced seismicity after termination of reservoir stimulations, *Geophysics*, **75**(6), MA53–MA62, doi:10.1190/1.3506005.

Lapusta, N., J. R. Rice, Y. Ben-Zion, and G. Zheng (2000), Elastodynamic analysis for slow tectonic loading with spontaneous rupture episodes on faults with rate- and state-dependent friction, *Journal of Geophysical Research*, **105**, 23,765, doi:10.1029/2000JB900250.

Lee, H. S., and T. F. Cho (2002), Hydraulic Characteristics of Rough Fractures in Linear Flow under Normal and Shear Load, *Rock Mechanics and Rock Engineering*, **35**(4), 299–318, doi:10.1007/s00603-002-0028-y.

Lee, S., C. Jensen, and M. Lough (2000), Efficient Finite-Difference Model for Flow in a Reservoir With Multiple Length-Scale Variations, *SPE Journal*, **5**(3), 268–275, doi:10.2118/65095-PA.

Lee, S., M. Lough, and C. Jensen (2001), Hierarchical Modeling of Flow in Naturally Fractured Formations With Multiple Length Scales, *Water Resources Research*, **37**(3), 443–455, doi:10.1029/2000WR900340.

Lemmon, E., M. McLinden, and D. Friend (2016), Thermophysical Properties of Fluid Systems, in *NIST Chemistry WebBook, NIST Standard Reference Database Number 69*, edited by P. Linstrom and W. Mallard, National Institute of Standards and Technology, Gaithersburg, MD.

Li, L., and S. Lee (2008), Efficient Field-Scale Simulation of Black Oil in a Naturally Fractured Reservoir Through Discrete Fracture Networks and Homogenized Media, *SPE Reservoir Evaluation & Engineering*, **11**(04), 750–758, doi:10.2118/103901-PA.

Linker, M. F., and J. Dieterich (1992), Effects of variable normal stress on rock friction: Observations and constitutive equations, *Journal of Geophysical Research: Solid Earth*, **97**(B4), 4923–4940, doi:10.1029/92JB00017.

Lockner, D., and S. Stanchits (2002), Undrained poroelastic response of sandstones to deviatoric stress change, *Journal of Geophysical Research*, **107**(B12), 2353, doi:10.1029/2001JB001460.

Love, A. (1927), *A Treatise on the Mathematical Theory of Elasticity*, 4th ed., Dover Publications, New York.

Magnusdottir, L. (2013), Fracture Characterization in Geothermal Reservoirs Using Time-lapse Electric Potential Data, Ph.D. thesis, Stanford University.

Mai, P., and G. Beroza (2002), A spatial random field model to characterize complexity in earthquake slip, *Journal of Geophysical Research*, **107**(B11), 2308, doi:10.1029/2001JB000588.

Majer, E., and J. Peterson (2007), The impact of injection on seismicity at The Geysers, California Geothermal Field, *International Journal of Rock Mechanics and Mining Sciences*, **44**(8), 1079–1090, doi:10.1016/j.ijrmms.2007.07.023.

Majer, E., R. Baria, M. Stark, S. Oates, J. Bommer, B. Smith, and H. Asanuma (2007), Induced Seismicity Associated with Enhanced Geothermal Systems, *Geothermics*, **36**(3), 185–222, doi:10.1016/j.geothermics.2007.03.003.

Marone, C. (1998), The effect of loading rate on static friction and the rate of fault healing during the earthquake cycle, *Nature*, **391**, 69–72, doi:10.1038/nature34157.

Marone, C., and B. Kilgore (1993), Scaling Of The Critical Slip Distance For Seismic Faulting With Shear Strain In Fault Zones, *Nature*, **362**(6421), 618–621, doi:10.1038/362618a0.

Matsunaga, I., M. Kadowake, and H. Murphy (1983), Current summary of hydraulic fracturing experiments in Phase II reservoir, *Tech. rep.*, Los Alamos National Laboratory.

McClure, M. (2012), Modeling and Characterization of Hydraulic Stimulation and Induced Seismicity in Geothermal and Shale Gas Reservoirs, Ph.D. thesis, Stanford University.

McClure, M. (2015), Generation of large postinjection-induced seismic events by backflow from dead-end faults and fractures, *Geophysical Research Letters*, **42**, 6647–6654, doi:10.1002/2015GL065028.

McClure, M., and R. Horne (2011), Investigation of injection-induced seismicity using a coupled fluid flow and rate/state friction model, *Geophysics*, **76**(6), WC181–WC198, doi:10.1190/geo2011-0064.1.

McClure, M., and R. Horne (2014a), An investigation of stimulation mechanisms in Enhanced Geothermal Systems, *International Journal of Rock Mechanics and Mining Sciences*, **72**, 242–260, doi:10.1016/j.ijrmms.2014.07.011.

McClure, M., and R. Horne (2014b), Characterizing Hydraulic Fracturing With a Tendency-for-Shear-Stimulation Test, *SPE Reservoir Evaluation & Engineering*, **17**(2), 233–243, doi:10.2118/166332-PA.

McClure, M., A. Ghassemi, P. Fu, D. Bahrami, K. Chiu, D. George, D. Elsworth, J. Furtney, Q. Gan, B. Guo, R. Horne, K. Huang, K. Im, J. Norbeck, R. Podgorney, J. Rutqvist, V. Sesetty, Q. Tau, Q. Tao, M. White, S. White, and Y. Xia (2016a), Numerical simulators for enhanced

geothermal systems : Benchmark problems of single fracture deformation (Problems, 3, 6, and 7), *Computational Geosciences*, **submitted.**

McClure, M., M. Babazadeh, S. Shiozawa, and J. Huang (2016b), Fully Coupled Hydromechanical Simulation of Hydraulic Fracturing in Three-Dimensional Discrete Fracture Networks, *SPE Journal*, **21**(04), 1302–1320, doi:10.2118/173354-PA.

McClure, M. W., and R. N. Horne (2013), *Discrete Fracture Network Modeling of Hydraulic Stimulation: Coupling Flow and Geomechanics*, Springer Briefs in Earth Sciences, doi:10.1007/978-3-319-00383-2.

McGarr, A. (2014), Maximum magnitude earthquakes induced by fluid injection, *Journal of Geophysical Research: Solid Earth*, **119**, 1008–1019, doi:10.1002/2013JB010597.

McGarr, A., B. Bekins, N. Burkardt, J. Dewey, P. Earle, W. Ellsworth, S. Ge, S. Hickman, A. Holland, E. Majer, J. Rubinstein, and A. Sheehan (2015), Coping with earthquakes induced by fluid injection, *Science*, **347**(6224), 830–831, doi:10.1126/science.aaa0494.

McNamara, D., J. Rubinstein, E. Myers, G. Smoczyk, H. Benz, R. Williams, G. Hayes, D. Wilson, R. Herrmann, N. McMahon, R. Aster, E. Bergman, A. Holland, and P. Earle (2015a), Efforts to monitor and characterize the recent increasing seismicity in central Oklahoma, *The Leading Edge*, **34**(6), 628–639, doi:10.1190/tle34060628.1.

McNamara, D. E., H. M. Benz, R. B. Herrmann, E. A. Bergman, P. Earle, A. Holland, R. Baldwin, and A. Gassner (2015b), Earthquake hypocenters and focal mechanisms in central Oklahoma reveal a complex system of reactivated subsurface strike-slip faulting, *Geophysical Research Letters*, **42**(8), 2742–2749, doi:10.1002/2014GL062730.

Mindlin, R. (1936), Force at a point in the interior of a semi-infinite solid, *Journal of Applied Physics*, **7**(5), 195–202, doi:10.1063/1.1745385.

Moinfar, A., A. Varavei, K. Sepehrnoori, and R. Johns (2012), Development of a Novel and Computationally-Efficient Discrete-Fracture Model to Study IOR Processes in Naturally Fractured Reservoirs, in *Eighteenth SPE Improved Oil Recovery Symposium*, Society of Petroleum Engineers, doi:10.2118/154246-MS.

Moinfar, A., K. Sepehrnoori, R. Johns, and A. Varavei (2013), Coupled Geomechanics and Flow Simulation for an Embedded Discrete Fracture Model, in *SPE Reservoir Simulation Symposium*, 1998, pp. 1–17, The Woodlands, Texas, USA, doi:10.2118/163666-MS.

Moos, D., G. Vassilellis, R. Cade, J. Franquet, A. Lacazette, E. Bourtembour, and G. Daniel (2011), Predicting shale reservoir response to stimulation in the Upper Devonian of West Virginia, in *SPE Annual Technical Conference and Exhibition*, Denver, Colorado, USA, doi:145849-MS.

Mossop, A. (2001), Seismicity, subsidence and strain at The Geysers geothermal field, Ph.D. thesis, Stanford University.

Mukuhira, Y., H. Asanuma, H. Niitsuma, and M. Häring (2013), Characteristics of large-magnitude microseismic events recorded during and after stimulation of a geothermal reservoir at Basel, Switzerland, *Geothermics*, **45**, 1–17, doi:10.1016/j.geothermics.2012.07.005.

Murphy, H., and M. Fehler (1986), Hydraulic fracturing of jointed formations, in *SPE Paper 14088 presetend at the International Meeting on Petroleum Engineering*, pp. 489–496, Beijing, China, doi:10.2118/14088-MS.

NCEDC (2014), Northern California Earthquake Data Center, *Tech. rep.*, UC Berkeley Seismological Laboratory, doi:10.7932/NCEDC.

Nelson, P., N. Gianoutsos, and R. Drake (2015), Underpressure in Mesozoic and Paleozoic rock units in the Midcontinent of the United States, *AAPG Bulletin*, **99**(10), 1861–1892, doi:10.1306/04171514169.

Noda, H., E. Dunham, and J. Rice (2009), Earthquake ruptures with thermal weakening and the operation of major faults at low overall stress levels, *Journal of Geophysical Research: Solid Earth*, **114**(B07302), 1–27, doi:10.1029/2008JB006143.

Norbeck, J., and R. Horne (2015a), Injection-triggered seismicity: an investigation of porothermoelastic effects using a rate-and-state earthquake model, in *Fourtieth Workshop on Geothermal Reservoir Engineering*, Stanford, California, USA.

Norbeck, J., and R. Horne (2015b), Investigation of injection-triggered slip on basement faults: role of fluid leakoff on post shut-in seismicity, in *World Geothermal Congress*, April, pp. 19–25, Melbourne, Australia.

Norbeck, J., and R. Horne (2016a), Physical mechanisms related to microseismic-depletion-delineation field tests with application to reservoir surveillance, *SPE Journal*, **21**(04), 1279–1288, doi:10.2118/178926-PA.

Norbeck, J., and R. Horne (2016b), A numerical method for fractured reservoir poromechanics using a mixed-continuum embedded fracture model, in *Geothermal Resources Council Transactions*, Sacramento, California, USA.

Norbeck, J., E. Fonseca, D. V. Griffiths, and S.-W. Wong (2012), Natural fracture identification and characterization while drilling underbalanced, in *SPE Americas Unconventional Resources Conference*, Society of Petroleum Engineers, Pittsburgh, Pennsylvania, USA, doi:10.2118/154864-MS.

Norbeck, J., H. Huang, R. Podgorney, and R. Horne (2014), An integrated discrete fracture model for description of dynamic behavior in fractured reservoirs, in *Thirty-Ninth Workshop on Geothermal Reservoir Engineering*, Stanford, California, USA.

Norbeck, J., M. McClure, J. Lo, and R. Horne (2016a), An embedded fracture modeling framework for simulation of hydraulic fracturing and shear stimulation, *Computational Geosciences*, **20**(1), 1–18, doi:10.1007/s10596-015-9543-2.

Norbeck, J., M. McClure, and R. Horne (2016b), Revisiting stimulation mechanism at Fenton Hill and an investigation of the influence of fault heterogeneity on the Gutenberg-Richter b-value for rate-and-state earthquake simulations, in *41st Workshop on Geothermal Reservoir Engineering*, pp. 1–22, Stanford, California, USA.

Norbeck, J., M. McClure, and R. Horne (2016c), Analysis of hydromechanical reservoir response during fluid circulation at the Fenton Hill Enhanced Geothermal System test site, in *Proceedings of 38th New Zealand Geothermal Workshop*, Auckland, New Zealand.

Norbeck, J. H., and R. N. Horne (2016c), Evidence for a transient hydromechanical and frictional faulting response during the 2011 Mw 5.6 Prague, Oklahoma earthquake sequence, *Journal of Geophysical Research: Solid Earth*, **121**, doi:10.1002/2016JB013148.

Nowacki, W. (1986), *Thermoelasticity*, 2nd ed., Pergamon Press, Oxford.

NRC (2013), *Induced Seismicity Potential in Energy Technologies*, 1–225 pp., National Academic Press, doi:10.17226/13355.

Nur, A., and J. Booker (1972), Aftershocks caused by pore fluid flow?, *Science*, **175**(4024), 885–887, doi:10.1126/science.175.4024.885.

Obermann, A., T. Kraft, E. Larose, and S. Wiemer (2015), Potential of ambient seismic noise techniques to monitor the St. Gallen geothermal site (Switzerland), *Journal of Geophysical Research: Solid Earth*, **120**, 4301–4316, doi:10.1002/2014JB011817.

OCC (2016), Oklahoma Corporation Commission, `http://www.occeweb.com/`, accessed 17 July, 2016.

Ohtake, M. (1974), Seismic activity induced by water injection at Matsushiro, Japan, *J. Phys. Earth*, **22**, 163–176, doi:10.4294/jpe1952.22.163.

Okada, Y. (1992), Internal deformation due to shear and tensile faults in a half-space, *Bulletin of the Seismological Society of America*, **82**(2), 1018–1040.

Okubo, P., and K. Aki (1987), Fractal geometry in the San Andreas Fault System, *Journal of Geophysical Research*, **92**(B1), 345–355, doi:10.1029/JB092iB01p00345.

Peaceman, D. (1978), Interpretation of Well-Block Pressures in Numerical Reservoir Simulation, *SPE Journal*, **18**(03), 183–194, doi:10.2118/6893-PA.

Petersen, M., M. Moschetti, P. Powers, C. Mueller, K. Haller, A. Frankel, Y. Zeng, S. Rezaeian, S. Harmsen, O. Boyd, N. Field, R. Chen, K. Rukstales, N. Luco, R. Wheeler, R. Williams, and A. Olsen (2014), Documentation for the 2014 Update of the United States National Seismic Hazard Maps, *Tech. rep.*, United States Geological Survey, doi:http://dx.doi.org/10.3133/ofr20141091.

Petersen, M., C. Mueller, M. Moschetti, S. Hoover, A. Llenos, W. Ellsworth, A. Michael, J. Rubinstein, A. McGarr, and K. Rukstales (2016), 2016 One-Year Seismic Hazard Forecast for the Central and Eastern United States from Induced and Natural Earthquakes, *Tech. Rep. Version 1.1, June*, United States Geological Survey, doi:10.3133/OFR20161035.

Phillips, W. S., L. S. House, and M. C. Fehler (1997), Detailed joint structure in a geothermal reservoir from studies of induced microearthquake clusters, *Journal of Geophysical Research*, **102**(B6), 11,745–11,763, doi:10.1029/97JB00762.

Pine, R. J., and A. S. Batchelor (1984), Downward migration of shearing in jointed rock during hydraulic injections, *International Journal of Rock Mechanics and Mining Sciences and*, **21**(5), 249–263, doi:10.1016/0148-9062(84)92681-0.

Pluimers, S. (2015), Hierarchical Fracture Modeling Approach, Master's thesis, Delft University of Technology.

Pollard, D., and R. Fletcher (2005), *Fundamentals of Structural Geology*, Cambridge University Press, Cambridge.

Raleigh, C., J. Healy, and J. Bredehoeft (1976), An experiment in earthquake control at Rangely, Colorado, *Science*, **191**(4233), 1230–7, doi:10.1126/science.191.4233.1230.

Rana, R. (1984), Exploratory Study on the Influence of Thermal Stressing on the Strength and Porosity of Granite, Ph.D. thesis, Stanford University.

Rangarajan, R., M. Chiaramonte, M. Hunsweck, Y. Shen, and A. Lew (2015), Simulating curvilinear crack propagation in two dimensions with universal meshes, *International Journal for Numerical Methods in Engineering*, **102**(3-4), 632–670, doi:10.1002/nme.4731.

Rice, J., and Y. Ben-Zion (1996), Slip complexity in earthquake fault models., *Proceedings of the National Academy of Sciences of the United States of America*, **93**(9), 3811–3818, doi:10.1073/pnas.93.9.3811.

Rice, J., N. Lapusta, and K. Ranjith (2001), Rate and state dependent friction and the stability of sliding between elastically deformable solids, *Journal of the Mechanics and Physics of Solids*, **49**(9), 1865–1898, doi:10.1016/S0022-5096(01)00042-4.

Rice, J., E. Dunham, and H. Noda (2010), Thermo- and hydro-mechanical processes along faults during rapid slip, in *Meso-Scale Shear Physics in Earthquake and Landslide Mechanics*, edited by Y. Hatzor, J. Sulem, and I. Vardoulakis, pp. 3–16, CRC Press.

Rice, J. R. (1980), The mechanics of earthquake rupture, in *Physics of the Earth's Interior: Proc. Int. Sch. Phys. Enrico Fermi*, edited by A. Dziewonski and E. Boschi, pp. 555–649, Italian Physical Society/North Holland Publishing Company.

Rice, J. R. (1993), Spatio-temporal complexity of slip on a fault, *Journal of Geophysical Research*, **98**(B6), 9885, doi:10.1029/93JB00191.

Rice, J. R., and A. Ruina (1983), Stability of Steady Frictional Slipping, *Journal of Applied Mechanics*, **50**(2), 343–349, doi:10.1115/1.3167042.

Ripperger, J., J. P. Ampuero, P. M. Mai, and D. Giardini (2007), Earthquake source characteristics from dynamic rupture with constrained stochastic fault stress, *Journal of Geophysical Research: Solid Earth*, **112**(4), 1–17, doi:10.1029/2006JB004515.

Roeloffs, E. (1996), Poroelastic techniques in the study of earthquake-related hydrologic phenomena, *Advances in Geophysics*, **37**, 135–195, doi:10.1016/S0065-2687(08)60270-8.

Rojas, O., E. Dunham, S. Day, L. Dalguer, and J. Castillo (2009), Finite difference modelling of rupture propagation with strong velocity-weakening friction, *Geophysical Journal International*, **179**(3), 1831–1858, doi:10.1111/j.1365-246X.2009.04387.x.

Rothert, E., and S. Shapiro (2007), Statistics of fracture strength and fluid-induced microseismicity, *Journal of Geophysical Research: Solid Earth*, **112**(B04309), 1–16, doi:10.1029/2005JB003959.

Rubinstein, J., and A. Mahani (2015), Myths and Facts on Wastewater Injection, Hydraulic Fracturing, Enhanced Oil Recovery, and Induced Seismicity, *Seismological Research Letters*, **86**(4), 1060–1067, doi:10.1785/0220150067.

Rubinstein, J., W. Ellsworth, A. McGarr, and H. Benz (2014), The 2001-present induced earthquake sequence in the Raton Basin of northern New Mexico and southern Colorado, *Bulletin of the Seismological Society of America*, **104**(5), 2162–2181, doi:10.1785/0120140009.

Safari, R., and A. Ghassemi (2016), Three-dimensional poroelastic modeling of injection induced permeability enhancement and microseismicity, *International Journal of Rock Mechanics and Mining Sciences*, **84**, 47–58, doi:10.1016/j.ijrmms.2015.12.007.

Sasaki, S. (1998), Characteristics of microseismic events induced during hydraulic fracturing experiments at the Hijiori hot dry rock geothermal energy site, Yamagata, Japan, *Tectonophysics*, **289**(1-3), 171–188, doi:10.1016/S0040-1951(97)00314-4.

Saupe, D. (1988), The Science of Fractal Images, in *The Science of Fractal Images*, edited by H.-O. Peitgen and D. Saupe, pp. 71–136, Springer-Verlag, New York, doi:10.1007/978-1-4612-3784-6.

SED (2013), Earthquake chronology geothermal energy project in St. Gallen, `http://www.seismo.ethz.ch/sed/archive/Archiv_2013/copy_of_Chronologie_SG/index_EN`, accessed 16 November, 2013.

Segall, P. (1989), Earthquakes triggered by fluid extraction, *Geology*, **17**(10), 942–946, doi:10.1130/0091-7613.

Segall, P. (2010), *Earthquake and Volcano Deformation*, Princeton University Press, Princeton.

Segall, P., and S. Lu (2015), Injection-induced seismicity: Poroelastic and earthquake nucleation effects, *Journal of Geophysical Research: Solid Earth*, **120**, 1–22, doi:10.1002/2015JB012060.

Shapiro, S. A., S. Rentsch, and E. Rothert (2005), Characterization of hydraulic properties of rocks using probability of fluid-induced microearthquakes, *Geophysics*, **70**(2), F27–F33, doi:10.1190/1.1897030.

Shewchuk, J. (1996), Triangle: Engineering a 2D Quality Mesh Generator and Delaunay Triangulator, in *Applied Computational Geometry: Towards Geometric Engineering*, edited by M. Lin and D. Manocha, chap. Lecture No, pp. 203–222, Springer-Verlag.

Shiozawa, S., and M. McClure (2014), EGS Designs with Horizontal Wells, Multiple Stages, and Proppant, in *39th Stanford Geothermal Workshop*, Stanford, California, USA.

Shou, K., and S. Crouch (1995), A Higher Order Displacement Discontinuity Method for Analysis of Crack Problems, *Int. J. Rock Mech. Min. Sci. & Geomech. Abstr.*, **32**(1), 49–55, doi:10.1016/0148-9062(94)00016-V.

Sibson, R. (2014), Earthquake Rupturing in Fluid-Overpressured Crust: How Common?, *Pure and Applied Geophysics*, **171**(11), 2867–2885, doi:10.1007/s00024-014-0838-3.

Smith, I., D. Griffiths, and L. Margetts (2014), *Programming the Finite Element Method*, 5th ed., John Wiley & Sons, Ltd., Chichester.

Snow, D. (1965), A Parallel Plate Model of Fractured Permeable Media, Ph.D. thesis, University of California, Berkeley.

Sumy, D., E. Cochran, K. Keranen, M. Wei, and G. Abers (2014), Observations of static Coulomb stress triggering of the November 2011 M 5.7 Oklahoma earthquake sequence, *Journal of Geophysical Research: Solid Earth*, **119**(3), 1904–1923, doi:10.1002/2013JB010612.Received.

Sun, X., and S. Hartzell (2014), Finite-fault slip model of the 2011 Mw 5.6 Prague, Oklahoma earthquake from regional waveforms, *Geophysical Research Letters*, **41**(12), 4207–4213, doi:10.1002/2014GL060410.

Tene, M., M. Kobaisi, and H. Hajibeygi (2016), Algebraic multiscale method for flow in heterogeneous porous media with embedded discrete fractures (F-AMS), *Journal of Computational Physics*, **321**, 819–845, doi:10.1016/j.jcp.2016.06.012.

Tester, J., H. Murphy, C. Grigsby, R. Potter, and B. Robinson (1989), Fractured Geothermal Reservoir Growth Induced by Heat Extraction, *SPE Reservoir Engineering*, **4**(01), 97–104, doi:10.2118/15124-PA.

Tester, J., B. Anderson, B. Batchelor, A. Blackwell, R. DiPippo, E. Drake, and S. Petty (2006), The future of geothermal energy: Impact of enhanced geothermal systems (EGS) on the United States in the 21st century, *Tech. rep.*, Massachusetts Institute of Technology.

Thomas, M. (2013), Frictional properties of faults: from observation on the Longitudinal Valley Fault, Taiwan, to dynamic simulations, Ph.D. thesis, California Institute of Technology.

Timoshenko, S., and J. Goodier (1951), *Theory of Elasticity*, McGraw-Hill, New York.

Townend, J., and M. D. Zoback (2000), How faulting keeps the crust strong, *Geology*, **28**(5), 399–402, doi:10.1130/0091-7613(2000)28<399:HFKTCS>2.0.CO;2.

Valko, P., and M. Economides (1995), *Hydraulic Fracture Mechanics*, Wiley, Chichester.

van der Elst, N., M. Page, D. Weiser, T. Goebel, and S. Hosseini (2016), Induced earthquake magnitudes are as large as (statistically) expected, *Geophysical Research Letters*, **121**(6), 4575–4590, doi:10.1002/2016JB012818.

van Poollen, H., and D. Hoover (1970), Waste Disposal and Earthquakes at the Rocky Mountain Arsenal, Derby, Colorado, *Journal of Petroleum Technology*, pp. 983–993, doi:10.2118/2558-PA.

Vassilellis, G., C. Li, R. Seader, and D. Moos (2010), Investigating the Expected Long-Term Production Performance of Shale Reservoirs, in *Canadian Unconventional Resources & International Petroleum Conference*, October, pp. 1–12, Calgary, Alberta, Canada, doi:10.2118/138134-MS.

Vermylen, J., and M. Zoback (2011), Hydraulic Fracturing, Microseismic Magnitudes, and Stress Evolution in the Barnett Shale, Texas, USA, in *SPE Hydraulic Fracturing Technology Conference and Exhibition*, 2009, The Woodlands, Texas, USA, doi:10.2118/140507-MS.

Vinsome, P., and J. Westerveld (1980), a Simple Method for Predicting Cap and Base Rock, *Journal of Canadian Petroleum Technology*, **19**(03), 87–90, doi:10.2118/80-03-04.

Walsh, F., and M. Zoback (2015), Oklahoma's recent earthquakes and saltwater disposal, *Science Advances*, **1**(5), e1500,195, doi:10.1126/sciadv.1500195.

Walsh, F., and M. Zoback (2016), Probabilistic assessment of potential fault slip related to injection-induced earthquakes: Application to north central Oklahoma, USA, *Geology*, **44**(12), 1–4, doi:10.1130/G38275.1.

Walters, R., M. Zoback, J. Baker, and G. Beroza (2015), Characterizing and responding to seismic risk associated with earthquakes potentially triggered by saltwater disposal and hydraulic fracturing, *Seismological Research Letters*, **86**(4), 1–19, doi:10.1785/0220150048.

Warpinski, N. (2009), Microseismic monitoring: Inside and Out, *Journal of Petroleum Technology*, **61**(11), 80–85, doi:10.2118/118537-JPT.

Warpinski, N., J. Du, and U. Zimmer (2012), Measurements of Hydraulic-Fracture-Induced Seismicity in Gas Shales, *SPE Production & Operations*, **27**(03), 240–252, doi:10.2118/151597-PA.

Warren, J., and P. Root (1963), The Behavior of Naturally Fractured Reservoirs, *SPE Journal*, **3**(03), 245–255, doi:10.2118/426-PA.

Weingarten, M., S. Ge, J. Godt, B. Bekins, and J. Rubinstein (2015), High-rate injection is associated with the increase in U.S. mid-continent seismicity, *Science*, **348**(6241), 1336–1340, doi:10.1126/science.aab1345.

Weng, X., O. Kresse, C. Cohen, R. Wu, and H. Gu (2011), Modeling of Hydraulic-Fracture-Network Propagation in a Naturally Fractured Formation, *SPE Production & Operations*, **26**(4), 368–380, doi:10.2118/140253-PA.

White, M., and B. Phillips (2015), Code Comparison Study Fosters Confidence in the Numerical Simulation of Enhanced Geothermal Systems, in *Fourtieth Workshop on Geothermal Reservoir Engineering*, Stanford, California, USA.

White, M., D. Bahrami, G. Danko, D. Elsworth, P. Fu, J. Furtney, Q. Gao, A. Ghassemi, R. Horne, S. Kelkar, M. McClure, J. Norbeck, R. Podgorney, J. Rutqvist, E. Sonnenthal, Q. Tao, Y. Wong, and M. Safari (2016a), Numerical simulators for enhanced geothermal systems : GTO-CCS codes, *Computational Geosciences*, **submitted**.

White, S., S. Purohit, and L. Boyd (2015), Using GTO-Velo to Facilitate Communication and Sharing of Simulation Results in Support of the Geothermal Technologies Office Code Comparison Study, in *Fourtieth Workshop on Geothermal Reservoir Engineering*, Stanford, California, USA.

White, S., S. Kelkar, and D. Brown (2016b), Bringing Fenton Hill into the Digital Age: Data Conversion in Support of the Geothermal Technologies Office Code Comparison Study Challenge Problems, in *41st Workshop on Geothermal Reservoir Engineering*, Stanford, California, USA.

Willis-Richards, J., K. Watanabe, and H. Takahashi (1996), Progress toward a stochastic rock mechanics model of engineered geothermal systems, *Journal of Geophysical Research: Solid Earth*, **101**(B8), 17,481–17,496, doi:10.1029/96JB00882; doi:10.1029/9.

Witherspoon, P., J. Wang, K. Iwai, and J. Gale (1980), Validity of Cubic Law for fluid flow in a deformable rock fracture, *Water Resources Research*, **16**(6), 1016–1024, doi:10.1029/WR016i006p01016.

Xue, L., H.-B. Li, E. Brodsky, Z.-Q. Xu, Y. Kano, H. Wang, J. Mori, J.-L. Si, J.-L. Pei, W. Zhang, G. Yang, Z.-M. Sun, and Y. Huang (2013), Continuous permeability measurements record healing inside the Wenchuan earthquake fault zone, *Science*, **340**(6140), 1555–1559, doi:10.1126/science.1229223.

Yan, X., Z. Huang, J. Yao, Y. Li, and D. Fan (2016), An efficient embedded discrete fracture model based on mimetic finite difference method, *Journal of Petroleum Science and Engineering*, **145**, 11–21, doi:10.1016/j.petrol.2016.03.013.

Yang, Y., and M. Zoback (2014), The role of preexisting fractures and faults during multistage hydraulic fracturing in the Bakken Formation, *Interpretation*, **2**(3), SG25–SG39, doi:10.1190/INT-2013-0158.1.

Yeck, W., A. Sheehan, H. Benz, M. Weingarten, and J. Nakai (2016), Rapid response, monitoring, and mitigation of induced seismicity near Greeley, Colorado, *Seismological Research Letters*, **87**(4), 837–847, doi:10.1785/0220150275.

Zimmerman, R. (1992), Compressibility of sandstones, in *Developments in Petroleum Science*, vol. 29, edited by G. Chilingarian, Elsevier, Amsterdam, The Netherlands, doi:10.1016/0920-4105(92)90053-4.

Zoback, M. (2007), *Reservoir Geomechanics*, Cambridge University Press, Cambridge.

Zoback, M., and S. Gorelick (2012), Earthquake triggering and large-scale geologic storage of carbon dioxide., *Proceedings of the National Academy of Sciences of the United States of America*, **109**(26), 10,164–10,168, doi:10.1073/pnas.1202473109.